



**HAL**  
open science

# Multifunctional nanoparticles for imaging and tracking with potential applications in radiotherapy

Magali Lavenas

► **To cite this version:**

Magali Lavenas. Multifunctional nanoparticles for imaging and tracking with potential applications in radiotherapy. Material chemistry. Université de Bordeaux; Universidade de Aveiro (Portugal), 2017. English. NNT : 2017BORD0803 . tel-01967619

**HAL Id: tel-01967619**

**<https://theses.hal.science/tel-01967619>**

Submitted on 1 Jan 2019

**HAL** is a multi-disciplinary open access archive for the deposit and dissemination of scientific research documents, whether they are published or not. The documents may come from teaching and research institutions in France or abroad, or from public or private research centers.

L'archive ouverte pluridisciplinaire **HAL**, est destinée au dépôt et à la diffusion de documents scientifiques de niveau recherche, publiés ou non, émanant des établissements d'enseignement et de recherche français ou étrangers, des laboratoires publics ou privés.

THÈSE EN COTUTELLE PRÉSENTÉE  
POUR OBTENIR LE GRADE DE  
**DOCTEUR DE**  
**L'UNIVERSITÉ DE BORDEAUX**  
**ET DE L'UNIVERSITÉ D'AVEIRO**

ÉCOLE DOCTORALE DES SCIENCES CHIMIQUES  
ÉCOLE DOCTORALE DE QUÍMICA D'AVEIRO  
SPÉCIALITÉ PHYSICO-CHIMIE DE LA MATIÈRE CONDENSÉE

Par Magali LAVENAS

**Multifunctional nanoparticles for imaging and tracking with  
potential applications in radiotherapy**

Sous la direction de Marie-Hélène DELVILLLE  
et de João ROCHA

Soutenue le mercredi 6 décembre 2017

Membres du jury :

M. PIO Casimiro Adrião	Universidade de Aveiro	Président
Mme BEGIN-COLLIN Sylvie	Université de Strasbourg	Rapporteur
M. GERALDES Carlos FGC	Universidade de Coimbra	Rapporteur
Mme DELVILLE Marie-Hélène	ICMCB, CNRS	Directeur de thèse
M. ROCHA João	Universidade de Aveiro	Directeur de thèse
M. TOUPANCE Thierry	Université de Bordeaux	Examinateur
Mme BERMUDEZ Veronica Zea	Universidade de Trás-os-Montes e Alto Douro	Examinateur
M. FARINHA José	Universidade de Lisboa	Examinateur
M. CARLOS Luis D	Universidade de Aveiro	Invité



## English abstract

Cancer is one of the main cause of mortality in the world. Nanotechnologies are creating new approaches to cancer therapy, and it is of interest to design multimodal nanoparticles (NPs) and assess their therapeutic potential. The inorganic NPs studied in this thesis are based on metal oxides (*e.g.*, TiO<sub>2</sub> and HfO<sub>2</sub>) exhibiting functionalities that enable their localization and tracking by techniques, such as MRI and luminescence, as well as their quantification. When ionizing radiation impinges on these metal oxides, numerous electrons are generated, increasing considerably the energy transferred to tumors. Thus, radiotherapy becomes more efficient, while the irradiation dose of healthy tissues remains low.

In this context, NPs should be endowed with certain properties, such as the ability to cross biological barriers, and non-toxicity for humans. Moreover, it is important to be able to detect NPs in the human body, especially in the tumor target, via their magnetic or luminescence properties. For this purpose, rare-earth elements are inserted in the metal oxide matrices. As the lethal temperature for healthy and tumor cells is different, it is also essential to ascertain the temperature of the cells during the radiation treatment. This may be achieved based on the light emission of suitable pairs of rare-earth elements.

Titania (anatase) and hafnia (monoclinic) NPs were synthesized by the hydrothermal method enabling the control of morphology and size. Synthetic parameters were tuned to yield NPs of a size suitable for biological applications (30 – 60 nm). By adjusting the composition of a mixture of the structuring agents triethanolamine and oleic acid, TiO<sub>2</sub> NPs were prepared with a range of sizes and morphologies. Altering the pH changed the habit of hafnium oxide NPs, while increasing the temperature decreased NPs size. Furthermore, the hafnia matrices were doped with rare-earth elements, such as europium, terbium and gadolinium, endowing NPs with functionalities such as luminescence tracking, magnetic resonance imaging and nanothermometry. The measured relaxivity constants indicate the NPs are potential T<sub>2</sub>-weighted MRI contrast agents. Luminescence properties were also studied, and one nanothermometer (Eu<sub>0.01</sub>Tb<sub>0.03</sub>Gd<sub>0.16</sub>:HfO<sub>2</sub>) with room-temperature sensitivity of 0.1 %·K<sup>-1</sup> was obtained.

## Portuguese abstract

O cancro é hoje uma das principais causas de morte no mundo. As nanotecnologias estão a criar novas formas de tratamento das doenças oncológicas, sendo importante desenhar nanopartículas (NPs) multimodais e avaliar o seu potencial terapêutico. As NPs inorgânicas estudadas nesta tese são baseadas em óxidos de metais (nomeadamente  $\text{TiO}_2$  and  $\text{HfO}_2$ ) e exibem funcionalidades que permitem, quer a sua localização e rastreamento por técnicas como MRI e luminescência, quer a sua quantificação. Quando radiação ionizante incide nestes óxidos gera-se um grande número de electrões, o que aumenta consideravelmente a energia transferida para os tumores. Assim, a eficiência da radioterapia aumenta, ao mesmo tempo que a dose de radiação recebida pelos tecidos saudáveis permanece baixa.

Neste contexto, as NPs devem ser dotadas de certas propriedades, como a capacidade de atravessar membranas biológicas, e a não toxicidade para os seres humanos. É, também, importante poder detectar as NPs no corpo humano, em particular no tumor-alvo, através das suas propriedades magnéticas ou de luminescência. Para este efeito, inserem-se terras-raras nas matrizes dos óxidos de metais. Uma vez que a temperatura letal para as células saudáveis e para as tumorais é diferente, é importante poder medir a temperatura celular durante a irradiação, o que pode fazer-se com base na emissão de luz pelas terras-raras.

Sintetizaram-se NPs de titânia (anatase) e hafnia (monoclinica) pelo método hidrotérmico, que permitiu controlar a sua morfologia e o seu tamanho. Os parâmetros de síntese foram ajustados por forma a obter NPs com a dimensão adequada às aplicações biológicas (30 – 60 nm). Afinando a composição de uma mistura contendo os agentes estruturantes trietanolamina e ácido oleico, obtiveram-se NPs de  $\text{TiO}_2$  com uma gama de tamanhos e formas. A alteração do pH resultou na mudança do hábito das NPs de óxido de háfnio, enquanto que o aumento da temperatura diminuiu o seu tamanho. Doparam-se as matrizes de hafnia com terras-raras, como európio, térbio e gadolínio, que conferiram às NPs funcionalidades como rastreamento por luminescência, capacidade de imagem por ressonância magnética, e nanotermometria. As relaxividades medidas indicam que as NPs têm potencial como agentes de contraste MRI com ponderação  $T_2$ . As propriedades de luminescência foram, também, estudadas, tendo sido preparado um nanotermómetro ( $\text{Eu}_{0.01}\text{Tb}_{0.03}\text{Gd}_{0.16}:\text{HfO}_2$ ) com sensibilidade  $0.1 \text{ \%}\cdot\text{K}^{-1}$ , à temperatura ambiente.

## Acknowledgements

These three years are the conclusion of numerous exchanges and various collaborations. Therefore I really want to thank everyone who has contributed to this work.

I would like to start by warmly thanking my thesis supervisors, Marie-Hélène Delville and João Rocha, for their support throughout these three years, and for giving me the opportunity to achieve my thesis between two different labs.

I would like to say how grateful I am to the rapporteurs, Sylvie Bégin-Colin, Professor at the University of Strasbourg and Carlos FGC Geraldes, Professor at the University of Coimbra, who accepted to review my thesis. I also thank the members of the jury, who came to evaluate my work.

During my first year, I had the opportunity to participate in the supervision of two interns: Irene Tagliaro and Quentin Cachia. Thus, I was able to interact with them, and to teach them how I performed the synthesis. I want to especially thank Irene, with whom we worked a lot on the optimization of the synthesis of hafnium oxide nanoparticles.

I would also like to thank the labmates from ICMCB in Bordeaux and at the University of Aveiro, and especially Dimos and Guillaume, who are in “cotutelle” between these two universities too.

I would like to thank Marion Gayot, Philippe Legros, Michel Martineau and François Weill at Placamat and Marta Ferro, at the University of Aveiro, for allowing me to perform TEM analyses essential to my thesis. I want to thank the XRD service at ICMCB, and at the University of Aveiro as well. I am thankful for the time and help Duarte Ananias gave me for the luminescence characterization, and Luis Carlos’s help in the interpretation of the results. I also would like to thank Pedro Cruz, who taught me a lot about the relaxivity and helped me a lot on the relaxivity measurements performed in Coimbra and Carlos Geraldes, who allowed me to come to Coimbra to perform these analyses. I would also like to thank the team in CENBG, and especially Marina Simon and Hervé Seznec, for the discussion about the interactions of the nanoparticles and the cells. Finally, I would like to mention Marina’s help and the opportunity she gave me to do some experiments on the cell culture and their exposition to the nanoparticles.

I thank the financial support of FCT for a grant from CICECO - Aveiro Institute of Materials, POCI-01-0145-FEDER-007679 (FCT Ref. UID/CTM/50011/2013), financed by national funds through the FCT/MEC and when appropriate co-financed by FEDER under the PT2020 Partnership Agreement. I thank also the Idex of Bordeaux for funding as well as the COST action MP1202

## Lists of abbreviation:

ADME	Absorption distribution metabolism excretion
BET	Brunauer, Emmett and Teller
CA	Citric acid
CENBG	Centre d'études nucléaires de Bordeaux Gradignan
CICECO	Centre for Research in Ceramics and Composite Materials
CNS	Central nervous system
CT	Charge transfer
CTAB	Cetyltrimethylammonium bromide
DLS	Dynamic Light Scattering
DNA	Deoxyribonucleic acid
DOTA	1,4,7,10-tetracarboxylmethyl-1,4,7,10-tetraazacyclododecane
DRAM	Dynamic random access memory
DTPA	Diethylenetriaminepentaacetic acid
EDS	Energy-dispersive X-ray spectroscopy
EDX	Energy-dispersive X-ray spectroscopy
EPR	Enhanced permeability and retention
FFT	Fast Fourier transform
HRTEM	High resolution transmission electronic microscopy
ICDD	International center for diffraction data
ICMCB	Institut de chimie de la matière condensée de Bordeaux
ICP	Inductively Coupled Plasma
IEP	Isoelectric point
IV	Intravenous
JCPDS	Joint Committee on Powder Diffraction Standards
LIR	Luminescence Intensity Ratio
MOF	Metal organic framework
MRI	Magnetic resonance imaging
mRNA	Messenger ribonucleic acid
MWNTs	Multi-walled nanotubes
NIR	Near infrared
NMR	Nuclear magnetic resonance
NNs	Nanoneedles
NP	Nanoparticle
NPs	Nanoparticles
OA	Oleic acid
PEG	Polyethylene glycol
QDs	Quantum dots
RE	Rare earth
ROS	Reactive oxygen species

rt	Room temperature
SPIO	Superparamagnetic iron oxide
sSN	Scrolled nanosheet
STEM	Scanning transmission electronic microscopy
SWNTs	Single-walled nanotubes
TE	Echo time
TEM	Transmission electronic microscopy
TEOA	Triethanolamine
TOPO	Trioctylphosphine oxide
TR	Repetition time
USPIO	Ultrasmall superparamagnetic iron oxide
XRD	X-ray diffraction
Z	Atomic number

# Table of contents

Introduction.....	1
Chapter 1: State of the art.....	7
Chapter 2: Titanium dioxide, TiO <sub>2</sub> .....	39
Chapter 3: Hafnium dioxide, HfO <sub>2</sub> .....	93
Chapter 4: Optical imaging and nanothermometry....	149
Chapter 5: Relaxometry.....	189
Conclusions and perspectives.....	223

# Introduction



Cancer is one of the major cause of mortality in the world [1]. More than 90% of cancer-related deaths occur by the spread of malignant cells to vital organs [2], a process called metastasis [3]. Nowadays, several ways to destroy cancer cells have been developed, including chemotherapy, surgical therapy, hormonotherapy, immunotherapy and radiotherapy [4]. Each of these approaches has severe drawbacks. For instance, the ionizing radiation used in radiotherapy goes through healthy cells before reaching the tumor target. The emergence of nanotechnologies has led to new approaches in local cancer therapy. Nanoparticles (NPs) with high electron density offer the possibility to selectively release high amounts of energy within the cancer cells, when activated by ionizing radiation. Thus, cancer cells can be killed and the surrounding healthy cells survive the treatment [5]. In this context, it is crucial to design NPs with several functionalities [6-7], able to cross biological barriers while being non-toxic for the healthy cells of the human body. NPs must be amenable to tracking in the human body, especially in the tumor target using an imaging technique, *e.g.*, based on their magnetic or luminescence properties.

This thesis is part of a wider project entitled “Multiscale evaluation (from *in silico* to *in cellulo* and *in vivo*) of new anticancer strategies based on ionizing radiation and nanoparticles”. This project aims at answering the new challenges in the medical field, more precisely in the radiotherapy treatment and the optimization of the ionizing radiation effects. Such challenges encompass: (i) synthesis of nanoparticles; (ii) *in cellulo* quantitative definition of the nanoparticle’s dose (depending on the physicochemical characteristics of the nanoparticles, and on the biology); (iii) study of the *in cellulo/in vivo* internalization, bio-accumulation, and bio-persistence mechanisms of the nanoparticles; (iv) *in cellulo* and *in vivo* feasibility studies of the therapeutic potential; and (v) development of predictive methodologies (simulations) and experimental validation (micro dosimetry, proton irradiation by ion beam and medical beam). This project is a collaboration between several partners: CENBG, ICMCB, and the clinical services in radiotherapy at the Institut Bergonié in France. My thesis has been developed in the frame of a collaboration (“co-tutelle”) between ICMCB (Université de Bordeaux) and CICECO (Universidade de Aveiro), and its overarching goal is to develop, synthesize and characterize multifunctional nanoparticles that the biologists and doctors will use to *in cellulo* tests.

This thesis consists of the following five chapters.

The first chapter reviews the state-of-the-art, focusing first on the interactions between NPs and biological systems, and on the effects of the combination of NPs and radiotherapy. Next, the NP requirements to be suitable for biological applications and the nanomaterials already used in the biomedical field are described. Moreover, the choice of the two metal oxides ( $\text{TiO}_2$  and  $\text{HfO}_2$ ) studied in this thesis is explained.

Chapter 2 focuses on the development of  $\text{TiO}_2$  nanoparticles, describing the synthetic pathways available in the literature, and presenting our own work on the synthesis of such nanoparticles with controlled morphology and size.

Chapter 3 centers on the development of  $\text{HfO}_2$  nanoparticles. Firstly, the synthetic pathways reported in the literature are summarized. Secondly, I described our study on the effect of synthesis parameters, such as pH, amount of precursor, reaction time, and temperature, on the NP size and morphology. The chapter closes with a discussion of the syntheses of multifunctional lanthanide-bearing  $\text{HfO}_2$  nanoparticles, such as europium, terbium and gadolinium.

Chapter 4 reports on the characterization of the luminescence properties of the multifunctional nanoparticles previously synthesized. The use of NPs as ratiometric nanothermometers is also considered.

Chapter 5 presents the relaxivity properties of the multifunctional nanoparticles and discusses their potential application as MRI contrast agents.

## Bibliography

1. De Martel, C.; Ferlay, J.; Franceschi, S.; Vignat, J.; Bray, F.; Forman, D.; Plummer, M., Global burden of cancers attributable to infections in 2008: a review and synthetic analysis. *The Lancet Oncology* **2012**, *13* (6), 607-615.
2. Reya, T.; Morrison, S. J.; Clarke, M. F.; Weissman, I. L., Stem cells, cancer, and cancer stem cells. *Nature* **2001**, *414* (6859), 105-111.
3. Klein, C. A., The Metastasis Cascade. *Science* **2008**, *321* (5897), 1785-1787.
4. Fiandra, L.; Mazzucchelli, S.; De Palma, C.; Colombo, M.; Allevi, R.; Sommaruga, S.; Clementi, E.; Bellini, M.; Prospero, D.; Corsi, F., Assessing the in vivo targeting efficiency of multifunctional nanoconstructs bearing antibody-derived ligands. *ACS Nano* **2013**, *7* (7), 6092-6102.
5. Mazzucchelli, S.; Colombo, M.; Verderio, P.; Rozek, E.; Andreatta, F.; Galbiati, E.; Tortora, P.; Corsi, F.; Prospero, D., Orientation Controlled Conjugation of Haloalkane Dehalogenase Fused Homing Peptides to Multifunctional Nanoparticles for the Specific Recognition of Cancer Cells. *Angewandte Chemie International Edition* **2013**, *52* (11), 3121-3125.
6. Cho, K.; Wang, X.; Nie, S.; Shin, D. M., Therapeutic nanoparticles for drug delivery in cancer. *Clinical cancer research* **2008**, *14* (5), 1310-1316.
7. Le Trequesser, Q.; Seznec, H.; Delville, M.-H., Functionalized nanomaterials: their use as contrast agents in bioimaging: mono- and multimodal approaches. *Nanotechnology Reviews* **2013**, *2*, 125-169.



# Chapter 1: State of the art



## Table of contents

I - Nanoparticles for radiotherapy applications .....	10
I. 1. Cancer therapies.....	10
I. 1. a. Injection mode.....	10
I. 1. b. Mechanism of action .....	11
I. 2. Radiotherapy .....	14
I. 2. a. Radiotherapy principles and current limits .....	14
I. 2. b. Interactions between radiation and matter.....	15
I. 2. c. Interactions implications in radiotherapy .....	16
I. 3. What about radiotherapy and nanoparticles? .....	17
I. 3. a. Nanoparticles developed for radiotherapy .....	18
I. 3. b. Comparison between low and high Z atoms.....	19
I. 3. c. Biological approach.....	20
II - Multifunctional nanoparticles.....	22
II. 1. How to design nanoparticles for radiotherapy applications? .....	22
II. 1. a. Required characteristics of nanoparticles.....	22
II. 1. b. Pharmacokinetics, ADME .....	23
II. 1. c. Toxicity.....	25
II. 2. Some examples of nanoparticles used in biological applications .....	27
II. 2. a. Organic nanoparticles.....	27
II. 2. b. Inorganic nanoparticles .....	29
Conclusion .....	31
Bibliography.....	32

# I - Nanoparticles for radiotherapy applications

## I. 1. Cancer therapies

“Cancer” is a serious disease that is caused when cells in the body grow in an abnormal and uncontrolled way, killing normal cells and often causing death [1]. A cancer therapy is a treatment that helps killing tumor cells.

### I. 1. a. Injection mode

Several injection modes exist to introduce drugs inside human body such as inhalation, intravenous, transdermal [2] or also directly in the tumor [3].

Intravenous injection, often denoted IV or iv, is a way of introducing liquid substances into a vein. IV is usually used to correct electrolytes imbalances, for blood transfusion, in the case of dehydration, or for chemotherapy or radiotherapy [3]. The advantage of IV is the injection facility and the fact that the bioavailability of the injected drugs is 100% because they are directly introduced in blood vessels and can easily diffuse to all the body [4].

Transdermal drug delivery is the administration in the form of patches, which delivers drugs at a predetermined and controlled rate. Transdermal drug delivery devices are designed for active or passive targeting, allowing the drugs to be delivered across the skin barriers. In theory, transdermal patches work in a very simple way [2]. A relatively high drug payload is embedded in a patch, which is kept in contact with the skin for an extended period of time. Through a diffusion process, the drug enters the bloodstream directly through the skin. As the concentration is high on the patch and low in the blood, the drug keeps diffusing into the blood for a long period of time, maintaining constant drug concentration in the blood flow [2].

The brain is an important and complex organ and human evolution built very efficient ways to protect it. Delivery of drugs to the central nervous system (CNS) is a challenge in the treatment of neurological disorders as well as of brain tumors. Drugs may be administrated directly into the CNS. The major challenge to CNS drug delivery is the blood-brain barrier which limits the access of drugs to the brain.

Advances in cell biology understanding of blood-brain barrier have opened new possibilities for improving drug delivery to the CNS. Various strategies are available for this purpose including osmotic and chemical opening of the blood-brain barrier, and the use of transport

or carrier systems [5]. Other strategies involve bypassing the blood-barrier system [6]. Various pharmacological agents have been used to open this blood-brain barrier [7-8] and direct invasive methods can introduce therapeutics agents into the brain substance [9].

#### I. 1. b. Mechanism of action

The goal of targeted nanoscale drug delivery systems is to increase the drug's concentration in the tumor through either passive targeting (EPR effect) or active targeting and at the same time to decrease its concentration in normal tissues,

- improving the pharmacokinetics and pharmacodynamics profiles (cf. paragraph II. 1. b.), and drug solubility to allow intravenous administration;
- improving drug stability;
- improving internalization and intracellular delivery;
- enhancing efficacy and
- reducing side effects [10-11].

With a well-chosen targeting strategy, drug administration protocols may be simplified. Toxicity is reduced by delivering the drug to the targeted site and by decreasing harmful systemic effects. Thus, drugs can be administered in a smaller dose to produce the desired effect and can be selectively delivered to tumor cells. However, there are some drawbacks. The main one is the control of the release of the drugs. In addition, the second one is the complexity of the formulation, which needs to be developed.

Besides passive and active targeting, double targeting [12], dual targeting [13] and inverse targeting [14] have also been used but are out of the scope of the present work.

The principal schemes of drug targeting currently investigated in various experimental and clinical settings include [15-17]:

- Direct application of the drug in the affected zone (organ, tissue),
- Passive accumulation of the drug through leaky vasculature (tumors, infarcts, inflammation),
- Physical targeting based on abnormal pH and/or temperature in the target zone such as tumor or inflammation (pH- and temperature- sensitive drug carriers),
- Magnetic targeting of drugs attached to paramagnetic carriers under external magnetic field action,

- Use of vector molecules possessing high specific affinity toward the affected zone.

The parameters determining drug targeting efficacy are [6]:

- Target size
- Blood flow through the target
- Number of binding sites for the targeted drug/ drug carrier within the target
- Number and affinity of targeting moieties.

#### I. 1. b. i. Passive targeting

Drug delivery systems, which are targeted to systemic circulation, are characterized as passive delivery systems. In this technique, drug targeting occurs because of the body's natural response to physicochemical characteristics of the drug or drug carrier system [18].

Recent studies noticed that some drugs show prolonged circulation in the blood and accumulate passively in tumors even in the absence of targeting ligands. Thus, passive targeting is based on anatomical differences between normal and diseased tissues to deliver drugs (Figure 1).

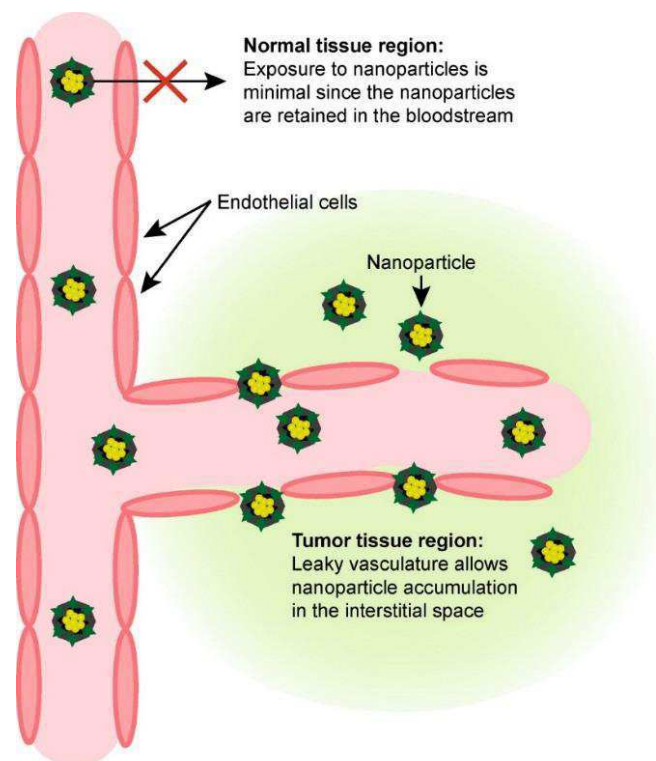


Figure 1: Structural differences between normal (healthy) tissue and tumor tissue [10]

Passive targeting involves nanocarriers transport through leaky tumor capillary fenestrations into tumor interstitium and cells by convection or passive diffusion. Then selective accumulation of nanocarriers and drug occurs by the Enhanced Permeability and Retention (EPR) effect [19]. Blood vessels in tumors are characterized by abnormalities [4]. Here are few examples of these abnormalities: high proportion of proliferating endothelial cells, pericyte deficiency and aberrant basement membrane formation leading to an enhanced vascular permeability. Moreover, the lack of lymphatic vessels or their non-functional presence in tumor tissue results in EPR effect [20] as shown in figure 2 [21].

Passive targeting approaches take advantage of natural anatomical structures or physiological processes, which direct the carrier in *in vivo* distribution. However, the pore sizes are not well known but they are likely to be between 200 nm and 1.2  $\mu\text{m}$  [19].

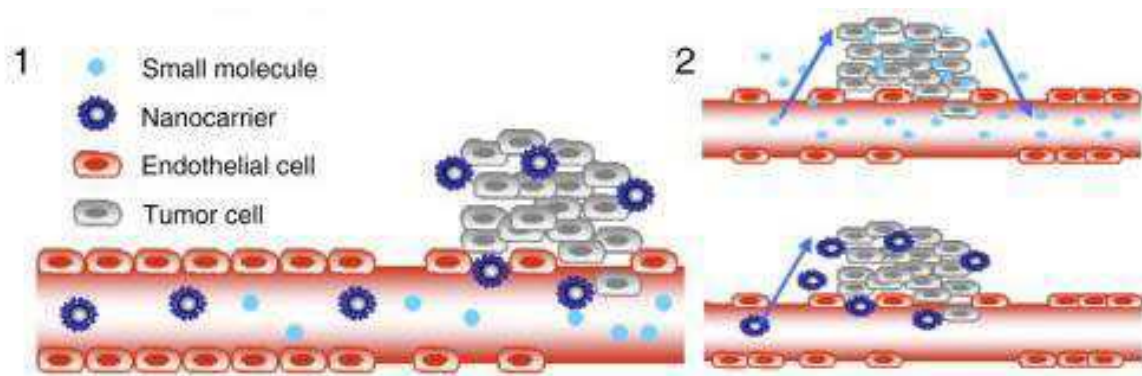


Figure 2: Passive targeting and Enhanced Permeability and Retention (EPR) effect [21]

Furthermore, the microenvironment surrounding normal and tumor cells is different. The hyper proliferation requires high metabolic rate [22]. The normal supply of oxygen and nutrients is not sufficient. This is why tumor cells use glycolysis to obtain extra energy, and create a local acidic environment [22-23]. Thus, nanotechnology can take advantage of these differences to design for example NPs bearing pH-sensitive drug-carrier bonding. Furthermore, cancer cells overexpress particular enzymes such as matrix metalloproteinases, which can induce specific bond cleavage between NPs and drugs [24-25].

#### I. 1. b. ii. Active targeting

In this approach, a carrier system bearing drugs reaches specific site rather than being uptaken by the reticuloendothelial system [26]. The active targeting supposes a surface modification of the nanocarriers, such as surface coating with either a bio adhesive, specific cell or tissue antibodies, or with albumin protein [27].

Active targeting requires the conjugation of a specific receptor ligand able to promote specific targeting. Active targeting is achieved by the molecular recognition of diseased cells by various signature molecules overexpressed at the diseased site as shown in Figure 3 [21]. Carrier specificity can be enhanced through surface functionalization with site-directed ligands, which bind or interact with specific tissues. Different kinds of ligands can be added to the NPs, such as DNA [28], proteins [29], mRNA, antibodies [30-31].

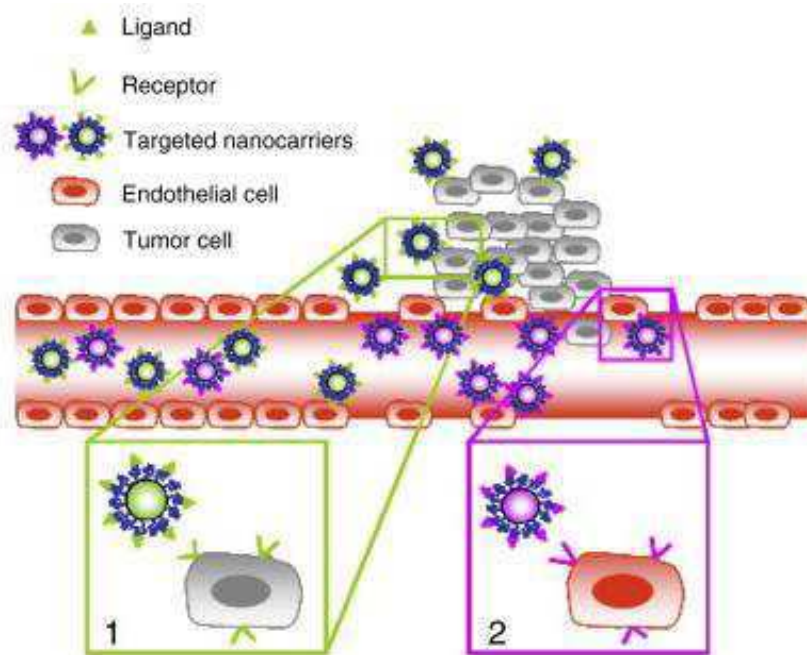


Figure 3: Active targeting [21]

## I. 2. Radiotherapy

### I. 2. a. Radiotherapy principles and current limits

Radiotherapy is based on ionizing radiations (considered as such when they have energy higher than 13.6 eV), such as gamma rays or X-rays focused on the tumor. The irradiation goal is to weaken, or even better, kill tumor cells, while limiting the damage to healthy surrounding cells. X-rays are collimated in the volume of the targeted cancer tissue thanks to slits appropriately designed. However, certain tumors are becoming resistant to ionizing radiation. Moreover, patients treated with radiations frequently experience important side effects due to the irradiation of the surrounding healthy tissues in front of or behind the target of the beam area [32]. Another issue is the fact that the tumor is not necessarily a perfect sphere

and during the irradiation, some tumor cells located far away from the central treated volume may not receive enough radiation to be killed. To solve this problem, multipolar irradiation [33] can be used. In this method, the patient is irradiated from different directions with very precise beams, which are adjusted to the actual tumor shape. This allows decreasing the irradiation to the surrounding healthy tissues, making the technique less aggressive to the patient.

Present nanotechnology knowledge may assist in devising better radiotherapy strategies. To better understand radiosensitization possible effects, interactions between matter and ionizing radiation are recalled.

### 1. 2. b. Interactions between radiation and matter

Figure 4 depicts the three principal interaction modes pertinent to radiation therapy (photoelectric, Compton and pair production processes) as a function of the incident beam energy and atomic number of the absorber matter [34]. For an absorber with  $Z$  similar to that of soft tissue ( $Z \approx 7$ ) and for mono energetic photons (photons with only one energy), the photoelectric effect dominates below 0.03 MeV, while above this energy the Compton effect leads up to *ca.* 24 MeV, when the pair production is the chief effect. However, for high  $Z$  elements (*e.g.*, Hf  $Z = 72$ ), the photoelectric effect is the dominant interaction below *ca.* 0.5 MeV, while between this energy and 5 MeV, the Compton effect leads. Above 5 MeV the pair production dominates.

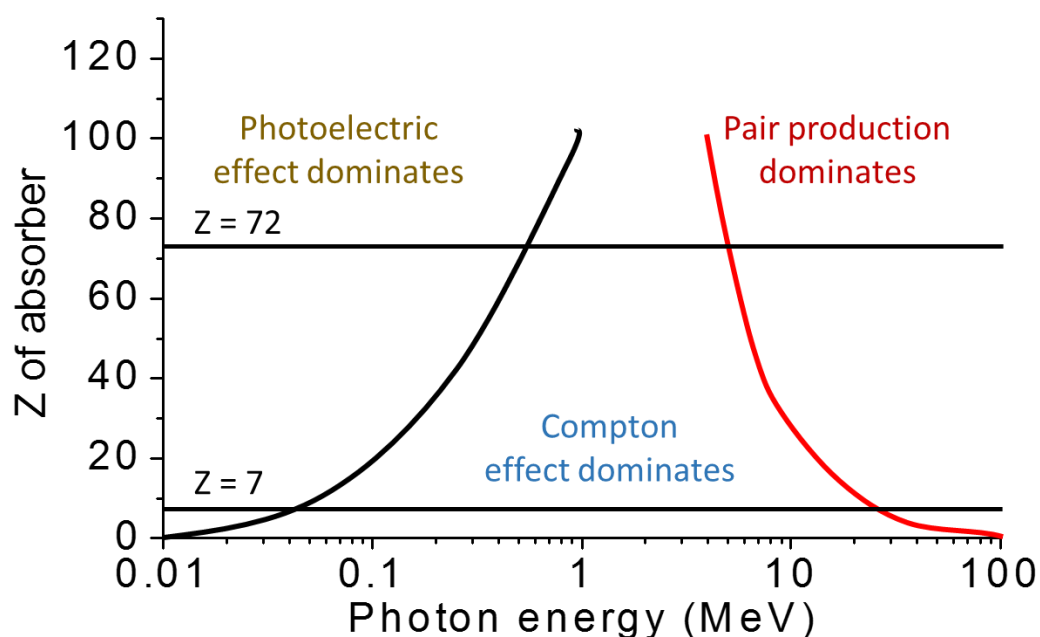


*Figure 4: Dominant process depending on Z number and photon energy [34]*

To summarize these effects let mention that:

1. The photoelectric effect is the dominant energy transfer mechanism for X and  $\gamma$  ray photons having energies below 50 keV in biological tissues, but it is less important at higher energies.
2. The Compton effect is the main absorption mechanism for X and  $\gamma$  rays in the energy range between 100 keV and 10 MeV. This is the range of energy used by most of radiotherapy protocols (with X or gamma rays).
3. The electron-hole pair production requires 1.02 MeV. This process then rapidly increases with the photon energy and, well above threshold, varies approximately as  $Z^2$ .

#### **I. 2. c. Interactions implications in radiotherapy**

The three major forms of interactions between radiation and matter, which are of clinical importance in radiotherapy are the Compton and photoelectric effects, and pair production. The Compton effect is the most important one in modern-day megavoltage radiation therapy. The reduced scattering suffered by high-energy radiation and the almost homogeneous tissue dosage is primarily due to the Compton effect.

Coherent scattering is of little importance in practical radiotherapy, but is important in X-ray crystallography analysis. Photoelectric effect has several important implications in practical radiology. In diagnostic radiology, the primary interaction mode is photoelectric. It is also responsible for the contrast effect. In therapeutic radiology, low-energy beams cause excessive absorption of energy in bone.

The attenuation produced by the Compton effect is described by the mass scattering coefficient and is practically the same for all substances except hydrogen-containing materials, like water and soft tissue, where the Compton effect is higher because of the higher electron density. Because for the Compton effect, the attenuation does not depend on the absorber's atomic number, concrete is as good as lead in shielding of megavoltage equipment. The absorption in the bones and in the soft tissues are similar, unlike in photoelectric effect seen in orthovoltage radiation era (200 to 500 keV) [35].

Protons and heavy particle beams have the ability to concentrate dose inside the target volume and minimize dose to surrounding normal tissues because of the Bragg peak effect and minimal scattering. However, there are several practical and fundamental difficulties with the use of these charged particles, including:

- Narrow Bragg peak makes it difficult to achieve a homogenous tumor dose.
- Generation of the charged particles requires expensive large machines.
- Production methods ensure that the field size is very narrow. So, for cancer treatment the beam has to be scanned back and forth across the treatment area.

Hydrogen-bearing materials, like fat, absorb more neutrons than heavier materials do and, thus, there is a 20% greater absorption in fat relative to muscle. Materials bearing atoms with low Z (*e.g.*, fat and paraffin) are better for neutron shielding as compared to lead as a greater absorption occurs.

Even if neutrons penetrate into matter, they are not commonly used in practical radiotherapy because of technical difficulties in their production and complicated dosimetry.

To conclude, despite several decades of research, photon-beams still constitute the main therapeutic modality in radiotherapy because of several unresolved technical problems with other forms of radiation.

### I. 3. What about radiotherapy and nanoparticles?

Radiotherapy is one of the most promising tools against cancer, even though it cannot be applied to all cancer types [36]. However, it still presents drawbacks that researchers are trying to overcome in order to improve efficacy in the treatment of tumor cells and to minimize side effects on healthy surrounding cells. A possible way to solve this problem is to use NPs, which can either weaken cancer cells and act like radiosensitizers or act as radioenhancers multiplying the radiotherapy effect. Various types of NPs have been studied [17], as depicted in Figure 5.

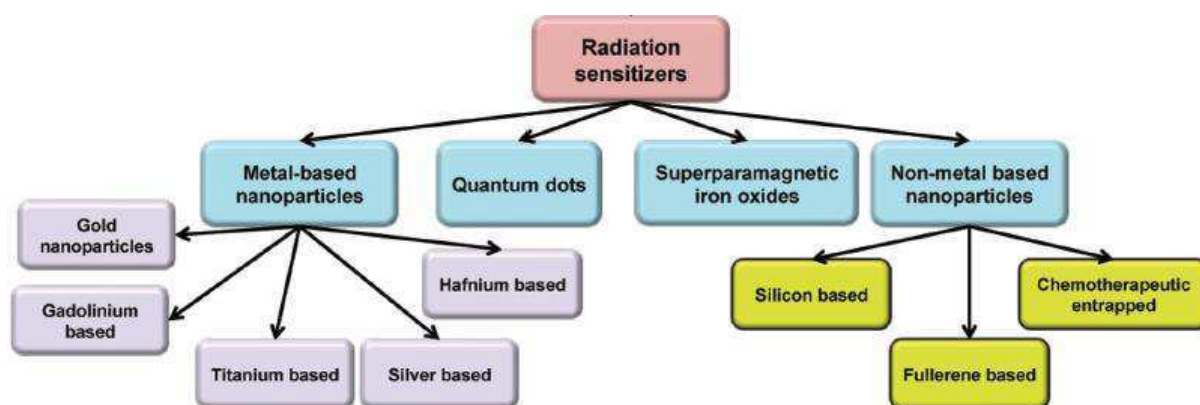


Figure 5: Different types of radiosensitizers [17]

### I. 3. a. Nanoparticles developed for radiotherapy

Gold-based nanoparticles have been the most widely explored for radio-sensitization, because of their high inertness, good biocompatibility, and easiness of chemical modification. Chang reported that gold nanoparticles of 3 to 50 nm showed a significant size-dependent radiation therapy enhancement effect [37]. The local distribution of Au nanoparticles inside cancer cells could also affect their radio-sensitization ability. Irvine made Au nanocapsules (Au nanoparticles embedded in the lipid membrane), which could be homogeneously distributed within the cytosol following endosomal escape. Such increased homogeneous distribution of Au nanoparticles within cancer cells led to a 3-fold increase in radiation-induced cell damage [38]. Some reports indicated that the surface coating of Au NPs might play some roles in their radiosensitizing ability, although the exact physical mechanisms needed further clarification [39-40].

Rare-earth elements have also been investigated for enhancing the efficacy of the radiation therapy. A few examples include  $Gd_2O_3$  NPs and rare-earth upconversion NPs interesting by their tracking *in vivo* by magnetic resonance and, optical imaging [41-46]. Le Duc *et al.* prepared 5 nm sized gadolinium oxide NPs with a polysiloxane coating [46]. These NPs could accumulate into the tumor upon intravenous injection, and produce strong radio-sensitizing effects under X-ray irradiation, leading to survival of mouse bearing tumors [47-48].

In addition to Au and rare-earth NPs, other high Z elements based NPs have also been developed for radiation therapy. For instance, bismuth has been used. The Shi group recently developed various bismuth sulfide based nanomaterials such as  $Bi_2S_3$ /PGLA

nanocapsules [49],  $\text{Bi}_2\text{S}_3$  embedded mesoporous silica NPs [50] for enhanced radiation therapy due to the high Z number of bismuth. Moreover, some research focuses on tungsten [51-52] and tantalum [53-54]. These materials demonstrated X-ray attenuation abilities and could concentrate X-ray energy within tumor to enhance the radiation therapy.

Hafnium is another high Z element explored for radio-sensitization [55].  $\text{HfO}_2$  NPs have been mentioned to cause thermal induced stress damage to cellular components.  $\text{HfO}_2$  NPs have been tried and tested for the previous effect on radiosensitization in HCT116 cells *in vitro* and *in vivo* mice models. The studies showed a good biocompatibility as well as significant radiosensitization using these NPs [55].

### I. 3. b. Comparison between low and high Z atoms

Radiation energy is absorbed and reemitted by the atoms present in the beam area. Usually low atomic number ( $Z < 10$ ) atoms, such as C, H, O and N, and also P ( $Z = 15$ ) and Ca ( $Z = 20$ ), the main elements present in cells, are then also hit by radiation. The induced mechanism in the case of these atoms is more simple because they have only a few electrons. However, atoms with a higher Z, like I ( $Z = 53$ ), Gd ( $Z = 64$ ), Au ( $Z = 79$ ) or Hf ( $Z = 72$ ) have a higher absorption cross-section [56] and are involved in various mechanisms of reemission [36], such as the Compton and photoelectric effects, pair production, and some electron cascades, such as Auger electrons [57] (Figure 6). Calculations have been performed to simulate interactions between photons and matter (cells with or without nanoparticles) by Geant4 [58-59] using Monte Carlo methods [60-62]. The idea of using NPs as radiosensitizers is based on their capacity to increase the radiation dose deposition in the targeted tissue, thanks to differences in their mass energy absorption coefficients [17].

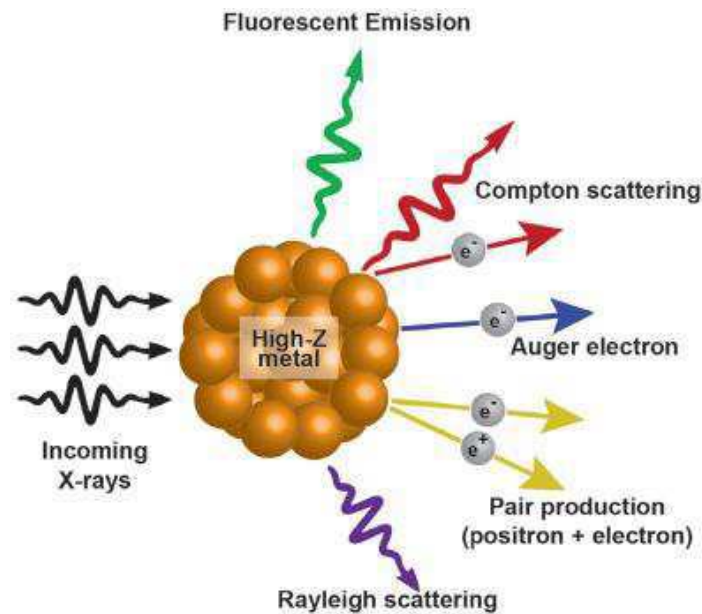


Figure 6: interaction of X-rays with high Z material NPs [17]

### 1. 3. c. Biological approach

Radiobiological phenomena are measured in terms of the energy deposited in biological system. The common unit is the Gray (Gy) defined as the energy (J) deposited divided by the mass (kg) [36]. The three processes previously described initiate biological reactions in the irradiated system. However, the biological response mechanisms induced by radiation in cellular systems are still not completely understood and are currently studied [63]. One such mechanism is single- and double-strand DNA breakage, which is often lethal [64-65]. A second mechanism is the production of reactive oxygen species (ROS), caused by the interaction of ionizing radiation of water, which attacks DNA and results in irreversible apoptosis. Although, normally, the damaged DNA is repaired by the cells, radiation causes cell death or genetic changes [66].

Cell death may be caused by apoptosis and necrosis. The latter, is a passive process in which cells pass through mitosis with unrepaired DNA strand breaks, leading to lethal chromosomal aberrations. Apoptosis, in contrast, is an active process characterized by programmed cell death in response to cellular stress [66].

When the presence of NPs is involved, two additional mechanisms are proposed for the effect of high Z NPs on cells under ionizing radiation, radioenhancement and radiosensitization [36].

- Radioenhancement is a physical effect. High Z NPs injected directly in the tumor locally increase the number of produced electrons and the number of redox processes and

ROS. These electrons interact mainly with the tumor cells components leading to selective cell apoptosis.

- In the radiosensitizing effect, NPs with low or high Z induce once internalized some element homeostasis. The cells are thus weakened and less likely to survive the ionizing radiation, promoting cell death, and as a consequence a decrease of the tumor size

To find out which mechanism is the more likely to take place for the systems we study in this thesis, the effect of ionizing radiation on cells with low (Ti,  $Z = 22$ ) and high (Hf,  $Z = 72$ ) Z will be compared.  $\text{HfO}_2$  [67] and  $\text{TiO}_2$  [68] have already been used in radiotherapy *in vitro* and *in vivo*. *In vivo* radiotherapy experiments in the presence of  $\text{HfO}_2$  NPs show a high percentage of tumor growth reduction upon irradiation, while NPs do not induce cell death without irradiation [55]. Moreover,  $\text{HfO}_2$  NPs seems to be non-toxic [69]. Nanobiotix, a French company, has already tested  $\text{HfO}_2$  NPs in phase I clinical trials and has obtained promising safety and antitumor activity results. Moreover, it is of great importance to be able to track and follow these NPs once injected, this is the reason why multifunctional nanoparticles are developed.

## II - Multifunctional nanoparticles

In this part, the properties as well as the design of NPs in order to use them in radiotherapy will be described.

### II. 1. How to design nanoparticles for radiotherapy applications?

Beyond radiosensitization properties, NPs have to possess numerous characteristics such as stability in physiological media, biocompatibility, and absence of toxicity... Furthermore, the optimal NPs properties are described according to an application in biomedical fields [70].

#### II. 1. a. Required characteristics of nanoparticles

For biomedical applications, NPs must have the following properties [71]:

- Dispersibility and colloidal stability in physiological media
- Biocompatibility and biodegradability allowing the excretion
- Non toxicity
- Selectivity for the target
- Stealthness to immune system

Concerning the first property, NPs should have an isoelectric point different from the physiological media pH value, to avoid any aggregation. Regarding the second and third property, they must not interfere with any biological cycles, such as the iron cycle. These three properties are correlated and linked to the physicochemical properties of chosen materials and depend to some extent on the used synthetic pathways. Chemical composition, size distribution, shape, surface properties, charge and crystallinity are the physicochemical features which have to be designed [70] according to biomedical applications requirements. Considering target selectivity, the NPs should be localized in tumor cells and, for this reason, antibodies are often grafted on NPs [72]. The target selectivity can be achieved through different methods such as active or passive targeting (cf. paragraph I. 1. b). Finally, to be effective, NPs should not be destroyed too early by the human immune system [73], circulating enough time in body fluids to reach their target. For instance, NPs may be coated with a shell inert towards immune system, such as polyvinyl alcohol, polylactic acid or polyethylene glycol (PEG), or they have a size that allows them not to be detected by the immune system [73].

NPs toxicity is also a key parameter. Thus, it is of importance to study their biological interactions with cells, proteins, blood and tissue.

### II. 1. b. Pharmacokinetics, ADME

Pharmacokinetics comprises absorption, distribution, metabolism, and excretion (ADME). The pharmacokinetics study can improve NPs design for diagnostic and therapeutic applications, improve the understanding of nanostructures non-specificity toward tissues and cell types, and improve toxicity determination [74].

#### II. 1. b. i. Absorption

Absorption is the process by which NPs proceed from the external site of exposure into an internal biological space, mainly central blood circulation [74]. Although the main absorption routes are oral, pulmonary, injection, nasal and dermal exposures, other routes are available such as ocular and intratumoral. Each absorption mode possesses a different mechanism of spreading in human body but NPs usually end up directly in blood or through passage of several physiological barriers. In the human body, NPs interact with opsonin proteins that they meet when circulating, the so-called opsonisation process [75]. Thus, a protein corona forms following the absorption of numerous proteins. This corona confers new surface properties to the particles and is usually composed of two layers. The inner shell includes proteins with a low exchange rate with the surrounding media, whereas the outer shell contains proteins with a faster exchange rate with media proteins. Thus, particles have new biological properties, which affect cellular and tissue responses. However, these new properties, which influence NPs biodistribution and internalization, are determined by NPs characteristics such as size, shape, and surface charge, as well as the administration way which has an effect on the different media the particles have to cross [76].

#### II. 1. b. ii. Distribution

This second pharmacokinetics step refers to NPs distribution to various tissues and organs via central blood circulation [74, 77]. However, NPs concentration in various tissues or organs depends on their properties and interaction with living system. NPs may stay within the tissue but outside cells, absorb on the cell membrane, or cross it to the cell inside. When NPs get into the cytoplasm, they are considered internalized. The exchanges can occur by several pathways such as exocytosis or endocytosis. In exocytosis, NPs are exported out of the cell via

secretory vesicles, while in endocytosis, they are carried into the cell. There are three types of endocytosis, phagocytosis, pinocytosis and receptor-mediated endocytosis. In phagocytosis (or “cellular eating”), the cell membrane engulfs NPs from the extracellular environment and form a phagosome. In pinocytosis (or “cellular drinking”) the cell engulfs drops of fluid by forming vesicles that are smaller than the phagosomes formed in phagocytosis. Like phagocytosis, pinocytosis is a non-specific process in which the cell takes in whatever solutes that are dissolved in the liquid it envelops. Unlike phagocytosis and pinocytosis, receptor-mediated endocytosis is an extremely selective process of importing materials into the cell. In receptor-mediated endocytosis, the cell will only take in an extracellular NP if it binds to its specific receptor protein on the cell membrane to form a coated vesicle. Similar to the digestive process in non-specific phagocytosis, this coated vesicle then fuses with a lysosome to digest the engulfed NPs and release them into the cytosol [78]. However, the distribution depends on NPs physical and chemical properties as well as the kind of cells such as blood, reticuloendothelial system, lymphatic system, brain cells and tumor cells [79].

#### II. 1. b. iii. Metabolism

NPs metabolism includes any process that alters their physicochemical properties and it depends on NPs composition and properties. Metabolic pathways are usually described and they involve chemical reactions with the NPs coating and core [11]. However, nowadays metabolism has not yet been properly studied.

#### II. 1. b. iv. Excretion

The fourth pharmacokinetics step is the excretion or elimination. There is a multitude of ways to eliminate an exogenous body from the human body, via the kidneys, expiration, seminal fluids, mammary glands, saliva, etc. However, if an organism is not able to eliminate NPs, then accumulation takes place [79].

To conclude this part, pharmacokinetics is strongly dependent on physical and chemical properties of NPs such as size, shape, surface charge, etc., characteristics that influence NPs toxicity [11].

### II. 1. c. Toxicity

NPs physicochemical properties as illustrated above not only play a strong role on their pharmacokinetics but also on their potential toxicity, aspect described in the following.

#### II. 1. c. i. Physicochemical properties

When the particles size decreases, the surface to volume ratio greatly increases resulting in increased reactivity and, consequently, possible toxicity increase [80]. The choice among the many mechanism of NPs internalization is very challenging [81]. For example, to take advantage of EPR effect (cf. paragraph I. 1. b. i) NPs size should be below 100 nm, and in a receptor mediated endocytosis around 30 nm [82]. In conclusion, there is a clear dependence of NPs uptake with size [36]. Furthermore, the formation of aggregates and agglomerates, as well as NPs shape and aspect ratio determine their toxicity [83]. For example, it was reported that rod-like NPs are potentially more toxic than spherical ones (at a constant NPs size and surface area). The elongated shapes can cause a higher inflammatory response because of their tendency to stick on to the cellular membrane [84-85]. Additionally, rod-like shapes can have a larger contact area with the cell membrane if they interact through NPs longitudinal axis [86]. The chance to tune dimensions and control NPs shape is an advantage of nanotechnology.

Regarding toxicity, the NPs surface charge is also an important parameter because it is related to their stability in the medium and it determines ions and biomolecules adsorption that can modify the organism response. Negatively charged and neutral NPs surfaces have a lower ability to cross the cellular membrane than positively charged surface. In general, cationic surfaces are considered more toxic than anionic surfaces because the cell membrane is made of phospholipids which are negatively charged [87].

#### II. 1. c. ii. Modification of biological mechanism

Consider Figure 7 [80]. Toxicity can be induced through several mechanisms. Growing knowledge of these mechanisms may result in new therapeutic opportunities in nanomedicine [11]. The first possible mechanism is free radicals production, such as reactive oxygen species (ROS) [80]. A second mechanism is the inflammatory response due to macrophages activation when NPs are detected [88]. Phagocytosis, antigen presentation and immunomodulation through the production of various cytokines and growth factors are the

actions of macrophages to an inflammatory response [11]. The third mechanism is the alteration of elements homeostasis. Metal NPs can modify normal cellular  $\text{Ca}^{2+}$  concentration (by increasing  $\text{Ca}^{2+}$  influx, inhibiting  $\text{Ca}^{2+}$  sequestration,...), and, thus, disturb and inhibit the regulatory roles of balanced intracellular  $\text{Ca}^{2+}$  concentration, such as cellular metabolism, signal transduction and gene expression. For example,  $\text{TiO}_2$  NPs internalization alters calcium homeostasis, decreasing cell proliferation associated with an early differentiation [85, 89]. NPs coating may also play a role on toxicity [90-91].

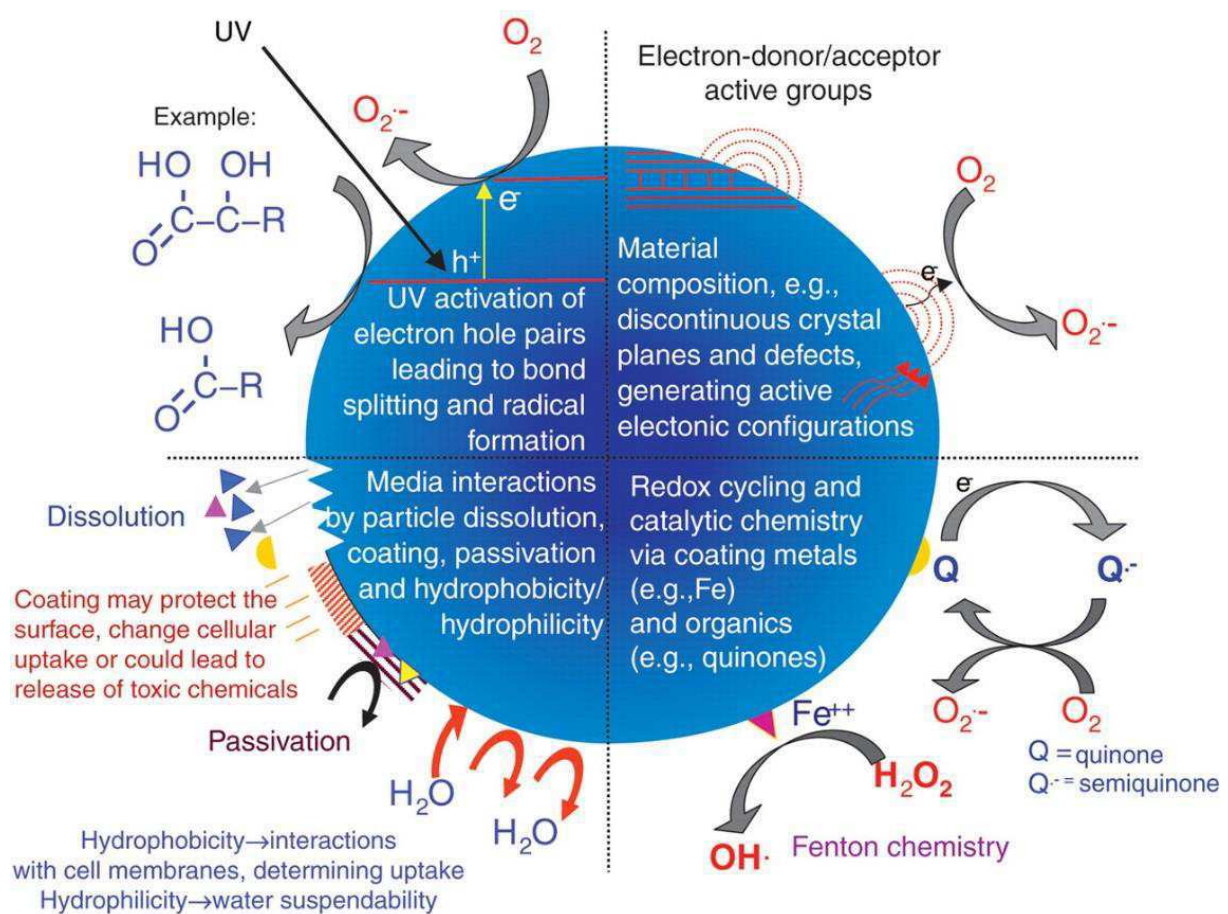


Figure 7: Possible mechanisms of interaction between NPs and biological tissue [80]

Figure 7 illustrates the importance of material composition, electronic structure, bonded surface species (e.g. metal-containing...), surface coatings (active or passive), and solubility, including the contribution of surface species and coatings and interactions with other environmental factors (e.g. UV activation, ionizing radiation...).

## II. 2. Some examples of nanoparticles used in biological applications

Several types of particles are used in biological field either to transport or deliver drugs, or for imaging and therapy. Organic, inorganic and hybrid particles dimensions are usually in the range 3 to 200 nm, depending on the chosen administration mode. Different shapes are available for use, such as spheres, anisotropic particles, tubes, etc.

### II. 2. a. Organic nanoparticles

Organic NPs have various sizes, shapes, composition and differ in terms of application such as drug loading capacity, releasing methods and delivery ability [16].

#### II. 2. a. i. Liposomes and micelles

A liposome and a micelle are tiny vesicles made of the same material (*e.g.* cell membrane). Liposomes and micelles can be filled with drugs and used as delivering agents to cancer cells [92-94]. Membranes are usually made of phospholipids, molecules that have a hydrophobic tail and a hydrophilic head group. Usually, phospholipids rearrange themselves into tiny spheres, smaller than a normal cell, either as bilayers or monolayers [95]. The bilayer structures are called liposomes [96] while the monolayer structures are called micelles [97]. Using different types of lipids, NPs size, surface charge and functionality can be changed and adapted to the wanted applications [98]. Main disadvantages of these NPs are the limited storage stability and the challenges in loading a broad variety as well as a large drug amount [99-100].

#### II. 2. a. ii. Polymer nanoparticles

Synthesis possibilities are huge and various due to the various chemical and physical properties of the polymers [101]. Size, shape, and surface can be controlled by synthetic conditions or by chosen monomers. That is the reason why polymers are a very interesting materials for drug delivery [102]. Furthermore, polymers can be biodegradable (degraded in the monomers, metabolized and removed from human body) or non-biodegradable. Polyethylene glycol and poly(L-glutamic acid) [103] are frequently used because of their biocompatibility and their stability, and they allow a stealth coating [104]. Drugs are grafted on the polymer chain which allows a high loading [105]. Main challenges of polymer NPs are proteins encapsulation [99].

### II. 2. a. iii. Dendrimers

Dendrimers are nanoscale compounds and constructed by successive addition of layers of branching groups. Each layer is called a generation. The last generation incorporates surface molecules that give dendrimers the desired functionalization for the chosen applications [106].

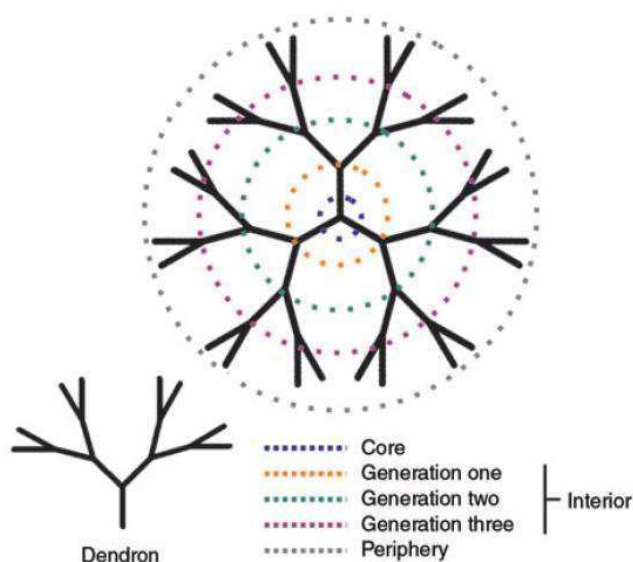


*Figure 8: Anatomy of a dendrimer. A dendrimer and a dendron are represented with solid lines. The colored dashed lines identify the various key regions of the dendrimers [106]*

Several methods of synthesis have been developed such as divergent growth method and convergent growth method [107]. The possibility of changing the size, shape and composition of dendrimers is very useful [108]. Moreover, dendrimers synthesis is reproducible and a divergent synthetic method exists, allowing a larger scale production. An useful dendrimers property is that as the generation number increases the dendrimers size increases and terminal groups become more tightly packed together, regulating release rates from drugs inside dendrimer [109]. There is also an increase of terminal groups (multiple ligand attachment) extending the affinity interaction probability [110]. Terminal groups can be hydrophobic or hydrophilic, either anionic [111] or cationic, and this determine their interactions in solvent [112]. Mendoza-Nava developed a  $^{177}\text{Lu}$ -dendrimer (polyamidoamine-G4)-folate-bombesin with gold nanoparticles in the dendritic cavity as a potential tool for theranostics.

### II. 2. a. iv. Carbon nanotubes

Carbon nanotubes are rolled up cylinders of graphene sheets exhibiting unparalleled physical, mechanical [113] and chemical properties. Depending on the number of graphene layers which composed a nanotube, carbon nanotubes are classified as single-walled nanotubes (SWNTs) or multi-walled nanotubes (MWNTs) [114]. Carbon nanotubes are considered one-dimensional nanomaterials because of their tiny diameters (1 – 2 nm) and long lengths (ranging from 50 nm to 1 cm). They behave distinctly from spherical NPs in biological environments, offering new opportunities in biomedical research [115]. Carbon nanotubes are insoluble in most physiological fluids, but they can be easily modified and made soluble [116]. With a suitable functionalization, carbon nanotubes can be used as drug delivery agent [117].

### II. 2. b. Inorganic nanoparticles

Inorganic NPs exhibit various sizes, shapes, and compositions. Therefore, properties can be fashioned for specific recognition, sensing, delivery and imaging [16]. One advantage of inorganic NPs is that they may have simultaneous drug delivery and detection capabilities [71, 118]. In order to be stealth to the immune system, inorganic NPs are often coated with biocompatible materials such as polyethylene glycol (PEG) [91] or silica [119]. This shell can be used also to functionalize the NPs as desired.

#### II. 2. b. i. NPs of gold or silver

##### ❖ Gold nanoparticles

Gold NPs are versatile materials for a broad range of applications with well characterized electronic and physical properties due to well-developed synthetic procedures such as reduction of diluted salt solutions (*e.g.* HAuCl<sub>4</sub>) by various reducing agents [120]. Thanks to synthetic pathway facility, colloidal gold NPs can be prepared in many shapes, such as spherical, cylindrical (nanorods), nanoshells, nanocages, nanostars, etc. Their surface is also easily modified with hundreds of molecules (including therapeutics, targeting agents...) [121]. Gold NPs present a very high visible absorption. The color of the NPs can be tuned depending on their size and shape. This effect is due to a localized surface plasmon resonance. One part of the absorbed energy is used for plasmon effect [122] and the rest is turned into heat, with potential hyperthermia applications [123]. They can also be used to detect biomarkers in

heart diseases, cancers and infectious agents diagnosis [124]. Moreover, as gold is an excellent absorber of X-rays, gold nanoparticles can enhance the radiotherapy effect [123, 125-126].

#### ❖ Silver nanoparticles

Like gold NPs, silver NPs possess suitable properties for being used in numerous technologies including biomedical, optical as well as antimicrobial applications. Silver NPs can be synthesized by reduction of diluted salt solutions (*e.g.* AgNO<sub>3</sub>) by various reducing agents [120]. However, as silver nanoparticles are highly toxic for humans, their use is avoided when possible [127].

#### II. 2. b. ii. Quantum dots

Quantum dots (QDs) are colloidal semiconductor NPs based on atoms stabilized by an organic ligand layer [128]. QDs properties have broad absorption spectra, very narrow emission spectra, long fluorescence lifetime and high photostability because of the quantum confinement effects due to their nanometer size [129]. These properties depend on the particle size. QDs are usually formed by atoms from group II (alkyl metals, metal oxides or organic salts) and group VI (Sulfur, Selenium and Tellurium) [130]. QDs can find applications for instance in *in vivo* imaging and in photodynamic therapy [120]. However, selenium or cadmium toxicity raised problems about their further applications in biomedicine.

#### II. 2. b. iii. Metal oxides

Metal oxides NPs are easily synthesized with a good size and shape control and are attracting more and more attention for biomedical applications. For instance, silica (SiO<sub>2</sub>) and titanium dioxide (TiO<sub>2</sub>) have been already much studied.

#### ❖ Silica (SiO<sub>2</sub>)

Mesoporous silica (50 to 300 nm) has free channels (mesopores) in which bioactive molecules adsorption is possible even with a high loading because of a high surface-to-volume ratio [131]. To control NPs size and pore size, a synthetic method using surfactant-templated synthesis has been developed [132]. Furthermore, silica is a biocompatible metal oxide and is commonly used as shell [133] that is easily functionalized with antibodies (for active targeting) [134] or fluorescent molecules (for imaging) [135].

### ❖ Titanium dioxide (TiO<sub>2</sub>)

Titanium dioxide can be obtained by different synthetic methods, which lead to different NPs size, shape and morphology [136-138]. Furthermore, TiO<sub>2</sub> finds various applications in nanomaterial science especially in nanomedicine. The photosensitization properties of TiO<sub>2</sub> are explored in photodynamic therapy [15]. Cell death is due to either reactive oxygen species (ROS) generation [15] or physiological consequences such as ionic homeostasis [89, 139].

## Conclusion

This chapter described the interactions between NPs and biological systems and, in particular, the possible effect of NPs on the radiotherapy efficiency. NPs requirements for an application in the biomedical field and the several types of NPs already used were detailed.

The goal of my thesis is to find out whether or not the hypothesis that metal oxide NPs bearing metal atoms with high Z values [36] have higher therapeutic effectiveness than other NPs is correct. A way of understanding how NPs influence radiosensitization is to compare metal oxides with different Z value atoms. This study is done in collaboration with CENBG and Institut Bergonié in Bordeaux, France. The effects of ionizing radiation on cells with low Z and with high Z NPs will be compared. Based on our knowledge on titanium dioxide NPs, the choice of hafnium in the same group of titanium was natural. The first goal was to prepare exactly the same NPs (size, shape, concentration) except for their composition. Secondly, in order to study the effect of ionizing radiation, NPs should be internalized by cells. Concerning their physicochemical properties and internalization mechanisms, NPs should have a size below 100 nm and, if possible, between 30 and 60 nm. Thirdly, in order to track the NPs in human body, the presence of magnetic or luminescence properties is important. Thus, gadolinium (magnetism), and europium and terbium (luminescence) will be inserted in the hafnium oxide lattice. Subsequently, in order to follow temperature variations caused by the ionizing radiation, hafnium oxide nanoparticles will be co-doped with terbium and europium to be turned into nanothermometers.

## Bibliography

1. Dictionary, O. E., "cancer". Oxford University Press.
2. Prausnitz, M. R.; Mitragotri, S.; Langer, R., Current status and future potential of transdermal drug delivery. *Nature Reviews Drug Discovery* **2004**, *3* (2), 115-124.
3. Roszek, B.; Geertsma, R., Nanotechnology in medical applications: state-of-the-art in materials and devices. **2005**.
4. Cho, K.; Wang, X.; Nie, S.; Shin, D. M., Therapeutic nanoparticles for drug delivery in cancer. *Clinical cancer research* **2008**, *14* (5), 1310-1316.
5. Olivier, J.-C., Drug transport to brain with targeted nanoparticles. *NeuroRx* **2005**, *2* (1), 108-119.
6. Torchilin, V. P., Drug targeting. *European Journal of Pharmaceutical Sciences* **2000**, *11*, Supplement 2, S81-S91.
7. Garcia-Garcia, E.; Andrieux, K.; Gil, S.; Couvreur, P., Colloidal carriers and blood–brain barrier (BBB) translocation: A way to deliver drugs to the brain? *International journal of pharmaceutics* **2005**, *298* (2), 274-292.
8. Ribot, E.; Bouzier-Sore, A.-K.; Bouchaud, V.; Miraux, S.; Delville, M.-H.; Franconi, J.-M.; Voisin, P., Microglia used as vehicles for both inducible thymidine kinase gene therapy and MRI contrast agents for glioma therapy. *Cancer gene therapy* **2007**, *14* (8), 724.
9. Manish, G.; Vimukta, S., Targeted drug delivery system: a review. *Research Journal of Chemical Science* **2011**, *1* (2), 135-8.
10. Nie, S.; Xing, Y.; Kim, G. J.; Simons, J. W., Nanotechnology applications in cancer. *Annual Review Biomedical Engineering* **2007**, *9*, 257-288.
11. Sharifi, S.; Behzadi, S.; Laurent, S.; Laird Forrest, M.; Stroeve, P.; Mahmoudi, M., Toxicity of nanomaterials. *Chemical Society Reviews* **2012**, *41*, 2323-2343.
12. Kim, D.; Lee, E. S.; Oh, K. T.; Gao, Z. G.; Bae, Y. H., Doxorubicin-Loaded Polymeric Micelle Overcomes Multidrug Resistance of Cancer by Double-Targeting Folate Receptor and Early Endosomal pH. *Small* **2008**, *4* (11), 2043-2050.
13. Peeters, N.; Small, I., Dual targeting to mitochondria and chloroplasts. *Biochimica et Biophysica Acta (BBA)-Molecular Cell Research* **2001**, *1541* (1), 54-63.
14. Schneider, C. M.; Mihaljev, T.; Herrmann, H. J., Inverse targeting—An effective immunization strategy. *Europhysics Letters* **2012**, *98* (4), 46002.
15. Bhattacharyya, S.; Kudgus, R. A.; Bhattacharya, R.; Mukherjee, P., Inorganic Nanoparticles in Cancer Therapy. *Pharm Res* **2011**, *28*, 237-259.
16. De, M.; Ghosh, P. S.; Rotello, V. M., Applications of nanoparticles in biology. *Advanced Materials* **2008**, *20*, 4225-4241.
17. Kwatra, D.; Venugopal, A.; Anant, S., Nanoparticles in radiation therapy: a summary of various approaches to enhance radiosensitization in cancer. *Translational Cancer Research* **2013**, *2* (4), 330-342.
18. Maeda, H., The enhanced permeability and retention (EPR) effect in tumor vasculature: the key role of tumor-selective macromolecular drug targeting. *Advances in Enzyme Regulation* **2001**, *41* (1), 189-207.
19. Park, J. H.; Lee, S.; Kim, J.-H.; Park, K.; Kim, K.; Kwon, I. C., Polymeric nanomedicine for cancer therapy. *Progress in Polymer Science* **2008**, *33* (1), 113-137.
20. Carmeliet, P.; Jain, R. K., Angiogenesis in cancer and other diseases. *Nature* **2000**, *407* (6801), 249-257.
21. Danhier, F.; Feron, O.; Préat, V., To exploit the tumor microenvironment: Passive and active tumor targeting of nanocarriers for anti-cancer drug delivery. *Journal of Controlled Release* **2010**, *148* (2), 135-146.
22. Pelicano, H.; Martin, D.; Xu, R., and; Huang, P., Glycolysis inhibition for anticancer treatment. *Oncogene* **2006**, *25* (34), 4633-4646.
23. Yatvin, M.; Kreutz, W.; Horwitz, B.; Shinitzky, M., pH-sensitive liposomes: possible clinical implications. *Science* **1980**, *210* (4475), 1253-1255.
24. Maeda, H., Tumor-Selective Delivery of Macromolecular Drugs via the EPR Effect: Background and Future Prospects. *Bioconjugate Chemistry* **2010**, *21* (5), 797-802.
25. Mansour, A. M.; Drevs, J.; Esser, N.; Hamada, F. M.; Badary, O. A.; Unger, C.; Fichtner, I.; Kratz, F., A new approach for the treatment of malignant melanoma: enhanced antitumor efficacy of an albumin-binding doxorubicin prodrug that is cleaved by matrix metalloproteinase 2. *Cancer Research* **2003**, *63* (14), 4062-4066.
26. Allen, T. M., Ligand-targeted therapeutics in anticancer therapy. *Nature Reviews Cancer* **2002**, *2* (10), 750-763.
27. Leamon, C. P.; Reddy, J. A., Folate-targeted chemotherapy. *Advanced drug delivery reviews* **2004**, *56* (8), 1127-1141.

28. Oster, C. G.; Wittmar, M.; Unger, F.; Barbu-Tudoran, L.; Schaper, A. K.; Kissel, T., Design of amine-modified graft polyesters for effective gene delivery using DNA-loaded nanoparticles. *Pharm Res* **2004**, *21* (6), 927-931.
29. He, H.; Fu, G.; Wang, Y.; Chai, Z.; Jiang, Y.; Chen, Z., Imprinting of protein over silica nanoparticles via surface graft copolymerization using low monomer concentration. *Biosensors and Bioelectronics* **2010**, *26* (2), 760-765.
30. Neouze, M.-A.; Schubert, U., Surface modification and functionalization of metal and metal oxide nanoparticles by organic ligands. *Monatshefte für Chemie-Chemical Monthly* **2008**, *139* (3), 183-195.
31. Mout, R.; Moyano, D. F.; Rana, S.; Rotello, V. M., Surface functionalization of nanoparticles for nanomedicine. *Chemical Society Reviews* **2012**, *41* (7), 2539-2544.
32. Durand, R. E.; Olive, P. L., Resistance of tumor cells to chemo- and radiotherapy modulated by the three-dimensional architecture of solid tumors and spheroids. *Methods in cell biology* **2001**, 211-234.
33. Moran, J. M.; Elshaikh, M. A.; Lawrence, T. S., Radiotherapy: what can be achieved by technical improvements in dose delivery? *The Lancet Oncology* **2005**, *6* (1), 51-58.
34. London, U. C., Topic 8 - Cosmic Ray Experiments, the Cerenkov Effect. <http://zuserver2.star.ucl.ac.uk/~idh/PHAS2112/Lectures/2009/Nuclear/topic8.html>.
35. Robin, H.; Brendan, H.; Lois, H.; Zdenka, K.; David, T.; Clive, B., Advances in kilovoltage x-ray beam dosimetry. *Physics in Medicine and Biology* **2014**, *59* (6), R183.
36. Kobayashi, K.; Usami, N.; Porcel, E.; Lacombe, S.; Le Sech, C., Enhancement of radiation effect by heavy elements. *Mutation Research, Reviews in Mutation Research* **2010**, *704*, 123-131.
37. Dou, Y.; Guo, Y.; Li, X.; Li, X.; Wang, S.; Wang, L.; Lv, G.; Zhang, X.; Wang, H.; Gong, X.; Chang, J., Size-Tuning Ionization To Optimize Gold Nanoparticles for Simultaneous Enhanced CT Imaging and Radiotherapy. *ACS Nano* **2016**, *10* (2), 2536-2548.
38. Yang, Y.-S.; Carney, R. P.; Stellacci, F.; Irvine, D. J., Enhancing radiotherapy by lipid nanocapsule-mediated delivery of amphiphilic gold nanoparticles to intracellular membranes. *ACS Nano* **2014**, *8* (9), 8992.
39. Xiao, F.; Zheng, Y.; Cloutier, P.; He, Y.; Hunting, D.; Sanche, L., On the role of low-energy electrons in the radiosensitization of DNA by gold nanoparticles. *Nanotechnology* **2011**, *22* (46), 465101.
40. Liu, C.-J.; Wang, C.-H.; Chien, C.-C.; Yang, T.-Y.; Chen, S.-T.; Leng, W.-H.; Lee, C.-F.; Lee, K.-H.; Hwu, Y.; Lee, Y.-C., Enhanced x-ray irradiation-induced cancer cell damage by gold nanoparticles treated by a new synthesis method of polyethylene glycol modification. *Nanotechnology* **2008**, *19* (29), 295104.
41. Fan, W.; Shen, B.; Bu, W.; Chen, F.; He, Q.; Zhao, K.; Zhang, S.; Zhou, L.; Peng, W.; Xiao, Q.; Ni, D.; Liu, J.; Shi, J., A smart upconversion-based mesoporous silica nanotheranostic system for synergetic chemo-/radio-/photodynamic therapy and simultaneous MR/UCL imaging. *Biomaterials* **2014**, *35* (32), 8992-9002.
42. Liu, Y.; Liu, Y.; Bu, W.; Xiao, Q.; Sun, Y.; Zhao, K.; Fan, W.; Liu, J.; Shi, J., Radiation-/hypoxia-induced solid tumor metastasis and regrowth inhibited by hypoxia-specific upconversion nanoradiosensitizer. *Biomaterials* **2015**, *49* (Supplement C), 1-8.
43. Xiao, Q.; Zheng, X.; Bu, W.; Ge, W.; Zhang, S.; Chen, F.; Xing, H.; Ren, Q.; Fan, W.; Zhao, K., A core/satellite multifunctional nanotheranostic for in vivo imaging and tumor eradication by radiation/photothermal synergistic therapy. *Journal of the American Chemical Society* **2013**, *135* (35), 13041-13048.
44. Liu, J.; Liu, Y.; Bu, W.; Bu, J.; Sun, Y.; Du, J.; Shi, J., Ultrasensitive nanosensors based on upconversion nanoparticles for selective hypoxia imaging in vivo upon near-infrared excitation. *Journal of the American Chemical Society* **2014**, *136* (27), 9701-9709.
45. Fan, W.; Shen, B.; Bu, W.; Chen, F.; Zhao, K.; Zhang, S.; Zhou, L.; Peng, W.; Xiao, Q.; Xing, H., Rattle-structured multifunctional nanotheranostics for synergetic chemo-/radiotherapy and simultaneous magnetic/luminescent dual-mode imaging. *Journal of the American Chemical Society* **2013**, *135* (17), 6494-6503.
46. Le Duc, G.; Miladi, I.; Alric, C.; Mowat, P.; Bräuer-Krisch, E.; Bouchet, A.; Khalil, E.; Billorey, C.; Janier, M.; Lux, F., Toward an image-guided microbeam radiation therapy using gadolinium-based nanoparticles. **2011**.
47. Morlieras, J.; Dufort, S.; Sancey, L.; Truillet, C.; Mignot, A.; Rossetti, F.; Dentamaro, M.; Laurent, S.; Vander Elst, L.; Muller, R. N., Functionalization of small rigid platforms with cyclic RGD peptides for targeting tumors overexpressing  $\alpha\beta3$ -integrins. *Bioconjugate Chemistry* **2013**, *24* (9), 1584-1597.
48. Dufort, S.; Bianchi, A.; Henry, M.; Lux, F.; Le Duc, G.; Jossierand, V.; Louis, C.; Perriat, P.; Crémillieux, Y.; Tillement, O.; Coll, J.-L., Nebulized Gadolinium-Based Nanoparticles: A Theranostic Approach for Lung Tumor Imaging and Radiosensitization. *Small* **2015**, *11* (2), 215-221.
49. Yao, M.-h.; Ma, M.; Chen, Y.; Jia, X.-q.; Xu, G.; Xu, H.-x.; Chen, H.-r.; Wu, R., Multifunctional Bi2S3/PLGA nanocapsule for combined HIFU/radiation therapy. *Biomaterials* **2014**, *35* (28), 8197-8205.

50. Ma, M.; Huang, Y.; Chen, H.; Jia, X.; Wang, S.; Wang, Z.; Shi, J., Bi2S3-embedded mesoporous silica nanoparticles for efficient drug delivery and interstitial radiotherapy sensitization. *Biomaterials* **2015**, 37 (Supplement C), 447-455.
51. Cheng, L.; Yuan, C.; Shen, S.; Yi, X.; Gong, H.; Yang, K.; Liu, Z., Bottom-up synthesis of metal-ion-doped WS2 nanoflakes for cancer theranostics. *ACS Nano* **2015**, 9 (11), 11090-11101.
52. Wen, L.; Chen, L.; Zheng, S.; Zeng, J.; Duan, G.; Wang, Y.; Wang, G.; Chai, Z.; Li, Z.; Gao, M., Ultrasmall Biocompatible WO<sub>3-x</sub> Nanodots for Multi-Modality Imaging and Combined Therapy of Cancers. *Advanced Materials* **2016**, 28 (25), 5072-5079.
53. Song, G.; Chen, Y.; Liang, C.; Yi, X.; Liu, J.; Sun, X.; Shen, S.; Yang, K.; Liu, Z., Catalase-Loaded TaOx Nanoshells as Bio-Nanoreactors Combining High-Z Element and Enzyme Delivery for Enhancing Radiotherapy. *Advanced Materials* **2016**, 28 (33), 7143-7148.
54. Song, G.; Chao, Y.; Chen, Y.; Liang, C.; Yi, X.; Yang, G.; Yang, K.; Cheng, L.; Zhang, Q.; Liu, Z., All-in-One Theranostic Nanoplatfrom Based on Hollow TaOx for Chelator-Free Labeling Imaging, Drug Delivery, and Synergistically Enhanced Radiotherapy. *Advanced Functional Materials* **2016**, 26 (45), 8243-8254.
55. Maggiorella, L.; Barouch, G.; Devaux, C.; Pottier, A.; Deutsch, E.; Bourhis, J.; Borghi, E.; Levy, L., Nanoscale radiotherapy with hafnium oxide nanoparticles. *Future Oncology* **2012**, 8, 1167-1181.
56. Scofield, J. H. *Theoretical photoionization cross sections from 1 to 1500 keV*; CALIFORNIA UNIV., LIVERMORE. LAWRENCE LIVERMORE LAB.: 1973.
57. Laster, B.; Thomlinson, W.; Fairchild, R., Photon activation of iododeoxyuridine: biological efficacy of Auger electrons. *Radiation research* **1993**, 133 (2), 219-224.
58. Incerti, S.; Habchi, C.; Moretto, P.; Olivier, J.; Seznec, H., Geant4 simulation of the new CENBG micro and nanoprobe facility. *Nuclear Instruments and Methods in Physics Research, Section B* **2006**, 249, 738-742.
59. Incerti, S.; Psaltaki, M.; Gillet, P.; Barberet, P.; Bardies, M.; Bernal, M. A.; Bordage, M. C.; Breton, V.; Davidkova, M.; Delage, E.; El Bitar, Z.; Francis, Z.; Guatelli, S.; Ivanchenko, A.; Ivanchenko, V.; Karamitros, M.; Lee, S. B.; Maigne, L.; Meylan, S.; Murakami, K.; Nieminen, P.; Payno, H.; Perrot, Y.; Petrovic, I.; Pham, Q. T.; Ristic-Fira, A.; Santin, G.; Sasaki, T.; Seznec, H.; Shin, J. I.; Stepan, V.; Tran, H. N.; Villagrasa, C., Simulating radial dose of ion tracks in liquid water simulated with Geant4-DNA: A comparative study. *Nuclear Instruments and Methods in Physics Research, Section B* **2014**, 333, 92-98.
60. Agostinelli, S.; Allison, J.; Amako, K.; Apostolakis, J.; Araujo, H.; Arce, P.; Asai, M.; Axen, D.; Banerjee, S.; Barrand, G.; Behner, F.; Bellagamba, L.; Boudreau, J.; Broglia, L.; Brunengo, A.; Burkhardt, H.; Chauvie, S.; Chuma, J.; Chytracsek, R.; Cooperman, G.; Cosmo, G.; Degtyarenko, P.; Dell'Acqua, A.; Depaola, G.; Dietrich, D.; Enami, R.; Feliciello, A.; Ferguson, C.; Fesefeldt, H.; Folger, G.; Foppiano, F.; Forti, A.; Garelli, S.; Giani, S.; Giannitrapani, R.; Gibin, D.; Gómez Cadenas, J. J.; González, I.; Gracia Abril, G.; Greeniaus, G.; Greiner, W.; Grichine, V.; Grossheim, A.; Guatelli, S.; Gumplinger, P.; Hamatsu, R.; Hashimoto, K.; Hasui, H.; Heikkinen, A.; Howard, A.; Ivanchenko, V.; Johnson, A.; Jones, F. W.; Kallenbach, J.; Kanaya, N.; Kawabata, M.; Kawabata, Y.; Kawaguti, M.; Kelner, S.; Kent, P.; Kimura, A.; Kodama, T.; Kokoulin, R.; Kossov, M.; Kurashige, H.; Lamanna, E.; Lampén, T.; Lara, V.; Lefebure, V.; Lei, F.; Liendl, M.; Lockman, W.; Longo, F.; Magni, S.; Maire, M.; Medernach, E.; Minamimoto, K.; Mora de Freitas, P.; Morita, Y.; Murakami, K.; Nagamatu, M.; Nartallo, R.; Nieminen, P.; Nishimura, T.; Ohtsubo, K.; Okamura, M.; O'Neale, S.; Oohata, Y.; Paech, K.; Perl, J.; Pfeiffer, A.; Pia, M. G.; Ranjard, F.; Rybin, A.; Sadilov, S.; Di Salvo, E.; Santin, G.; Sasaki, T.; Savvas, N.; Sawada, Y.; Scherer, S.; Sei, S.; Sirotenko, V.; Smith, D.; Starkov, N.; Stoecker, H.; Sulkimo, J.; Takahata, M.; Tanaka, S.; Tcherniaev, E.; Safai Tehrani, E.; Tropeano, M.; Truscott, P.; Uno, H.; Urban, L.; Urban, P.; Verderi, M.; Walkden, A.; Wander, W.; Weber, H.; Wellisch, J. P.; Wenaus, T.; Williams, D. C.; Wright, D.; Yamada, T.; Yoshida, H.; Zschesche, D., Geant4—a simulation toolkit. *Nuclear Instruments and Methods in Physics Research Section A: Accelerators, Spectrometers, Detectors and Associated Equipment* **2003**, 506 (3), 250-303.
61. Incerti, S.; Seznec, H.; Simon, M.; Barberet, P.; Habchi, C.; Moretto, P., Monte Carlo dosimetry for targeted irradiation of individual cells using a microbeam facility. *Radiation Protection Dosimetry* **2009**, 133, 2-11.
62. Incerti, S.; Zhang, Q.; Andersson, F.; Moretto, P.; Grime, G. W.; Merchant, M. J.; Nguyen, D. T.; Habchi, C.; Pouthier, T.; Seznec, H., Monte Carlo simulation of the CENBG microbeam and nanobeam lines with the Geant4 toolkit. *Nuclear Instruments and Methods in Physics Research, Section B* **2007**, 260, 20-27.
63. Morgan, W. F.; Sowa, M. B., Non-targeted effects induced by ionizing radiation: Mechanisms and potential impact on radiation induced health effects. *Cancer Letters* **2015**, 356 (1), 17-21.
64. Foley, E. A.; Carter, J. D.; Shan, F.; Guo, T., Enhanced relaxation of nanoparticle-bound supercoiled DNA in X-ray radiation. *Chemical Communications* **2005**, (25), 3192-3194.
65. Zheng, Y.; Hunting, D. J.; Ayotte, P.; Sanche, L., Radiosensitization of DNA by gold nanoparticles irradiated with high-energy electrons. **2009**.

66. Pawlik, T. M.; Keyomarsi, K., Role of cell cycle in mediating sensitivity to radiotherapy. *International Journal of Radiation Oncology\*Biophysics\*Physics* **2004**, *59* (4), 928-942.
67. Marill, J.; Anesary, N. M.; Zhang, P.; Vivet, S.; Borghi, E.; Levy, L.; Pottier, A., Hafnium oxide nanoparticles: toward an in vitro predictive biological effect? *Radiation Oncology* **2014**, *9*, 150/1-150/23.
68. Townley, H. E.; Rapa, E.; Wakefield, G.; Dobson, P. J., Nanoparticle augmented radiation treatment decreases cancer cell proliferation. *Nanomedicine* **2012**, *8*, 526-536.
69. Garcia-Saucedo, C.; Field, J. A.; Otero-Gonzalez, L.; Sierra-Alvarez, R., Low toxicity of HfO<sub>2</sub>, SiO<sub>2</sub>, Al<sub>2</sub>O<sub>3</sub> and CeO<sub>2</sub> nanoparticles to the yeast, *Saccharomyces cerevisiae*. *Journal of Hazardous Materials* **2011**, *192*, 1572-1579.
70. Jolivet, J.-P.; Cassaignon, S.; Chaneac, C.; Chiche, D.; Durupthy, O.; Portehault, D., Design of metal oxide nanoparticles: Control of size, shape, crystalline structure and functionalization by aqueous chemistry. *Comptes Rendus Chimie* **2010**, *13*, 40-51.
71. Le Trequesser, Q.; Sez nec, H.; Delville, M.-H., Functionalized nanomaterials: their use as contrast agents in bioimaging: mono- and multimodal approaches. *Nanotechnology Reviews* **2013**, *2*, 125-169.
72. Fiandra, L.; Mazzucchelli, S.; De Palma, C.; Colombo, M.; Allevi, R.; Sommaruga, S.; Clementi, E.; Bellini, M.; Prosperi, D.; Corsi, F., Assessing the in vivo targeting efficiency of multifunctional nanoconstructs bearing antibody-derived ligands. *ACS Nano* **2013**, *7* (7), 6092-6102.
73. Moghimi, S. M.; Szebeni, J., Stealth liposomes and long circulating nanoparticles: critical issues in pharmacokinetics, opsonization and protein-binding properties. *Progress in lipid research* **2003**, *42* (6), 463-478.
74. Hagens, W. I.; Oomen, A. G.; de Jong, W. H.; Cassee, F. R.; Sips, A. J. A. M., What do we (need to) know about the kinetic properties of nanoparticles in the body? *Regulatory Toxicology and Pharmacology* **2007**, *49*, 217-229.
75. Parham, P., Elements of immune system and their roles in defense, The Immune System. Garland Science Publishing, New York, NY: 2005.
76. Monopoli, M. P.; Aaberg, C.; Salvati, A.; Dawson, K. A., Biomolecular coronas provide the biological identity of nanosized materials. *Nature Nanotechnology* **2012**, *7*, 779-786.
77. Roa, W.; Xiong, Y.; Chen, J.; Yang, X.; Song, K.; Yang, X.; Kong, B.; Wilson, J.; Xing, J. Z., Pharmacokinetic and toxicological evaluation of multi-functional thiol-6-fluoro-6-deoxy-D-glucose gold nanoparticles in vivo. *Nanotechnology* **2012**, *23* (37), 375101.
78. Petros, R. A.; DeSimone, J. M., Strategies in the design of nanoparticles for therapeutic applications. *Nature Reviews Drug Discovery* **2010**, *9* (8), 615-627.
79. Li, M.; Al-Jamal, K. T.; Kostarelos, K.; Reineke, J., Physiologically Based Pharmacokinetic Modeling of Nanoparticles. *ACS Nano* **2010**, *4* (11), 6303-6317.
80. Nel, A.; Xia, T.; Mädler, L.; Li, N., Toxic Potential of Materials at the Nanolevel. *Science* **2006**, *311* (5761), 622-627.
81. Desai, M.; Labhassetwar, V.; Walter, E.; Levy, R.; Amidon, G., The Mechanism of Uptake of Biodegradable Microparticles in Caco-2 Cells Is Size Dependent. *Pharm Res* **1997**, *14* (11), 1568-1573.
82. Gao, H.; Shi, W.; Freund, L. B., Mechanics of receptor-mediated endocytosis. *Proceedings of the National Academy of Sciences of the United States of America* **2005**, *102* (27), 9469-9474.
83. Albanese, A.; Tang, P. S.; Chan, W. C., The effect of nanoparticle size, shape, and surface chemistry on biological systems. *Annual review of biomedical engineering* **2012**, *14*, 1-16.
84. Hsiao, I.-L.; Huang, Y.-J., Effects of various physicochemical characteristics on the toxicities of ZnO and TiO<sub>2</sub> nanoparticles toward human lung epithelial cells. *Science of the Total Environment* **2011**, *409* (7), 1219-1228.
85. Simon, M.; Saez, G.; Muggioli, G.; Lavenas, M.; Le Trequesser, Q.; Michelet, C.; Devès, G.; Barberet, P.; Chevet, E.; Dupuy, D.; Delville, M.-H.; Sez nec, H., In situ quantification of diverse titanium dioxide nanoparticles unveils selective endoplasmic reticulum stress-dependent toxicity. *Nanotoxicology* **2017**, *11* (1), 134-145.
86. Ferrari, M., Nanogeometry: beyond drug delivery. *Nature nanotechnology* **2008**, *3* (3), 131-132.
87. Goodman, C. M.; McCusker, C. D.; Yilmaz, T.; Rotello, V. M., Toxicity of gold nanoparticles functionalized with cationic and anionic side chains. *Bioconjugate Chemistry* **2004**, *15* (4), 897-900.
88. Roy, R.; Kumar, S.; Tripathi, A.; Das, M.; Dwivedi, P. D., Interactive threats of nanoparticles to the biological system. *Immunology Letters* **2014**, *158* (1), 79-87.
89. Simon, M.; Barberet, P.; Delville, M.-H.; Moretto, P.; Sez nec, H., Titanium dioxide nanoparticles induced intracellular calcium homeostasis modification in primary human keratinocytes. Towards an in vitro explanation of titanium dioxide nanoparticles toxicity. *Nanotoxicology* **2011**, *5* (2), 125-139.
90. Kirchner, C.; Liedl, T.; Kudera, S.; Pellegrino, T.; Muñoz Javier, A.; Gaub, H. E.; Stölzle, S.; Fertig, N.; Parak, W. J., Cytotoxicity of colloidal CdSe and CdSe/ZnS nanoparticles. *Nano Letters* **2005**, *5* (2), 331-338.

91. Otsuka, H.; Nagasaki, Y.; Kataoka, K., PEGylated nanoparticles for biological and pharmaceutical applications. *Advanced drug delivery reviews* **2012**, *64*, 246-255.
92. Batrakova, E.; Dorodnych, T. Y.; Klinskii, E. Y.; Kliushnenkova, E.; Shemchukova, O.; Goncharova, O.; Arjakov, S.; Alakhov, V. Y.; Kabanov, A., Anthracycline antibiotics non-covalently incorporated into the block copolymer micelles: in vivo evaluation of anti-cancer activity. *British journal of cancer* **1996**, *74* (10), 1545.
93. Nakanishi, T.; Fukushima, S.; Okamoto, K.; Suzuki, M.; Matsumura, Y.; Yokoyama, M.; Okano, T.; Sakurai, Y.; Kataoka, K., Development of the polymer micelle carrier system for doxorubicin. *Journal of Controlled Release* **2001**, *74* (1), 295-302.
94. Nasongkla, N.; Bey, E.; Ren, J.; Ai, H.; Khemtong, C.; Guthi, J. S.; Chin, S.-F.; Sherry, A. D.; Boothman, D. A.; Gao, J., Multifunctional polymeric micelles as cancer-targeted, MRI-ultrasensitive drug delivery systems. *Nano Letters* **2006**, *6* (11), 2427-2430.
95. Adams, M. L.; Lavasanifar, A.; Kwon, G. S., Amphiphilic block copolymers for drug delivery. *Journal of pharmaceutical sciences* **2003**, *92* (7), 1343-1355.
96. Malam, Y.; Loizidou, M.; Seifalian, A. M., Liposomes and nanoparticles: nanosized vehicles for drug delivery in cancer. *Trends in pharmacological sciences* **2009**, *30* (11), 592-599.
97. Matsumura, Y., Poly (amino acid) micelle nanocarriers in preclinical and clinical studies. *Advanced drug delivery reviews* **2008**, *60* (8), 899-914.
98. Wu, J.; Liu, Q.; Lee, R. J., A folate receptor-targeted liposomal formulation for paclitaxel. *International journal of pharmaceutics* **2006**, *316* (1), 148-153.
99. Horn, D.; Rieger, J., Organic nanoparticles in the aqueous phase - theory, experiment and use. *Angewandte Chemie International Editions* **2001**, *40*, 4330-4361.
100. Sharma, A.; Sharma, U. S., Liposomes in drug delivery: Progress and limitations. *International journal of pharmaceutics* **1997**, *154* (2), 123-140.
101. Schlüter, D. A.; Hawker, C.; Sakamoto, J., *Synthesis of Polymers: New Structures and Methods*. John Wiley & Sons: 2012.
102. Gref, R.; Lück, M.; Quellec, P.; Marchand, M.; Dellacherie, E.; Harnisch, S.; Blunk, T.; Müller, R. H., 'Stealth' corona-core nanoparticles surface modified by polyethylene glycol (PEG): influences of the corona (PEG chain length and surface density) and of the core composition on phagocytic uptake and plasma protein adsorption. *Colloids and Surfaces B: Biointerfaces* **2000**, *18* (3-4), 301-313.
103. Li, C., Poly (L-glutamic acid)-anticancer drug conjugates. *Advanced drug delivery reviews* **2002**, *54* (5), 695-713.
104. Duncan, R., The dawning era of polymer therapeutics. *Nature Reviews Drug Discovery* **2003**, *2* (5), 347-360.
105. Rawat, M.; Singh, D.; Saraf, S.; Saraf, S., Nanocarriers: promising vehicle for bioactive drugs. *Biological and Pharmaceutical Bulletin* **2006**, *29* (9), 1790-1798.
106. Lee, C. C.; MacKay, J. A.; Frechet, J. M. J.; Szoka, F. C., Designing dendrimers for biological applications. *Nature Biotechnology* **2005**, *23*, 1517-1526.
107. Boas, U.; Christensen, J. B.; Heegaard, P. M., Dendrimers: design, synthesis and chemical properties. *Journal of Materials Chemistry* **2006**, *16* (38), 3785-3798.
108. Svenson, S.; Tomalia, D. A., Dendrimers in biomedical applications—reflections on the field. *Advanced drug delivery reviews* **2005**, *57* (15), 2106-2129.
109. Nanjwade, B. K.; Bechra, H. M.; Derkar, G. K.; Manvi, F. V.; Nanjwade, V. K., Dendrimers: Emerging polymers for drug-delivery systems. *European Journal of Pharmaceutical Sciences* **2009**, *38* (3), 185-196.
110. Gillies, E. R.; Fréchet, J. M. J., Dendrimers and dendritic polymers in drug delivery. *Drug Discovery Today* **2005**, *10* (1), 35-43.
111. Wiwattanapatapee, R.; Carreño-Gómez, B.; Malik, N.; Duncan, R., Anionic PAMAM dendrimers rapidly cross adult rat intestine in vitro: a potential oral delivery system? *Pharm Res* **2000**, *17* (8), 991-998.
112. Jevprasesphant, R.; Penny, J.; Jalal, R.; Attwood, D.; McKeown, N.; D'emanuele, A., The influence of surface modification on the cytotoxicity of PAMAM dendrimers. *International journal of pharmaceutics* **2003**, *252* (1), 263-266.
113. Tu, Z.-c.; Ou-Yang, Z.-c., Single-walled and multiwalled carbon nanotubes viewed as elastic tubes with the effective Young's moduli dependent on layer number. *Physical Review B* **2002**, *65* (23), 233407.
114. Nygaard, U. C.; Hansen, J. S.; Samuelsen, M.; Alberg, T.; Marioara, C. D.; Løvik, M., Single-walled and multi-walled carbon nanotubes promote allergic immune responses in mice. *Toxicological Sciences* **2009**, kfp057.
115. Liu, Z.; Tabakman, S.; Welsher, K.; Dai, H., Carbon nanotubes in biology and medicine: in vitro and in vivo detection, imaging and drug delivery. *Nano Research* **2009**, *2*, 85-120.

116. Bianco, A.; Kostarelos, K.; Partidos, C. D.; Prato, M., Biomedical applications of functionalised carbon nanotubes. *Chemical Communications* **2005**, (5), 571-577.
117. Bianco, A.; Kostarelos, K.; Prato, M., Applications of carbon nanotubes in drug delivery. *Current Opinion in Chemical Biology* **2005**, *9*, 674-679.
118. Sharma, H.; Mishra, P. K.; Talegaonkar, S.; Vaidya, B., Metal nanoparticles: a theranostic nanotool against cancer. *Drug Discovery Today* **2015**, *20*, 1143-1151.
119. Guerrero-Martínez, A.; Pérez-Juste, J.; Liz-Marzán, L. M., Recent progress on silica coating of nanoparticles and related nanomaterials. *Advanced Materials* **2010**, *22* (11), 1182-1195.
120. Gasparyan, V., Preparation and application of various nanoparticles in biology and medicine. *Nanotechnology Development* **2013**, *3*, 6-11.
121. Brown, S. D.; Nativo, P.; Smith, J.-A.; Stirling, D.; Edwards, P. R.; Venugopal, B.; Flint, D. J.; Plumb, J. A.; Graham, D.; Wheate, N. J., Gold Nanoparticles for the Improved Anticancer Drug Delivery of the Active Component of Oxaliplatin. *Journal of the American Chemical Society* **2010**, *132*, 4678-4684.
122. Jain, P. K.; Lee, K. S.; El-Sayed, I. H.; El-Sayed, M. A., Calculated absorption and scattering properties of gold nanoparticles of different size, shape, and composition: applications in biological imaging and biomedicine. *J. Phys. Chem. B* **2006**, *110* (14), 7238-7248.
123. Hainfeld, J. F.; Lin, L.; Slatkin, D. N.; Dilmanian, F. A.; Vadas, T. M.; Smilowitz, H. M., Gold nanoparticle hyperthermia reduces radiotherapy dose. *Nanomedicine: Nanotechnology, Biology and Medicine* **2014**, *10* (8), 1609-1617.
124. Thompson, D. T., Using gold nanoparticles for catalysis. *Nano Today* **2007**, *2* (4), 40-43.
125. Hainfeld, J. F.; Dilmanian, F. A.; Slatkin, D. N.; Smilowitz, H. M., Radiotherapy enhancement with gold nanoparticles. *Journal of Pharmacy and Pharmacology* **2008**, *60*, 977-985.
126. Chithrani, D. B.; Jelveh, S.; Jalali, F.; van Prooijen, M.; Allen, C.; Bristow, R. G.; Hill, R. P.; Jaffray, D. A., Gold nanoparticles as radiation sensitizers in cancer therapy. *Radiation research* **2010**, *173* (6), 719-728.
127. Kittler, S.; Greulich, C.; Diendorf, J.; Koller, M.; Epple, M., Toxicity of silver nanoparticles increases during storage because of slow dissolution under release of silver ions. *Chemistry of Materials* **2010**, *22* (16), 4548-4554.
128. Biju, V.; Itoh, T.; Ishikawa, M., Delivering quantum dots to cells: bioconjugated quantum dots for targeted and nonspecific extracellular and intracellular imaging. *Chemical Society Reviews* **2010**, *39* (8), 3031-3056.
129. Galian, R. E.; de la Guardia, M., The use of quantum dots in organic chemistry. *Trends in Analytical Chemistry* **2009**, *28*, 279-291.
130. Burda, C.; Chen, X.; Narayanan, R.; El-Sayed, M. A., Chemistry and Properties of Nanocrystals of Different Shapes. *Chemical Reviews* **2005**, *105*, 1025-1102.
131. Slowing, I. I.; Trewyn, B. G.; Giri, S.; Lin, V. Y., Mesoporous silica nanoparticles for drug delivery and biosensing applications. *Advanced Functional Materials* **2007**, *17* (8), 1225-1236.
132. Qiao, Z.-A.; Zhang, L.; Guo, M.; Liu, Y.; Huo, Q., Synthesis of Mesoporous Silica Nanoparticles via Controlled Hydrolysis and Condensation of Silicon Alkoxide. *Chemistry of Materials* **2009**, *21*, 3823-3829.
133. Zhu, Y.; Shi, J., A mesoporous core-shell structure for pH-controlled storage and release of water-soluble drug. *Microporous and Mesoporous Materials* **2007**, *103* (1-3), 243-249.
134. Michel, R. B.; Brechbiel, M. W.; Mattes, M. J., A comparison of 4 radionuclides conjugated to antibodies for single-cell kill. *Journal of Nuclear Medicine* **2003**, *44* (4), 632-640.
135. Pinho, S. L. C.; Faneca, H.; Geraldes, C. F. G. C.; Rocha, J.; Carlos, L. D.; Delville, M.-H., Silica nanoparticles for bimodal MRI-optical imaging by grafting Gd<sup>3+</sup> and Eu<sup>3+</sup>/Tb<sup>3+</sup> complexes. *European Journal of Inorganic Chemistry* **2012**, *2012*, 2828-2837.
136. Barnard, A. S.; Curtiss, L. A., Prediction of TiO<sub>2</sub> nanoparticle phase and shape transitions controlled by surface chemistry. *Nano Letters* **2005**, *5*, 1261-1266.
137. Park, H. K.; Kim, D. K.; Kim, C. H., Effect of solvent on titania particle formation and morphology in thermal hydrolysis of TiCl<sub>4</sub>. *Journal of the American Ceramic Society* **1997**, *80*, 743-749.
138. Nian, J.-N.; Teng, H., Hydrothermal Synthesis of Single-Crystalline Anatase TiO<sub>2</sub> Nanorods with Nanotubes as the Precursor. *The Journal of Physical Chemistry B* **2006**, *110*, 4193-4198.
139. Le Trequesser, Q.; Saez, G.; Devès, G.; Michelet, C.; Barberet, P.; Delville, M.-H.; Seznec, H., In situ titanium dioxide nanoparticles quantitative microscopy in cells and in *C. elegans* using nuclear microprobe analysis. *Nuclear Instruments and Methods in Physics Research, Section B* **2014**, *341*, 58-64.



# Chapter 2: Titanium dioxide,





## Table of contents

Introduction.....	43
I - Titanium dioxide properties .....	43
I. 1. Structural and thermodynamic properties .....	43
I. 2. Electronic and optical properties .....	45
I. 3. Some applications of TiO <sub>2</sub> .....	46
II - Several routes to synthesize TiO <sub>2</sub> nanoparticles.....	47
II. 1. Sol-gel synthesis route .....	47
II. 2. Hydrothermal or solvothermal synthesis.....	50
II. 3. Morphology control.....	51
II. 3. a. Morphology control by pH .....	52
II. 3. b. Morphology control by structuring agents .....	52
II. 4. Other synthesis routes .....	54
III - State of the art: the known two-step synthesis of TiO <sub>2</sub> NPs starting from P25 .....	55
III. 1. Precursor: P25 from Degussa/Evonik.....	55
III. 2. First step toward controlled TiO <sub>2</sub> NPs: Titanium dioxide based scrolled nanosheets (sNSs).....	57
III. 3. Second step product: Titanium dioxide nanoneedles (NNs).....	60
IV - Results on the synthesis of nanoneedles .....	62
IV. 1. First step toward controlled TiO <sub>2</sub> NPs: Titanium dioxide based scrolled nanosheets (sNSs).....	62
IV. 2. Second step product: Titanium dioxide nanoneedles (NNs) .....	65
IV. 2. a. Effect of the reaction time .....	68
IV. 2. b. Effect of the nanosheet aging .....	70
IV. 2. c. Initial pH of the reaction.....	71
IV. 3. Control of the NNs shape and morphology with structuring agents.....	72

IV. 3. a. Triethanolamine (TEOA) OR oleic acid (OA).....	73
IV. 3. b. Triethanolamine (TEOA) AND oleic acid (OA).....	75
IV. 4. Preliminary results on the interaction of NPs with cells.....	77
V - Inserting rare-earth elements in TiO <sub>2</sub> matrix.....	79
Conclusion .....	82
Experimental section.....	83
Characterization methods.....	84
Bibliography.....	85

## Introduction

TiO<sub>2</sub> is commonly used in the daily life in the sunscreen, in the food industry as a food coloring (E 171). However, the toxicity of this oxide especially at the nanometer scale has not been studied. That is the reason why we decided to study the synthesis of TiO<sub>2</sub> nanoparticles of different morphologies and to study their toxicity to different cell lines [1].

## I - Titanium dioxide properties

Titanium is the ninth most abundant element in the earth's crust. Titanium is generally found in its oxidized form such as ilmenite (FeTiO<sub>3</sub>), perovskite (CaTiO<sub>3</sub>) or titanate (CaTiSiO<sub>5</sub>). Pure titanium can be obtained by an extraction process with chlorides. This process allows the synthesis of titanium tetrachloride (TiCl<sub>4</sub>) which can be reduced via the Kroll process to obtain pure solid titanium [2]. Titanium dioxide can also be extracted from several ores by sulfuric acid treatment with a production of titanyl sulfate (TiOSO<sub>4</sub>). This compound can then be hydrolyzed and dehydrated to give TiO<sub>2</sub> [3-5].

### I. 1. Structural and thermodynamic properties

TiO<sub>2</sub> is claimed as chemically inert compound with a high refractive index (2.61) which presents a photocatalytic activity [6] under UV light due to its 3.2 eV band gap. Three crystal phases can be found, rutile, anatase and brookite, and their structural and thermodynamic properties are gathered in Table 1.

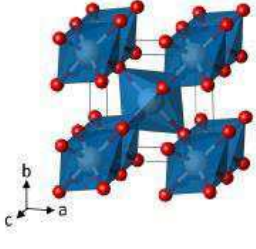
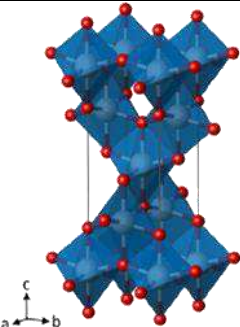
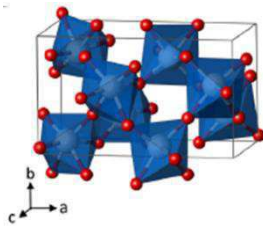
Phase	Rutile	Anatase	Brookite
Crystal system	Tetragonal	Tetragonal	Orthorhombic
Space group	P4 <sub>2</sub> /mnm	I4 <sub>1</sub> /amd	Pbca
Unit cell (Å)	a = 4.594 Å c = 2.958 Å Z = 2	a = 3.785 Å c = 9.5143 Å Z = 4	a = 9.184 Å b = 5.447 Å c = 5.145 Å Z = 8
Distance (Ti <sup>4+</sup> - O <sup>2-</sup> )(Å)	1.95 – 1.99	1.93 – 1.98	1.86 – 2.04
Coordination number	[Ti <sup>4+</sup> ] = 6 [O <sup>2-</sup> ] = 3	[Ti <sup>4+</sup> ] = 6 [O <sup>2-</sup> ] = 3	[Ti <sup>4+</sup> ] = 6 [O <sup>2-</sup> ] = 3
Atomic packing factor	0.705	0.645	0.655
Density (g.cm <sup>-3</sup> )	4.24	3.89	4.12
Hardness (Mohs)	6.0 – 6.5	5.5 – 6.0	5.5 – 6.0
Refractive index	2.61 – 2.89	2.48 – 2.56	2.58 – 2.70
Enthalpy of formation Δ <sub>f</sub> H <sup>0</sup> (298.15 K) (kJ.mol <sup>-1</sup> )	- 944.50 ± 0.96	- 939.27 ± 1.26	- 941.00
Entropy of formation Δ <sub>f</sub> S <sup>0</sup> (298.15 K) (kJ.mol <sup>-1</sup> .K <sup>-1</sup> )	50.37 ± 0.21	49.95 ± 0.42	-
Structure			

Table 1: Physical and thermodynamic properties of the three crystal phases of TiO<sub>2</sub> [7]

While rutile is the thermodynamically stable phase, anatase and brookite are metastable and irreversibly transform to rutile at high temperature (750 – 915 °C) [8-10]. The structures of these solids comprise “TiO<sub>6</sub>” octahedra interconnected in several ways [11]. In rutile, two opposite edges of each octahedron are shared, forming a chain along the [001] axis. In anatase, the “TiO<sub>6</sub>” octahedra are arranged in zigzag and share four edges. Brookite has an orthorhombic structure in which the octahedra share three edges and vertices [12-13]. Although rutile is the most common form in nature, below 100 nm anatase becomes the most thermodynamically stable phase [14-16].

## I. 2. Electronic and optical properties

Because of the high value of the refractive index (Table 1), TiO<sub>2</sub> reflects 96% of the light and appears as a white powder, reason for which it is a pigment widely used especially in the painting industry [17]. Titanium oxide is a semi-conductor material and the electronic band gaps of anatase, rutile and brookite are 3.26 eV, 3.05 eV and 2.96 eV, respectively [18-19]. In this way, photons with an energy higher than the band-gap (in the case of TiO<sub>2</sub>, UV light has enough energy) induce the transfer of an electron from the valence to the conduction band, with the production of an electron-hole pair. In the case of semiconductors, and depending on their kinetics, the electron and hole can recombine or an electron localized at a surface site can reduce an electron acceptor (A) absorbed at the semiconductor. The hole generated in the valence band oxidizes an electron donor (D) absorbed at another surface site (Figure 1). In the case of titanium dioxide, the acceptor is usually the oxygen molecule while the donor may be water or hydroxyl groups on organic compounds [16, 20].

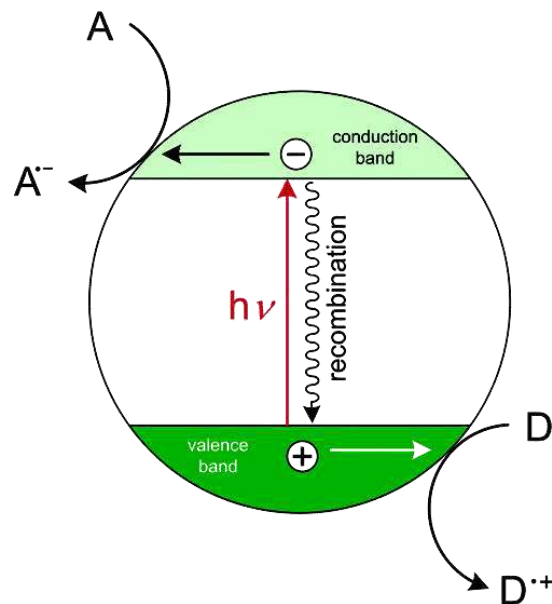


Figure 1: Mechanism of photocatalysis at a semiconductor particle [20]

### I. 3. Some applications of TiO<sub>2</sub>

Due to the strong white color, around 70% of synthesized TiO<sub>2</sub> is used as pigment for paintings, plastics, paper and cosmetic products. The remaining of the production finds its applications in antimicrobial, catalytic or medical uses [21]. Nanometric TiO<sub>2</sub> finds new applications, *e.g.*, in cosmetics and sunscreens, even if it is still used as pigments [22-23]. Due to its electrical properties, and its large band gap, it can absorb UV from the sun. Moreover, due to its nanometric scale, the sunscreens are more transparent, and less viscous [5, 24]. TiO<sub>2</sub> NPs are sometimes covered with a layer of alumina or silica to passivate their surface [25]. Nowadays, TiO<sub>2</sub> NPs are also used in the pharmaceutical and food industry as food coloring under the name E171 [5], and also in toothpaste and drugs as thinner or excipient [21].

## II - Several routes to synthesize TiO<sub>2</sub> nanoparticles

NPs can be synthesized by top-down and bottom-up approaches. The principle of top-down approach is to start from a solid material and gradually grind it in order to obtain particles with smaller and smaller sizes. Mechanical milling usually uses steel balls in a rotational closed chamber with a micrometric powder to be grinded. The obtained size of the object generally depends on the size of the steel balls used, the rotation speed, the temperature and the grinding time [26]. However, this process is not suitable to synthesize NPs with a controlled morphology and that is the reason why the bottom-up approach is more suitable.

The goal of a bottom-up approach is to build a nanomaterial atom-by-atom or molecule-by-molecule. The advantages of this approach are the control of NP size, morphology and structure playing with the synthetic parameters. Here is a description of some of the routes to synthesize TiO<sub>2</sub> NPs with various morphologies.

### II. 1. Sol-gel synthesis route

In the sol-gel method, a colloidal suspension, or a sol, is formed from the hydrolysis and polymerization reactions of the precursors. The precursors are usually inorganic metal salts or metal organic compounds such as M(OR)<sub>4</sub> metal alkoxides consisting of a metal atom (M) surrounded by alkoxide groups such as methoxy, ethoxy, and butoxy group. The “sol” is a colloidal suspension of clusters in a liquid, upon which a gel is formed when these clusters grow to macroscopic dimensions [27]. Figure 2 shows the reaction scheme for the chemical synthesis by sol-gel process. The mechanism of the formation of a metal oxide bond from metal alkoxide precursors comprises the hydrolysis of the alkoxide moiety followed by a condensation reaction which eliminates H<sub>2</sub>O or ROH groups [28]. These reactions usually take place in a solution containing traces of water and an alcohol such as ethanol or methanol. While such reactions are typically carried out at room temperature, subsequent annealing of the resulting nanomaterials at high temperatures is often used to drive the condensation reactions to completion and to obtain a higher degree of crystallinity [27, 29].

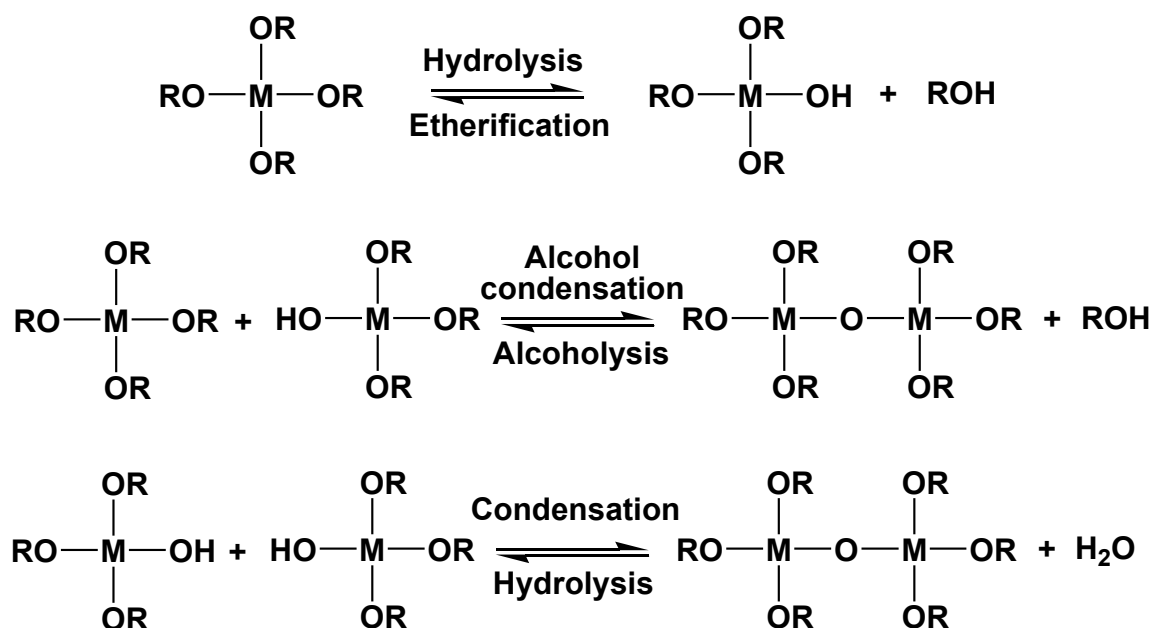


Figure 2: Reaction scheme of the sol-gel process. The formation of M – OH bond takes place via a hydrolysis reaction while the formation of metal oxide bond takes place via a condensation reaction.

Moreover, the precursor reactivity is linked to the electron – withdrawing behavior of the alkoxide groups, which increases the electrophilic behavior of the metal. The rate of hydrolysis depends on several parameters, such as the amount of water and precursor, the temperature [27, 30-31]. During the condensation step, the seed amount depends on several parameters and particularly on the monomer concentration in the synthesis media. Thus, a growth phase is initiated and stopped when the whole precursor is consumed. Hence, the particle size is correlated to the number of synthesized seeds [32] and the amount of precursors [33].

In early examples, particles of TiO<sub>2</sub> of several hundred of nanometers were obtained [34]. The preparation of uniform TiO<sub>2</sub> spheres by hydrolysis of TiCl<sub>4</sub> in highly acidic conditions containing sulfate ions and then aging of this solution for long periods of time (days or weeks) for example, was reported by Matijević *et al.* (Figure 3) [34].

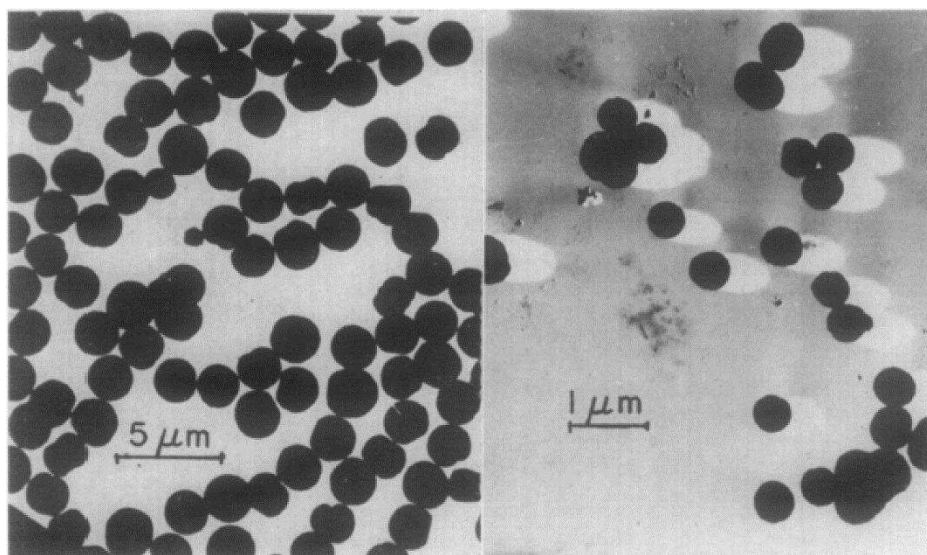


Figure 3: TEM of rutile TiO<sub>2</sub> sol particles obtained by sol-gel synthesis at different ratios TiCl<sub>4</sub>/HCl/Na<sub>2</sub>SO<sub>4</sub> [34]

Barringer and Bowen reported the synthesis of uniform micrometer-size particles through the fast hydrolysis of titanium ethoxide or isopropoxide precursors [35]. More recently, by a similar procedure but with addition of polymers to promote the pore formation, the synthesis of porous and nonporous monodisperse spheres were described [36].

However, one of the main problems faced in sol-gel chemistry is the control of the hydrolysis and condensation rates of titanium precursors, which are usually too fast because of the presence of water in solution. To overcome this issue, a modification of the precursor with complexing ligands has been developed to reduce the hydrolysis rate. For example, Sclan used acetylacetonate as such a ligand and conducted the hydrolysis in the presence of *p*-toluenesulfonic acid to obtain crystalline, dispersible anatase NPs (1 – 5 nm) [37]. Khanna *et al.* used myristic acid to prepare 5 nm anatase nanocrystals with colloidal stability [38], while Jiu *et al.* used a combination of the surfactants F127 and CTAB to drive the hydrolysis of titanium isopropoxide modified by acetylacetonate to obtain anatase particles of 3 – 5 nm in size [39-40].

The polyol method has emerged in recent years as a good alternative to the sol-gel method to obtain crystalline particles at moderate temperatures and is based on the reaction between a polyalcohol and a metal salt. TiO<sub>2</sub> particles were prepared by this method by first heating titanium isopropoxide in diethylene glycol at 140 °C, followed by addition of water and increasing the temperature up to 180 °C, resulting in irregular anatase crystallites 30 – 200 nm

in size [41]. Similarly, titanium butoxide was thermally decomposed in 1,4-butanediol at 300 °C to yield anatase particles of 15 nm [42]. However, the size and the shape of the particles were not really well controlled.

In the early 1990s, Sugimoto developed the “gel-sol” method, based on the preparation of a metal hydroxide gel that is then aged to obtain a sol in which colloidal particles are dispersed. The synthesis starts with the replacement of the isopropoxy groups on titanium by the ethoxy groups of the triethanolamine generating a gel useful to slow down the hydrolysis rate. The gel was then added to aqueous ammonia, and heated at 100 °C to form a second gel composed mainly of titanium hydroxide. The gel was aged at 140 °C for 3 days, producing anatase particles with spherical or spindle like morphology depending on the pH of the initial solution [43]. The gel-sol process is a very good synthesis method to control the size and the morphology of nanoparticles [44-45]. The main drawback of sol-gel and gel-sol method is the use of expensive precursors, such as alkoxides.

## II. 2. Hydrothermal or solvothermal synthesis

The hydrothermal (or solvothermal) term refers to any reaction in an aqueous (non-aqueous) solvent under high pressure and high temperature (below the critical condition). The hydrothermal syntheses are often carried out in a sealed Teflon vessel surrounded by a stainless steel autoclave. The extreme conditions inside the autoclave allow the dissolution and the recrystallization of compounds, which are insoluble at room temperature and atmospheric pressure. As in the sol-gel process, metal alkoxides can be used as precursors. The starting reagents are introduced in the autoclave, which is then sealed and heated in an oven. Several parameters can be controlled such as the precursor concentration, the filling ratio of the autoclave, and the temperature, and these parameters influence the autogenous pressure inside the autoclave. The pressure inside the autoclave may play a key role in the solubility and in the crystal growth rates of the NPs in the case of low boiling point solvents. Therefore, adjusting these parameters leads to various shapes and morphologies [16, 46-48]. This method has been widely used to synthesize titanium dioxide spherical nanoparticles [49-50], nanotubes [51-53], nanorods [54-55], small platelets [56] or nanoplates [57], or spindles [58-59].

### II. 3. Morphology control

The morphology control discussed in this part is common to the two sol-gel and hydrothermal routes mentioned above. The surface energy of the particles is an important parameter in morphology control. The shape of a crystal can be predicted using the Gibbs-Curie-Wulff theorem [60-63]. In standard conditions the surface with the highest free energy will grow faster. In a crystal, the surfaces with the highest energy tend to be minimized. Thus, the shape of the nanoparticles is controlled by the competition between the growth kinetics of the several faces [64-66].

In the case of TiO<sub>2</sub>, the thermodynamically stable form is a truncated bipyramid (Figure 4). The surface energy depends on the coordination number of the titanium atoms. The (101) surface has five and six-fold coordinated titanium atoms, whereas the (001) only has only five-fold coordinated titanium atoms. Thus, the surface (001) is more reactive than the (101) surface and will be minimized [15].

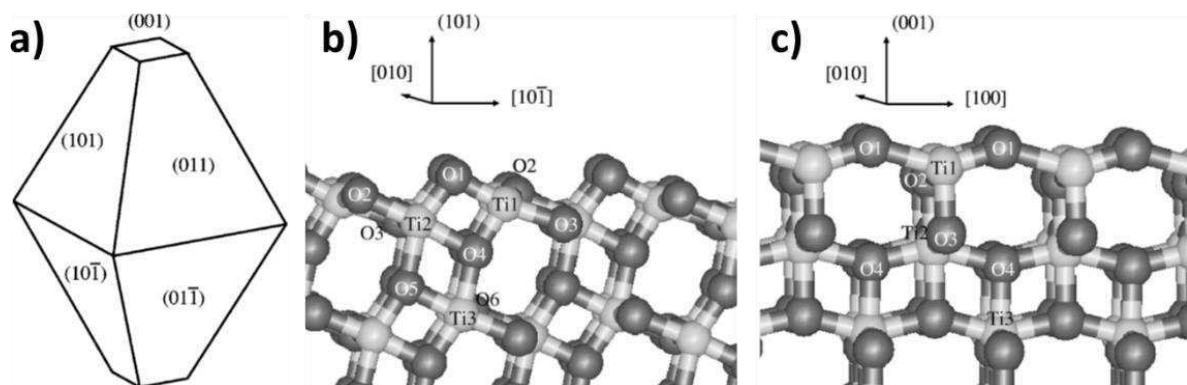


Figure 4: (a) truncated bipyramid, thermodynamically stable form of anatase according to Wulff theorem; structures of the relaxed stoichiometric of (b) (101) surface, and (c) (001) surface [15]

### II. 3. a. Morphology control by pH

pH is an important parameter of crystal growth. It can modify the precursor's reactivity, selectively catalyze a reaction, as well as play a role in the surface chemistry. Figure 5 describes the predicted evolution of the shape of anatase nanocrystals as a function of pH [66]. These nanocrystals vary from truncated bipyramid (acidic condition) to a more elongated form (basic condition) with the formation of (100) surface.

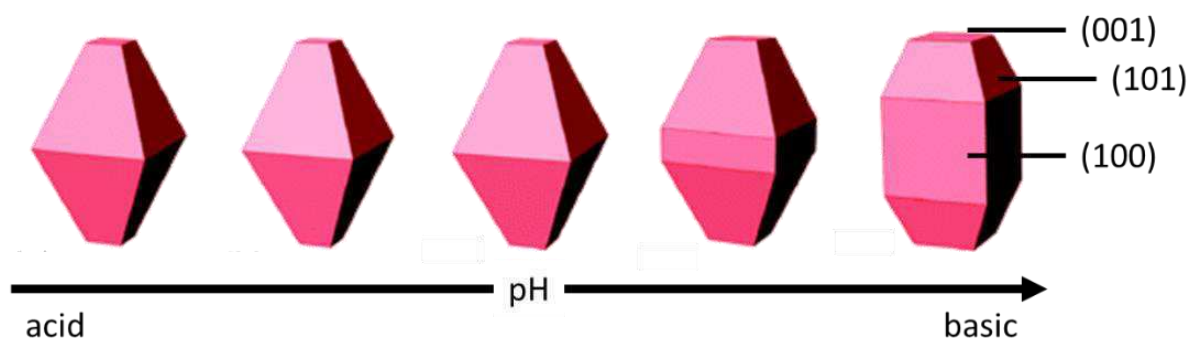


Figure 5: Predicted morphologies for anatase as a function of the pH [66]

The free energy of the surface varies as a function of the protonation state, related to the pH [67]. At pH above 7 and when the surfaces are not protonated, the (101) surface becomes more reactive than the (100) surface and is, thus, minimized. This evolution has been experimentally demonstrated several times [43, 50, 54, 68-69]. It is, thus, possible to control the NP morphology by adjusting the pH value and taking advantage of the thermodynamics. However, the disadvantage is that only thermodynamically favored morphologies are obtained. To overcome this issue, the use of structuring agents can lead to nanoparticles with more diversified morphology as illustrated further on.

### II. 3. b. Morphology control by structuring agents

The principle of NP morphology control by structuring agents is the blocking of the growth of given facets in one or several directions. The structuring agents are specifically adsorbed on one or several crystal surfaces inducing a steric hindrance and preventing their further growth. Consequently, the choice and the concentration of structuring agents are key factors to obtain the targeted morphology. Figure 6 shows an example of TiO<sub>2</sub> NP synthesis assisted by structuring agents. The combined use of some of these agents allows the formation of several morphologies.

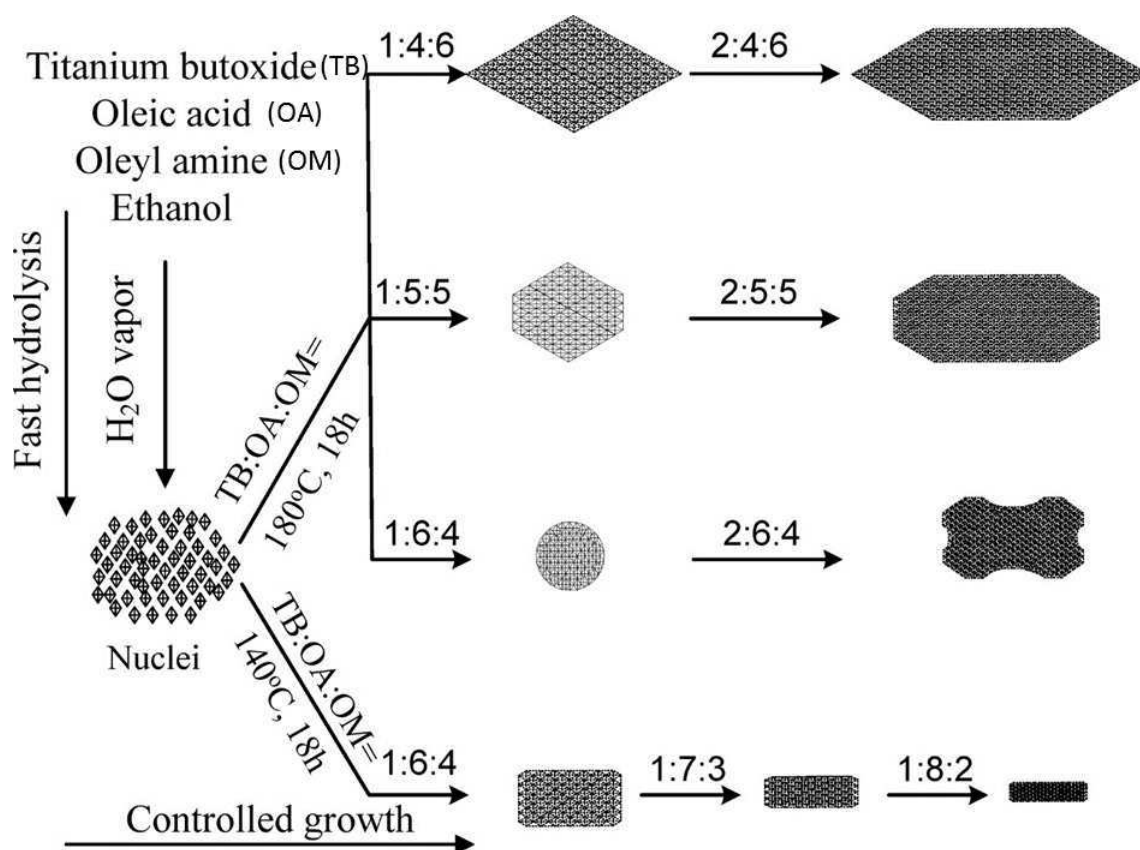


Figure 6: Schematic illustration of the overall formation and shape evolution of TiO<sub>2</sub> NPs using structuring agents [70]

The most commonly used structuring agents are secondary or tertiary amines and carboxylic acids. Thus, TiO<sub>2</sub> NP such as nanospheres [70-73], nanowires [74], nanorods [70-71, 74-76], nanocubes [72], or nanoneedles [72-73] can be synthesized.

The main limitation of the use of structuring agents is the washing process to eliminate the organic molecules which can be a time consuming step. Although washing with water or with several organic solvents is possible, often the organic molecules with high affinity for the metal oxide remain strongly coordinated and can induce toxicity, which is a huge drawback for biomedical applications.

## II. 4. Other synthesis routes

There are other ways of preparing TiO<sub>2</sub> NPs, including aerosol spray synthesis, physical and chemical vapor deposition, pyrolysis, sonochemical synthesis and microwave assisted synthesis [16]. Some synthetic routes to TiO<sub>2</sub> NPs are depicted on Table 2.

Synthesis route	State	Synthesis temperature	Size and morphology	Annealing	References
<b>Sol-gel</b>	Liquid	20 – 150 °C	Controlled	Yes	[27, 43-45, 72, 76-79]
<b>Hydrothermal / Solvothermal</b>	Liquid	100 °C to 200 °C	Controlled	No	[46, 48, 54, 69, 80-90]
<b>Aerosol spray</b>	Solid	High temperature	Controlled/Aggregation	No	[91-95]
<b>Physical and chemical vapor deposition</b>	Gas	200 – 700 °C	Film with controlled thickness	Yes / No	[96-97]
<b>Pyrolysis</b>	Gas	< 100 °C	Controlled	Yes	[98]
<b>Sonochemical</b>	Liquid		Controlled	Yes	[99-102]
<b>Microwave</b>	Liquid	> 100 °C	Controlled	Yes / No	[103-108]

*Table 2: Main synthetic routes to TiO<sub>2</sub> nanoparticles*

We have decided to focus on hydrothermal synthesis because it affords crystalline nanoparticles without the need for annealing. The criteria of small size and good dispersity are essential for biological applications and, thus, we have circumvented annealing in order to avoid NP aggregation/growth, which prevent their re-dispersion in aqueous media.

### III - State of the art: the known two-step synthesis of TiO<sub>2</sub> NPs starting from P25

The titanium precursor choice is a key factor. Beside the titanium alkoxides often used for TiO<sub>2</sub> synthesis it is also possible to start the synthesis of controlled-shape NPs using already formed NPs such as P25 (See part III. 1). The principle is based on the total deconstruction of TiO<sub>2</sub> in highly alkaline media. While the alkoxides are very reactive the species obtained by this way (scrolled nanosheets) provide a slower generation of Ti<sup>4+</sup> monomeric species and, thus facilitates the control of the shape [109].

#### III. 1. Precursor: P25 from Degussa/Evonik

Titanium dioxide P25 is industrially produced by aerosol spray synthesis. A liquid containing an inorganic precursor is passed through a flame and the temperature rise leads to a rapid transformation of the precursor, initiating the formation of NPs that coalesce and sinter. The spray method creates a competition between agglomeration and sintering of the particles leading to nanoscale objects. Indeed, by controlling the precursor concentration, the flame and the temperature, it is possible to control the size of the final objects. This technique generates very small NPs. Figure 7 describes the synthesis process and the reaction equations.

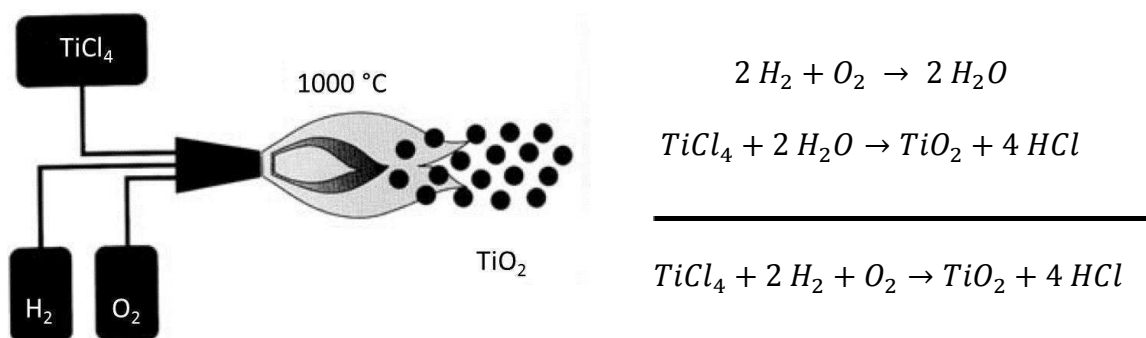


Figure 7: (left) Aerosol process with TiCl<sub>4</sub> as precursor [110]; (right) reaction equations

Degussa/Evonik-P25 is composed of anatase and rutile crystallites in a ratio of 70:30 or 80:20. Indeed, the X-Ray diffraction (XRD) pattern of P25 (Figure 8) shows the presence of anatase (ICDD PDF no. 21-1272) and rutile (ICDD PDF no. 21-1276). The peaks are labeled with the corresponding Miller indices. Considering the main peaks of anatase (101) and rutile (110), the average crystallite sizes are, respectively, 26 and 36 nm.

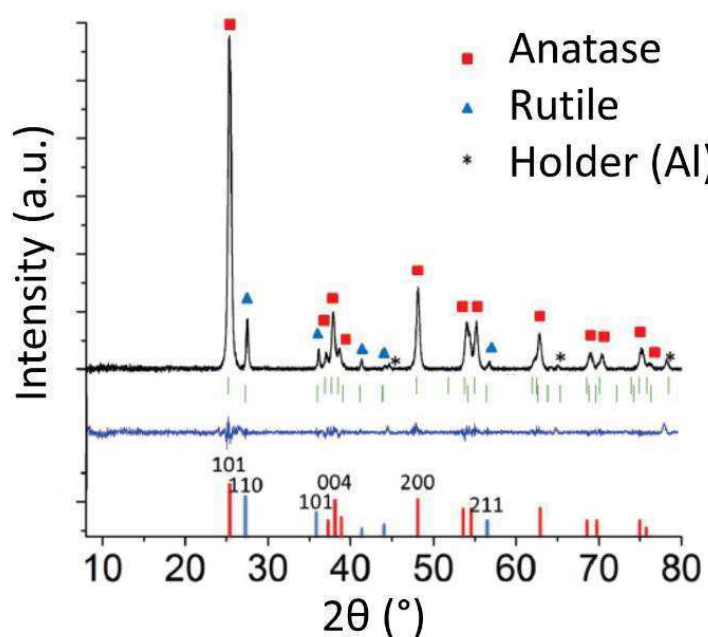


Figure 8: XRD pattern of P25

The TEM images (Figure 9) were also used to determine the NP size as well as their shape. The analysis of P25 reveals the surface projection of random isotropic forms: spheres, cubes, square base bipyramid. The statistical size distribution is measured using the ImageJ software, on more than 300 NPs (Figure 9). Titanium dioxide P25 NPs range between 10 and 50 nm with an average size of 26 nm and a standard deviation of 8 nm. The standard deviation provides an indication of the size homogeneity. P25 NPs have a strong tendency to aggregate, reported in the literature due to the synthetic procedure, and for this reason, they are not the best choice for biomedical applications.

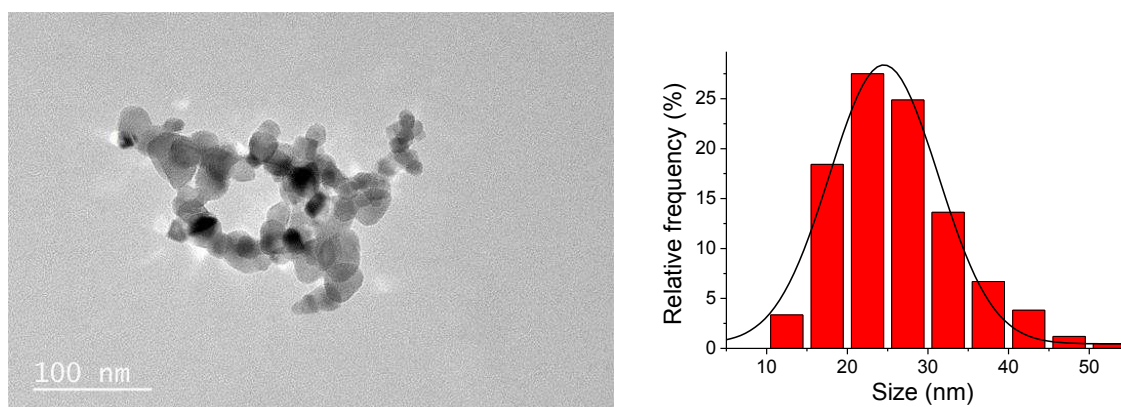


Figure 9: (left) TEM image of P25, (right) size distribution of P25 nanoparticle diameter

### III. 2. First step toward controlled TiO<sub>2</sub> NPs: Titanium dioxide based scrolled nanosheets (sNSs)

The synthesis of TiO<sub>2</sub> scrolled nanosheets by the hydrothermal route has been introduced by Kasuga *et al.*, in the late 90s [51-52, 111]. These objects exhibit a cylindrical morphology with an empty central cylinder and a large aspect ratio. Their high specific surface area is of interest for many applications, such as catalysis [112-113], energy storage [114], photovoltaic [115], or in the biomedical field [116-118].

This synthesis comprises heating between 60 and 180 °C for 20 hours to 2 – 3 days in an autoclave a TiO<sub>2</sub> powder (usually P25) with an aqueous solution of sodium hydroxide (5 to 10 M). Scrolled nanosheets with a length of more than 100 nm, an external diameter of 8 nm and an internal diameter of 5 nm, are obtained after washing with an aqueous diluted hydrochloric acid solution (0.1 M) (Figure 10). The experimental conditions are controlled because different particle morphologies can be obtained depending on the temperature and bases used, as shown in Figure 11 and Figure 12 [119].

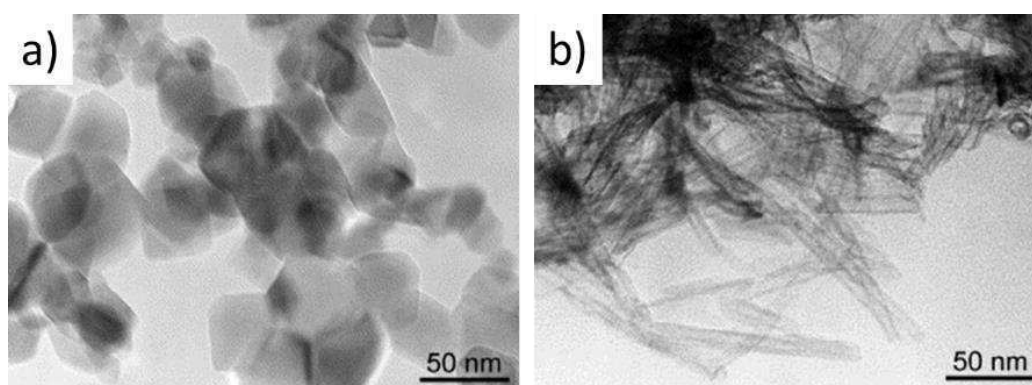


Figure 10: TEM images of (a) commercially P25, and (b) P25 treated with 10M aqueous NaOH at 110 °C for 20 h [111]

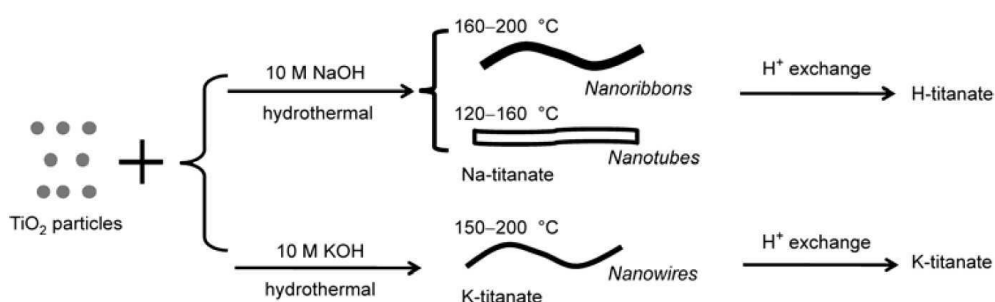


Figure 11: Synthesis processes to obtain several "titanate" structures [120]

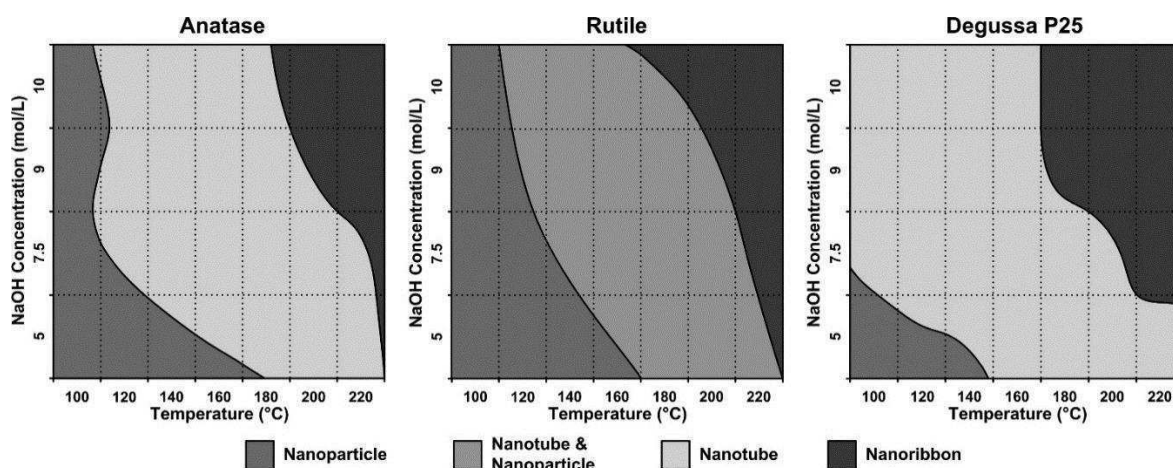


Figure 12: Morphological diagrams of hydrothermally treated anatase, rutile, and P25. Dependence of morphological phase diagrams on the hydrothermal conditions and TiO<sub>2</sub> precursors (anatase, rutile, and Degussa P25) [121]

Since the discovery of this synthesis, numerous studies were performed in order to elucidate the reaction mechanism for the formation of the scrolled nanosheets [122-130]. I will present two of these mechanisms: the peeling-scrolling mechanism and the oriented nanotube crystal growth from nanoloop seeds.

Peeling – scrolling is the more commonly accepted mechanism (Figure 13) [128]:

- Crystalline TiO<sub>2</sub> NPs are decomposed into a disordered phase with a cleavage of the Ti-O-Ti bonds by the alkaline solution and the formation of “TiO<sub>6</sub>” species;
- Formation of plates/sheets of H<sub>2</sub>Ti<sub>3</sub>O<sub>7</sub> with an alignment of “TiO<sub>6</sub>” species;
- Individual trititanate layers are peeled off from the plates – exfoliation;
- And scrolled up into nanotubes.

The principal driving force of the cleavage of the Ti-O-Ti bonds is the surface tension due to an asymmetry related to H deficiency in the plates surface layers. The mechanism is presented in Figure 13.

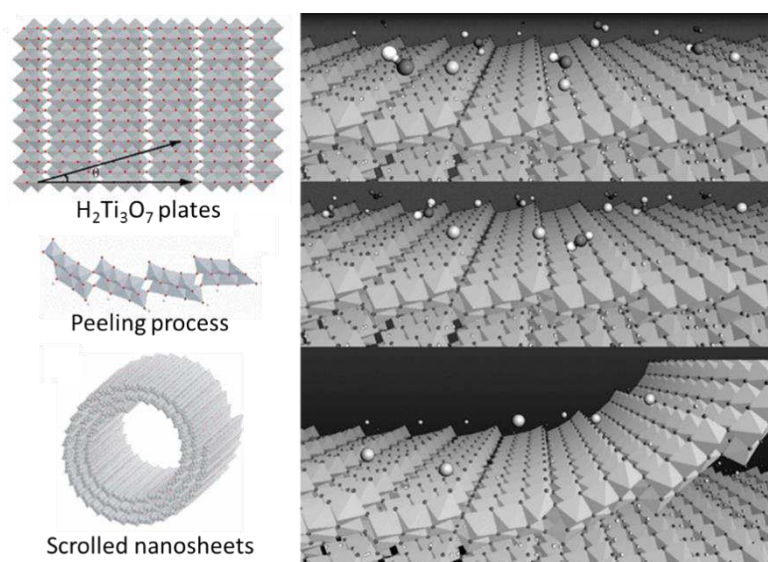


Figure 13: Reaction mechanism with the formation of  $\text{H}_2\text{Ti}_3\text{O}_7$  plates, the peeling process and the scrolling of nanosheets [128]

In the oriented nanotube crystal growth from nanoloop seeds investigated by Kukovecz *et al.* [125], pressure and basic conditions lead to the dissolution of the parent nanoparticles forming “ $\text{TiO}_6$ ” monomers. These monomers react to form sheets of sodium titanate ( $\text{Na}_2\text{Ti}_3\text{O}_7$ ), which then scroll and continue to grow through the long axis. This model differs from the previous one by the absence of a sodium titanate sheet stacking. The mechanism is presented in Figure 14.

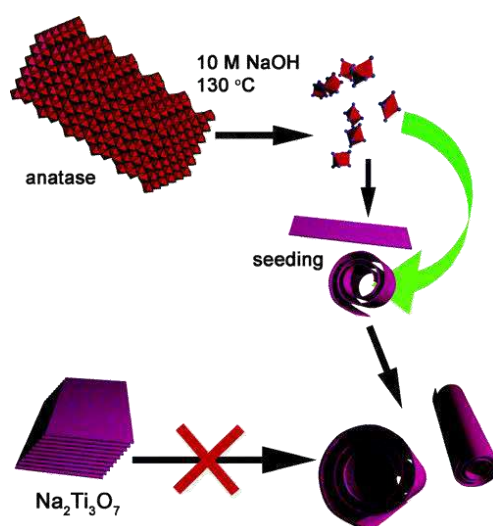


Figure 14: Reaction mechanism based on the oriented nanotube crystal growth from nanoloop seeds [125]

The scrolled nanosheets can be used as precursors for the synthesis of nanoparticles with a shape and size control. Indeed, their tubular structure allows structural reorganisation under hydrothermal and mild conditions (pH < 11) to form nanoparticles with a controlled morphology [120]. The nucleation/growth from “TiO<sub>6</sub>” octahedra allows the formation of TiO<sub>2</sub> nanoparticles with a specific orientation, which depends on the experimental conditions.

### III. 3. Second step product: Titanium dioxide nanoneedles (NNs)

The obtained scrolled nanosheets are used to synthesize nanoneedles in a second hydrothermal treatment. This synthesis, described by Nian and Teng, takes advantage of the pH control to form particles with several morphologies [54]. Sodium hydroxide is added to an aqueous solution of the scrolled nanosheets in order to adjust the pH. Then, a hydrothermal treatment is performed in an autoclave at temperature below 200 °C for 2 – 3 days. According to the predicted morphology (described in II. 3. a), high pH allows the formation of elongated nanoparticles, here assimilated to nanoneedles (NNs) (Figure 15). Here is the reaction pathway of the synthesis of titanium dioxide nanoneedles from scrolled nanosheets:

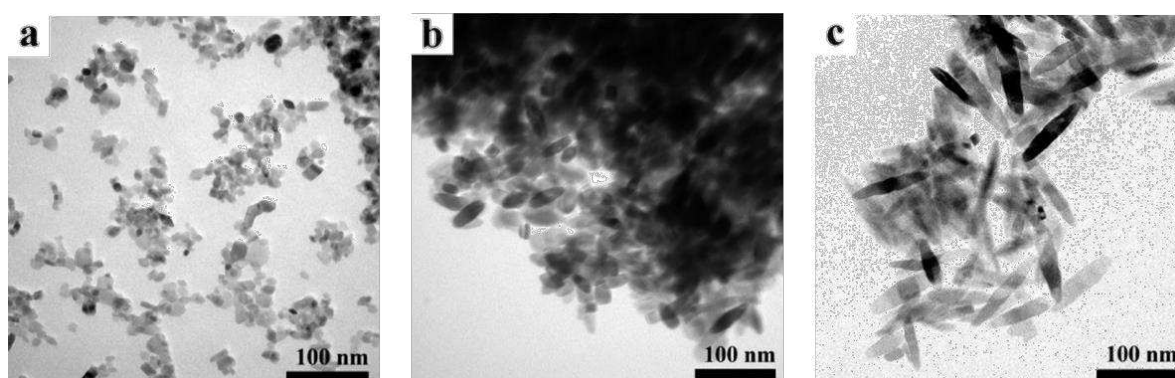
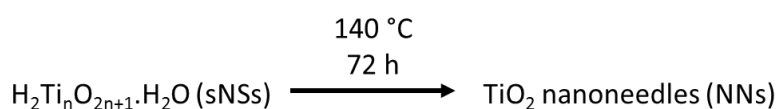


Figure 15: TEM images of TiO<sub>2</sub> nanoparticles prepared from hydrothermal treatment (at 175 °C, for 48 h) of nanotube suspensions with pH values of (a) 2.2, (b) 4.0, and (c) 5.6 [54]

The formation of nanoparticles with a controlled morphology described by Xu *et al.* [120] (Figure 16) is claimed to start with a process of dissolution – nucleation of the nanosheets followed by crystal growth. First, a dissolution of the nanosheets occurs forming “TiO<sub>6</sub>” octahedra. Then, there is a nucleation of the seeds on the surface of the nanosheets. During this step, the “TiO<sub>6</sub>” octahedra self-organize and then self-assemble [131]. The high temperature allows a fast growth of TiO<sub>2</sub> and its crystallization. As predicted by Barnard [66], the crystal growth of anatase seeds at pH above 7 is carried out through (001) because it is the surface with the highest free energy.

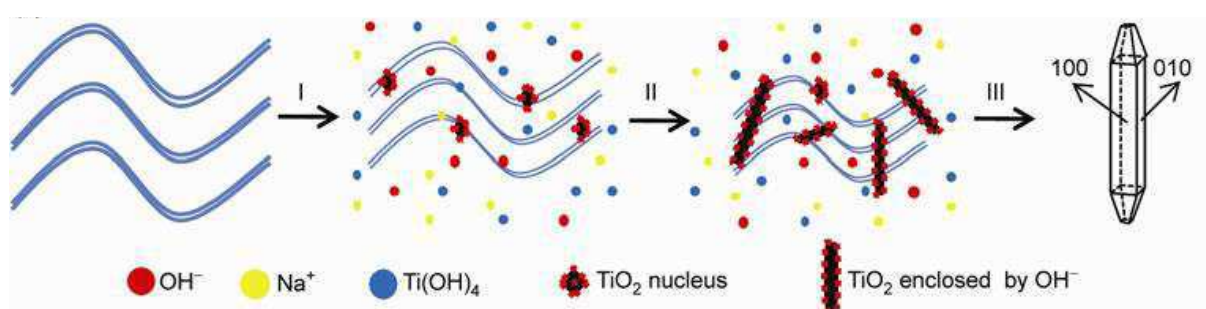


Figure 16: Schematic of the dissolution and nucleation mechanism for Na-titanate nanotubes transformation (I) Na-titanate decomposition, (II) TiO<sub>2</sub> nucleation, and (III) TiO<sub>2</sub> nuclei growth in basic conditions detailed by Xu *et al.* [120]

Another theory, by Li [132], has been proposed to explain the formation of elongated objects. In this model, HO<sup>-</sup> ions are progressively released during nanosheet dissolution and can be adsorbed selectively on the (100) and (010) surfaces, lowering their free energy and, thus, decreasing their growth. The nanoneedles are more elongated when the release of HO<sup>-</sup> ions is important. The reaction stops with the consumption of the totality of the nanosheets.

In the following part, the synthesis and characterization of the scrolled nanosheets and the nanoneedles are described.

## IV - Results on the synthesis of nanoneedles

We decided to synthesize our TiO<sub>2</sub> nanoparticles as described by Nian and Kasuga [54] and to choose the following experimental conditions summarized in Figure 17. The autoclave filling ratio is kept identical to 0.6 in all the experiments.

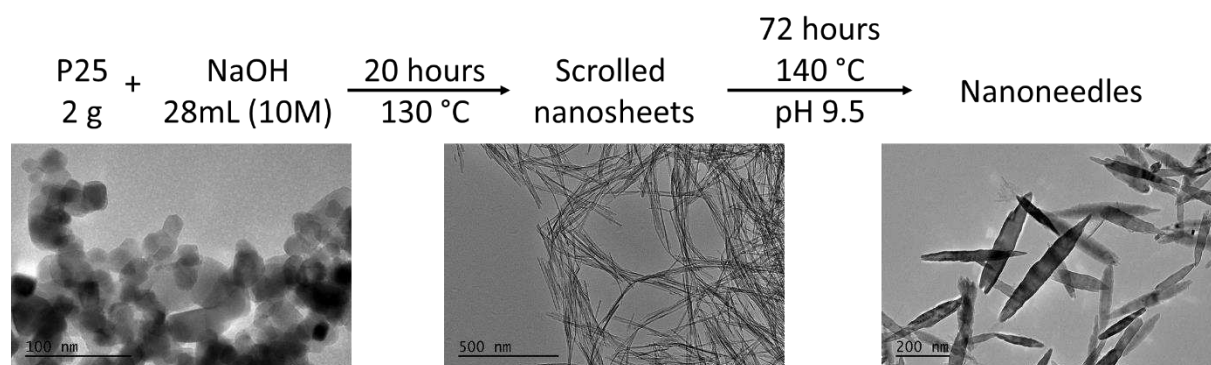
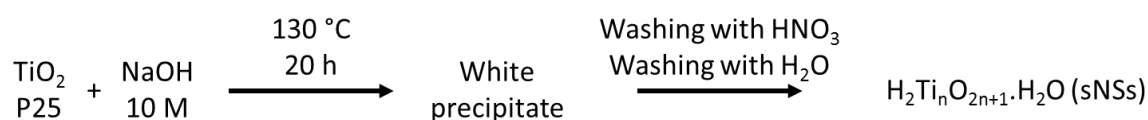


Figure 17: Titanium dioxide nanoneedles synthesis pathway

### IV. 1. First step toward controlled TiO<sub>2</sub> NPs: Titanium dioxide based scrolled nanosheets (sNSs)

The titanium dioxide based scrolled nanosheets are obtained from a hydrothermal treatment of P25 in basic conditions at 130 °C for 20 hours (first reaction in Figure 17). The commonly accepted reactions [54] are given. See the experimental part (Experimental section).



The size and shape of the scrolled nanosheets are ascertained by TEM; Figure 18 shows elongated nanoobjects of variable lengths. The particle's transparency in their central part indicates lower density and confirms the tubular morphology. Some of the sheets are not completely scrolled and, therefore, still exhibit a lamellar structure. The tube's length varies from ten to several hundred of nm, while the diameter of the tubes is *ca.* 9 nm with a standard deviation of 1.5 nm.

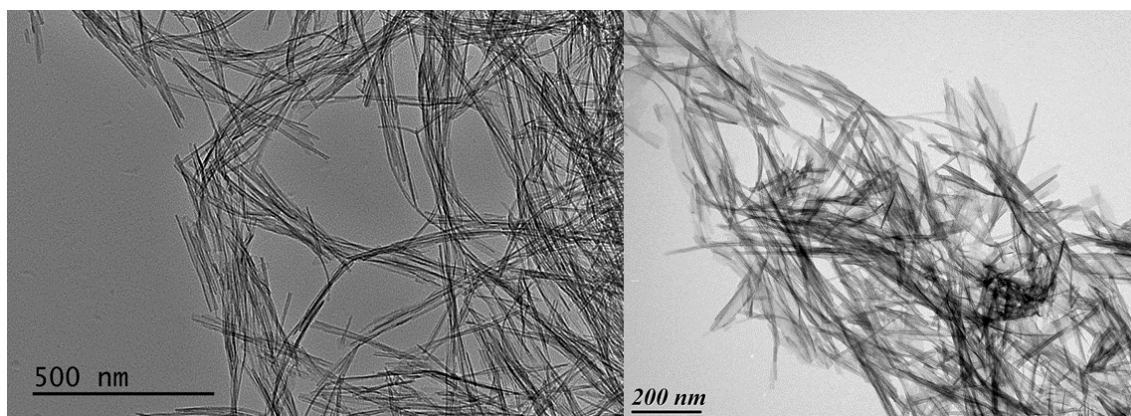


Figure 18: TEM images of scrolled nanosheets at two magnifications after the acid washing

The XRD pattern of TiO<sub>2</sub> scrolled nanosheets is presented in figure 19. The XRD analysis is performed before and after acid washing and drying at 40 °C (cf. Experimental section). The two diffractograms represent, respectively, the sodium titanate (before the acid washing) and hydrogen titanate (after the acid washing) phases. The evolution of the diffraction patterns matches a structural modification that occurs with the acid treatment: Na<sup>+</sup> ions are replaced by H<sup>+</sup> between the sheets [52]. The resulting crystalline phase has been the subject of debates in the scientific community [133-134]. However, the obtained product is very often considered to be a protonated form of a titanium oxide or hydrogeno titanate, formulated as H<sub>2m</sub>Ti<sub>n</sub>O<sub>2n+m</sub> [81]. The four main peaks at 10°, 24°, 28° and 48° 2θ in Figure 19 have been attributed to layered titanates such as A<sub>2</sub>Ti<sub>2</sub>O<sub>5</sub>·H<sub>2</sub>O where A is either Na<sup>+</sup> or H<sup>+</sup> depending on the degree of washing [54]. The peak at 10° 2θ is due to the interlayer distance between sheets (0.7 – 0.8 nm) [81].

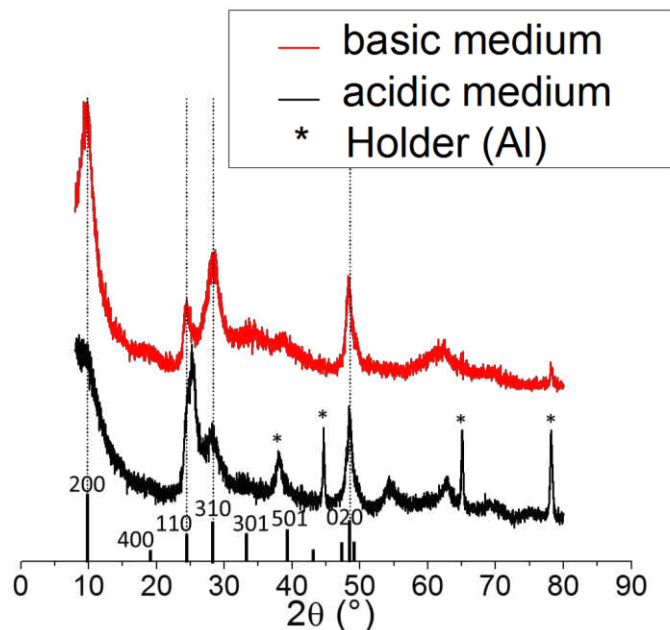


Figure 19: XRD diffractograms of TiO<sub>2</sub> scrolled nanosheets (JCPDS 47-0124) [54]

It was suggested that these A<sub>2</sub>Ti<sub>2</sub>O<sub>5</sub>·H<sub>2</sub>O titanates are built of two-dimensional layers in which “TiO<sub>6</sub>” octahedra are combined through edge sharing as illustrated in Figure 20.

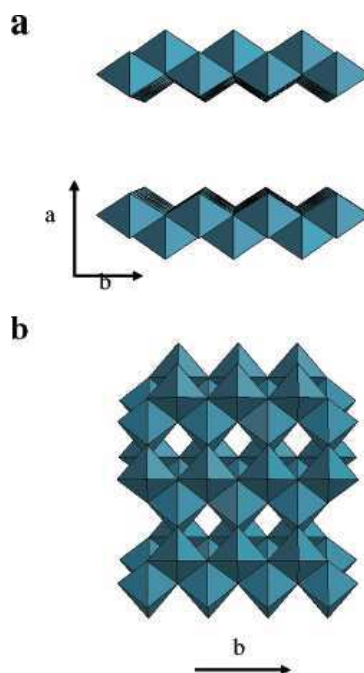


Figure 20: Structure models: (a) protonic titanate, A<sub>2</sub>Ti<sub>2</sub>O<sub>5</sub>·H<sub>2</sub>O, projected along the [001] direction (with hidden interlayer H<sup>+</sup> and HO<sup>-</sup>); (b) anatase TiO<sub>2</sub> projected along the [101] direction.

The lattice is orthorhombic, and the layered structure results in a large elongation of the unit cell along the [001] direction. Exchangeable A<sup>+</sup> resides in between the layers, and the interlayer distance varies with the Na<sup>+</sup>/H<sup>+</sup> exchange. To form nanotubes, the individual layers

are assumed to peel off and scroll along the [001] direction of the A<sub>2</sub>Ti<sub>2</sub>O<sub>5</sub>·H<sub>2</sub>O structure with the tube axis directing along the [010] direction. The diameter of the tubes is 9 nm, and the length ranges from several tens to several hundreds of nanometers.

#### IV. 2. Second step product: Titanium dioxide nanoneedles (NNs)

The reaction was performed by systematically treating a suspension of 0.7 g of scrolled nanosheets for 72 hours at 140 °C while varying others parameters such as the reaction time, aging of the precursor and pH. In the case of the nanoneedles shown in Figure 21 (a) the pH was set to pH 9.8. The nanosystems have an elongated shape and a length between 70 and 750 nm. The statistical distribution of the lengths and widths has been measured on 300 NPs (Figure 21 (b) and (c)). The average length is 350 nm, with a standard deviation of 130 nm, and the average width is 46 nm, with a standard deviation of 10 nm. The nanoneedles are well dispersed on the TEM grid and do not show aggregation.

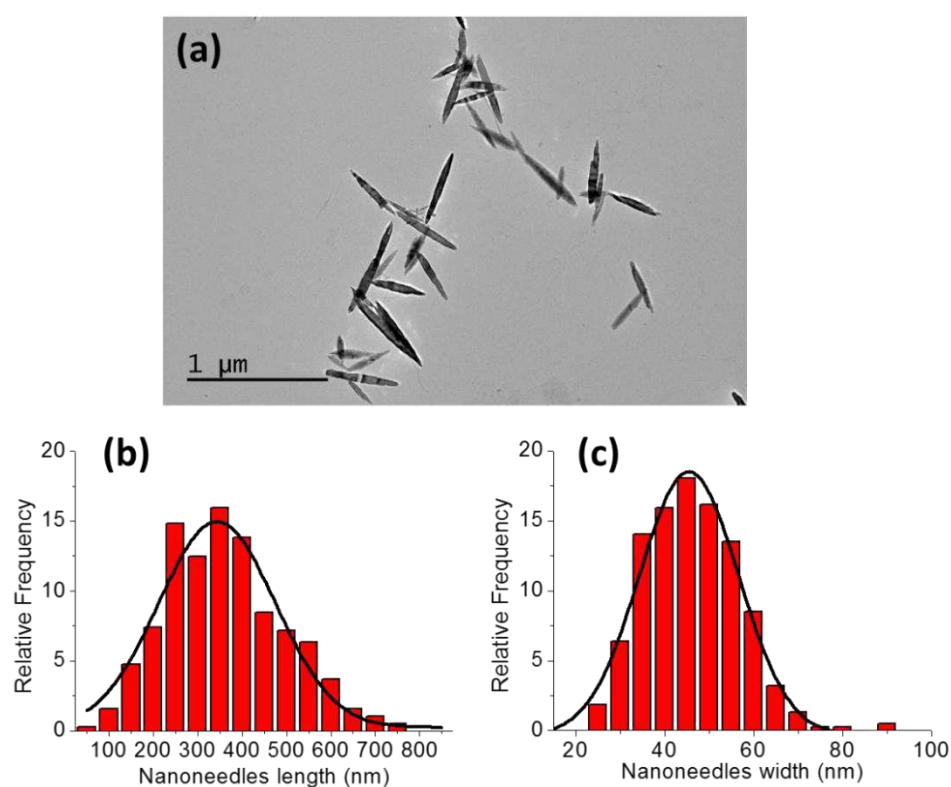


Figure 21: (a) TEM image of nanoneedles, (b) (c) statistical distribution of nanoneedles length and width respectively

To determine the crystalline structure of the product, XRD analysis was performed (Figure 22). Anatase is commonly obtained at low temperature [135] and, accordingly, the diffractogram exhibits the characteristic peaks of well crystallized anatase. An average crystallite size of 26

nm was determined using the Scherrer formula and the strongest anatase reflection (101). However, this formula considers spherical particles and not nanoparticles with an anisotropic shape. This is why, the size obtained by XRD is closer to the width of the nanoneedles.

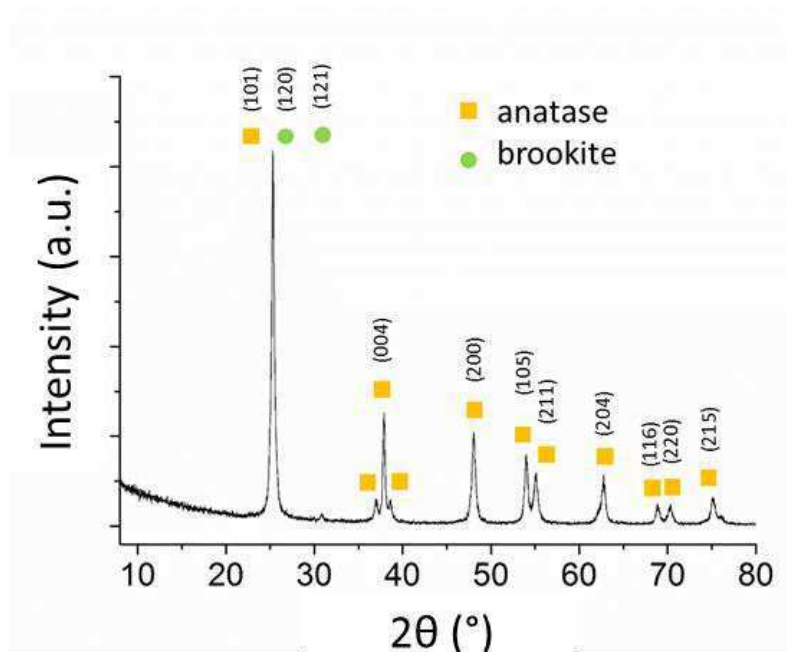


Figure 22: XRD pattern of titanium dioxide nanoneedles

Peak	FWHM (°)	Crystallite size (nm)
(101)	0.527	16
(004)	0.226	36
(200)	0.38	21

Table 3: Full width at half maximum (FWHM) and crystallite sizes of the three main peaks of the XRD pattern of anatase

By a “Le Bail” refinement of the XRD pattern, the nanoneedles are composed of 96% of anatase and 4% of brookite. The results of these refinements are shown in Table 4. The cell parameters of anatase are very close to the published ones (JCPDS 21-1272), and the cell parameters of the brookite are very different from the published ones. The differences can be explained by a very low intensity of the brookite peaks.

Phase	Space group	Proportion	Cell parameters (Å, °)					
			a	b	c	$\alpha$	$\beta$	$\gamma$
Anatase	I 4 <sub>1</sub> /amd	96%	3.7877	3.7877	9.4959	90	90	90
Brookite	Pbca	4%	7.8799	6.1338	5.9399	90	90	90

Table 4: Summary of the information obtained by a “Le Bail” refinement of the XRD pattern of the nanoneedles

The facets in the nanoneedles have been described in the previous part (cf. III. 3). Thus, the NNs can present the (101), (001), and (010) / (100) along their length. These data have been verified by the study of the crystal orientation of the nanoneedles by HRTEM. Figure 23 depicts the HRTEM images and the Fourier transform. The study of the orientation and of the localization of the diffraction spots obtained by Fourier transform shows that the nanoobjects are elongated along the [001] axis. The anatase crystallizes under a truncated bipyramid with 8 equivalents of the (101) facets and 2 equivalents of the (001) facets. This configuration is, however, only possible for small nanoneedles [66-67]. When the nanoneedles are long enough (> 30 nm), the (100) facet appears (Figure 23). The crystal axis has been ascribed by the Fourier transform and the lattice spacings are shown in red. Moreover, the shape of the nanoneedles is not perfectly homogeneous and, thus, it is difficult to quantify the proportion of the several facets.

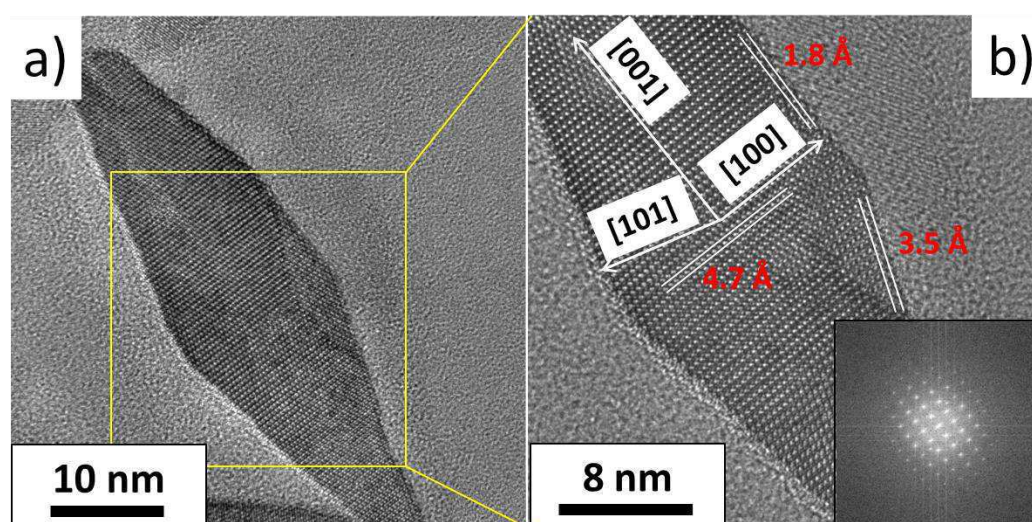


Figure 23: HRTEM pictures at two magnifications and Fourier transform of a nanoneedle longer than 30 nm

To explain why the enhanced crystal growth has a preferential direction along the [001] of anatase, it has been assumed that it should be related to the constraints imposed by the configuration and crystalline structure of the nanotube precursors. Thus, the correlation between the crystalline structures of the starting nanotubes and the nanoneedles could offer insights into the mechanistic steps of the transformation of nanotubes to anatase TiO<sub>2</sub> nanoneedles. Indeed, upon hydrothermal treatment of the nanotubes, the structure is assumed to proceed with the rupture of the layer and the subsequent dissolution of small fragments or “TiO<sub>6</sub>” octahedra (this is still to be demonstrated), followed by their

rearrangement to form anatase crystals whose size depends on the pH during the hydrothermal treatment. The preferential elongation in the anatase [001] is ascribed to the specific feature of the nanotubes. The zigzag configuration of the edge-shared “TiO<sub>6</sub>” octahedra of the nanotube walls, (Figure 20a) with projection along the [001] of the titanate, is indeed very similar to the unit layer of the TiO<sub>2</sub> anatase projected along the [001] (Figure 20b). It is proposed that, upon hydrothermal treatment, the titanate framework thanks to a lower pH and a possibility of generating Ti-O-Ti bonds, shrinks locally, reduce the interlayer distance, and transform into anatase TiO<sub>2</sub> structure.

In order to further characterize the nanoneedles, specific surface area (BET) analysis was performed on the nanoneedles (Table 5). P25 has a specific surface area of 56 m<sup>2</sup>/g, which is in agreement with Degussa data (50 ± 15 m<sup>2</sup>/g). For the nanoneedles, the specific surface area is of 86 m<sup>2</sup>/g in accord with the theoretical calculated value (115 m<sup>2</sup>/g), if we consider a bipyramid with a square based with an average size of L = 45 nm and l = 15 nm. Last, the specific surface area for the scrolled nanosheets is 380 m<sup>2</sup>/g. The particles can be classified as follows by their surface specific area:

Specific surface area (P25) < Specific surface area (NNs) << Specific surface area (sNSs)

<b>Nanoparticle types</b>	<b>Specific surface area (m<sup>2</sup>/g)</b>
P25	56
Scrolled nanosheets	380
Nanoneedles	86

*Table 5: Specific surface area of P25, scrolled nanosheets and nanoneedles obtained by BET method*

The nanoneedles shown in Figure 21 have a length above 200 nm and are a bit too long for the aimed applications. That is the reason why, several parameters have been studied in order to decrease the size of the nanoneedles: reaction time, precursor aging, pH and the use of structuring agents

#### IV. 2. a. Effect of the reaction time

To optimize the operating conditions, the influence of the reaction time on the length of the nanoneedles is a crucial parameter and was, hence, studied. The hydrothermal treatment of the sNSs was performed at 140 °C and pH 9.8, for one, three and six days using the same batch of scrolled nanosheets. Figure 24 shows the TEM images of the obtained nanoneedles. Based

on these representative images of the samples, the reaction time is indeed an important factor playing a major role on two parameters. The first one is the reaction yield and the overall consumption of all the SNSs, since after one day the rate of scrolled nanosheets is close to 50%, while it strongly decreases after 3 days, to disappear after 6 days. The second parameter is the average length of the nanoneedles which decreases from 539 nm after one day to 246 nm after 6 days. In the beginning of the reaction, long nanoneedles are present with a size similar to the size of the scrolled nanosheets as if the nanosheets were able to unwrap and restack because of a much lower reaction pH than during their synthesis. When the reaction time increases the length of the nanoneedles decreases progressively.

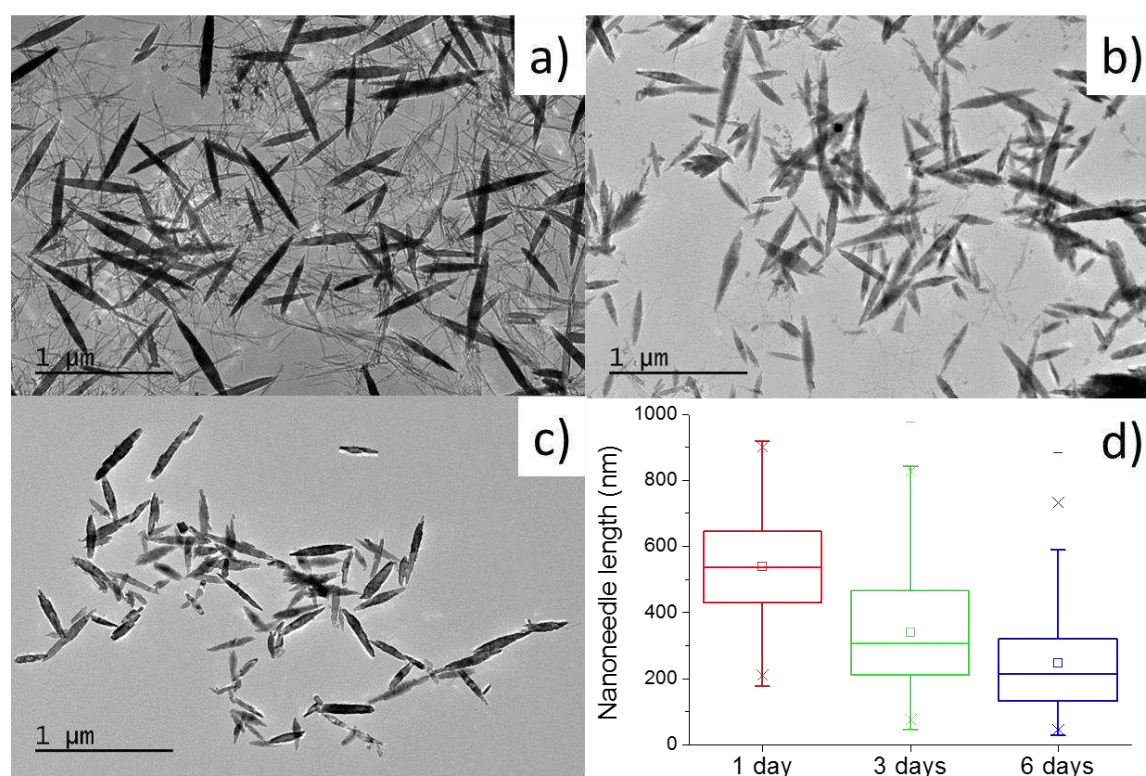


Figure 24: TEM images of nanoneedles after (a) 1 day, (b) 3 days, (c) 6 days. (d) box chart on nanoneedle length

Thus, in order to decrease the length of the nanoneedles the reaction time should increase. Assuming, this variation is linear, 9 days are necessary to reach a length as short as 60 nm which is not really worth considering. Therefore in order to have a completion of the reaction, the following parameter were fixed in further studies: pH 9.8, hydrothermal treatment at 140 °C for 3 days and we studied the aging of the scrolled nanosheets.

#### IV. 2. b. Effect of the nanosheet aging

To assess the reproducibility of the results, we repeated the experiments several times and encountered problems attributed to the aging of the nanosheets. When old nanosheets (kept in water medium at neutral pH for more than one month) were hydrothermally treated in the same way as freshly prepared ones, they only led to very small nanoparticles rather than nanoneedles (Figure 25).

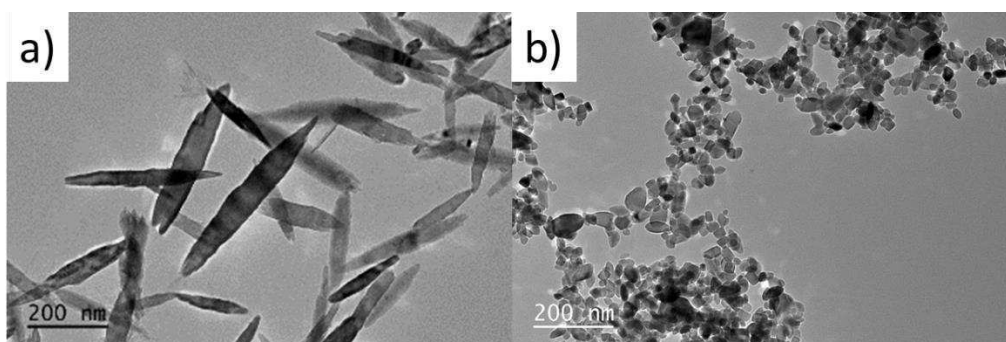


Figure 25: Nanoneedles obtained from (a) fresh nanosheets and (b) old nanosheets

A more systematic study of the aging of the nanosheets was made keeping the nanosheets at room temperature in water for 0, 15 and 31 days to see the impact on the nanoneedles length as shown in Figure 26.

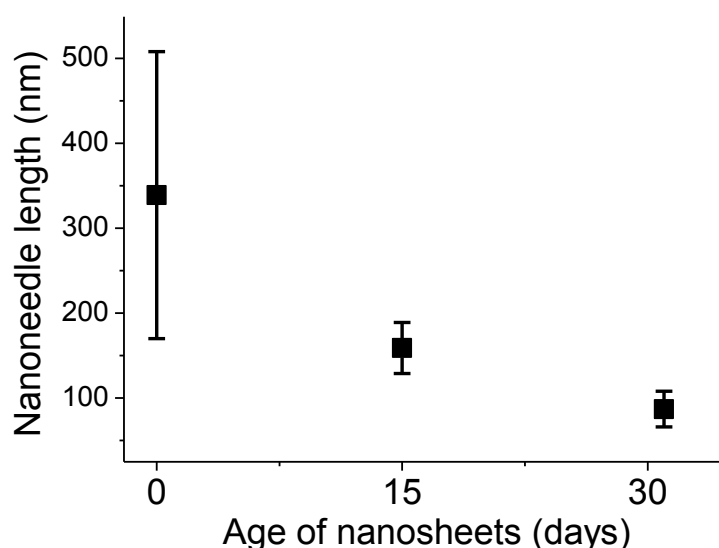
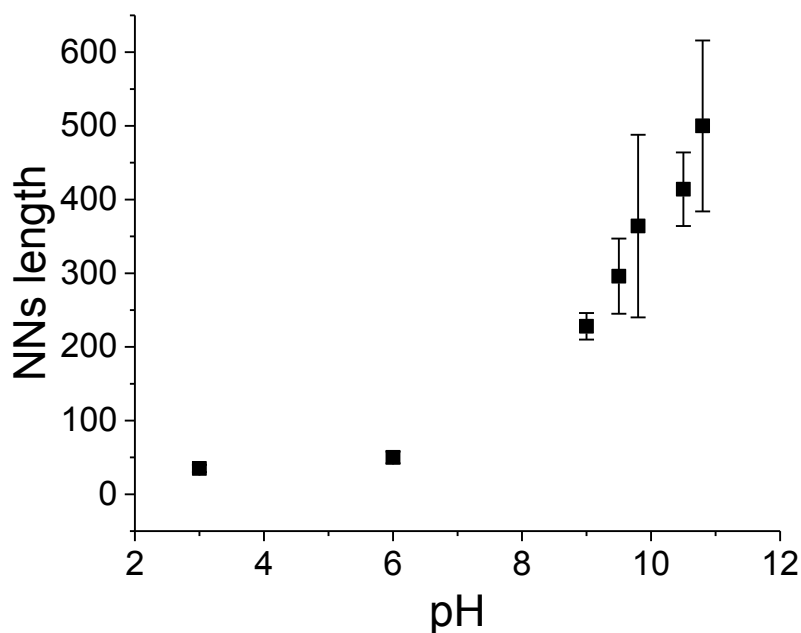


Figure 26: Variation of nanoneedle length as a function of the age of nanosheets

These results are in agreement with some work also reported by Bavykin [136] who showed that the stability of scrolled nanosheets in solution could not necessarily be considered as granted and that it also depended on the pH and on the counter anion solutions. Playing with nanosheet aging to decrease the nanoparticle size is far too time consuming. We have investigated another parameter, the pH of the reaction medium.

#### IV. 2. c. Initial pH of the reaction

The initial synthesis pH was adjusted with nitric acid on freshly prepared scrolled nanosheets. The experiments were performed at different pHs at least 3 times and up to 8 times for some of them. In each case, the statistics on the NNs length were performed on at least 300 NPs. The variation of the length of the nanoneedles is illustrated on Figure 27.



*Figure 27: Variation of the lengths of nanoneedles with the pH. Each dots represents an average of 3 to 8 experiments (each experiments giving rise to statistics on 300 NPs), errors bars represent the statistics on these experiments*

At pH 3 and at pH 6, only small nanoobjects were obtained (with an aspect ratio of 1 at pH 3 and 1.5 at pH 6). The size of the nanoneedles in acidic conditions confirmed the results obtained and published by Nian [54]. Controlling the pH effectively allows a control of the length of the nanoneedles.

### IV. 3. Control of the NPs shape and morphology with structuring agents

We nevertheless tried to synthesize the NPs in the presence of structuring agents which are known (i) to provide a selective control on crystal facets [109], and (ii) to help controlling the NPs size (mind that the NPs are to be used for *in vitro* and *in vivo* biological testing and their length must be decreased significantly to 30 – 60 nm). The choice of structuring agents was based on a contribution by Sugimoto and collaborators who showed that triethanolamine (TEOA) and oleic acid (OA) could be used as structuring agents to control the growth and morphology of the nanoparticles. TEOA was used by Sugimoto in the gel-sol method, which is a bottom up approach, to control the release of “Ti<sup>4+</sup>” from the gel formed by the stabilization of titanium isopropoxide [44, 72].

	pH	Shape	
<b><u>Primary amines:</u></b>			
Diethylenetriamine (DETA)	9.5	Elongated ellipsoidal particles	
Ethylenediamine (ED)			
Trimethylenediamine (TMD)			
Triethylenetetramine (TETA)			
<b><u>Secondary amines:</u></b>			
Diethylamine (DEA)	9.5	Large ellipsoids with small aspect ratio	
<b><u>Tertiary amines:</u></b>			
Trimethylamine (TMA)			
Triethylamine (TEA)	>11	Ellipsoidal particles	
Triethanolamine (TEOA)			
Sodium oleate	10.5	Cuboids	
Sodium stearate			

Table 6: Structuring agents studied by Sugimoto in his gel-sol synthesis [72]

Sugimoto demonstrated that in basic conditions, secondary amines, such as diethylamine, and tertiary amines, such as trimethylamine and triethylamine, acted as complexing agents of Ti<sup>4+</sup> ions to promote the growth of ellipsoidal particles with a low aspect ratio. While primary amines such as diethylenetriamine, ethylenediamine, trimethylenediamine and triethylenetetraamine acted rather as shape controllers to produce ellipsoids with a high aspect ratio (Table 6). Furthermore, he showed that sodium oleate and sodium stearate acted as colloidal stabilizers and allowed the synthesis of well dispersed cuboids [72].

Sugimoto studied the influence and the role of TEOA as a trap in the liberation of titanium from the gel formed from titanium alkoxides before the formation of the TiO<sub>2</sub> nanoparticles,

and our goal here was to apply this approach to a top down approach, starting with scrolled nanosheets as a source of “Ti<sup>4+</sup>”.

Thus, based on the work by Sugimoto, we decided to use two structuring agents, triethanolamine and oleic acid and to study their influence on the reactivity of scrolled nanosheets and their effects on the size and shape of the resulting nanoneedles.

#### IV. 3. a. Triethanolamine (TEOA) OR oleic acid (OA)

Before using a mixture of these two structuring agents, the synthesis of nanoneedles was performed with a single one, at pH 9.8. To compare the results, the same batch of starting scrolled nanosheets was used. TEOA or OA was added to the scrolled nanosheets and then the pH was adjusted to 9.8 with an aqueous solution of sodium hydroxide. Attempts with 0, 500 and 1000 μL of structuring agents in a suspension containing 0.7 g of SNSs were reacted for 72 hours at 140 °C. The same attempts were carried out for OA. The molar ratios between TEOA and Ti are 0.45 with 500 μL and 0.9 with 1000 μL of TEOA. The molar ratios between OA and Ti are 0.2 with 500 μL and 0.4 with 1000 μL of OA (Figure 28).

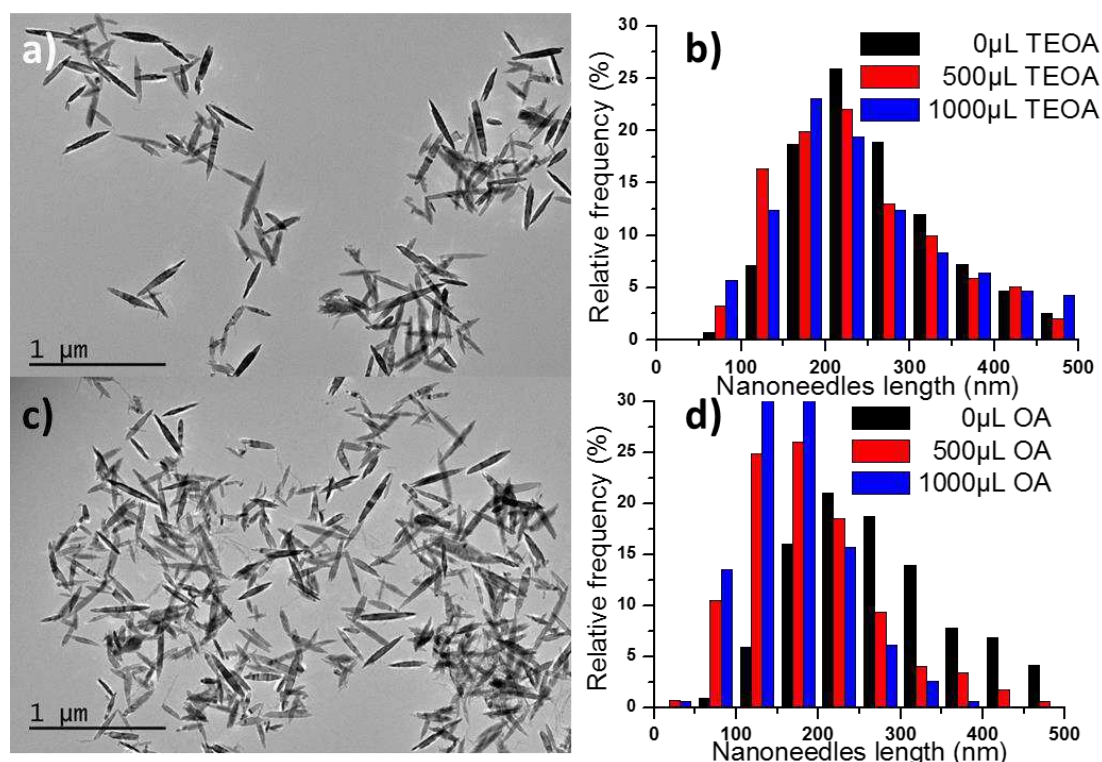


Figure 28: (a) (c) TEM images of nanoneedles prepared with 500 μL of triethanolamine (TEOA) and oleic acid (OA) respectively; (b) (d) nanoneedles length distribution for initial pH of 9.8

Upon addition of various amounts of TEOA, the nanoneedles length remains constant at *ca.* 250 nm and the morphology is also unchanged. Upon addition of various amounts of OA, the length of the nanoneedles is *ca.* 200 nm, with a standard deviation of 100 nm, while no difference is observed in the shape of the nanoparticles. Thus, we can conclude that TEOA or OA alone have no effect on the nanoneedles length and shape, for the same starting set of scrolled nanosheets.

If we take care of the age of the scrolled nanosheets and of the washing steps, it is possible to have trustable reproducible results. Figure 29 summarizes the statistics on the length of the nanoneedles on at least three different experiments on freshly prepared scrolled nanosheets.

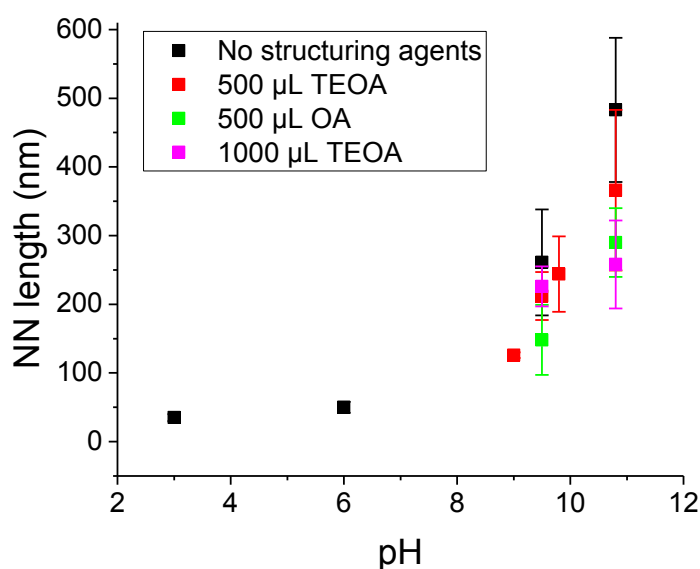


Figure 29: Nanoneedle length average with or without structuring agents (TEOA or OA). The error bars are obtained by means of at least 3 experiments.

Thus, averaging these experiments, we confirmed that the structuring agents have no significant effect on the nanoneedle length not only on a single set of starting material but on different sets of experiments.

Instead of starting from an amorphous gel of Ti(OH)<sub>x</sub> as in Sugimoto's case where the OH can be easily replaced by TEOA or OA [72], I started from scrolled nanosheets which need to be rolled out and then restacked. So, the structuring agents at the working pH may be inefficient to interact with the scrolled nanosheets and liberate the "TiO<sub>6</sub>" octahedra from the crystallized structure and to control the morphology of the nanoparticles. On the contrary, Sugimoto showed that at pH 9.6, going from TIPO to amorphous Ti(OH)<sub>x</sub> gel, he could obtain

TiO<sub>2</sub> nanoparticles with TEOA on its own (Figure 30). However, at high pH (> 11.7), he encountered the same problem as we did: the predominant influence of the basicity of the medium yielding longer nanoneedles. In our case, pH > 11.7 prevented the unfolding and the restacking of the scrolled nanosheets and the few NNs which were nevertheless formed were very long.

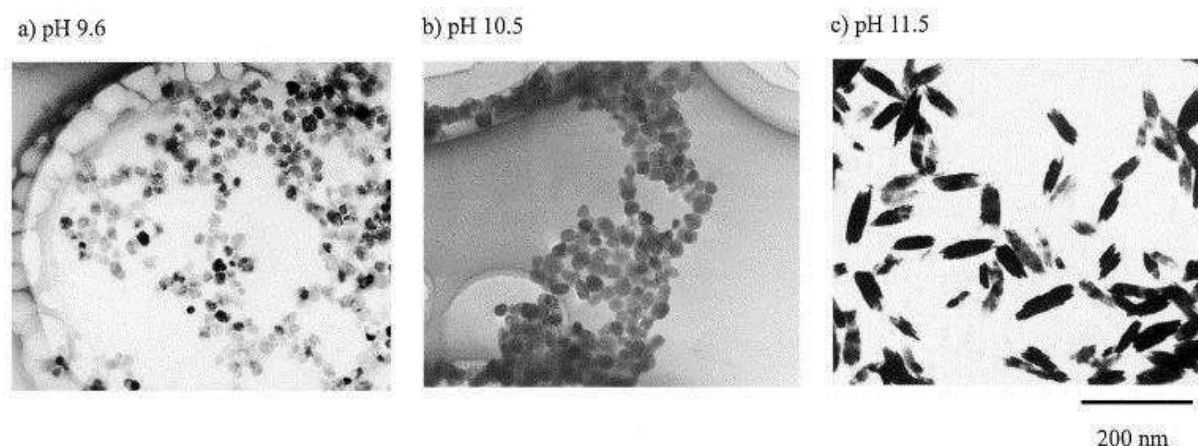


Figure 30: Effect of initial pH on the shape control of TiO<sub>2</sub> particles by TEOA at [TEOA]/[TIPO] = 2.0 obtained by gel-sol synthesis at 140 °C for 3 days [72] (Compare with Figure 28a for pH 9.8)

#### IV. 3. b. Triethanolamine (TEOA) AND oleic acid (OA)

We then tried a combination of these two structuring agents and decided to fix the quantity of TEOA at 500 μL and vary that of OA (see Table 7 for the ratio). The TEM images of NPs obtained with various amounts of OA shown in Table 7 illustrate the synergetic effect of the combined use of these two structuring agents. With a fixed amount of TEO, increasing the OA amount decreases the length of the nanoneedles and, eventually, the nanoneedles turn into nanorods. This can be explained by the formation of a complex between “Ti” surface and carboxylate anions [75], which controls the growth on (101) plane. However, this is only speculation because in our case we have a top-down process. The nanosheets can react as follows: (i) the scrolled nanosheets break in small fragments, which can then rearrange, and the structuring agents might control the size of the fragments when they break, (ii) the scrolled nanosheets dissolve to form “TiO<sub>6</sub>” octahedra, which agglomerate and then we can suggest that the structuring agents control the growth as described by Sugimoto, (iii) or the both can happen.

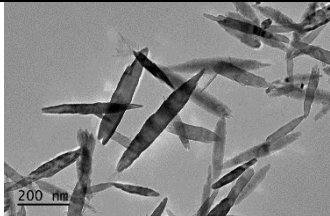
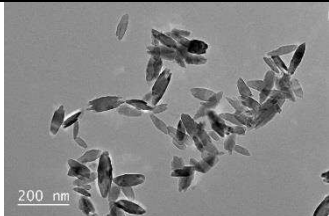
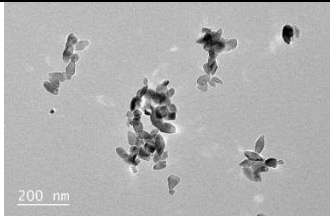
TEOA (μL)	0	500	500
OA (μL)	0	500	1000
TEOA/Ti OA/Ti (%mol)	-	0.45 0.2	0.45 0.4
TEM images			
TEM size (nm±std)	350 (± 100)	87 (± 30)	56 (± 20)
Aspect ratio	7	2.5	1.5

Table 7: Variation of nanoneedle size and shape with the amount of oleic acid at a fixed concentration of TEOA at pH 9.8

Further experiments were performed at pH 9.5 (Figure 31). Thus, the decrease of the size of the nanoneedles with the increase of the amount of the oleic acid was confirmed.

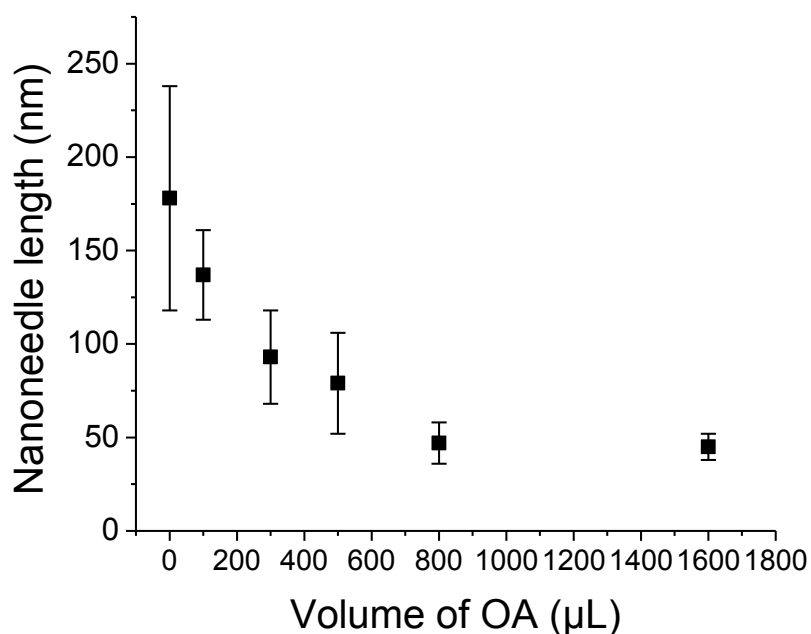


Figure 31: Nanoneedles length with the amount of oleic acid at a fixed concentration of TEOA (500 μL) at pH 9.5

TEOA is reported to be an effective shape controller to obtain elongated ellipsoidal particles, presumably due to the adsorption of the amine to the specific planes parallel to the *c*-axis, favoring the growth of the [001] plane [72, 78]. The increase of the OA to Ti ratio allows decreasing the length of the nanoneedles.

To conclude, the use of surfactants in nanoparticle synthesis is a convenient way to control their size and the shape. The objective of synthesizing nanoparticles with a size between 30 and 60 nm has been achieved.

#### IV. 4. Preliminary results on the interaction of NPs with cells

Certain biological tools have already been developed to study the effects of the ionizing radiation on cells in the presence of NPs, such as survival clonogenic assay, cellular proliferation, and study of cell signaling pathways. From the physical point of view, some modeling of the interaction of ionizing radiation and nanoparticles has also been developed by introducing data for irradiation and nanoparticles in Monte Carlo (Geant4) simulation [137-139].

Moreover, the study by high resolution ion beam micro-analysis of the NPs cells internalization developed at CENBG highlighted the behavior differences depending on the cell lines or on the type of NPs [1, 140]. Indeed, the internalization studies showed that whatever the morphologies and sizes, NPs were mainly localized in the cytoplasm and the rate of internalization depended on the cell types. In this way, TiO<sub>2</sub> NPs were studied on three cell lines, HeLa (Cancer human cells), HUVEC (human tissue cells), HEKn (Human Epidermal Keratinocytes), showing different behavior depending on the culture media, type of NPs (morphology, size...) and the cell lines. The presence of TiO<sub>2</sub> NPs modifies the ionic and cellular homeostasis, and a threshold of the amount of TiO<sub>2</sub> NPs in cells exists to observe the increase of the intracellular Ca<sup>2+</sup> concentration. This increase is responsible for the modification of the cell proliferation, stress of the endoplasmic reticulum, and mitochondrial anomalies. Thus, these results allow the definition of a toxicity level depending on the shape of TiO<sub>2</sub> nanoparticles for a given cell type. Thus, we can classify the TiO<sub>2</sub> NPs according to their toxicity, and show that the scrolled nanosheets of TiO<sub>2</sub> are the most toxic [1]. This preliminary work was carried out using the NPs that I have prepared and that are reported in this thesis.

Furthermore, others have characterized the cellular response to the ionizing radiation. Several cell lines (Sarcoma cells: IB115 and IB106, HeLa cells) were studied at 1, 2 or 6 Gy with 6 MeV of photons, 9 MeV of electrons or 3 MeV of protons at CENBG using a methodology which combines survival clonogenic assay, cell proliferation, and DNA damage [141]. This study showed the various response as a function of cell lines, irradiation dose and ionizing radiation types. The results are essential to define the combined effects of ionizing radiation and nanoparticles.

Some preliminary results showed that the activation pathways observed in the case of the NP toxicity were also induced by ionizing radiation. This conclusion was forthcoming from the study of 10 genes involved in cell stress (apoptosis, ROS, inflammation, endoplasmic reticulum stress, etc.). Likewise, for cells irradiated at 0, 2 and 6 Gy the PIXE analysis, which quantifies the distribution of chemical elements [142], showed an increase of the intracellular Ca<sup>2+</sup> concentration.

## V - Inserting rare-earth elements in TiO<sub>2</sub> matrix

In order to track the NPs after their uptake by cells, rare-earth elements were embedded in the TiO<sub>2</sub> matrix. Because of the large difference between the sizes of Ti<sup>4+</sup> and trivalent rare-earth ions, this matrix insertion is not trivial and only few papers report it. Eu-doped TiO<sub>2</sub> NPs were synthesized by certain sol-gel routes. However, these papers show no TEM images [143-146] or, occasionally, TEM reveals aggregated NPs [147-150]. This is because the sol-gel route used involves a heat treatment that leads to agglomerated NPs, unsuitable for bioapplications. Eu-doped TiO<sub>2</sub> NPs were also prepared by hydrothermal routes reported in [151-158]. However, for our purposes, the best synthetic way is the one developed by Haifeng Zou [152-153, 155-156], similarly to the method we have used for the synthesis of nanoneedles. However, these syntheses led to nanoparticles, which were not characterized by EDX. Thus, the repartition of europium in the nanoparticles of TiO<sub>2</sub> couldn't be determined.

Figure 32 shows the XRD of the undoped, and 5% Eu, 5% Tb doped TiO<sub>2</sub> nanoneedles prepared from P25.

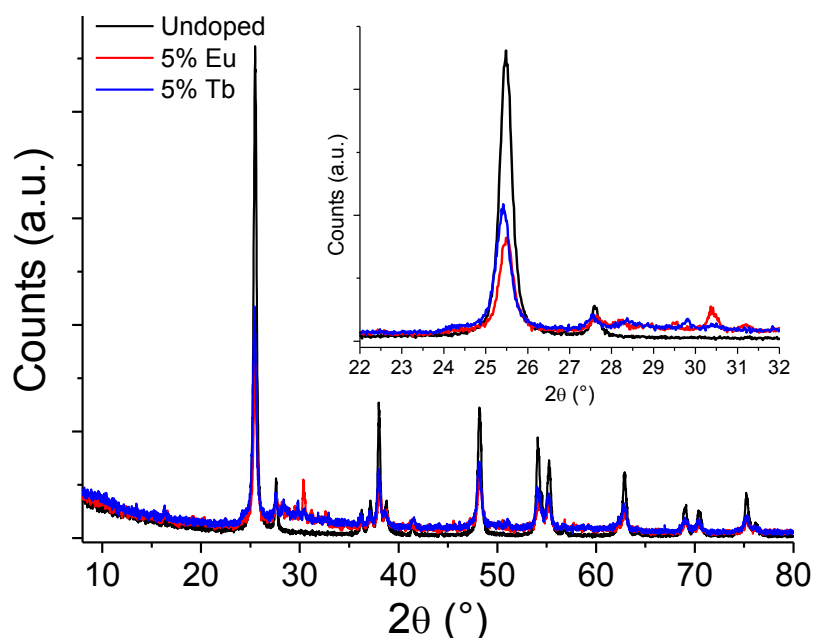


Figure 32: XRD of undoped, 5% Eu, 5% Tb-doped TiO<sub>2</sub>

The XRD patterns show, mainly, the presence of the anatase phase. The peak at 30.4° in the diffractogram of Eu-doped TiO<sub>2</sub> is ascribed to Eu<sub>2</sub>Ti<sub>2</sub>O<sub>7</sub> (JCPDS 23-1072) or EuO (JCPDS 18-0507) [146].

The TEM images in Figure 33 show that as usual in the absence of the rare-earth elements, 350 nm long nanoneedles were obtained. While in the same conditions, addition of europium and terbium resulted in unfinished reaction with remaining nanosheets, concomitant with small nanoparticles and long nanorods. The composition of these nanorods was ascertained by EDX mapping (Figure 34 and Figure 35) revealing that the small nanoparticles contain titanium, *i.e.*, anatase (according to XRD). The long nanorods are essentially made of europium and terbium, presumably in the oxide form, and probably below the XRD detection limit (< 5%).

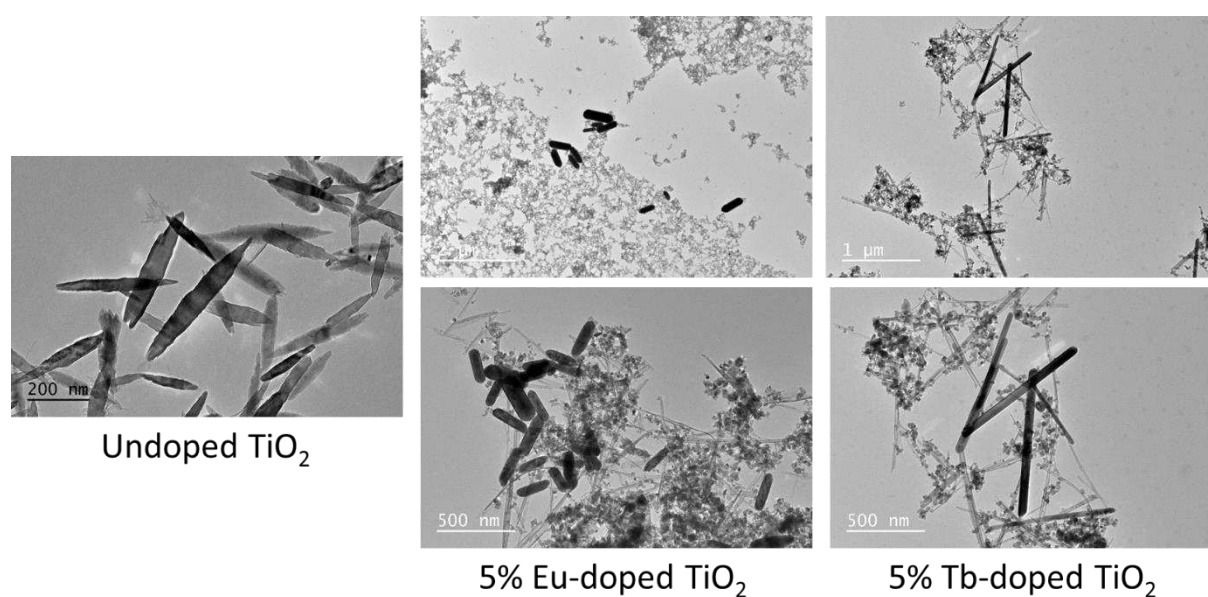


Figure 33: TEM images of undoped TiO<sub>2</sub>, 5% Eu-doped TiO<sub>2</sub> and 5% Tb-doped TiO<sub>2</sub>

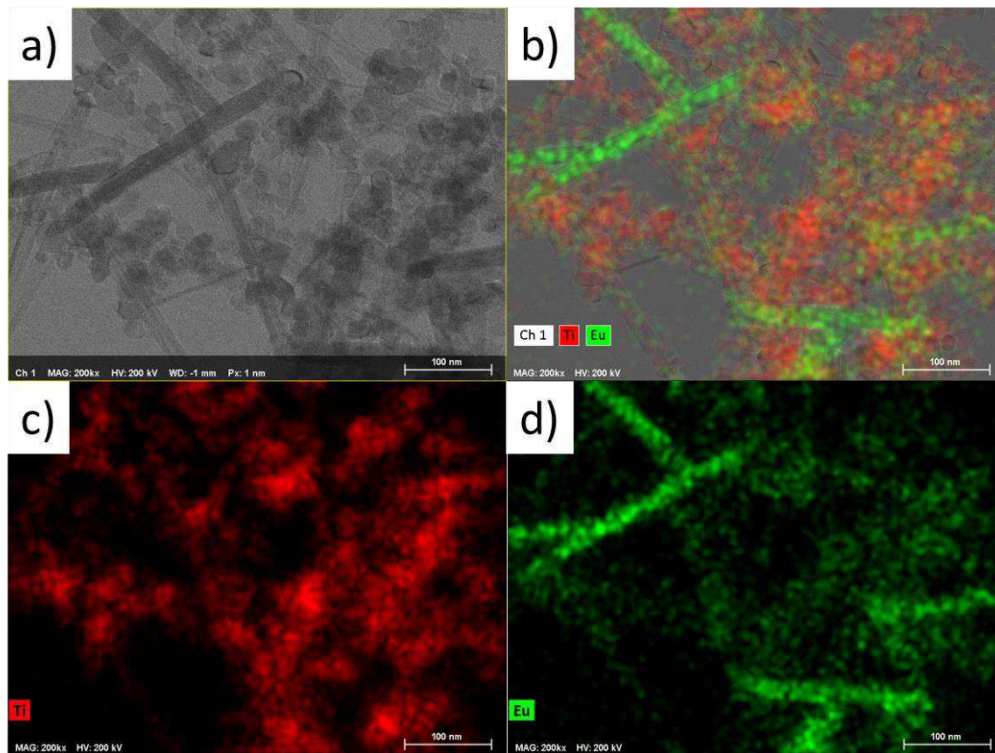


Figure 34: a) STEM images of 5% Eu-doped TiO<sub>2</sub>, b) overlapping of EDX mapping of c) Ti (in red) and d) Eu (in green)

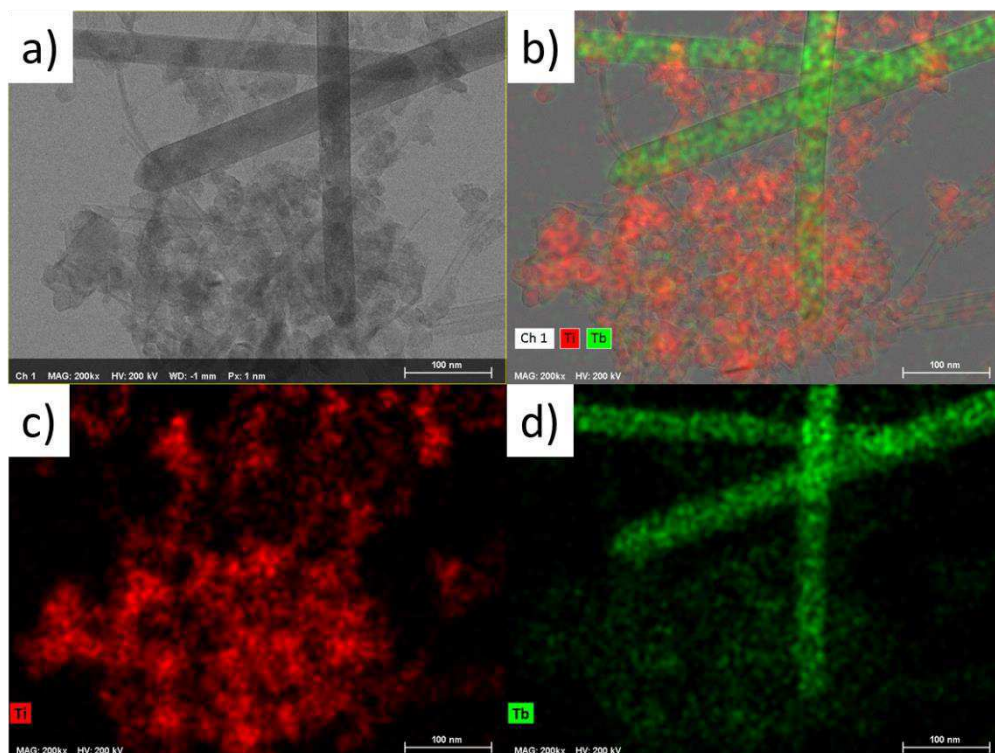


Figure 35: a) STEM images of 5% Tb-doped TiO<sub>2</sub>, b) overlapping of EDX mapping of c) Ti (in red) and d) Tb (in green)

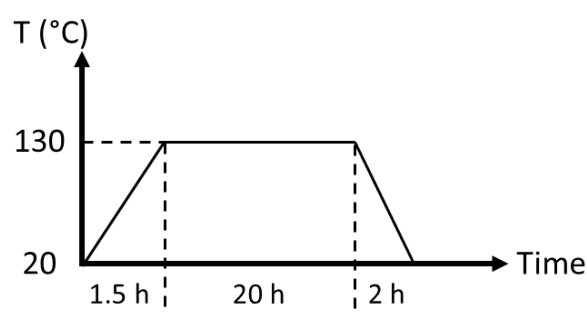
## Conclusion

I have accomplished the hydrothermal synthesis of TiO<sub>2</sub> nanoparticles, and by adjusting the composition of a mixture of the structuring agents, triethanolamine and oleic acid, TiO<sub>2</sub> nanoparticles were prepared with a range of sizes and morphologies. Judicious choice of the synthetic parameters and structuring agents allows tuning the size and the morphology of the nanoparticles. The goal of preparing 30 to 60 nm TiO<sub>2</sub> NPs has been achieved. However, the insertion of lanthanides in the TiO<sub>2</sub> matrix could not be accomplished.

## Experimental section

### ❖ Scrolled nanosheets synthesis of titanium dioxide

The scrolled nanosheets synthesis has been adapted from the work from Kasuga [51-52, 111]. In a 50 mL Teflon autoclave, 2 g of TiO<sub>2</sub> P25 and 28 mL of a freshly prepared 10 M NaOH solution are mixed. The autoclave is closed and manually shaken. The Teflon autoclave is then placed in the stainless steel autoclave and moved to an oven (Mettert 1400 W) with the following heating cycle:



At the end of the synthesis, the autoclave is opened. The white slurry is washed with nitric acid (0.1 M) for 5 minutes and with centrifugation steps at 5000 rpm for 5 minutes. The experiment is repeated several times until the supernatant becomes acid (ascertained with pH paper). 450 to 500 mL of solution are needed in total. Then, the samples are washed with distilled water and centrifuged between two washing cycles until the pH of the supernatant becomes around 7. The scrolled nanosheets are either kept in water or dried at 40 °C.

### ❖ Nanoneedles synthesis of titanium dioxide

The synthesis of nanoneedles use the scrolled nanosheets previously prepared according to Nian [54]. A 1 M NaOH solution is added dropwise to one third of the scrolled nanosheets suspension corresponding to 0.7 g of powder, in order to reach the required pH (measured with a pH-meter). The volume is then adjusted to 30 mL and added to a 50 mL Teflon vessel in the stainless steel autoclave. The autoclave is placed in an oven at 140 °C for 72 hours after which the mixture is naturally cooled down and washed with distilled water until pH 7 (centrifugation steps: 9000 rpm, 10 minutes).

❖ Rare-earth doped nanoneedles synthesis

Before adding the NaOH solution, according to the desired doping percentage, rare-earth chlorides are added to the solution. Then, the same hydrothermal treatments are applied to the mixture as well as the same washing treatment.

## Characterization methods

See this part at the end of chapter 3.

## Bibliography

1. Simon, M.; Saez, G.; Muggioli, G.; Lavenas, M.; Le Trequesser, Q.; Michelet, C.; Devès, G.; Barberet, P.; Chevet, E.; Dupuy, D.; Delville, M.-H.; Seznec, H., In situ quantification of diverse titanium dioxide nanoparticles unveils selective endoplasmic reticulum stress-dependent toxicity. *Nanotoxicology* **2017**, *11* (1), 134-145.
2. Kroll, W., The production of ductile titanium. *Transactions of the Electrochemical Society* **1940**, *78* (1), 35-47.
3. Clark, R. J. H., *The chemistry of titanium and vanadium*. Elsevier: 1968.
4. COMBRES, Y., Métallurgie et recyclage du titane et de ses alliages. *Techniques de l'ingénieur. Matériaux métalliques* **1997**, *3* (M2355), M2355. 1-M2355. 3.
5. Lan, Y.; Lu, Y.; Ren, Z., Mini review on photocatalysis of titanium dioxide nanoparticles and their solar applications. *Nano Energy* **2013**, *2* (5), 1031-1045.
6. DeVore, J. R., Refractive indices of rutile and sphalerite. *JOSA* **1951**, *41* (6), 416-419.
7. Fujishima, A.; Hashimoto, K.; Watanabe, T., *TiO<sub>2</sub> photocatalysis: fundamentals and applications*. BKC Incorporated: 1999.
8. Hanaor, D. A.; Assadi, M. H.; Li, S.; Yu, A.; Sorrell, C. C., Ab initio study of phase stability in doped TiO<sub>2</sub>. *Computational Mechanics* **2012**, *50* (2), 185-194.
9. Ye, X.; Sha, J.; Jiao, Z.; Zhang, L., Thermoanalytical characteristic of nanocrystalline brookite-based titanium dioxide. *Nanostructured Materials* **1997**, *8* (7), 919-927.
10. Hanaor, D. A.; Sorrell, C. C., Review of the anatase to rutile phase transformation. *J Mater Sci* **2011**, *46* (4), 855-874.
11. Landmann, M.; Rauls, E.; Schmidt, W., The electronic structure and optical response of rutile, anatase and brookite TiO<sub>2</sub>. *Journal of physics: condensed matter* **2012**, *24* (19), 195503.
12. Liao, Y.; Que, W.; Jia, Q.; He, Y.; Zhang, J.; Zhong, P., Controllable synthesis of brookite/anatase/rutile TiO<sub>2</sub> nanocomposites and single-crystalline rutile nanorods array. *Journal of Materials Chemistry* **2012**, *22* (16), 7937-7944.
13. Satoh, N.; Nakashima, T.; Yamamoto, K., Metastability of anatase: size dependent and irreversible anatase-rutile phase transition in atomic-level precise titania. *Scientific Reports* **2013**, *3*, 1959.
14. Banfield, J., Thermodynamic analysis of phase stability of nanocrystalline titania. *Journal of Materials Chemistry* **1998**, *8* (9), 2073-2076.
15. Lazzeri, M.; Vittadini, A.; Selloni, A., Structure and energetics of stoichiometric TiO<sub>2</sub> anatase surfaces. *Physical Review B* **2001**, *63* (15), 155409.
16. Chen, X.; Mao, S. S., Titanium dioxide nanomaterials: synthesis, properties, modifications, and applications. *Chemical Reviews* **2007**, *107* (7), 2891-2959.
17. Diebold, U., The surface science of titanium dioxide. *Surface science reports* **2003**, *48* (5-8), 53-229.
18. Wunderlich, W.; Oekermann, T.; Miao, L.; Hue, NT, Tanemura. S. and Tanemura, M. *J. Ceram. Process. Res* **2004**, *4*, 342.
19. Di Paola, A.; Bellardita, M.; Palmisano, L., Brookite, the least known TiO<sub>2</sub> photocatalyst. *Catalysts* **2013**, *3* (1), 36-73.
20. Szaciłowski, K.; Macyk, W.; Drzewiecka-Matuszek, A.; Brindell, M.; Stochel, G., Bioinorganic photochemistry: frontiers and mechanisms. *Chemical Reviews* **2005**, *105* (6), 2647-2694.
21. Weir, A.; Westerhoff, P.; Fabricius, L.; von Goetz, N., Titanium dioxide nanoparticles in food and personal care products. *Environmental science & technology* **2012**, *46* (4), 2242.
22. Pfaff, G.; Reynders, P., Angle-dependent optical effects deriving from submicron structures of films and pigments. *Chemical Reviews* **1999**, *99* (7), 1963-1982.
23. Braun, J. H.; Baidins, A.; Marganski, R. E., TiO<sub>2</sub> pigment technology: a review. *Progress in organic coatings* **1992**, *20* (2), 105-138.
24. Newman, M. D.; Stotland, M.; Ellis, J. I., The safety of nanosized particles in titanium dioxide–and zinc oxide–based sunscreens. *Journal of the American Academy of Dermatology* **2009**, *61* (4), 685-692.
25. Labille, J.; Feng, J.; Botta, C.; Borschneck, D.; Sammut, M.; Cabie, M.; Auffan, M.; Rose, J.; Bottero, J.-Y., Aging of TiO<sub>2</sub> nanocomposites used in sunscreen. Dispersion and fate of the degradation products in aqueous environment. *Environmental Pollution* **2010**, *158* (12), 3482-3489.
26. Yadav, T. P.; Yadav, R. M.; Singh, D. P., Mechanical milling: a top down approach for the synthesis of nanomaterials and nanocomposites. *Nanoscience and Nanotechnology* **2012**, *2* (3), 22-48.
27. Brinker, C.; Scherer, G. In *The Physics and Chemistry of sol-gel processing, 1990*, Academic Press, New York, Schmidt H., Macromol. Symp, 2000; p 43.

28. Ibrahim, S. A.; Sreekantan, S. In *Effect of pH on TiO<sub>2</sub> nanoparticles via sol-gel method*, Advanced Materials Research, Trans Tech Publ: 2011; pp 184-189.
29. Hench, L. L.; West, J. K., The sol-gel process. *Chemical Reviews* **1990**, *90* (1), 33-72.
30. Livage, J. E.; King, R., Encyclopedia of Inorganic Chemistry. *Encyclopedia of Inorganic Chemistry* **1995**, *7*.
31. Brinker, C. J.; Clark, D. E.; Ulrich, D. R., *Better ceramics through chemistry: symposium held February 1984 in Albuquerque, New Mexico, USA*. North-Holland: 1984.
32. Nozawa, K.; Delville, M.-H.; Ushiki, H.; Panizza, P.; Delville, J.-P., Growth of monodisperse mesoscopic metal-oxide colloids under constant monomer supply. *Physical Review E* **2005**, *72* (1), 011404.
33. Nozawa, K.; Gailhanou, H.; Raison, L.; Panizza, P.; Ushiki, H.; Sellier, E.; Delville, J.; Delville, M., Smart control of monodisperse Stöber silica particles: effect of reactant addition rate on growth process. *Langmuir* **2005**, *21* (4), 1516-1523.
34. Matijević, E.; Budnik, M.; Meites, L., Preparation and mechanism of formation of titanium dioxide hydrosols of narrow size distribution. *Journal of Colloid and Interface Science* **1977**, *61* (2), 302-311.
35. Barringer, E. A.; Bowen, H. K., Formation, Packing, and Sintering of Monodisperse TiO<sub>2</sub> Powders. *Journal of the American Ceramic Society* **1982**, *65* (12), C-199-C-201.
36. Eiden-Assmann, S.; Widoniak, J.; Maret, G., Synthesis and Characterization of Porous and Nonporous Monodisperse Colloidal TiO<sub>2</sub> Particles. *Chemistry of Materials* **2004**, *16* (1), 6-11.
37. Scolan, E.; Sanchez, C., Synthesis and Characterization of Surface-Protected Nanocrystalline Titania Particles. *Chemistry of Materials* **1998**, *10* (10), 3217-3223.
38. Khanna, P. K.; Singh, N.; Charan, S., Synthesis of nano-particles of anatase-TiO<sub>2</sub> and preparation of its optically transparent film in PVA. *Materials Letters* **2007**, *61* (25), 4725-4730.
39. Jiu, J.; Wang, F.; Sakamoto, M.; Takao, J.; Adachi, M., Preparation of nanocrystalline TiO<sub>2</sub> with mixed template and its application for dye-sensitized solar cells. *Journal of The Electrochemical Society* **2004**, *151* (10), A1653-A1658.
40. Jiu, J.; Isoda, S.; Adachi, M.; Wang, F., Preparation of TiO<sub>2</sub> nanocrystalline with 3–5nm and application for dye-sensitized solar cell. *Journal of Photochemistry and Photobiology A: Chemistry* **2007**, *189* (2), 314-321.
41. Feldmann, C.; Jungk, H.-O., Polyol-Mediated Preparation of Nanoscale Oxide Particles. *Angewandte Chemie International Edition* **2001**, *40* (2), 359-362.
42. Klongdee, J.; Petchkroh, W.; Phuempoonsathaporn, K.; Praserttham, P.; Vangnai, A. S.; Pavarajarn, V., Activity of nanosized titania synthesized from thermal decomposition of titanium (IV) n-butoxide for the photocatalytic degradation of diuron. *Science and Technology of Advanced Materials* **2005**, *6* (3), 290-295.
43. Sugimoto, T.; Okada, K.; Itoh, H., Synthetic of Uniform Spindle-Type Titania Particles by the Gel-Sol Method. *Journal of Colloid and Interface Science* **1997**, *193* (1), 140-143.
44. Sugimoto, T.; Zhou, X.; Muramatsu, A., Synthesis of uniform anatase TiO<sub>2</sub> nanoparticles by gel-sol method: 3. Formation process and size control. *Journal of Colloid and Interface Science* **2003**, *259* (1), 43-52.
45. Sugimoto, T.; Zhou, X., Synthesis of Uniform Anatase TiO<sub>2</sub> Nanoparticles by the Gel-Sol Method. *Journal of Colloid and Interface Science* **2002**, *252* (2), 347-353.
46. Suchanek, W. L.; Riman, R. E. In *Hydrothermal synthesis of advanced ceramic powders*, Advances in Science and Technology, Trans Tech Publ: 2006; pp 184-193.
47. Riman, R. E.; Suchanek, W. L.; Lencka, M. M. In *Hydrothermal crystallization of ceramics*, Annales de Chimie Science des Matériaux, Elsevier: 2002; pp 15-36.
48. Byrappa, K.; Yoshimura, M., Handbook of Hydrothermal Technology A technology for Crystal Growth and Materials Processing. Toronto, Will% Andrew Publishing **2001**, 531-535.
49. Kobayashi, M.; Petrykin, V. V.; Kakihana, M.; Tomita, K.; Yoshimura, M., One-step synthesis of TiO<sub>2</sub> (B) nanoparticles from a water-soluble titanium complex. *Chemistry of Materials* **2007**, *19* (22), 5373-5376.
50. Aruna, S.; Tirosh, S.; Zaban, A., Nanosize rutile titania particle synthesis viaa hydrothermal method without mineralizers. *Journal of Materials Chemistry* **2000**, *10* (10), 2388-2391.
51. Kasuga, T.; Hiramatsu, M.; Hoson, A.; Sekino, T.; Niihara, K., Titania nanotubes prepared by chemical processing. *Advanced Materials* **1999**, *11* (15), 1307-1311.
52. Kasuga, T.; Hiramatsu, M.; Hoson, A.; Sekino, T.; Niihara, K., Formation of titanium oxide nanotube. *Langmuir* **1998**, *14* (12), 3160-3163.
53. Deng, Q.; Wei, M.; Ding, X.; Jiang, L.; Ye, B.; Wei, K., Brookite-type TiO<sub>2</sub> nanotubes. *Chemical Communications* **2008**, (31), 3657-3659.
54. Nian, J.-N.; Teng, H., Hydrothermal Synthesis of Single-Crystalline Anatase TiO<sub>2</sub> Nanorods with Nanotubes as the Precursor. *The Journal of Physical Chemistry B* **2006**, *110*, 4193-4198.

55. Kandiel, T. A.; Feldhoff, A.; Robben, L.; Dillert, R.; Bahnemann, D. W., Tailored titanium dioxide nanomaterials: anatase nanoparticles and brookite nanorods as highly active photocatalysts. *Chemistry of Materials* **2010**, *22* (6), 2050-2060.
56. Gu, L.; Wang, J.; Cheng, H.; Du, Y.; Han, X., Synthesis of nano-sized anatase TiO<sub>2</sub> with reactive {001} facets using lamellar protonated titanate as precursor. *Chemical Communications* **2012**, *48* (55), 6978-6980.
57. Menzel, R.; Duerrbeck, A.; Liberti, E.; Yau, H. C.; McComb, D.; Shaffer, M. S., Determining the Morphology and Photocatalytic Activity of Two-Dimensional Anatase Nanoplatelets Using Reagent Stoichiometry. *Chemistry of Materials* **2013**, *25* (10), 2137-2145.
58. Yang, M.-H.; Chen, P.-C.; Tsai, M.-C.; Chen, T.-T.; Chang, I.-C.; Chiu, H.-T.; Lee, C.-Y., Alkali metal ion assisted synthesis of faceted anatase TiO<sub>2</sub>. *CrystEngComm* **2013**, *15* (15), 2966-2971.
59. Zhao, M.; Li, L.; Lin, H.; Yang, L.; Li, G., A facile strategy to fabricate large-scale uniform brookite TiO<sub>2</sub> nanospindles with high thermal stability and superior electrical properties. *Chemical Communications* **2013**, *49* (63), 7046-7048.
60. Li, R.; Zhang, X.; Dong, H.; Li, Q.; Shuai, Z.; Hu, W., Gibbs–Curie–Wulff Theorem in Organic Materials: A Case Study on the Relationship between Surface Energy and Crystal Growth. *Advanced Materials* **2016**, *28* (8), 1697-1702.
61. Wulff, G., *Zeitschrift fur Kristallographie* **1901**, 449-530.
62. Markov, I. V., *Crystal growth for beginners: fundamentals of nucleation, crystal growth and epitaxy*. World scientific: 2016.
63. Mullin, J., *Crystallisation*, 4th Edition<sup>1</sup>. Butterworth-Heinemann, Oxford, UK: 2001.
64. Kumar, S.; Nann, T., Shape Control of II–VI Semiconductor Nanomaterials. *Small* **2006**, *2* (3), 316-329.
65. Tao, A. R.; Habas, S.; Yang, P., Shape Control of Colloidal Metal Nanocrystals. *Small* **2008**, *4* (3), 310-325.
66. Barnard, A. S.; Curtiss, L. A., Prediction of TiO<sub>2</sub> nanoparticle phase and shape transitions controlled by surface chemistry. *Nano Letters* **2005**, *5*, 1261-1266.
67. Barnard, A. S.; Zapol, P.; Curtiss, L. A., Anatase and rutile surfaces with adsorbates representative of acidic and basic conditions. *Surface Science* **2005**, *582* (1), 173-188.
68. Gao, Y.; Elder, S. A., TEM study of TiO<sub>2</sub> nanocrystals with different particle size and shape. *Materials Letters* **2000**, *44* (3), 228-232.
69. Penn, R. L.; Banfield, J. F., Morphology development and crystal growth in nanocrystalline aggregates under hydrothermal conditions: insights from titania. *Geochimica et cosmochimica acta* **1999**, *63* (10), 1549-1557.
70. Dinh, C.-T.; Nguyen, T.-D.; Kleitz, F.; Do, T.-O., Shape-controlled synthesis of highly crystalline titania nanocrystals. *ACS Nano* **2009**, *3* (11), 3737-3743.
71. Jun, Y.-w.; Casula, M. F.; Sim, J.-H.; Kim, S. Y.; Cheon, J.; Alivisatos, A. P., Surfactant-Assisted Elimination of a High Energy Facet as a Means of Controlling the Shapes of TiO<sub>2</sub> Nanocrystals. *Journal of the American Chemical Society* **2003**, *125* (51), 15981-15985.
72. Sugimoto, T.; Zhou, X.; Muramatsu, A., Synthesis of uniform anatase TiO<sub>2</sub> nanoparticles by gel–sol method: 4. Shape control. *Journal of Colloid and Interface Science* **2003**, *259* (1), 53-61.
73. Yun, H. J.; Lee, H.; Joo, J. B.; Kim, W.; Yi, J., Influence of Aspect Ratio of TiO<sub>2</sub> Nanorods on the Photocatalytic Decomposition of Formic Acid. *The Journal of Physical Chemistry C* **2009**, *113* (8), 3050-3055.
74. Liu, C.; Sun, H.; Yang, S., From Nanorods to Atomically Thin Wires of Anatase TiO<sub>2</sub>: Nonhydrolytic Synthesis and Characterization. *Chemistry - A European Journal* **2010**, *16*, 4381-4393, S4381/1-S4381/7.
75. Cozzoli, P. D.; Kornowski, A.; Weller, H., Low-Temperature Synthesis of Soluble and Processable Organic-Capped Anatase TiO<sub>2</sub> Nanorods. *Journal of the American Chemical Society* **2003**, *125*, 14539-14548.
76. Joo, J.; Kwon, S. G.; Yu, T.; Cho, M.; Lee, J.; Yoon, J.; Hyeon, T., Large-Scale Synthesis of TiO<sub>2</sub> Nanorods via Nonhydrolytic Sol–Gel Ester Elimination Reaction and Their Application to Photocatalytic Inactivation of *E. coli*. *The Journal of Physical Chemistry B* **2005**, *109* (32), 15297-15302.
77. Sanchez, C.; Ribot, F., Design of hybrid organic-inorganic materials synthesized via sol-gel chemistry. *New Journal of Chemistry* **1994**, *18* (10), 1007-1047.
78. Zhou, X.; Peng, Z.; Wang, Z.; Wang, X., Effect of trimethylamine on the formation of anatase titania nanoparticles by gel-sol method. *Colloid journal* **2008**, *70* (1), 26-32.
79. Isley, S. L.; Penn, R. L., Titanium Dioxide Nanoparticles: Effect of Sol-Gel pH on Phase Composition, Particle Size, and Particle Growth Mechanism. *The Journal of Physical Chemistry C* **2008**, *112*, 4469-4474.
80. Byrappa, K.; Adschiri, T., Hydrothermal technology for nanotechnology. *Progress in Crystal Growth and Characterization of Materials* **2007**, *53* (2), 117-166.
81. Bavykin, D. V.; Friedrich, J. M.; Walsh, F. C., Protonated titanates and TiO<sub>2</sub> nanostructured materials: synthesis, properties, and applications. *Advanced Materials* **2006**, *18* (21), 2807-2824.

82. Vaezi, M. R.; Arefian, N. A.; Tabriz, M. F.; Kandjani, A. E., Effects of the pH of initial solution on hydrothermally synthesized TiO<sub>2</sub> nanoparticles. *International Journal of Engineering* **2012**, *25*, 131-135.
83. Souverein, B.; Elen, K.; De Dobbelaere, C.; Kelchtermans, A.; Peys, N.; D'Haen, J.; Mertens, M.; Mullens, S.; Van den Rul, H.; Meynen, V.; Cool, P.; Hardy, A.; Van Bael, M. K., Hydrothermal synthesis of a concentrated and stable dispersion of TiO<sub>2</sub> nanoparticles. *Chemical Engineering Journal* **2013**, *223*, 135-144.
84. Yang, X. H.; Li, Z.; Sun, C.; Yang, H. G.; Li, C., Hydrothermal stability of {001} faceted anatase TiO<sub>2</sub>. *Chemistry of Materials* **2011**, *23* (15), 3486-3494.
85. Malinger, K. A.; Maguer, A.; Thorel, A.; Gaunand, A.; Hochepeid, J.-F., Crystallization of anatase nanoparticles from amorphous precipitate by a continuous hydrothermal process. *Chemical Engineering Journal* **2011**, *174*, 445-451.
86. Xu, Y.; Fang, X.; Xiong, J.; Zhang, Z., Hydrothermal transformation of titanate nanotubes into single-crystalline TiO<sub>2</sub> nanomaterials with controlled phase composition and morphology. *Materials Research Bulletin* **2010**, *45*, 799-804.
87. Lim, Y. W. L.; Tang, Y.; Cheng, Y. H.; Chen, Z., Morphology, crystal structure and adsorption performance of hydrothermally synthesized titania and titanate nanostructures. *Nanoscale* **2010**, *2*, 2751-2757.
88. Yang, H. G.; Sun, C. H.; Qiao, S. Z.; Zou, J.; Liu, G.; Smith, S. C.; Cheng, H. M.; Lu, G. Q., Anatase TiO<sub>2</sub> single crystals with a large percentage of reactive facets. *Nature* **2008**, *453* (7195), 638-641.
89. Testino, A.; Bellobono, I. R.; Buscaglia, V.; Canevali, C.; D'Arienzo, M.; Polizzi, S.; Scotti, R.; Morazzoni, F., Optimizing the Photocatalytic Properties of Hydrothermal TiO<sub>2</sub> by the Control of Phase Composition and Particle Morphology. A Systematic Approach. *Journal of the American Chemical Society* **2007**, *129*, 3564-3575.
90. Hidalgo, M.; Aguilar, M.; Maicu, M.; Navío, J. A.; Colón, G., Hydrothermal preparation of highly photoactive TiO<sub>2</sub> nanoparticles. *Catalysis Today* **2007**, *129* (1), 50-58.
91. Aerosol processes. Available from [www.uio.no](http://www.uio.no) **2008**.
92. Mädler, L., Liquid-fed aerosol reactors for one-step synthesis of nano-structured particles. *KONA Powder and Particle Journal* **2004**, *22*, 107-120.
93. Strobel, R.; Pratsinis, S. E., Flame aerosol synthesis of smart nanostructured materials. *Journal of Materials Chemistry* **2007**, *17* (45), 4743-4756.
94. Pratsinis, S. E., Flame aerosol synthesis of ceramic powders. *Progress in Energy and Combustion Science* **1998**, *24* (3), 197-219.
95. Kammler, H. K.; Mädler, L.; Pratsinis, S. E., Flame synthesis of nanoparticles. *Chemical engineering & technology* **2001**, *24* (6), 583-596.
96. Djenadic, R.; Winterer, M., *Chemical vapor synthesis of nanocrystalline oxides, in Nanoparticles from the gasphase: Formation, structure, properties*. Springer Science & Business Media: 2012.
97. Xie, H.; Gao, G.; Tian, Z.; Bing, N.; Wang, L., Synthesis of TiO<sub>2</sub> nanoparticles by propane/air turbulent flame CVD process. *Particuology* **2009**, *7* (3), 204-210.
98. Pardis, S. Synthèse de nanoparticules d'oxydes de titane par pyrolyse laser-Etude des propriétés optiques et de la structure électronique. Paris 11, 2011.
99. Yu, J. C.; Zhang, L.; Yu, J., Direct sonochemical preparation and characterization of highly active mesoporous TiO<sub>2</sub> with a bicrystalline framework. *Chemistry of Materials* **2002**, *14* (11), 4647-4653.
100. Zhu, Y.; Li, H.; Koltypin, Y.; Hachohen, Y. R.; Gedanken, A., Sonochemical synthesis of titania whiskers and nanotubes. *Chemical Communications* **2001**, (24), 2616-2617.
101. Hassanjani-Roshan, A.; Kazemzadeh, S. M.; Vaezi, M. R.; Shokuhfar, A., Effect of sonication power on the sonochemical synthesis of titania nanoparticles. *Journal of Ceramic Processing Research* **2011**, *12* (3), 299-303.
102. Baranchikov, A. Y. e.; Ivanov, V. K.; Tretyakov, Y. D., Sonochemical synthesis of inorganic materials. *Russian Chemical Reviews* **2007**, *76* (2), 133-151.
103. Anel Perales-Martinez, I.; Rodriguez-Gonzalez, V.; Lee, S.-W., Insights into nanocube-like morphological transformation of P25 by microwave-assisted hydrothermal method. *Materials Letters* **2014**, *123*, 10-13.
104. Menendez-Flores, V. M.; Nakamura, M.; Kida, T.; Jin, Z.; Murakami, N.; Ohno, T., Controlled structure of anatase TiO<sub>2</sub> nanoparticles by using organic additives in a microwave process. *Applied Catalysis, A* **2011**, *406*, 119-123.
105. Chen, Y.-C.; Lo, S.-L.; Kuo, J., Effects of titanate nanotubes synthesized by a microwave hydrothermal method on photocatalytic decomposition of perfluorooctanoic acid. *Water Research* **2011**, *45*, 4131-4140.
106. Wu, X.; Jiang, Q.-Z.; Ma, Z.-F.; Fu, M.; Shangguan, W.-F., Synthesis of titania nanotubes by microwave irradiation. *Solid State Communications* **2005**, *136*, 513-517.
107. Dar, M. I.; Chandiran, A. K.; Grätzel, M.; Nazeeruddin, M. K.; Shivashankar, S. A., Controlled synthesis of TiO<sub>2</sub> nanoparticles and nanospheres using a microwave assisted approach for their application in dye-sensitized solar cells. *Journal of Materials Chemistry A* **2014**, *2* (6), 1662-1667.

108. Nakate, U. T., Photocatalytic properties of microwave-synthesized TiO<sub>2</sub> and ZnO nanoparticles using malachite green dye. *Journal of Nanoparticles* **2013**, 2013.
109. Liu, G.; Yang, H. G.; Pan, J.; Yang, Y. Q.; Lu, G. Q.; Cheng, H.-M., Titanium Dioxide Crystals with Tailored Facets. *Chemical Reviews* **2014**, *114* (19), 9559-9612.
110. Aerosol processes. Available from [www.uio.no](http://www.uio.no)
111. Kasuga, T., Formation of titanium oxide nanotubes using chemical treatments and their characteristic properties. *Thin Solid Films* **2006**, *496* (1), 141-145.
112. Sun, X.; Li, Y., Synthesis and characterization of ion-exchangeable titanate nanotubes. *Chemistry-A European Journal* **2003**, *9* (10), 2229-2238.
113. Wang, C.; Zhang, X.; Zhang, Y.; Jia, Y.; Yang, J.; Sun, P.; Liu, Y., Hydrothermal Growth of Layered Titanate Nanosheet Arrays on Titanium Foil and Their Topotactic Transformation to Heterostructured TiO<sub>2</sub> Photocatalysts. *The Journal of Physical Chemistry C* **2011**, *115* (45), 22276-22285.
114. Kim, M. S.; Lee, T.-W.; Park, J. H., Controlled TiO<sub>2</sub> Nanotube Arrays as an Active Material for High Power Energy-Storage Devices. *Journal of The Electrochemical Society* **2009**, *156* (7), A584-A588.
115. Lee, K.-M.; Suryanarayanan, V.; Huang, J.-H.; Thomas, K. R. J.; Lin, J. T.; Ho, K.-C., Enhancing the performance of dye-sensitized solar cells based on an organic dye by incorporating TiO<sub>2</sub> nanotube in a TiO<sub>2</sub> nanoparticle film. *Electrochimica Acta* **2009**, *54* (16), 4123-4130.
116. Mirjolet, C.; Papa, A. L.; Crehange, G.; Raguin, O.; Seignez, C.; Paul, C.; Truc, G.; Maingon, P.; Millot, N., The radiosensitization effect of titanate nanotubes as a new tool in radiation therapy for glioblastoma: A proof-of-concept. *Radiotherapy and Oncology* **2013**, *108*, 136-142.
117. Papa, A.-L.; Boudon, J.; Bellat, V.; Loiseau, A.; Bisht, H.; Sallem, F.; Chassagnon, R.; Bérard, V.; Millot, N., Dispersion of titanate nanotubes for nanomedicine: comparison of PEI and PEG nanohybrids. *Dalton Transactions* **2015**, *44* (2), 739-746.
118. Kubota, S.; Johkura, K.; Asanuma, K.; Okouchi, Y.; Ogiwara, N.; Sasaki, K.; Kasuga, T., Titanium oxide nanotubes for bone regeneration. *Journal of Materials Science: Materials in Medicine* **2004**, *15* (9), 1031-1035.
119. Liu, N.; Chen, X.; Zhang, J.; Schwank, J. W., A review on TiO<sub>2</sub>-based nanotubes synthesized via hydrothermal method: Formation mechanism, structure modification, and photocatalytic applications. *Catalysis Today* **2014**, *225*, 34-51.
120. Xu, D.; Li, J.; Yu, Y.; Li, J., From titanates to TiO<sub>2</sub> nanostructures: Controllable synthesis, growth mechanism, and applications. *Science China Chemistry* **2012**, *55* (11), 2334-2345.
121. Morgan, D. L.; Liu, H.-W.; Frost, R. L.; Waclawik, E. R., Implications of Precursor Chemistry on the Alkaline Hydrothermal Synthesis of Titania/Titanate Nanostructures. *The Journal of Physical Chemistry C* **2010**, *114* (1), 101-110.
122. Bavykin, D. V.; Walsh, F. C., Elongated Titanate Nanostructures and Their Applications. *European Journal of Inorganic Chemistry* **2009**, *2009* (8), 977-997.
123. Runkel, M.-C.; Wittich, O.; Feldhoff, A.; Wark, M.; Bredow, T., Theoretical and Experimental Study of Anatase Nanotube Formation via Sodium Titanate Intermediates. *The Journal of Physical Chemistry C* **2015**, *119* (9), 5048-5054.
124. Yang, J.; Jin, Z.; Wang, X.; Li, W.; Zhang, J.; Zhang, S.; Guo, X.; Zhang, Z., Study on composition, structure and formation process of nanotube Na<sub>2</sub>Ti<sub>2</sub>O<sub>4</sub>(OH)<sub>2</sub>. *Dalton Transactions* **2003**, (20), 3898-3901.
125. Kukovecz, Á.; Hodos, M.; Horváth, E.; Radnóczy, G.; Kónya, Z.; Kiricsi, I., Oriented Crystal Growth Model Explains the Formation of Titania Nanotubes. *The Journal of Physical Chemistry B* **2005**, *109* (38), 17781-17783.
126. Li, M.-J.; Chi, Z.-Y.; Wu, Y.-C., Morphology, Chemical Composition and Phase Transformation of Hydrothermal Derived Sodium Titanate. *Journal of the American Ceramic Society* **2012**, *95* (10), 3297-3304.
127. Tsai, C.-C.; Teng, H., Structural Features of Nanotubes Synthesized from NaOH Treatment on TiO<sub>2</sub> with Different Post-Treatments. *Chemistry of Materials* **2006**, *18* (2), 367-373.
128. Zhang, S.; Peng, L.-M.; Chen, Q.; Du, G.; Dawson, G.; Zhou, W., Formation Mechanism of H<sub>2</sub>Ti<sub>3</sub>O<sub>7</sub> Nanotubes. *Physical Review Letters* **2003**, *91* (25), 256103.
129. Wu, D.; Liu, J.; Zhao, X.; Li, A.; Chen, Y.; Ming, N., Sequence of Events for the Formation of Titanate Nanotubes, Nanofibers, Nanowires, and Nanobelts. *Chemistry of Materials* **2006**, *18* (2), 547-553.
130. Ren, L.; Qi, X.; Liu, Y.; Zou, X.; Huang, Z.; Li, J.; Yang, L.; Zhong, J., Morphological alteration of anatase titania nanostructures depend on the amount of Na ion intercalation. *Crystal Research and Technology* **2012**, *47* (7), 738-745.
131. Jolivet, J.-P., *De la solution à l'oxyde-2e ED: Chimie aqueuse des cations métalliques-synthèse de nanostructures chimie aqueuse des cations métalliques synthèse de nanostructures*. EDP Sciences: 2016.
132. Li, J.; Cao, K.; Li, Q.; Xu, D., Tetragonal faceted-nanorods of anatase TiO<sub>2</sub> with a large percentage of active {100} facets and their hierarchical structure. *CrystEngComm* **2012**, *14* (1), 83-85.

133. Khan, M. A.; Jung, H.-T.; Yang, O.-B., Synthesis and characterization of ultrahigh crystalline TiO<sub>2</sub> nanotubes. *The Journal of Physical Chemistry B* **2006**, *110* (13), 6626-6630.
134. Lan, Y.; Gao, X.; Zhu, H.; Zheng, Z.; Yan, T.; Wu, F.; Ringer, S. P.; Song, D., Titanate nanotubes and nanorods prepared from rutile powder. *Advanced Functional Materials* **2005**, *15* (8), 1310-1318.
135. Zhang, H.; Banfield, J. F., Size dependence of the kinetic rate constant for phase transformation in TiO<sub>2</sub> nanoparticles. *Chemistry of Materials* **2005**, *17* (13), 3421-3425.
136. Bavykin, D. V.; Lapkin, A. A.; Friedrich, J. M.; Walsh, F. C. In *Acid transformation of TiO<sub>2</sub> nanotubes to nanoparticles*, Proc. NSTI Nanotechnol. Conf., 2005; pp 655-658.
137. Incerti, S.; Barberet, P.; Deves, G.; Michelet, C.; Francis, Z.; Ivantchenko, V.; Mantero, A.; El Bitar, Z.; Bernal, M.; Tran, H., Comparison of experimental proton-induced fluorescence spectra for a selection of thin high-Z samples with Geant4 Monte Carlo simulations. *Nuclear Instruments and Methods in Physics Research Section B: Beam Interactions with Materials and Atoms* **2015**, *358*, 210-222.
138. Ph, B.; Vianna, F.; Karamitros, M.; Brun, T.; Gordillo, N.; Ph, M.; Incerti, S.; Seznec, H., Monte-Carlo dosimetry on a realistic cell monolayer geometry exposed to alpha particles. *Physics in Medicine & Biology* **2012**, *57* (8), 2189.
139. Incerti, S.; Psaltaki, M.; Gillet, P.; Barberet, P.; Bardiès, M.; Bernal, M.; Bordage, M.-C.; Breton, V.; Davidkova, M.; Delage, E., Simulating radial dose of ion tracks in liquid water simulated with Geant4-DNA: A comparative study. *Nuclear Instruments and Methods in Physics Research Section B: Beam Interactions with Materials and Atoms* **2014**, *333*, 92-98.
140. Le Trequesser, Q.; Deves, G.; Saez, G.; Daudin, L.; Barberet, P.; Michelet, C.; Delville, M.-H.; Seznec, H., Single Cell In Situ Detection and Quantification of Metal Oxide Nanoparticles Using Multimodal Correlative Microscopy. *Analytical Chemistry* **2014**, *86*, 7311-7319.
141. Muggioli, G.; Pomorski, M.; Claverie, G.; Berthet, G.; Mer-Calfati, C.; Saada, S.; Devès, G.; Simon, M.; Seznec, H.; Barberet, P., Single  $\alpha$ -particle irradiation permits real-time visualization of RNF8 accumulation at DNA damaged sites. *Scientific Reports* **2017**, *7*.
142. Michelet, C.; Barberet, P.; Moretto, P.; Seznec, H., Development and applications of STIM-and PIXE-tomography: A review. *Nuclear Instruments and Methods in Physics Research Section B: Beam Interactions with Materials and Atoms* **2015**, *363*, 55-60.
143. Taiju, T.; Elly, S.; Katsuyasu, K., Spectroscopy Study on the Location and Distribution of Eu 3+ Ions in TiO<sub>2</sub> Nanoparticles. *Japanese Journal of Applied Physics* **2008**, *47* (9R), 7428.
144. Xu, Z.; Yang, Q.; Xie, C.; Yan, W.; Du, Y.; Gao, Z.; Zhang, J., Structure, luminescence properties and photocatalytic activity of europium doped-TiO<sub>2</sub> nanoparticles. *J Mater Sci* **2005**, *40* (6), 1539-1541.
145. Antić, Ž.; Krsmanović, R. M.; Nikolić, M. G.; Marinović-Cincović, M.; Mitrić, M.; Polizzi, S.; Dramićanin, M. D., Multisite luminescence of rare earth doped TiO<sub>2</sub> anatase nanoparticles. *Materials Chemistry and Physics* **2012**, *135* (2-3), 1064-1069.
146. Ningthoujam, R. S.; Sudarsan, V.; Vatsa, R. K.; Kadam, R. M.; Jagannath; Gupta, A., Photoluminescence studies on Eu doped TiO<sub>2</sub> nanoparticles. *Journal of Alloys and Compounds* **2009**, *486* (1-2), 864-870.
147. Setiawati, E.; Kawano, K., Stabilization of anatase phase in the rare earth; Eu and Sm ion doped nanoparticle TiO<sub>2</sub>. *Journal of Alloys and Compounds* **2008**, *451* (1-2), 293-296.
148. Pal, M.; Pal, U.; Jiménez, J. M. G. Y.; Pérez-Rodríguez, F., Effects of crystallization and dopant concentration on the emission behavior of TiO<sub>2</sub>:Eu nanophosphors. *Nanoscale Research Letters* **2012**, *7* (1), 1.
149. Leostean, C.; Stefan, M.; Pana, O.; Cadis, A. I.; Suci, R. C.; Silipas, T. D.; Gautron, E., Properties of Eu doped TiO<sub>2</sub> nanoparticles prepared by using organic additives. *Journal of Alloys and Compounds* **2013**, *575*, 29-39.
150. Borlaf, M.; Colomer, M. T.; Moreno, R.; de Andrés, A., Structural and Photoluminescence Study of Eu<sup>3+</sup>/TiO<sub>2</sub> Xerogels as a Function of the Temperature Using Optical Techniques. *Journal of the American Ceramic Society* **2015**, *98* (1), 338-345.
151. Bo, C.; Erick, S. V.; Tetsuro, J., Synthesis of Eu-doped photoluminescent titania nanotubes via a two-step hydrothermal treatment. *Nanotechnology* **2006**, *17* (9), 2234.
152. Chang, M.; Song, Y.; Zhang, H.; Sheng, Y.; Zheng, K.; Zhou, X.; Zou, H., Hydrothermal assisted sol-gel synthesis and multisite luminescent properties of anatase TiO<sub>2</sub>: Eu<sup>3+</sup> nanorods. *RSC Advances* **2015**, *5* (73), 59314-59319.
153. Zhang, H.; Sheng, Y.; Zheng, K.; Zhou, X.; Shi, Z.; Xu, X.; Zou, H., Hydrothermal Fabrication and Luminescence Properties of One-Dimensional TiO<sub>2</sub>:Eu<sup>3+</sup> Spindlelike Nanorods. *European Journal of Inorganic Chemistry* **2014**, *2014* (21), 3305-3311.

154. Qi, X.; Song, Y.; Sheng, Y.; Zhang, H.; Zhao, H.; Shi, Z.; Zou, H., Controllable synthesis and luminescence properties of TiO<sub>2</sub>:Eu<sup>3+</sup> nanorods, nanoparticles and submicrospheres by hydrothermal method. *Optical Materials* **2014**, *38*, 193-197.
155. Li, H.; Zheng, K.; Xu, X.; Zhao, H.; Song, Y.; Sheng, Y.; Huo, Q.; Zou, H., Facile synthesis of TiO<sub>2</sub>:Eu<sup>3+</sup> spindle shaped nanoparticles from titanate nanobelt precursors. *Powder Technology* **2012**, *228*, 277-283.
156. Li, H.; Sheng, Y.; Zhao, H.; Song, Y.; Gao, F.; Huo, Q.; Zou, H., Facile synthesis and luminescent properties of TiO<sub>2</sub>:Eu<sup>3+</sup> nanorods and spindle-shaped nanoparticles from titanate nanotubes precursors. *Materials Research Bulletin* **2012**, *47* (12), 4322-4328.
157. Luo, W.; Li, R.; Liu, Y.; Chen, X., Sensitized Luminescence of Sm<sup>3+</sup>,Eu<sup>3+</sup>-Codoped TiO<sub>2</sub> Nanoparticles. *Journal of Nanoscience and Nanotechnology* **2010**, *10* (3), 1693-1698.
158. Vranješ, M.; Kuljanin-Jakovljević, J.; Radetić, T.; Stoiljković, M.; Mitrić, M.; Šaponjić, Z. V.; Nedeljković, J., Structure and luminescence properties of Eu<sup>3+</sup> doped TiO<sub>2</sub> nanocrystals and prolate nanospheroids synthesized by the hydrothermal processing. *Ceramics International* **2012**, *38* (7), 5629-5636.



# Chapter 3: Hafnium dioxide, $\text{HfO}_2$



## Table of contents

Introduction.....	97
I - Selected hafnium dioxide properties and applications .....	97
II - Routes to the synthesis of HfO <sub>2</sub> nanoparticles .....	100
II. 1. Precipitation synthesis .....	100
II. 2. Sol-gel synthesis .....	101
II. 3. Solvothermal synthesis.....	102
II. 4. Hydrothermal synthesis .....	102
III - Hafnium dioxide synthesis and characterization .....	104
III. 1. Previous studies.....	104
III. 2. Study of various parameters .....	105
III. 2. a. pH influence.....	106
III. 2. b. Role of the reaction time at 120 °C and several pH values.....	110
III. 2. c. Amount of HfCl <sub>4</sub> .....	114
III. 2. d. Temperature.....	116
III. 2. e. Structuring agents .....	117
III. 3. Characterization of HfO <sub>2</sub> nanoparticles .....	123
III. 3. a. Powder X-Ray diffraction.....	123
III. 3. b. High Resolution Transmission Electron Microscopy .....	124
III. 3. c. Zetametry.....	125
IV - Doping HfO <sub>2</sub> with lanthanides for tracking and imaging .....	126
IV. 1. Lanthanide mono doping .....	126
IV. 1. a. With europium (Eu <sup>3+</sup> ) .....	127
IV. 1. b. With terbium (Tb <sup>3+</sup> ).....	128
IV. 2. Lanthanide bi-doping and tri-doping .....	131

IV. 2. a. Synthesis challenges.....	131
IV. 2. b. Europium, Terbium and Gadolinium for nanothermometry .....	133
Conclusion .....	136
Experimental part.....	137
Characterization methods.....	138
Bibliography.....	145

## Introduction

Hafnium and titanium are in the same group of the Periodic Table, but the former has a higher atomic number. The synthesis of nanoparticles containing these two elements and their behavior under ionizing radiation allows us to investigate the role of nanoparticles in the enhancement of the radiotherapy treatment. Thus, this chapter focuses on the synthesis and characterization of hafnium oxide nanoparticles, and is divided in four parts. The first one presents the properties and applications of hafnium oxide, the second part summarizes the main synthetic routes, and the choice we made corresponding to the required specifications in terms of nanoparticle's size and shape. The third part describes our results on the synthesis and characterization of HfO<sub>2</sub> nanoparticles, and the fourth one features the insertion of lanthanides in the HfO<sub>2</sub> matrix to endow them with multifunctionality.

### I - Selected hafnium dioxide properties and applications

Hafnium is a group 4, period 6 element, and has an atomic weight of 178.49 and an atomic radius of 159 pm. Although hafnium was predicted in 1869 by Dmitri Mendeleev it was isolated for the first time only in 1922. In its elemental form, hafnium has a silver-grey appearance. Hafnium does not exist as a free element in nature, being found in zirconia compounds such as zircon [1].

HfO<sub>2</sub> is a chemically inert compound with a high melting point (*ca.* 2900 °C) and an electrical insulator with a band gap of 5.3 – 5.7 eV [2]. Hafnia adopts the structure of zirconia (ZrO<sub>2</sub>). In contrast to TiO<sub>2</sub>, which features six-coordinated Ti in all phases, zirconia and hafnia consist of seven or eight-coordinate metal centers. A variety of crystalline phases exists including cubic (Fm-3m), tetragonal (P4<sub>2</sub>/nmc), monoclinic (P2<sub>1</sub>/c), and orthorhombic (Pbca and Pnam) [3]. Table 1 gathers the structural and thermodynamic properties of these crystalline phases [4].

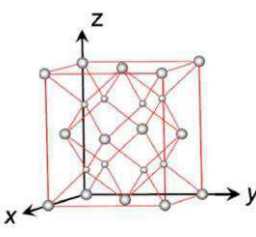
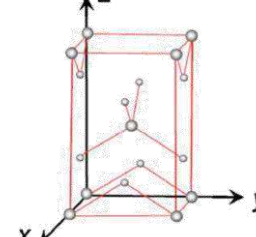
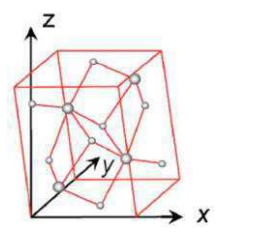
Phase	Cubic	Tetragonal	Monoclinic
Space group	Fm-3m	P4 <sub>2</sub> /nmc	P2 <sub>1</sub> /c
Unit cell (Å)	a = 5.11 Å Z = 4	a = 5.15 Å c = 5.28 Å Z = 4	a = 5.11 Å b = 5.17 Å c = 5.28 Å α = 99.35° Z = 4
Distance (Hf <sup>4+</sup> - O <sup>2-</sup> )(Å)	-	-	2.03 – 2.20
Coordination number	[Hf <sup>4+</sup> ] = 8 [O <sup>2-</sup> ] = 4	[Hf <sup>4+</sup> ] = 8 [O <sup>2-</sup> ] = 4	[Hf <sup>4+</sup> ] = 7 – 8 [O <sup>2-</sup> ] = 3 – 4
Density (g.cm <sup>-3</sup> )	10.30	10.01	9.68
Hardness (GPa)	12 - 15		
Band gap (eV)	5.51	5.82	-
Refractive index	1.98 – 2.02		
Enthalpy of formation Δ <sub>f</sub> H <sup>0</sup> (298.15 K) (kJ.mol <sup>-1</sup> ) [5]	- 1144.7 ± 1.26		
Structure			

Table 1: Physical and thermodynamic of 3 crystalline phases of HfO<sub>2</sub> [4, 6-7]

Monoclinic phase forms at a relatively low temperature, while the tetragonal phase is obtained above 2000 K, and the cubic phase forms above 2870 K [4, 8-9].

Hafnium dioxide is used in optical coatings and as a high-k dielectric in DRAM (dynamic random access memory) capacitors and in advanced metal-oxide-semiconductor devices [10]. The use of high-k dielectrics can make the charge storage area smaller so as to increase the memory capacity [11-12]. The high-k dielectrics allow the improvement of the operation in flash-memory devices, also enhancing the rewrite speed and charge storage duration and reducing the programming (write/erase) voltages [11-12]. Although several high-k dielectric materials have been studied, the high hafnium oxide dielectric constant (*ca.* 25) makes it one of the most promising candidates as gate dielectric metal oxide films [13-14]. Hafnium based oxides were indeed introduced by Intel® in 2007, replacing silicon oxide as a gate insulator in field-effect transistor [15].

Recently, the potential biomedical applications of hafnium dioxide have been assessed, especially its use as a radioenhancer in radiotherapy [16-22]. For instance, HfO<sub>2</sub> coupled with silicon nanowires is used for sensitive detection of small nucleic acid oligomers, and is also used to enable double- and single-stranded DNA transport through nanopores fabricated in ultrathin (2 – 7 nm thick) freestanding HfO<sub>2</sub> membranes [23-24]. An HfO<sub>2</sub> biosensor is developed for early stage detection of human interleukin-10 to avoid heart failure [25]. HfO<sub>2</sub> metal-oxide semiconductor (MOS) capacitor based dosimeter has been fabricated on single crystalline n-type silicon for the detection of ionizing radiation [26]. Crystalline HfO<sub>2</sub> NPs has been used to improve the radiation dose within tumor tissues [16]. The densely packed HfO<sub>2</sub> nanoparticles can selectively absorb the high energy gamma/X-ray radiations, allowing a higher production of electrons in the tumor tissues by localizing the damage on cancer cells [16]. The company Nanobiotix has started a clinical trial on hafnium oxide nanoparticles coated with a polymer layer, presumably PEG. The goal was to kill cancer cells more efficiently taking advantage of the process of radioenhancement. A clinical trial of NBTXR3 in soft tissue sarcoma was performed at the Institute Bergonié, in Bordeaux [27].

## II - Routes to the synthesis of HfO<sub>2</sub> nanoparticles

This section describes the various synthetic routes reported in the literature to prepare HfO<sub>2</sub> NPs.

### II. 1. Precipitation synthesis

Precipitation synthesis is a simple method to obtain metal oxide NPs, consisting of mixing and stirring a chloride precursor of hafnium in 0.4 M – 1 M NaOH aqueous solutions, followed by a calcination step to obtain the oxides which are crystallized [28]. In this method, the precipitation step is essential and crucial because processes such as nucleation, growth and coarsening (Ostwald ripening), occur. The coarsening process is essentially the consumption of small particles by larger one during the growth process. Thus, the rate of addition of reactants, stirring time, and temperature are parameters that tailor size and morphology. In the nucleation step, numerous crystallites are synthesized and may tend to agglomerate together to form larger structures, which are more stable thermodynamically [29].

Ramadoss synthesized HfO<sub>2</sub> NPs from hafnium tetrachloride and a base, such as potassium hydroxide [30] or sodium hydroxide [28]. A white mixture was obtained, washed and dried at 100 °C. The obtained hafnium hydroxide was further calcined at 500 °C for 2 hours, leading to the formation of HfO<sub>2</sub> NPs. Advantages of this method are its simplicity and low-cost processing. The calcination step, is a drawback because it tends to agglomerate NPs.

Jayaraman *et al.* prepared hafnium oxide nanoparticles of different sizes (8.79, 7.16, 6.78 nm) by the precipitation method, by varying the stirring time (6, 8 and 12 hours). The XRD pattern and Raman spectra of the NPs revealed that this material crystallized in the monoclinic structure. SEM and TEM images showed that the HfO<sub>2</sub> NPs were spherical in shape after the calcination at 500 °C [22, 31].

## II. 2. Sol-gel synthesis

Sol-gel synthesis is a well-known process presenting several advantages, including a relatively low reaction temperature, and a good control of compositions. This method is often used to prepare metal oxides, especially SiO<sub>2</sub> and TiO<sub>2</sub>. The process encompasses the conversion of monomers into a colloidal solution (called sol), which is the precursor for an integrated particles network (called gel). Typical precursors are metal alkoxides which are often expensive.

An alternative metal alkoxide-free way to prepare NPs is to use the polymerized complex derived sol-gel method, also known as Pechini method, which employs inorganic salts as precursors, citric acid as chelating agent and ethylene glycol as cross-linking agent [32]. Therefore, the heat treatment step is mandatory to obtain the oxides. Ramos-Gonzales developed a method involving the formation of an organic polymeric network [33]. Ramos-Gonzales compares the polymerized complex and polymer precursor methods. In the former method, citric acid and ethylene glycol are used as the chelating and polymerizable reagents, respectively. In the polymer precursor method, poly(acrylic acid) is used as the chelating agent. The precursors or the mixture or the final products were heat-treated at 500 °C or 800 °C. Essentially, the monoclinic crystalline phase was obtained, even if the polymerized complex method may also yield the cubic phase. The particle size obtained by TEM and XRD varied between 4 and 11 nm [33].

Tang proposed another sol-gel derived method, the nonhydrolytic sol-gel synthesis [34]. In this method, the condensation between a metal halide and a metal alkoxide in the presence of coordination ligands forms metal-oxide-metal bridges with the elimination of the alkyl halide. Reaction is conducted under argon at 360 °C or 400 °C, between hafnium isopropoxide, and hafnium chloride or bromide with trioctylphosphine oxide (TOPO), to form HfO<sub>2</sub> NPs whose size and crystal structure depend on the preparation conditions, such as the reaction temperature and the type of halide used [35].

The advantage of these sol-gel methods is the monodispersity of the NPs, while the main drawbacks are (i) the use of expensive metal alkoxides and (ii) the use of organic TOPO ligands unsuitable for bio applications.

### II. 3. Solvothermal synthesis

The solvothermal method available in the literature for the synthesis of HfO<sub>2</sub> NPs uses benzyl alcohol as solvent to produce small NPs with good crystallinity. For example, Niederberger developed a route that involved a simple ether elimination process between two alkoxide precursors leading to the formation of the Hf-O-Hf bond. HfO<sub>2</sub> formed nanoparticles with slightly elongated shape, typically 6 nm long and 3 – 4 nm wide [36]. Buha developed a synthetic route from hafnium tetrachloride in benzyl alcohol to form nanoparticles with a size around 6 nm which crystallized in the monoclinic phase [37].

A hydrothermal synthesis was proposed by Štefanić [38-39], based on a reaction under mild temperature (90 °C or 120 °C), that leads to crystalline NPs with a small crystallite size.

However, these reactions have the drawback of requiring a long time (between 2 and 7 days) and for this reason, faster microwave-assisted or sonically-assisted hydrothermal treatments have been developed. For instance, it is possible with the microwave-assisted reaction to reduce the time to *ca.* 5 min at 220 °C in benzyl alcohol [40] or to *ca.* 1 hour at 140 °C in water [41], while the sonically-assisted one reduces the reaction time to one to three hours at 250 °C in water [42].

### II. 4. Hydrothermal synthesis

Concerning the different synthetic methods reported in literature, the precipitation and sol-gel methods require a calcination step to obtain crystalline product. This step uses high temperature and favors NPs sintering, which should be avoided because it prevents a good redispersion in aqueous media, especially in biological media, and the formation of a stable colloidal suspension. Solvothermal synthesis should also be avoided because organic solvents are in general not biocompatible. Thus, the most promising method for biological applications is the hydrothermal method. We focused then on the various syntheses reported in the literature and presented in Table 2.

Starting material	pH	Base	T (°C)	Time (h)	Shape & TEM size (nm)	XRD size (nm)	Phase	ref
<b>Hydrothermal treatment</b>								
HfOCl <sub>2</sub>	3	NaOH	90-120	48	-	9	monoclinic	[39]
	7			600		30		
	9.5			150		35		
	13			24		5		
HfOCl <sub>2</sub>	-	NH <sub>4</sub> OH	700	3	Roundish 30	33	monoclinic	[43]
HfCl <sub>4</sub>	-	NH <sub>4</sub> OH	120	40	Rhombic 800	< 10	monoclinic	[44]
HfCl <sub>4</sub>	12	NaOH	200	1.5	-	-	amorphous	[45]
HfCl <sub>4</sub>	-	KOH	<350 >400	0.2	Rhombic, 16	16	monoclinic	[46-47]
					Oval, 16	15	monoclinic	
HfOCl <sub>2</sub>	-	NH <sub>4</sub> OH	250	3	Elongated and agglomerated	13	monoclinic + amorphous	[42]
<b>Ultrasonically assisted hydrothermal treatment</b>								
HfOCl <sub>2</sub>	-	NH <sub>4</sub> OH	250	3	Elongated and agglomerated	15	monoclinic	[42]
<b>Microwave assisted hydrothermal treatment</b>								
HfCl <sub>4</sub>	4,7,9		130-225	1-5	-	21-25	monoclinic	[48]
HfCl <sub>4</sub>	>14	KOH	140	1	Rice-like 85-105	5	monoclinic	[41]

*Table 2: Several hydrothermal treatment to synthesize HfO<sub>2</sub> nanoparticles*

The temperature of the hydrothermal treatment should be below 200 °C to avoid the sintering of the nanoparticles and the nanoparticles should have a size between 30 and 60 nm. We decided to choose to reproduce the synthesis developed by Štefanić [39].

## III - Hafnium dioxide synthesis and characterization

### III. 1. Previous studies

Based on the literature study detailed above, it sounds logical to choose not only the hydrothermal synthesis but also the one described by Štefanić [39] to prepare hafnium oxide nanoparticles with the appropriate surface properties. In his paper, Štefanić reported the hydrothermal synthesis of HfO<sub>2</sub> nanoparticles starting from the solubilization of a powder of hafnium tetrachloride in water at various pH values, temperatures, reaction times, and bases. pH values were 3, 7, 9.5 and 13. For each pH value he tested two temperatures 90 °C and 120 °C, 2 bases (NaOH and Me<sub>4</sub>NOH), and reaction times ranging from 4 hours to 2 months. The results are gathered in a table which gives the XRD crystallite sizes (calculated by Scherrer formula) [49] and the degree of crystallinity of the synthesized NPs and the crystal structures when appropriate. Štefanić showed that HfO<sub>2</sub> NPs were obtained either as amorphous, monoclinic (m-), tetragonal (t-) or cubic (c-) phases, depending on the temperature but not in a systematic way. NPs exhibit different XRD crystallite sizes and with different ratios of crystalline form/amorphous material. In this paper, Štefanić, varying, in a systematic way, the parameters of the reaction (pH, temperature, time and nature of the base) observed different NPs crystallite sizes but he could not rationalize how these parameters influence the dimensions of the NPs themselves since no TEM images of the NPs were available. However, some trends on the crystallite size could be deduced from his work:

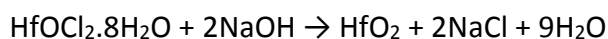
- The shorter the reaction time and the lower the temperature, the higher the amount of amorphous product;
- Low crystallite size is obtained at low and high pH values.

Based on these data, we chose to reproduce the procedure by Štefanić, confirm his XRD results and, in particular, obtain TEM images of the NPs and ascertain their effective size. Some modifications were introduced into Štefanić procedure and a more detailed method has been defined, taking in account Jayaraman's work [22]. We considered the stirring time of the reaction and fixed it to one hour in between final addition of the base solution and the beginning of the hydrothermal process.

### III. 2. Study of various parameters

I now describe the study of the effect of pH, reaction time and temperature on the preparation of NPs with size between 30 and 70 nm. TEM size was statistically determined from on, at least, 300 nanoparticles. The XRD crystallite size was ascertained using Scherer's formula. I use the terms "smooth" when the nanoparticle is almost monocrystalline, and "granular" when the nanoparticle comprises several tiny entities (cluster of smaller crystallites). The nanoparticles were synthesized by the hydrothermal method. The detailed experimental procedure is described in the experimental part of this chapter.

Hafnium tetrachloride was used as a precursor. HfCl<sub>4</sub> is water sensitive and its dissolution in water is exothermic and produces 4 equivalent of HCl (experimentally visible by gas release). Upon further addition of 1 M NaOH solution the formation of a milky-white suspension is visible. The white color comes from the formation of a reaction intermediate identified as hafnium tetrahydroxide, Hf(OH)<sub>4</sub>, or as hafnium chlorohydroxide, HfOCl<sub>2</sub>, depending on the authors [28, 38, 50].



Or Hf(OH)<sub>4</sub> instead of HfOCl<sub>2</sub>·8H<sub>2</sub>O

As an example, Table 3 compares the XRD data obtained by Štefanić and in this thesis.

pH	T(°C)	Time (h)	Base	XRD crystalline size Štefanić [39](nm)	XRD crystalline size obtained (nm)
3	120	24	NaOH	8.5 (5)	9
3	120	48	NaOH	9.3 (7)	10
9.5	120	76	NaOH	38 (8)	27
13	120	24	NaOH	5.6 (2)	8

*Table 3: Results of HfO<sub>2</sub> synthesis compared with the results of Štefanić [39]*

These results are in good agreement confirming the reproducibility of the experiments. We therefore went on with this procedure optimizing different parameters so as to obtain a particle size close to 30 nm.

## III. 2. a. pH influence

The influence of the pH on the size of the NPs was checked by choosing the same values as Štefanić 3, 9.5 and 13, while keeping the temperature (120 °C), reaction time (48 h) and amount of HfCl<sub>4</sub> (1 g) constant. TEM and XRD results are gathered in Table 4.

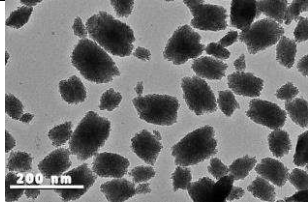
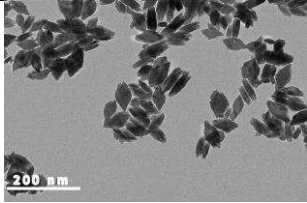
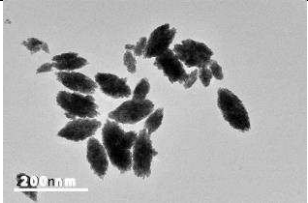
pH value	3	9.5	13
Štefanić XRD size (nm)	9.3 (± 7)	38 (± 8)	5.6 (± 2)
XRD size (nm)	10	34	8
TEM images	 (Figure 2)	 (Figure 3)	 (Figure 4)
TEM size (nm±std)	111 ± 28	84 ± 16	98 ± 32
Shapes	Rectangular, granular	Rhombus, smooth	Rice-like, granular

Table 4: Characterization by XRD and TEM of the HfO<sub>2</sub> NPs (conditions: 1 g HfCl<sub>4</sub>, 120 °C, 48h) at pH 3, 9.5 and 13

Moreover, the XRD patterns of the nanoparticles obtained at these three pH values are shown in figure 1 and XRD data are further studied in detail (cf. III. 3. a). Thus, we can compare the crystallinity of these NPs one with the other and with those obtained by Štefanić [39]. Our crystallite sizes agree well with those obtained by Štefanić. Small crystallite sizes are obtained at low and high pH whereas at pH 9.5, more crystalline particles were obtained.

Considering Figure 1, XRD patterns of pH 3 and 13 samples show a broadening of the reflections, which is in agreement with the granular shape of these agglomerated NPs revealed by TEM (Figure 2, Figure 3 and Figure 4).

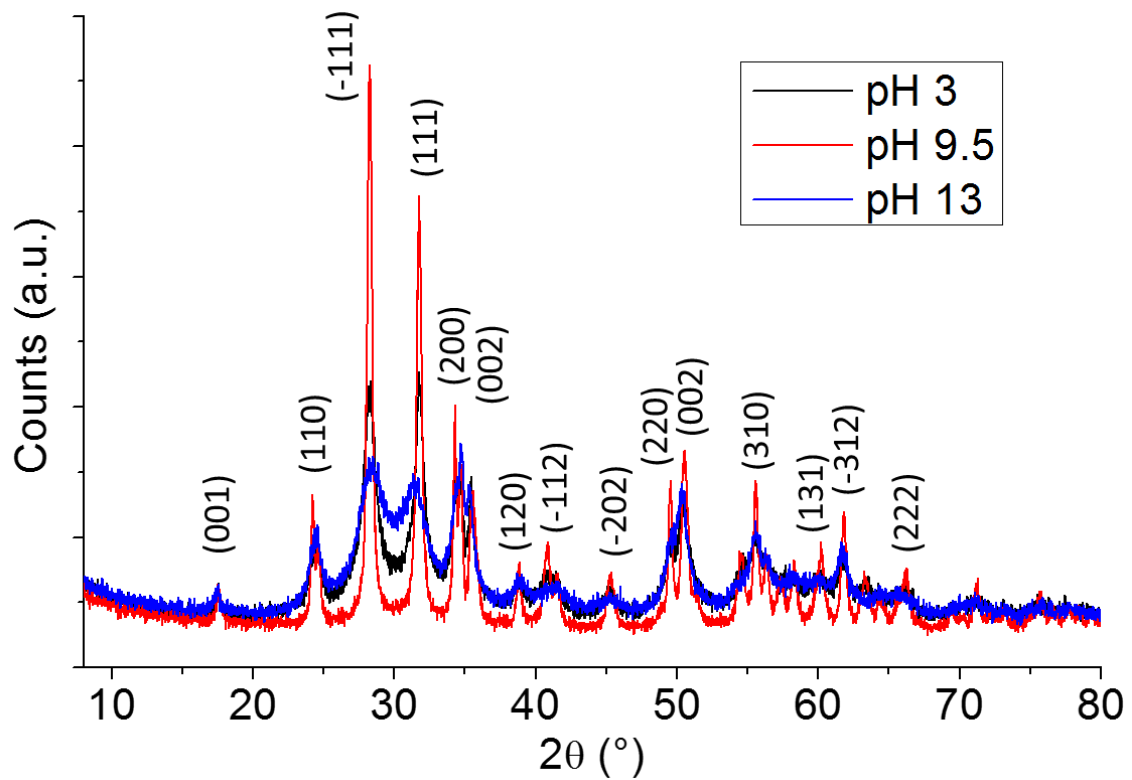


Figure 1: XRD patterns of HfO<sub>2</sub> NPs (conditions: 1 g HfCl<sub>4</sub>, 120 °C, 48h) at several pH values

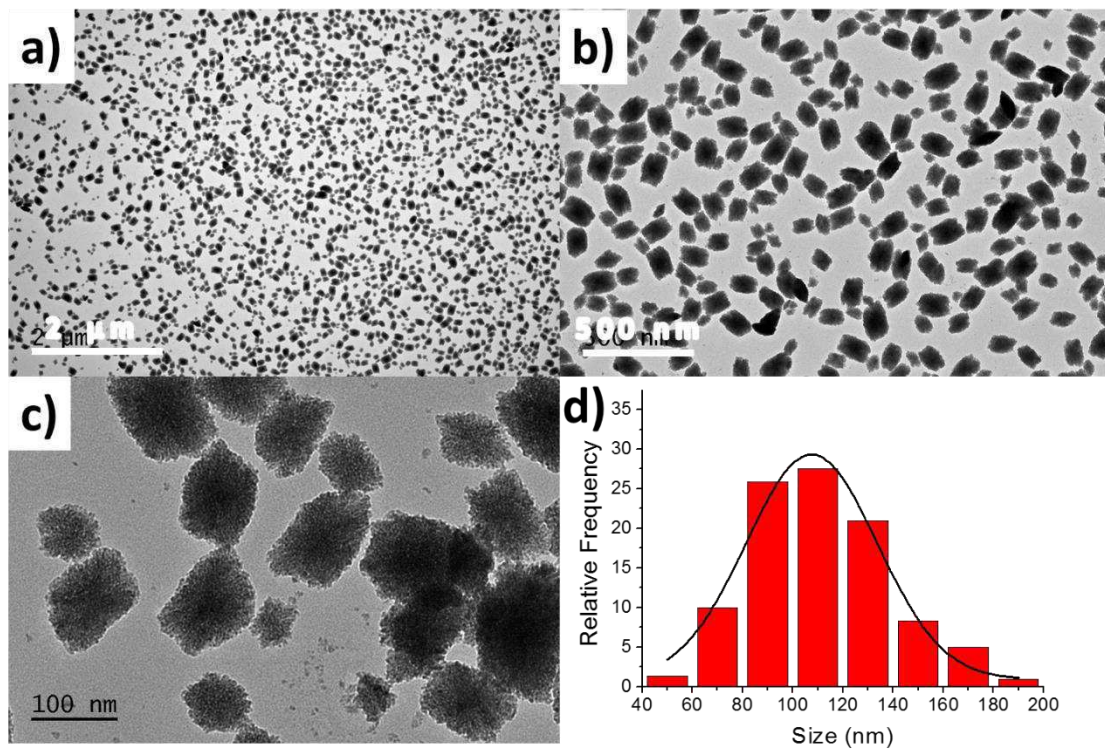


Figure 2: a,b,c) TEM images of HfO<sub>2</sub> NPs (pH 3, 120 °C, 48 h) , d) Size distribution of NPs

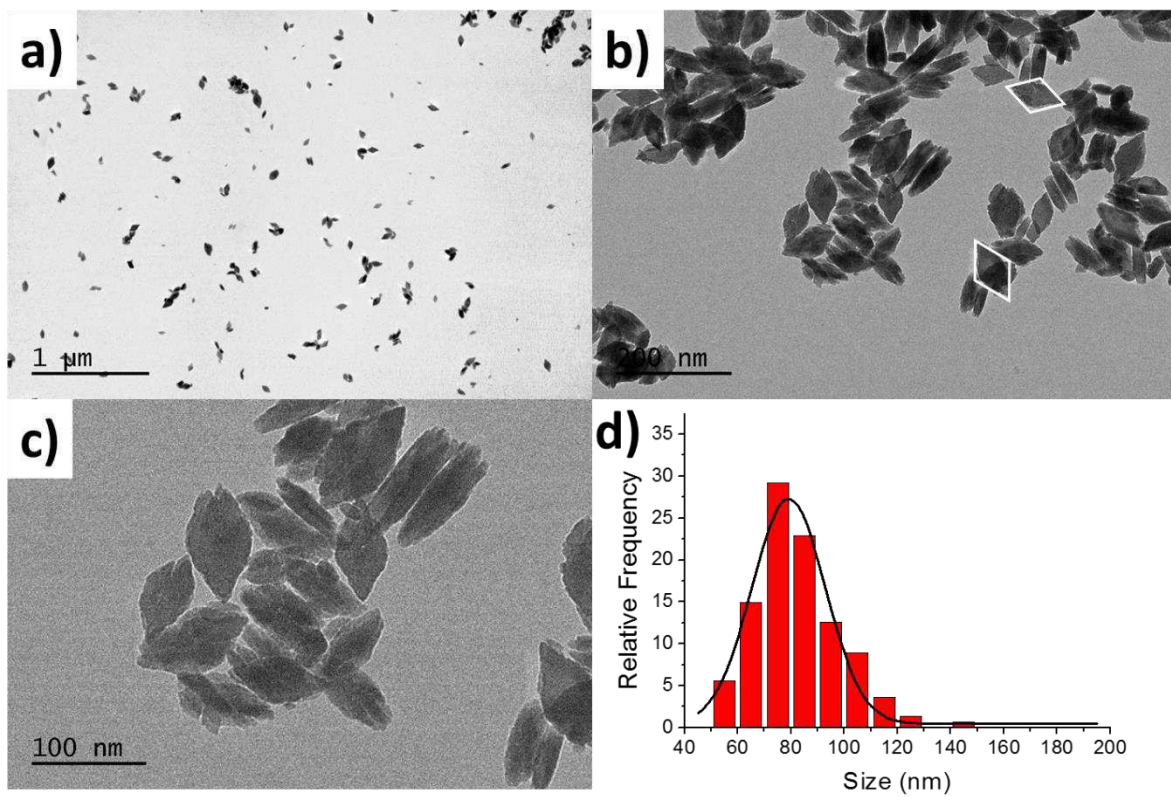


Figure 3: a,b,c) TEM images of HfO<sub>2</sub> NPs (pH 9.5, 120 °C, 48 h) , d) Size distribution of NPs

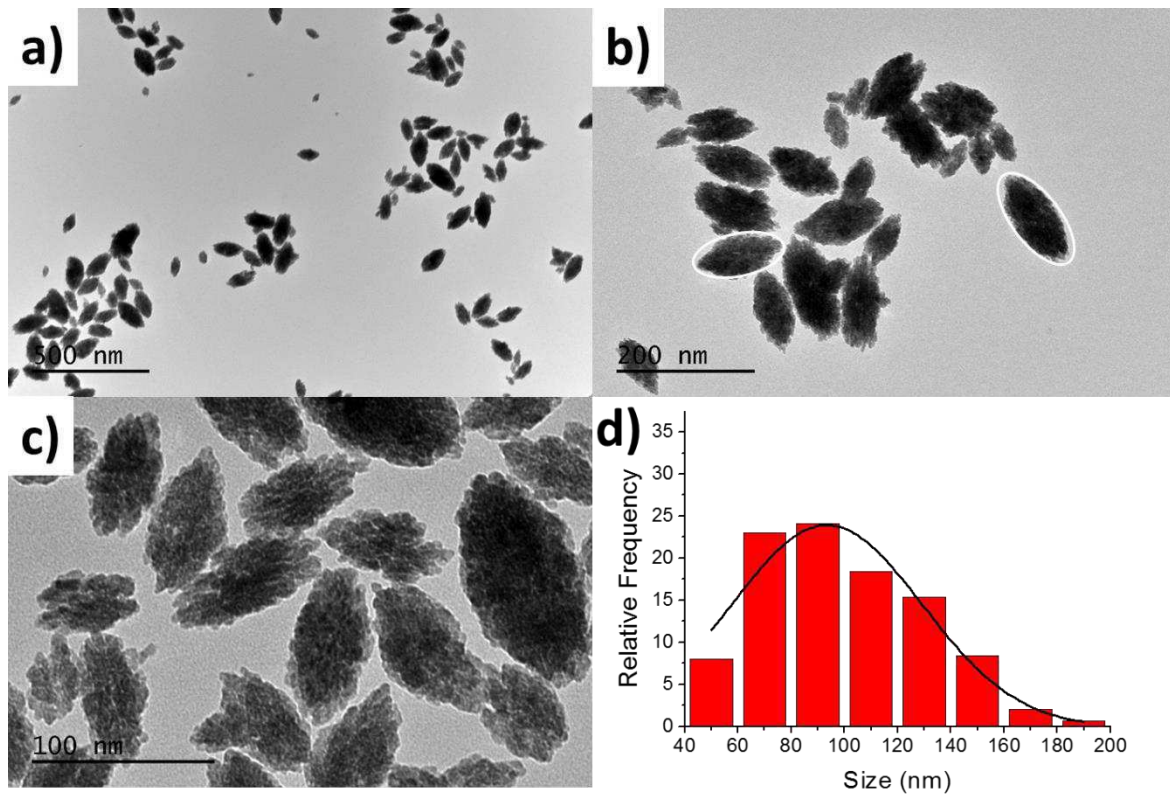


Figure 4: a,b,c) TEM images of HfO<sub>2</sub> NPs (pH 13, 120 °C, 48 h), d) Size distribution of NPs

Thus, adjusting the pH value allows changing the morphology and the shape of the synthesized nanoparticles from granular rectangular parallelepipeds at low pH to granular rice-like objects (white forms in Figure 4) at high pH, while at intermediate pH values rhombic single crystals (white rhombus in Figure 3) are obtained. At pH 3 and 13, the primary NPs forming the aggregates are very small, *ca.* 8 – 9 nm, resulting in broadened XRD reflections, while at pH 9.5, the primary NPs are larger, *ca.* 20 – 25 nm. Thus, the pH value modifies the size and the shape of the primary NPs forming the larger aggregates.

### III. 2. b. Role of the reaction time at 120 °C and several pH values

The effect of the reaction time was studied from 24 hours to 76 hours at different pH values. The others parameters were set to 1 g of HfCl<sub>4</sub> and 120 °C and 60% filling ratio of the autoclave.

- **pH 3**

The TEM pictures, the crystallite sizes obtained by XRD and the particle sizes and shapes obtained by TEM are gathered in table 5.

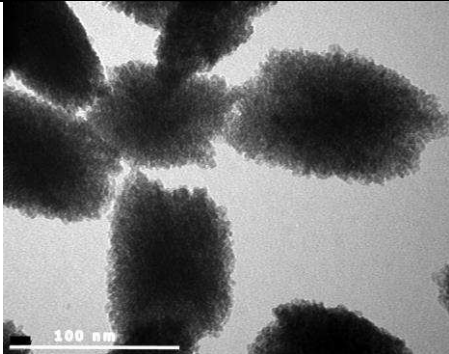
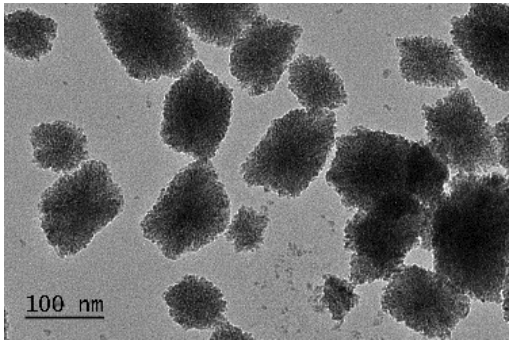
Reaction time	24h	48h
TEM images		
TEM size (nm±std)	104 ± 22	111 ± 28
XRD size (nm)	9	10
Shapes	Rectangular, granular	Rectangular, granular

Table 5: Characterizations by XRD and TEM of the HfO<sub>2</sub> NPs (conditions: 1 g HfCl<sub>4</sub>, 120 °C, pH 3) at two reaction times

The results obtained for these syntheses during either 24 hours or 48 hours are quite similar. TEM size and XRD crystallite size do not vary significantly. Thus, increasing the reaction time at pH 3 does not modify the size and not the shape of the NPs.

- pH 9.5

The same experiments were performed at pH 9.5. The TEM pictures and the size, shape are shown in Figure 5 and in table 6, respectively.

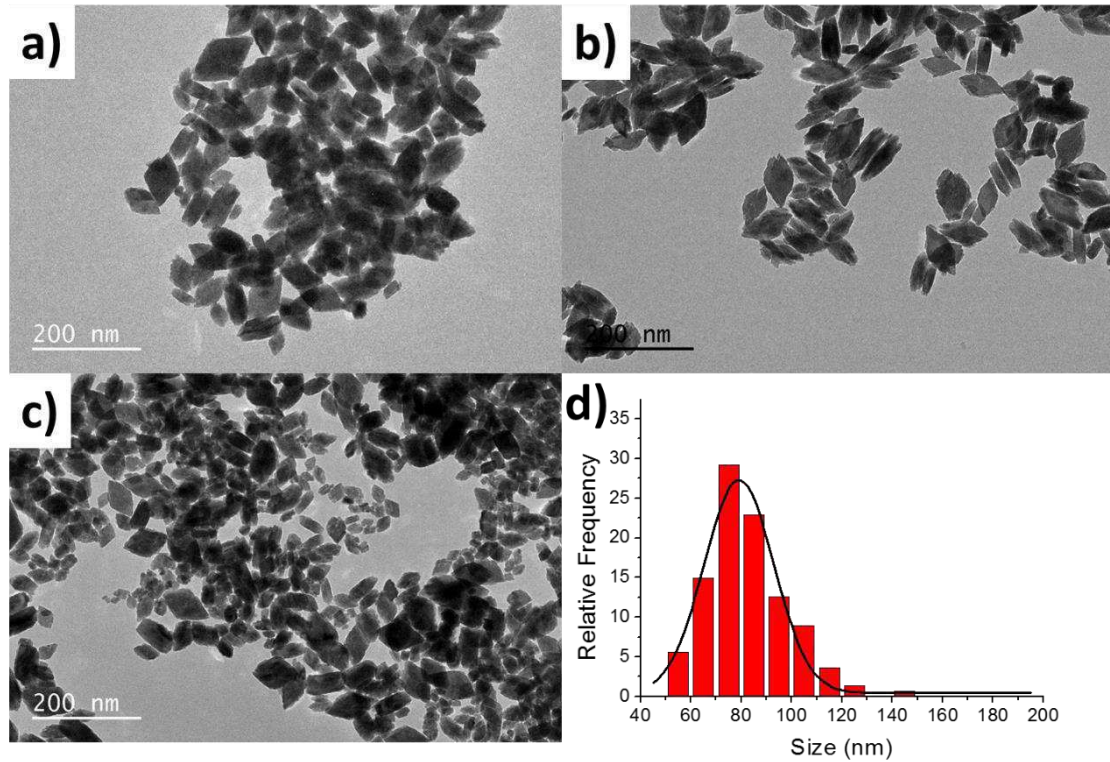


Figure 5: TEM pictures at pH 9.5, 120 °C, for (a) 24 h, (b) 48 h, (c) 76 h, (d) size distribution of the NPs for 48 hours

Reaction time	24h	48h	76h
TEM size (nm±std)	88 ± 18	84 ± 16	89 ± 17
XRD size (nm)	33	34	29
Shapes	Rhombus, smooth	Rhombus, smooth	Rhombus, smooth

Table 6: Characterizations by XRD and TEM of the HfO<sub>2</sub> NPs (conditions: 1 g HfCl<sub>4</sub>, 120 °C, pH 9.5) at several reaction times

Again, the results obtained for 24, 48 and 76 hours syntheses show that the TEM size and the XRD crystallite size do not vary significantly. Thus, increasing the reaction time at pH 9.5 does not modify the size and the shape of the NPs.

Since the reaction time did not seem to affect the size and shape of the NPs above 24 hours, we tried to reduce it down to 12 hours. A shorter time, in fact resulted in a lack of repeatability of the experiment and in some cases (Figure 6a and Figure 6b) there are still a lot of starting material as also mentioned Štefanić.

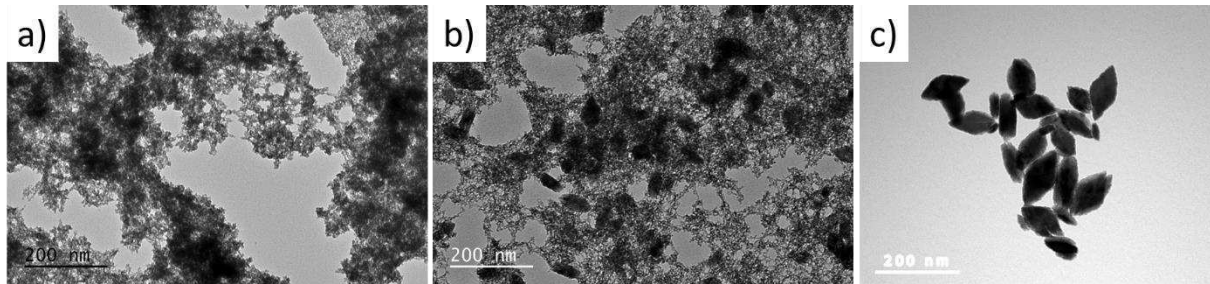


Figure 6: TEM images of 3 batches of HfO<sub>2</sub> (conditions: 1 g HfCl<sub>4</sub>, 120 °C, pH 9.5) for 12 hours

We then also checked the reproducibility of the experiment performed for 24 hours as illustrated in Figure 7. Again after 24 hours (Figure 7), at 120 °C, we obtained either an amorphous product (Figure 7a) or a mixture of amorphous and crystalline products (Figure 7b), as also mentioned in Štefanić's paper or a crystalline product (Figure 7c). We then confirmed by TEM the results obtained by Štefanić who quantified the percentage of amorphous phase in the mixture by XRD analysis. The same experiment performed for 48 hours always gave a crystalline product.

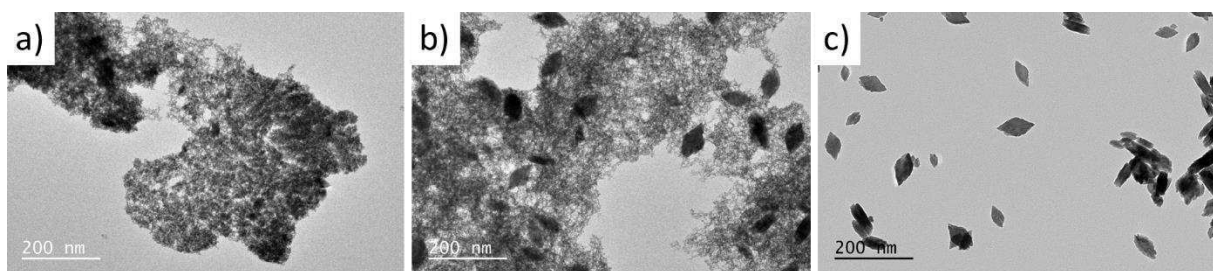
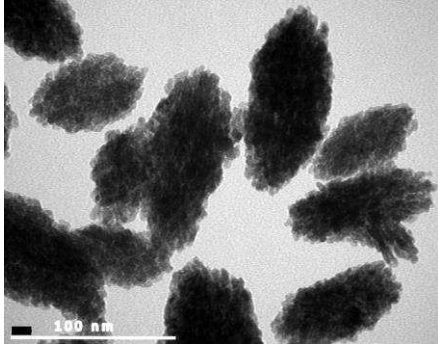
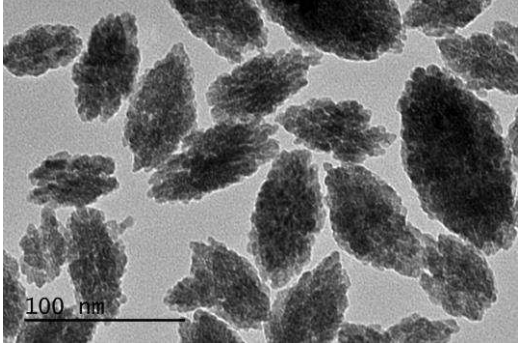


Figure 7: TEM images of 3 batches of HfO<sub>2</sub> (conditions: 1 g HfCl<sub>4</sub>, 120 °C, pH 9.5) for 24 hours

- **pH 13**

The same syntheses were also performed at pH 13. The obtained results are shown in table 7.

Reaction time	24h	48h
TEM images		
TEM size (nm±std)	110 ± 32	98 ± 32
XRD size (nm)	8	8
Shapes	Rice-like, granular	Rice-like, granular

*Table 7: Characterizations by XRD and TEM of the HfO<sub>2</sub> NPs (conditions: 1 g HfCl<sub>4</sub>, 120 °C, pH 13) at two reaction times*

Once again, increasing the reaction time induces no significant variation of NP size and shape at pH 13.

Štefanić demonstrated that the ratio of hydrothermal crystallization (ratio between the amount of crystalline and amorphous phase) is pH and temperature dependent. It is high at low and high pH, low in a mild basic pH and very low at pH 7 (See figure 8) [39]. The same behavior was observed in the crystallization process of ZrO<sub>2</sub>. Denkwicz [51], has studied the crystallization process of ZrO<sub>2</sub>, and showed that the reaction mechanism for ZrO<sub>2</sub> growth is pH dependent, with three regimes controlling the crystallization: dissolution/precipitation at low pH, solubility controlled regime at intermediate pH values, and a gel chemistry controlled regime at high pH values.

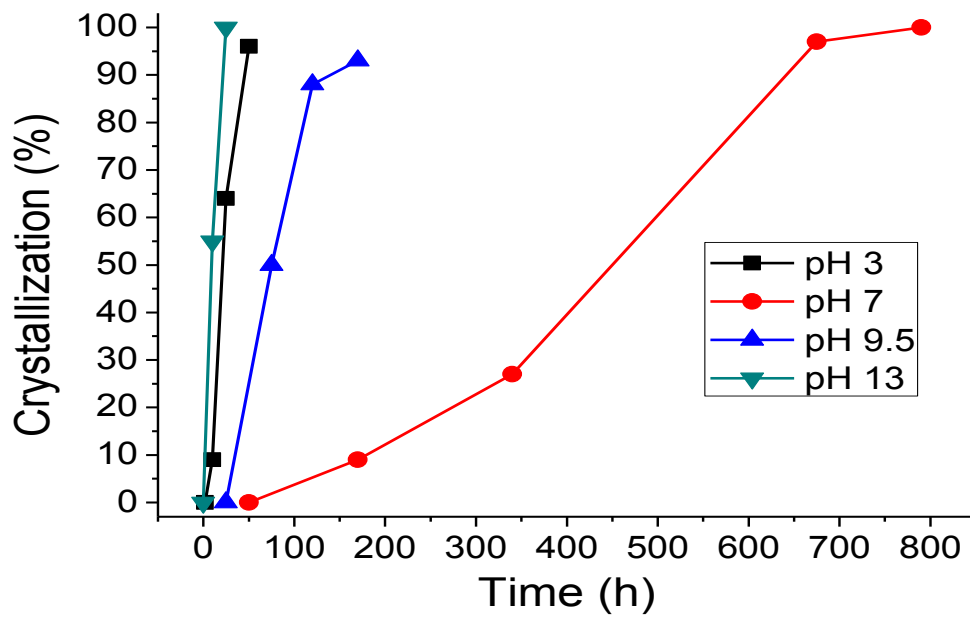


Figure 8: The fraction of crystal phase as a function of hydrothermal treatment time at 120 °C [39]

To sum up, for the three studied pH values, and in agreement with the experiments reported previously, when operating at 120 °C, increasing the time of the hydrothermal treatment from 12 to 76 hours does not modify NPs shape or size. It helps increasing the amount of crystalline phase since a reaction time of 48 hours is mandatory to obtain a pure phase. The only pH value, leading single-crystal nanoparticles is 9.5.

### III. 2. c. Amount of HfCl<sub>4</sub>

Since we are working in confined media, the influence of the amount of the Hf-bearing precursor may be crucial and will be studied. Experiments were performed with 0.3 g and with 1.0 g of precursor HfCl<sub>4</sub>. The results of the reaction performed at 120 °C for 48 hours at pH 9.5 and 13 are gathered in Table 8 and Table 9, respectively.

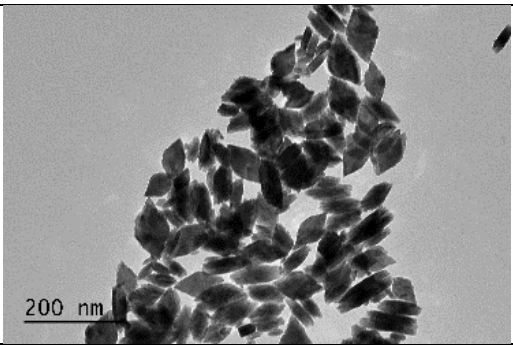
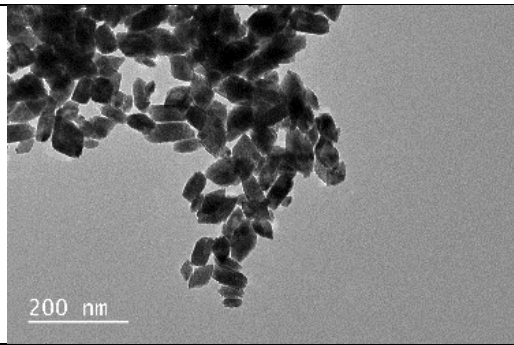
HfCl <sub>4</sub> amount	0.3 g	1.0 g
TEM images		
TEM size (nm±std)	84 ± 19	84 ± 16
XRD size (nm)	30	34
Shapes	Rhombus, smooth	Rhombus, smooth

Table 8: Characterizations by XRD and TEM of the synthesis pH 9.5, 120 °C, and 48 hours

At pH 9.5, no significant variation of XRD and TEM size is observed. However, at pH 13, there is a slight increase of the XRD and TEM size when one third of starting material is used. This can be explained by the fact that the dilution increases the growth of the few crystallites already formed, instead of generating new crystallite seeds in the first steps of the nucleation reaction. However, this slight modification leads us to conclude that the amount of hafnium precursor does not have an important influence on the size of the particles.

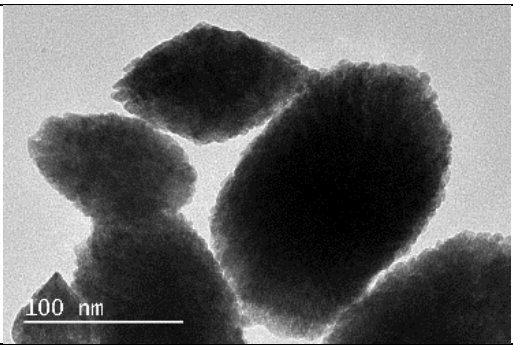
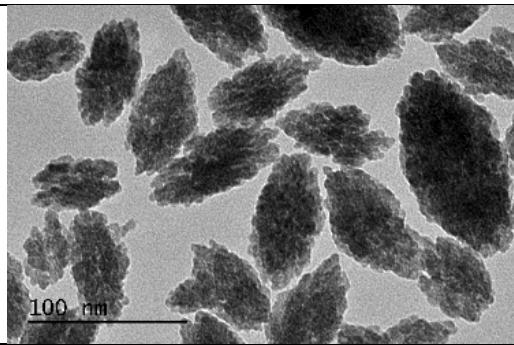
HfCl <sub>4</sub> amount	0.3 g	1 g
TEM images		
TEM size (nm±std)	128 ± 36	98 ± 32
XRD size (nm)	14	8
Shapes	Rice-like, granular	Rice-like, granular

Table 9: Characterizations by XRD and TEM of the synthesis pH 13, 120 °C, and 48 hours

## III. 2. d. Temperature

Next, we have tested the effect of the hydrothermal treatment temperature (120 °C, 150 °C and 180 °C), while keeping the pH at 9.5 (at this pH the NPs exhibit the larger size of primary crystallites but are present as individual NPs). Table 10 gathers TEM and XRD sizes for several temperatures and reaction times.

TEM size (std) (nm)				XRD size (nm)					
	24h	48h	76h		24h	48h	76h		
120 °C	88 ± 18	84 ± 16	89 ± 17	Decreasing size ↓	120 °C	33	34	Decreasing size ↓	
150 °C	62 ± 20	69 ± 19	72 ± 17		150 °C	26	26		26
180 °C	28 ± 8	24 ± 8	22 ± 6		180 °C	18	20		18

Table 10: Results of the syntheses performed at pH 9.5 for 1 g HfCl<sub>4</sub> for three reaction times and temperatures

Increasing the temperature from 120 °C to 180 °C decreases the TEM and XRD sizes. Thus, essentially single-crystal nanoparticles are obtained. Table 10 also shows that there is no variation of TEM and XRD sizes as a function of the reaction time, for all temperatures confirming that the reaction time does not either impact the NP size at 150 °C and 180 °C (Figure 9).

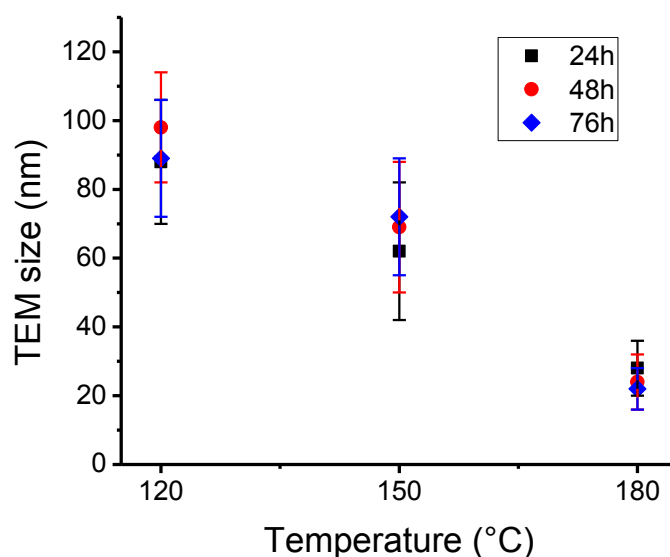


Figure 9: Decrease of the NP average size (TEM) as a function of the reaction temperature

The rhombic shape remains at 150 °C and 180 °C (Figure 10).

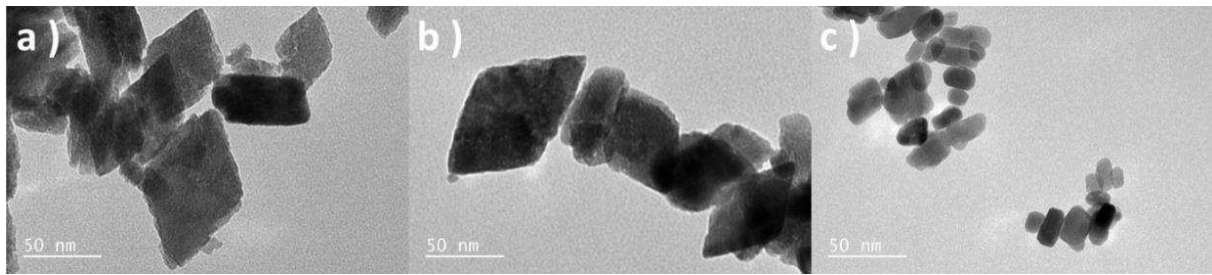


Figure 10: TEM images of HfO<sub>2</sub> NPs synthesized at pH 9.5, 48 hours a) 120 °C, b) 150 °C, c) 180 °C

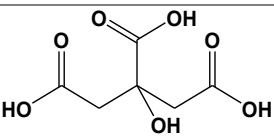
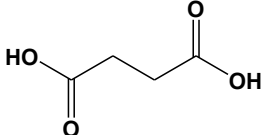
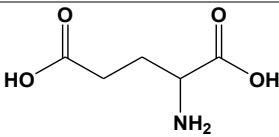
Therefore, the goal to obtain nanoparticles in the range 30 to 60 nm has been achieved. The biological testing and the functionalization of the nanoparticles with lanthanides may now start.

However, to avoid a such high temperature we tried to use chemical structuring agent as already done in the literature [52].

### III. 2. e. Structuring agents

At this point we are able to synthesize HfO<sub>2</sub> NPs with a size *ca.* 30 nm, which is suitable for biological applications. In order to decrease the temperature of reaction, we resorted to using structuring agents to control the growth of the NPs, as exemplified with the synthesis of titanium dioxide nanoparticles in the previous part. The “structuring agent” concept is taken from the literature which highlights the possibility of influencing the surface activity of TiO<sub>2</sub> NPs to enhance a preferential growth direction of the crystallites and, thus, provide some control over the final shape [52]. The term “structuring agent” is used with the meaning that the presence of additives modifies the crystal’s growth during the hydrothermal reaction.

In the synthesis of TiO<sub>2</sub> [53] and ZrO<sub>2</sub> [54], additives like citric acid, are used to modify the shape of the nanocrystals in hydrothermal and sol-gel processes. Additives have previously been used by Liu who synthesized HfO<sub>2</sub> nanorods of 33 nm length and 9 nm width, through a chemical solution method, using dodecanediol and oleylamine [55]. Table 11 shows a list of the additives studied in this work.

Reagent	Representation	pKa
Citric acid		3.13 – 4.76 – 6.40
Trimethylamine		(9.81)
Succinic acid		4.2 – 5.6
Glutamic acid		2.10 - 4.07 - 9.47

*Table 11: Reagents used as additives*

- **Citric acid (CA)**

Citric acid was added to the reaction, right after the introduction of HfCl<sub>4</sub> in water and then the pH was adjusted by adding a solution of NaOH (1 M). Nevertheless, according to the previous experiments and results, working at pH 9.5 produces nanoparticles with the largest crystallite size and, for this reason, the synthesis with citric acid was performed at pH 9.5. However, at this pH the mixture of hafnium tetrachloride and citric acid is soluble in distilled water. Even after the hydrothermal treatment for 48 hours at 120 °C, the obtained solution is still transparent with no formation of the desired nanomaterial. This is the reason why, we increased the pH until the formation of the characteristic white suspension which occurred at pH 13.

The results such as TEM images, TEM size obtained statistically and XRD size obtained by Scherer formula are gathered in table 12.

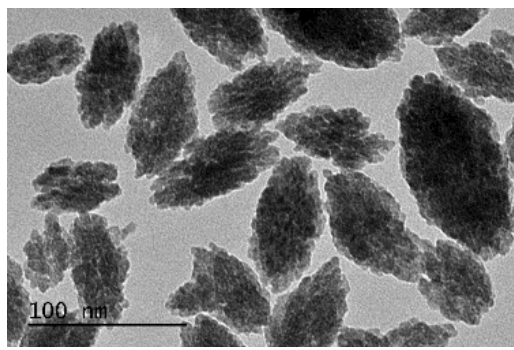
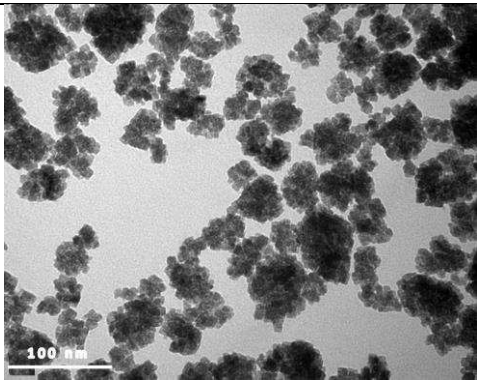
	Without Citric acid	With Citric acid
TEM images		
TEM size (nm±std)	98 (± 32)	44 (± 11)
XRD size (nm)	8	8
Shapes	Rice-like, granular	No shape, granular

Table 12: Comparative results with and without citric acid at pH 13, 120 °C and 48 h

The presence of citric acid prevents the formation of large aggregates of hafnium oxide NPs, which are obtained in the synthesis without citric acid. The individual crystallite size remains the same in both syntheses, *i.e.*, it is not affected by citric acid (Figure 11).

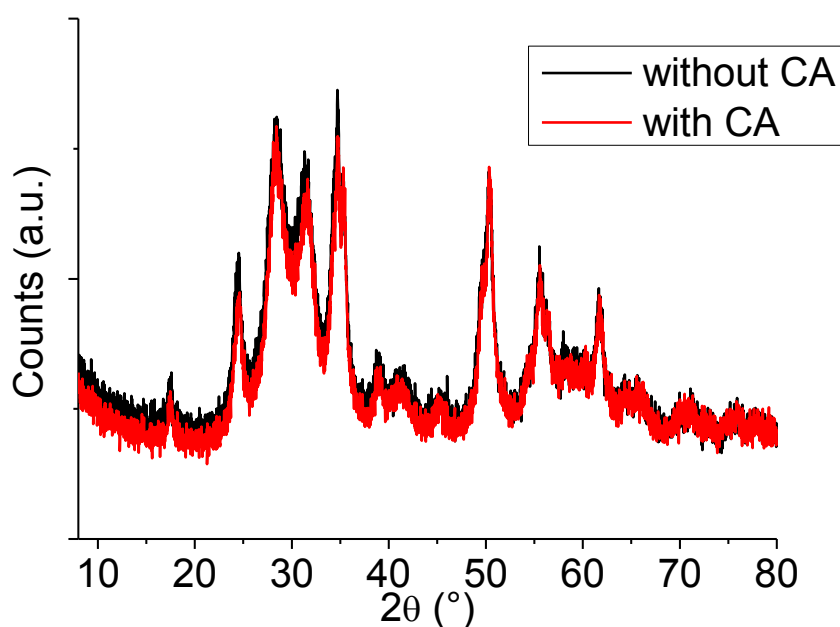


Figure 11: XRD patterns of HfO<sub>2</sub> NPs (conditions: 1 g HfCl<sub>4</sub>, 120 °C, 48h) at pH 13 with and without citric acid (CA)

The FTIR absorption spectrum of HfO<sub>2</sub> (Figure 12) was used to probe the presence of adsorbed species on the surface of NPs. The main bands at 765, 673 and 606 cm<sup>-1</sup> are due to the formation of Hf – O bonds that have spectroscopic active phonon modes in the range of 800 – 400 cm<sup>-1</sup> [30]. The broad absorption peak at 3679 cm<sup>-1</sup> can be attributed to the stretching vibration of the H – O bond, indicating the presence of hydroxyl groups on the surface of HfO<sub>2</sub> NPs. In our case, contrary to Ramadoss data [30], the intensity of these hydroxyl vibrations is rather low indicating fewer O-H groups on the surface.

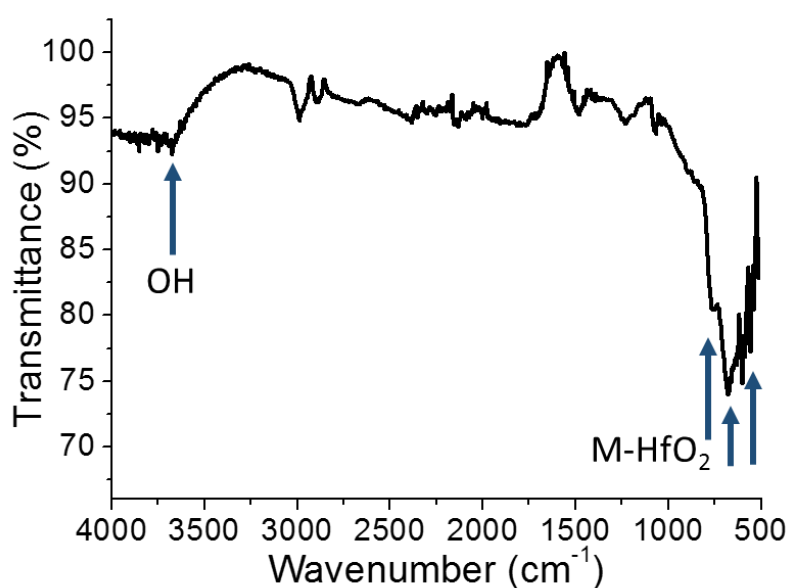


Figure 12: FTIR spectrum of HfO<sub>2</sub> NPs

Figure 13 presents the FTIR spectra of HfO<sub>2</sub> NPs (synthesized at pH 13), HfO<sub>2</sub> NPs synthesized with citric acid and, for comparison, the spectrum of citric acid. The spectrum of the product obtained upon addition of citric acid shows changes in the region 1700 – 1400 cm<sup>-1</sup> ascribed to the asymmetric and symmetric stretching vibrations of the carbonyl groups of the citrate anions [56]. The broad band at 3400 cm<sup>-1</sup>, characteristic of the O – H stretching vibration is enhanced in the NPs synthesized with citric acid, suggesting an increase in the number of surface hydroxyl groups, on the alcohol function of the citrate and on the carboxyl groups. This broad band can be also due to the H<sub>2</sub>O trapped in the first coordination sphere of the NPs because these were dried below 100 °C.

We can also compare the FT-IR spectrum of HfO<sub>2</sub> NPs with citric acid with the spectrum of citric acid (Figure 13). The band at 1720 cm<sup>-1</sup> characteristic of the carboxylic functional groups shifts to 1614 cm<sup>-1</sup> when the carboxylate groups are grafted onto the surface of hafnium oxide NPs.

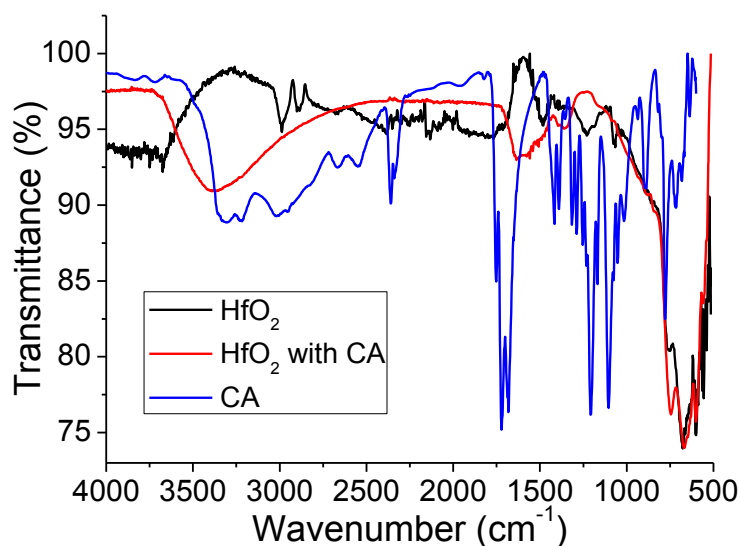


Figure 13: FT-IR spectra of HfO<sub>2</sub> nanoparticles with and without citric acid (pH 13, 48 h, 120 °C)

- **Other structuring agents**

We have tried using other structuring agents to decrease the size of HfO<sub>2</sub> NPs. Moreover, to take advantage of the interaction between hafnium and carboxylic groups, we choose structuring agents with carboxylic or amine groups and steric hindrance, in order to reduce the NP growth [32]. Trimethylamine, succinic acid and glutamic acid were added to the synthesis medium. Succinic acid has been used as a structuring agent in the synthesis of TiO<sub>2</sub> NPs [57]. The presence of the carboxylic groups and the steric hindrance are thought to control the growth of TiO<sub>2</sub> crystals. Trimethylamine was used in the synthesis of TiO<sub>2</sub> NPs prepared by amine assisted sol-gel method [58]. TEM images, TEM size and XRD size results are gathered in Figure 14 and in Table 13. The molar ratio between structuring agent and hafnium tetrachloride is 1.

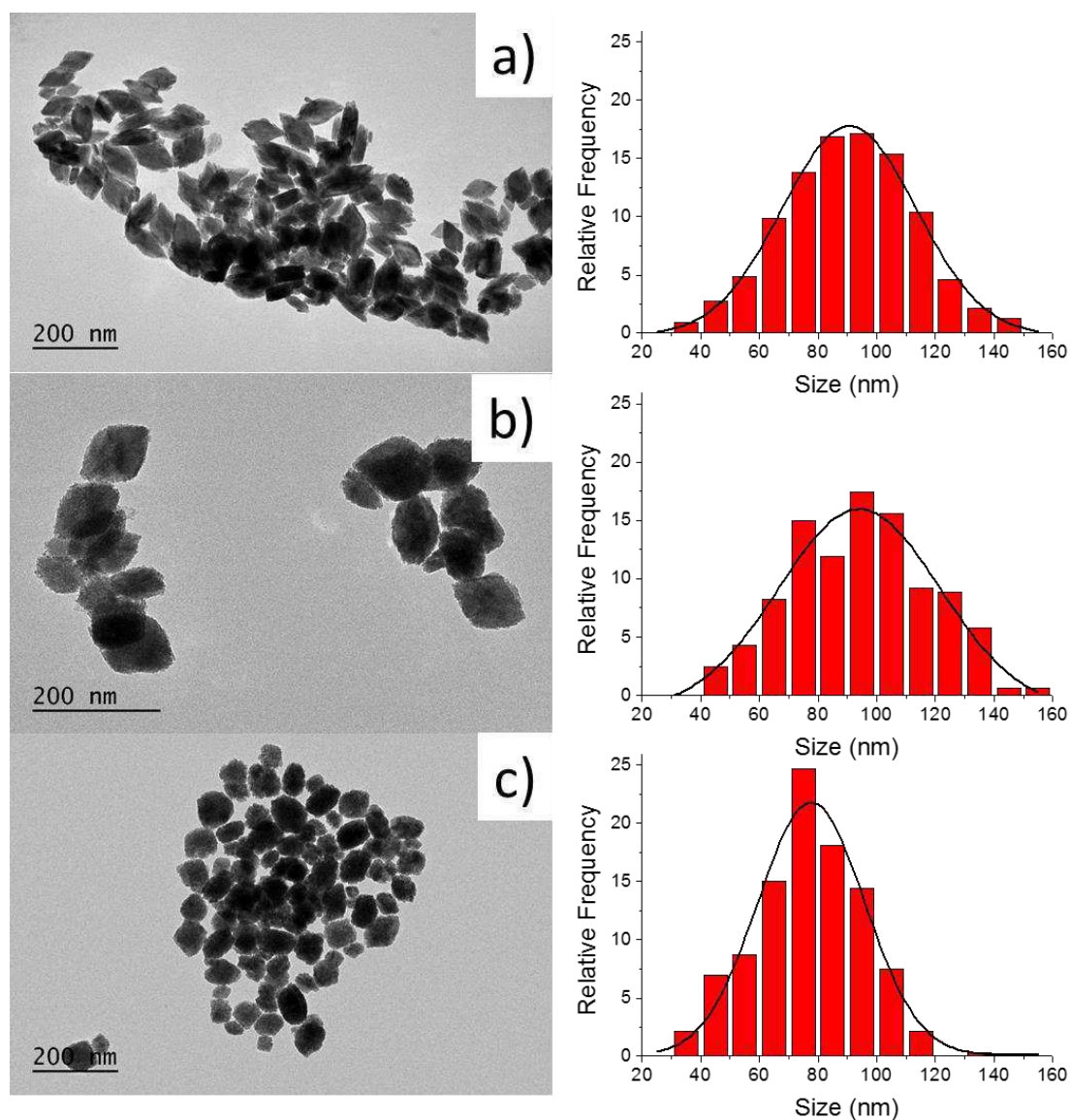


Figure 14: TEM pictures and size distribution for (a) trimethylamine, (b) succinic acid and (c) glutamic acid (pH 9.5, 48 h, 120 °C)

	trimethylamine	succinic acid	glutamic acid
TEM size (nm $\pm$ std)	91 $\pm$ 23	94 $\pm$ 27	77 $\pm$ 18
XRD size (nm)	20	36	23
Shapes	Rhombus, smooth	Rhombus, smooth	More spherical, smooth

Table 13: Syntheses using three different structuring agents (pH 9.5, 48 h, 120 °C)

None of these structuring agents seem to have the positive effect of citric acid on the cluster size reduction. Moreover, the shape of the nanoparticles synthesized with these structuring agents remains almost the same. Nevertheless, succinic acid and glutamic acid slightly

decrease the sharpness of the edges and angles of the rhombic shape leading to more spherical particles. We conclude that trimethylamine, succinic acid and glutamic acid have no effect on the synthesis of hafnium oxide nanoparticles.

The study of the structuring agents does not allow us to obtain nanoparticle size suitable for biological applications at 120 °C. Before focusing on rare-earth insertion, I will expound on HfO<sub>2</sub> characterization studies.

### III. 3. Characterization of HfO<sub>2</sub> nanoparticles

#### III. 3. a. Powder X-Ray diffraction

Although all samples were characterized by powder X-ray diffraction, here, I shall only exemplify the pattern of HfO<sub>2</sub> NPs synthesized at pH 9.5, 180 °C and for 48 hours (Figure 15).

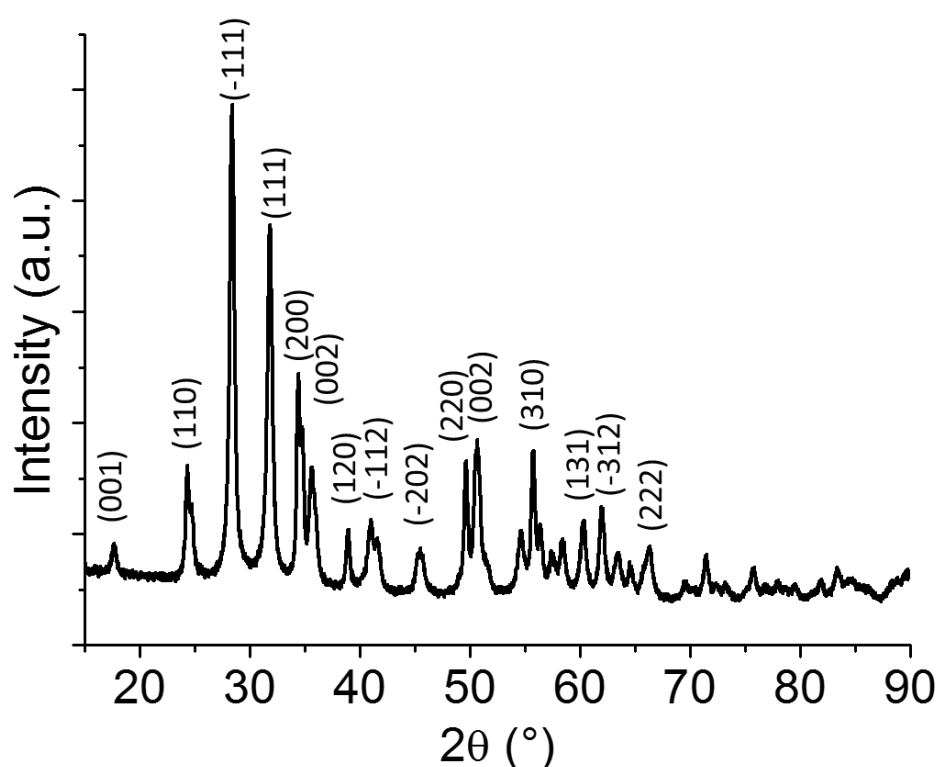


Figure 15: XRD pattern of HfO<sub>2</sub> nanoparticles synthesized at pH 9.5, 180 °C and for 48 hours

The pattern shows the characteristic reflections of monoclinic hafnium oxide (ICDD PDF no. 00-006-0318). Full pattern matching and Rietvelt refinement were performed using FullProf software, allowing the determination of the cell parameters. The parameters found are in agreement with those reported by Wang [4] and Zhao [7].

a (Å)	b (Å)	c (Å)	$\alpha$ (°)	$\beta$ (°)	$\gamma$ (°)
5.313	5.183	5.135	90.0	99.6	90.0

Thus, we conclude that the monoclinic structure is not too distorted and is relatively closed to the cubic structure. This observation is very relevant for the study of the insertion of lanthanides in HfO<sub>2</sub> matrices.

### III. 3. b. High Resolution Transmission Electron Microscopy

Figure 16 shows high resolution transmission electron microscopy (HRTEM) evidence on HfO<sub>2</sub> NPs synthesized at pH 9.5, 180 °C and for 48 hours. The HRTEM image clearly shows the atomic planes, with 5 Å in between (measured with ImageJ software, a value consistent with the cell parameter).

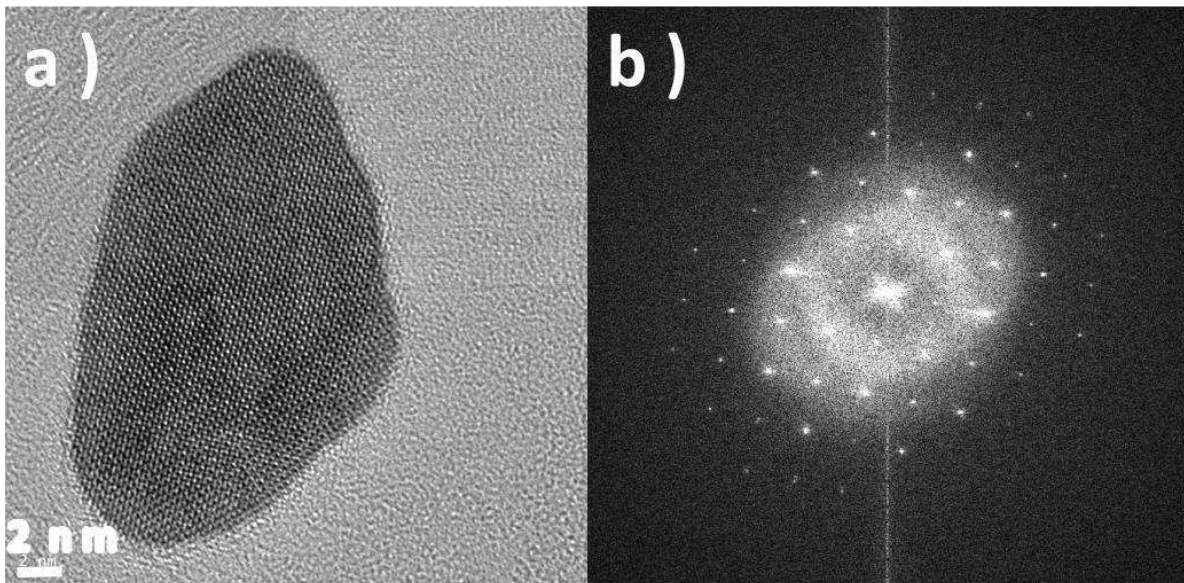


Figure 16: a) HRTEM picture of a single HfO<sub>2</sub> NP, b) fast Fourier Transform (FFT)

## III. 3. c. Zetametry

The isoelectric point of HfO<sub>2</sub> NPs was determined using Zetametry. Figure 17 and figure 18 show the result for HfO<sub>2</sub> NPs synthesized at pH 9.5 and for 48 hours and, respectively, 120 °C and 180 °C.

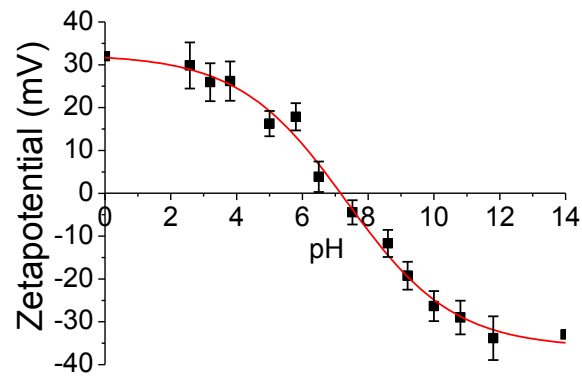


Figure 17: Zeta potential as a function of pH for HfO<sub>2</sub> synthesized at 120 °C, pH 9.5 and for 48 hours

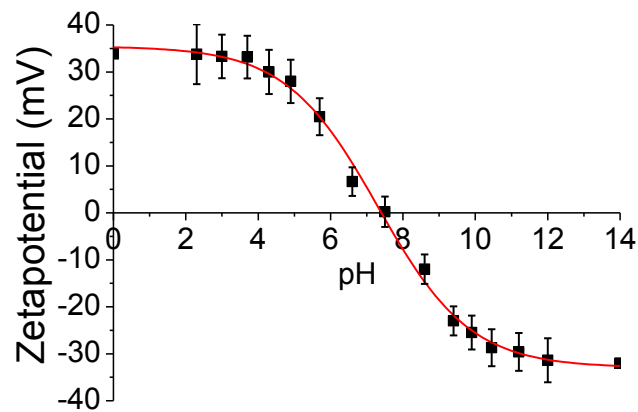


Figure 18: Zeta potential as a function of pH for HfO<sub>2</sub> synthesized at 180 °C, pH 9.5 and for 48 hours

The obtained curves were fitted with a sigmoidal function and, in both cases, the isoelectric point found to be 7.3. At first, this value may seem inconvenient because at physiological pH the particles will not be well dispersed. However, physiological media are much more complex than milliQ water.

## IV - Doping HfO<sub>2</sub> with lanthanides for tracking and imaging

In order to be able to track the NPs in human body, it is of interest to add in luminescence and magnetic properties, for example, by the insertion of rare-earth (RE) trivalent elements. As the sizes of these ions and tetravalent hafnium are not too different (table 14), the insertion of the former in the HfO<sub>2</sub> lattice is possible.

RE elements	Eu <sup>3+</sup>	Gd <sup>3+</sup>	Tb <sup>3+</sup>	Hf <sup>4+</sup>	Ti <sup>4+</sup>
Ionic radius (pm)	94.7	93.8	92.3	85	74.5

Table 14: Ionic radius of selected elements [59]

### IV. 1. Lanthanide mono doping

The insertion of trivalent lanthanides in the matrix of hafnium oxide has just begun to be investigated. Table 15 gathers the few papers I found on the insertion of europium and terbium in the matrix of hafnium oxide.

Starting material	T (°C) time (h) annealing	Ln precursor	[Ln]	TEM (nm)	XRD size (nm)	phase	ref
<b>Sol-gel synthesis</b>							
HfCl <sub>4</sub>	600 °C ? yes	EuNO <sub>3</sub>	0.5 mol% 3 mol% 5 mol%	500 – 5000	1000 – 2000	monoclinic	[60]
Hf(OEt) <sub>4</sub>	100 °C 24 h yes	EuNO <sub>3</sub> TbNO <sub>3</sub>	1 mol% 1 mol%	(-)	(-)	monoclinic	[61]
Hf(O <sup>t</sup> Bu) <sub>4</sub>	220 °C 96 h No	Eu(OAc) <sub>3</sub> Tb(OAc) <sub>3</sub>	0.01 mol% to 10 mol%	3 nm	< 3	monoclinic to cubic (> 5% Ln)	[62]
<b>Hydrothermal synthesis</b>							
HfOCl <sub>2</sub>	300 °C 3 h No	EuCl <sub>3</sub>	20 mol% 30 mol%	7 – 9	8 – 10	cubic	[43]
HfOCl <sub>2</sub>	200 °C 6 h Yes	EuCl <sub>3</sub>	5 mol% 10 mol% 15 mol%	4.3 nm	2.3 – 5.1	tetragonal	[63]
HfCl <sub>4</sub>	200 °C 80 min No	TbCl <sub>3</sub>	0 – 20 mol%	9 – 14	11.6	amorphous -> tetragonal	[45]
HfCl <sub>4</sub>	120 °C 72 h No	EuCl <sub>3</sub>	3 at%	800	(-)	monoclinic	[44]

Table 15: Methods to synthesize HfO<sub>2</sub> NPs doped with Eu and Tb

According to our goal, the insertion of lanthanides in the matrix of hafnium oxide nanoparticles was performed via hydrothermal synthesis starting from lanthanide trichloride and with the same conditions we have previously used to prepare pure hafnium oxide nanoparticles (*e.g.*, pH 9.5, 180 °C and 48 hours).

#### IV. 1. a. With europium (Eu<sup>3+</sup>)

Europium (III) chloride is added to an aqueous solution of hafnium tetrachloride and the pH is stabilized around 9.5. Then, the mixture is subjected to a hydrothermal treatment at 180 °C for 48 hours. These experimental conditions were chosen due to the study made before on the synthesis of HfO<sub>2</sub> NPs (*cf.* III. 2. d). Furthermore, the ratios were chosen according to the literature found on the insertion of RE elements in the hafnium dioxide matrix [41, 44].

The RE element compositions quoted in Table 16 are nominal values of molar percentages.

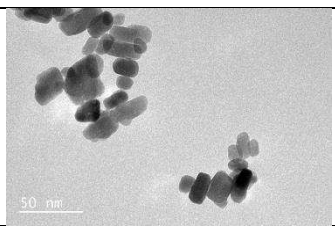
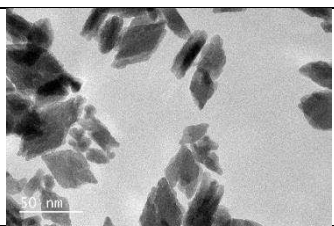
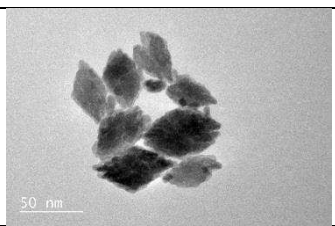
%Eu	0%	5%	10%
TEM images			
TEM size (nm±std)	24 ± 8	39 ± 9	47 ± 9
XRD size (nm)	20	21	21
Shapes	Rhombus, smooth	Rhombus, smooth	Rhombus, smooth

Table 16: Results of Eu<sup>3+</sup> insertion reaction at 180 °C for 48 hours at pH 9.5

Table 16 shows that the lanthanide insertion does not modify the shape of the NPs but slightly increases the TEM size (still in the required range for biological applications). Powder XRD (Figure 19) shows only the HfO<sub>2</sub> reflections, and no evidence for the formation of europium oxide. When europium ions are inserted the HfO<sub>2</sub> lattice expands due to the larger ionic radius of the lanthanide. Importantly, the individual reflections shift to smaller angles as the europium content increases, indicating that Eu<sup>3+</sup> is inserted in the HfO<sub>2</sub> lattice.

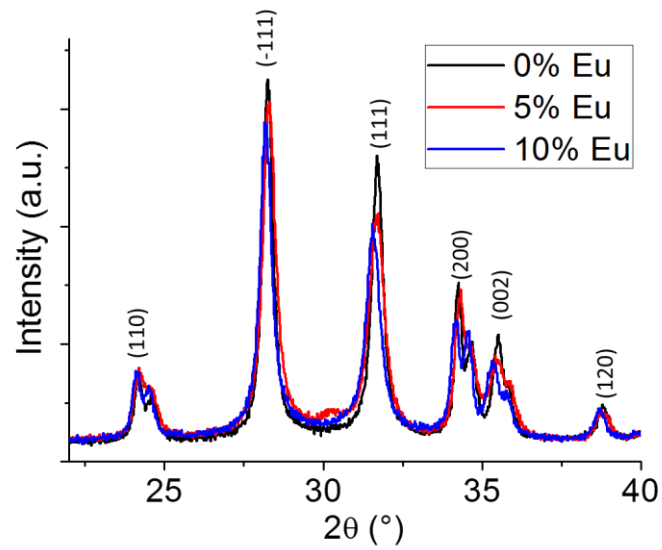


Figure 19: XRD patterns of HfO<sub>2</sub> NPs with and without Eu<sup>3+</sup>

#### IV. 1. b. With terbium (Tb<sup>3+</sup>)

The same study was performed using terbium as a doping element (Table 17, Figure 20)

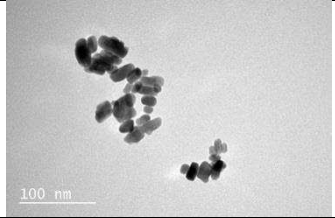
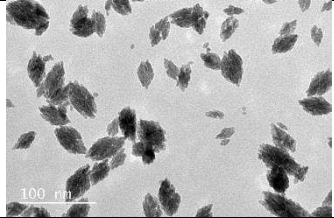
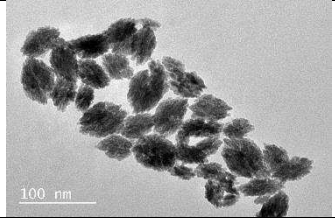
%Tb	0%	5%	10%
TEM images			
TEM size (nm±std)	24 ± 8	39 ± 12	41 ± 10
XRD size (nm)	20	15	13
Shapes	Rhombus, smooth	Rhombus, Almost smooth	Rhombus, Almost smooth

Table 17: Results of Tb<sup>3+</sup> insertion reaction at 180 °C for 48 hours at pH 9.5

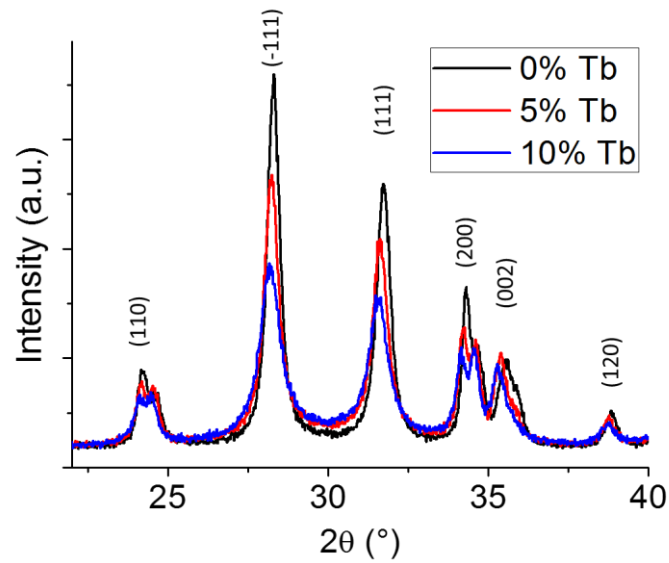


Figure 20: XRD pattern of HfO<sub>2</sub> NPs with and without Tb<sup>3+</sup>

Sample doped with 10% of terbium was further studied by energy-dispersive X-ray spectroscopy (EDS), in order to ascertain the RE distribution within hafnium oxide NPs (Figure 21). Clearly, terbium is evenly distributed across the particles, in a way similar to the hafnium distribution, supporting its insertion in the HfO<sub>2</sub> lattice.

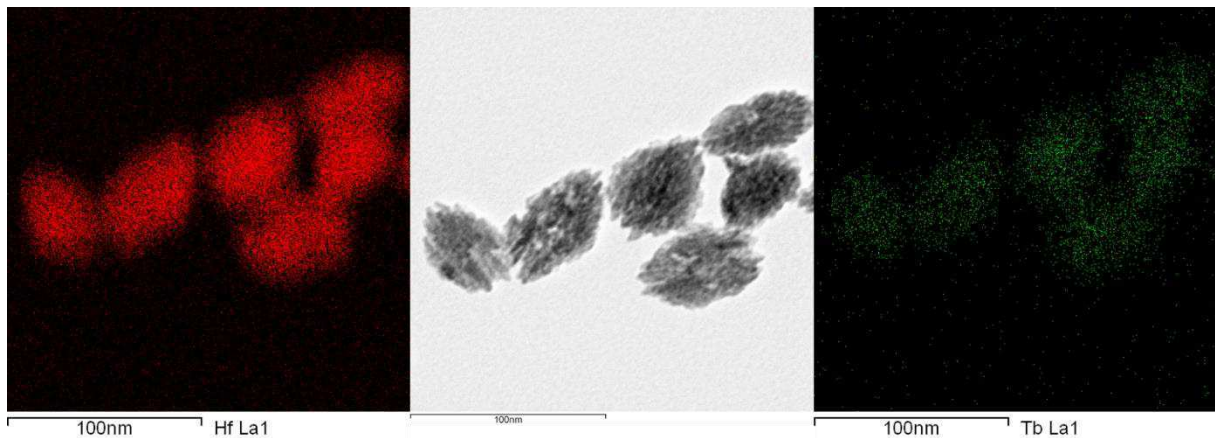


Figure 21: TEM pictures with hafnium mapping (left) and terbium mapping (right) obtained by EDS

Moreover, an analysis of the Tb and Hf distribution was made along the yellow line drawn on STEM image of a NP, in order to determine if the terbium was equally distributed inside the nanoparticle. Figure 22 shows that the distribution of hafnium is higher in the middle of the NP, which is normal because in TEM picture we analyze the projection of a NP. And we observed the same behavior for terbium distribution. Thus, we conclude that the terbium is randomly distributed inside the HfO<sub>2</sub> NPs.

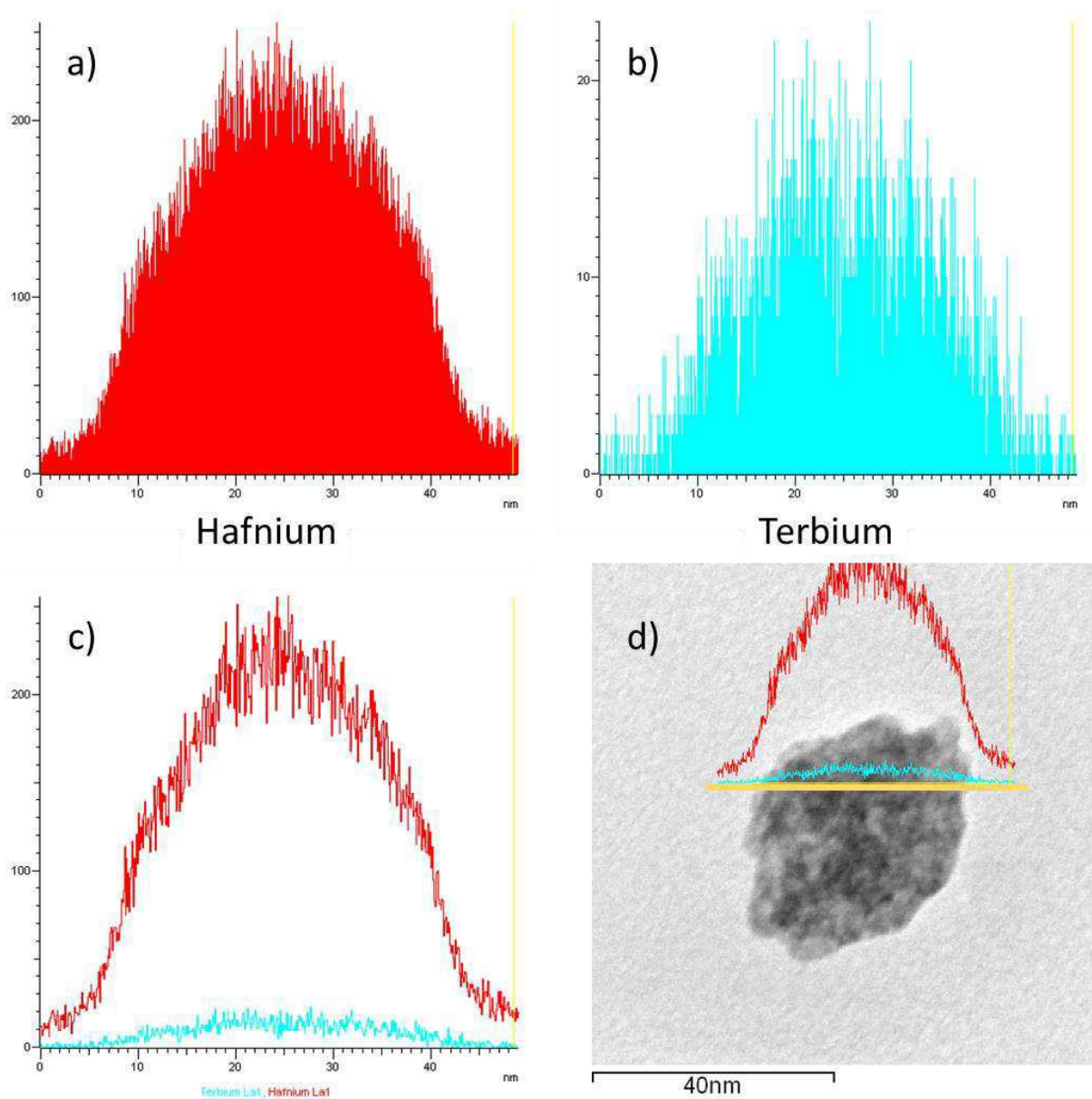


Figure 22: Distribution profiles of hafnium (a) and terbium (b) along the yellow line drawn on STEM image of a NP (d). (c) overlap of the two distributions

## IV. 2. Lanthanide bi-doping and tri-doping

### IV. 2. a. Synthesis challenges

In order to obtain NPs which can also behave as both nanothermometers and contrast agents in Magnetic Resonance Imaging (MRI), I have proceeded to dope HfO<sub>2</sub> NPs with europium, terbium (thermometry) and gadolinium (MRI). An additional requirement is the presence of a substantial amount of gadolinium so that its statistical presence on the periphery of the NP allows the detection of a MRI signal. Preliminary synthesis experiments with increasing amounts of RE in the HfO<sub>2</sub> matrix had also shown that there is a phase transition from monoclinic (ICDD PDF no.00-006-0318) to cubic (ICDD PDF no. 00-053-0560), as illustrated with europium (figure 23) and gadolinium (figure 24). These syntheses have also determined the RE amount that produces only a pure (cubic) phase.

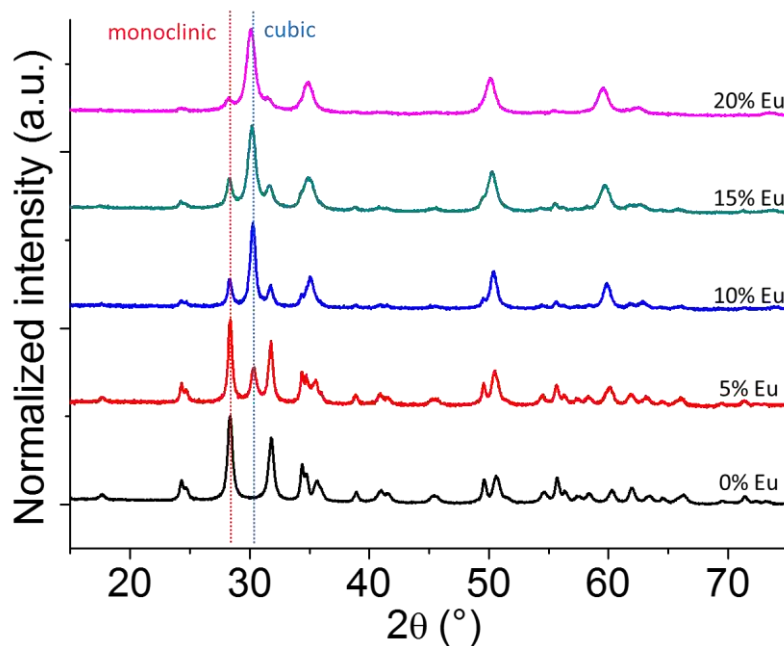


Figure 23: XRD patterns of HfO<sub>2</sub> nanoparticles increasing Eu<sup>3+</sup> molar content

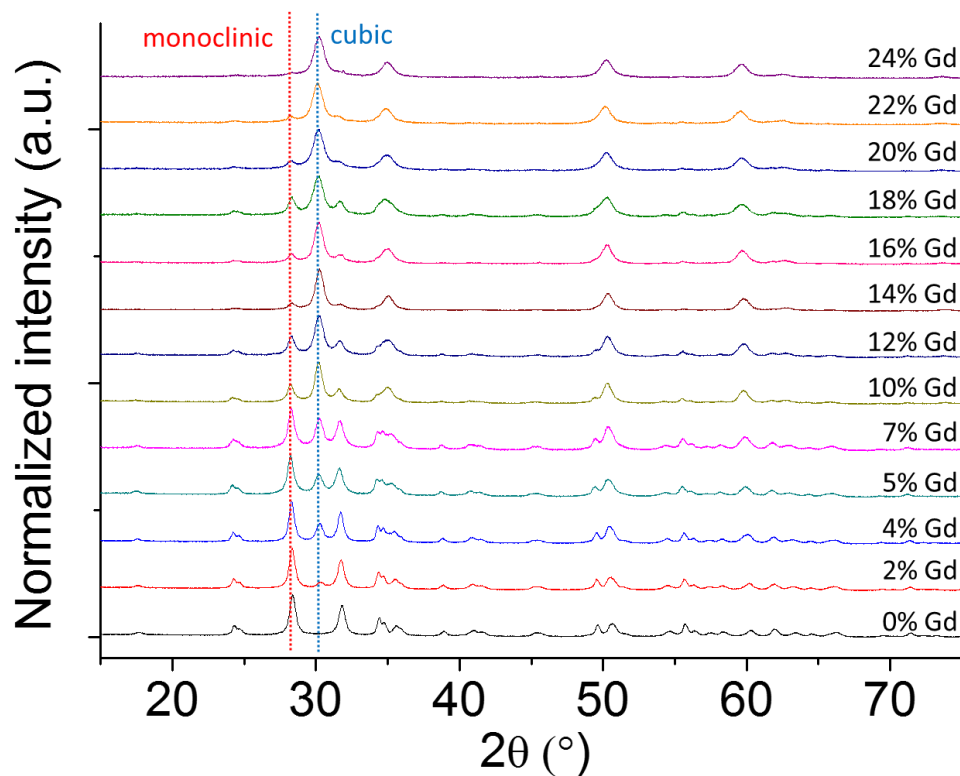


Figure 24: XRD patterns of HfO<sub>2</sub> nanoparticles with increasing Gd<sup>3+</sup> molar content

These diffractograms show a coexistence of two phases (monoclinic and cubic) for RE molar ratios below 20%. Above this value, only the cubic phase remains.

The stabilization of HfO<sub>2</sub> cubic phase by RE insertion had already been reported. For example, Lauria *et al.*, show the stabilization of cubic hafnium oxide upon europium and lutetium (1% Eu and 10% Lu) insertion [62].

Using the same hydrothermal synthesis, upon insertion of 20% Gd<sup>3+</sup> (or 15% Eu<sup>3+</sup>) into the HfO<sub>2</sub> matrix, the shape of the nanoparticles changed from rhombic to approximately spherical as observed by TEM (Figure 25 and Figure 26). This can be explained by the higher symmetry of the HfO<sub>2</sub> in the cubic phase.

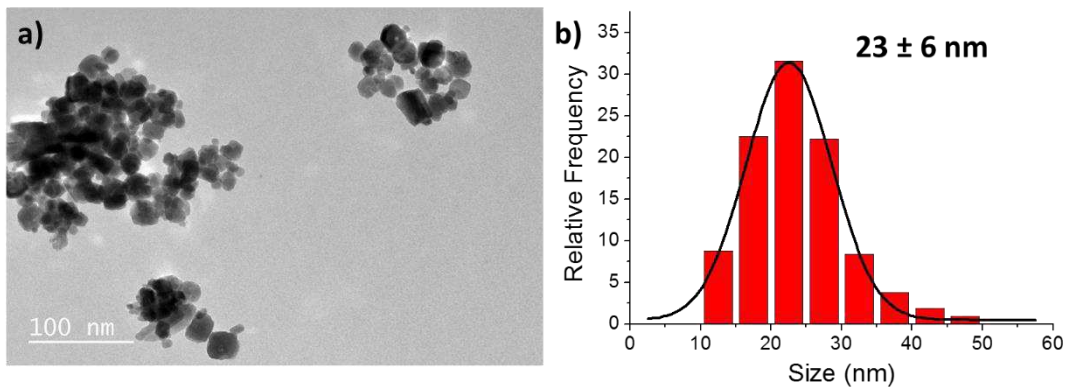


Figure 25: (a) TEM image of hafnium oxide nanoparticles synthesized at pH 9.5, 48h, and 180 °C with 15% of Eu<sup>3+</sup>, (b) Size distribution of NP diameter

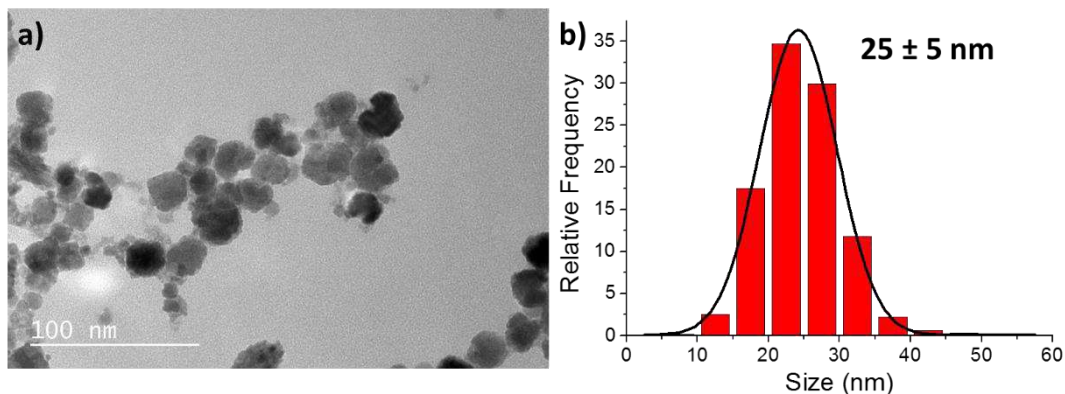


Figure 26: (a) TEM image of hafnium oxide nanoparticles synthesized at pH 9.5, 48h, and 180 °C with 20% of Gd<sup>3+</sup>, (b) Size distribution of NP diameter

Knowing that at least 20% RE doping is required to obtain the pure HfO<sub>2</sub> cubic phase, I proceeded to synthesize NPs doped with europium, terbium and gadolinium adding up to 20% of RE.

#### IV. 2. b. Europium, Terbium and Gadolinium for nanothermometry

I have succeeded in preparing three types of NPs with various amounts of europium, terbium and gadolinium, altogether adding up to 20% RE insertion. The synthesis parameters used were pH 9.5, 48 hours and 180 °C. The powder XRD patterns in Figure 27 confirm that the HfO<sub>2</sub> NPs crystallize in the cubic phase.

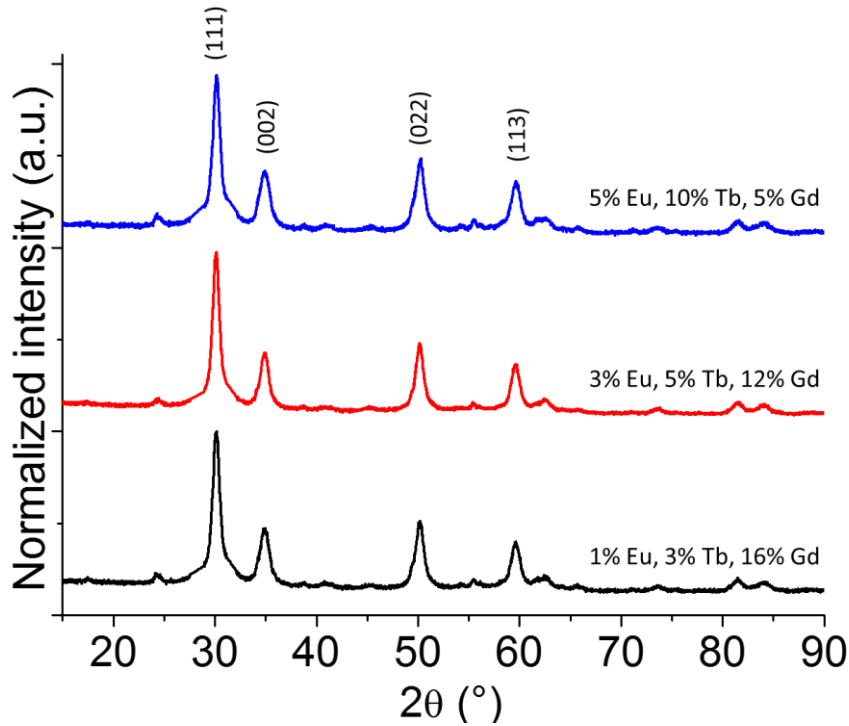


Figure 27: XRD patterns of HfO<sub>2</sub> NPs with RE amounts adding up to 20%

Moreover, the morphology of these NPs and 20% Gd<sup>3+</sup> doped NPs is the same (Figure 26(a)).

Figure 28 shows the TEM pictures of these NPs with their size distribution.

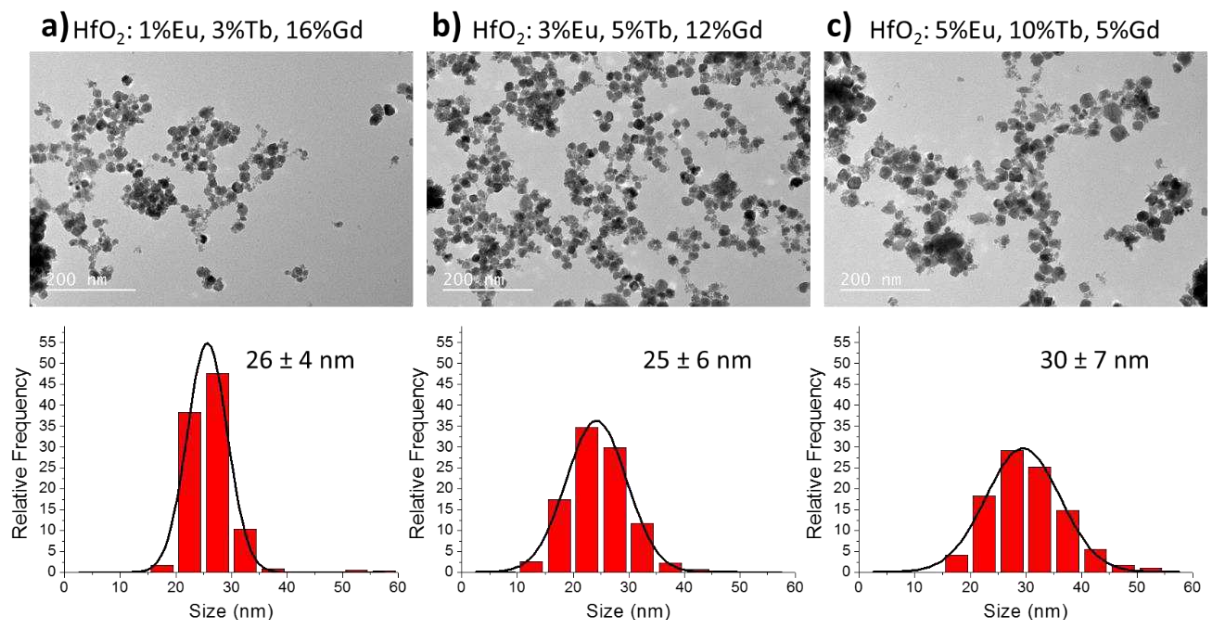


Figure 28: TEM pictures and size distribution of HfO<sub>2</sub> NPs doped with various amount of lanthanides (a) 1%Eu, 3%Tb, 16%Gd (b) 3%Eu, 5%Tb, 12%Gd (c) 5%Eu, 10%Tb, 5%Gd

Thus, spheroidal NPs are obtained with a size of 25 – 30 nm which is suitable for biomedical applications and comparable with the size of the TiO<sub>2</sub> NPs previously used.

Elemental analysis was performed in order to ascertain the nominal relative composition of lanthanides inserted in the hafnium oxide matrix (ICP results shown in Table 18).

	%Eu (theor.)	%Eu (ICP)	%Tb (theor.)	%Tb (ICP)	%Gd (theor.)	%Gd (ICP)
HfO <sub>2</sub> : 1%Eu, 3%Tb, 16%Gd	1	1.8	3	4.2	16	18.9
HfO <sub>2</sub> : 3%Eu, 5%Tb, 12%Gd	3	2.5	5	6.5	12	15.4
HfO <sub>2</sub> : 5%Eu, 10%Tb, 5%Gd	5	6.3	10	12.6	5	6.7

Table 18: Elemental analysis obtained by ICP (Inductively Coupled Plasma). The given percentages are molar percentages of lanthanides

The ICP results showed that the real lanthanides composition is slightly different from the nominal composition. However, the increase of europium and terbium and the decrease in gadolinium in molar percentage between these three samples are preserved. The amounts of gadolinium and terbium determined by ICP are always a bit higher than the nominal amounts. However, in the following chapters the following abbreviations will be used:

$\text{Eu}_{0.01}\text{Tb}_{0.03}\text{Gd}_{0.16}:\text{HfO}_2$  for HfO<sub>2</sub>: 1%Eu, 3%Tb, 16%Gd,

$\text{Eu}_{0.03}\text{Tb}_{0.05}\text{Gd}_{0.12}:\text{HfO}_2$  for HfO<sub>2</sub>: 3%Eu, 5%Tb, 12%Gd and,

$\text{Eu}_{0.05}\text{Tb}_{0.10}\text{Gd}_{0.05}:\text{HfO}_2$  for HfO<sub>2</sub>: 5%Eu, 10%Tb, 5%Gd

## Conclusion

The synthesis of HfO<sub>2</sub> NPs with a controlled size and morphology was accomplished. Moreover, our goal to reach a suitable size for ensuing biological applications was achieved by adjusting several parameters such as the pH and the reaction temperature. In acid or basic conditions, large nanoparticles (*ca.* 100 nm) were obtained with a small XRD size (5 – 10 nm). However, at pH 9.5, the nanoparticles were smaller (*ca.* 85 nm) with a larger XRD size (*ca.* 34 nm). The increase of the temperature allows the decrease of the size of the nanoparticles to 30 nm. Unlike TiO<sub>2</sub>, the structuring agents, I used, didn't have the same effect on the decrease of the size of the nanoparticles of HfO<sub>2</sub>. Furthermore, lanthanides were inserted in the hafnium dioxide matrix, thus leading to nanoparticles with several functionalities, such as the tracking via luminescence, the tracking via MRI, the temperature detection and the therapy. The following chapters aim at studying the luminescence of our nanoparticles as well as their potential applications as nanothermometers (chapter 4) and MRI contrast agents (chapter 5).

## Experimental part

The reagents are hafnium tetrachloride (HfCl<sub>4</sub>) purchased from Alfa Aesar, sodium hydroxide (NaOH) from Sigma Aldrich, and milliQ water. First, 1 g (3.1 mmol) of HfCl<sub>4</sub> is carefully added to 10 mL of water in a fume hood. In this step, 4 equivalent of hydrochloric acid is produced as a gas. Then, under continuous stirring, a 1 M solution of NaOH is added dropwise until reaching the required pH value. The volume is adjusted to 40 mL with distilled water. Then, the reaction mixture is stirred *for one hour at room temperature* and finally poured in a 50 mL Teflon container placed in a stainless steel autoclave in an oven (already at the setting temperature). After the reaction finishes and the autoclaves are cooled down to room temperature (out of the oven), the white mixture is subjected to centrifugation steps for 10 min at 9,000 rpm. The clear supernatant is finally removed and, after adding distilled water, the mixture is left for 10 min in an ultrasound bath. These two steps are repeated three times. This is a general procedure for all the reactions, only the pH, the temperature and the reaction time were changed.



Figure 29: Stainless steel autoclave (right) and the Teflon container (left)

The structuring agents are added just before the dissolution of HfCl<sub>4</sub> in water, and before adjusting the pH value. An aqueous solution of structuring agent is prepared with a molar ratio (1:1 structuring agent: HfCl<sub>4</sub>) and the HfCl<sub>4</sub> powder is added to this aqueous solution. Then, the reaction procedure is as described in the experimental part.

RE elements doping is carried out from RE(III) chloride precursors. The right amount is added just after the addition of hafnium tetrachloride to distilled water.

## Characterization methods

### ❖ Powder X-Ray diffraction (XRD)

The powder X-ray diffraction technique gives information on the crystalline phase of the nanoparticles and also on the crystallite size [64] [ENREF 17](#). The instrument used is a powder diffractometer PANalytical X'Pert Pro. The X-rays are produced by a copper source with wavelengths of 1.54056 Å and 1.54443 Å corresponding at K<sub>α</sub>. The X-rays are collected after transmission. Experimentally, the powder are crushed in an agate mortar with a pestle. Then, the fine powder is put on an aluminum support and finally flattened with a glass microscope slide. The diffractograms are then analyzed using Eva software and Fullprof.

The XRD technique is based on the elastic coherent diffusion (scattering) of the X-rays from the atoms present in the solid structure. The electronic clouds of the atoms act as scattering centers for the X-rays. The atoms of a crystalline material are arranged in a fixed regular geometry, inherent to the crystal. The distances between the atoms in the lattice are comparable to the wavelength of the X-rays. Therefore, constructive and destructive interference occur when the incident radiation interacts with the atoms of the sample. The condition of constructive interference is given by the Bragg's law:

$$2 d_{hkl} \sin \theta = n \lambda$$

Where  $n$  is the order of diffraction,  $\lambda$  is the wavelength of the incident radiation,  $d_{hkl}$  is the interplanar distance and  $\theta$  is the incident angle between the direction of the incoming radiation and the plans of the crystal lattice (Figure 30).

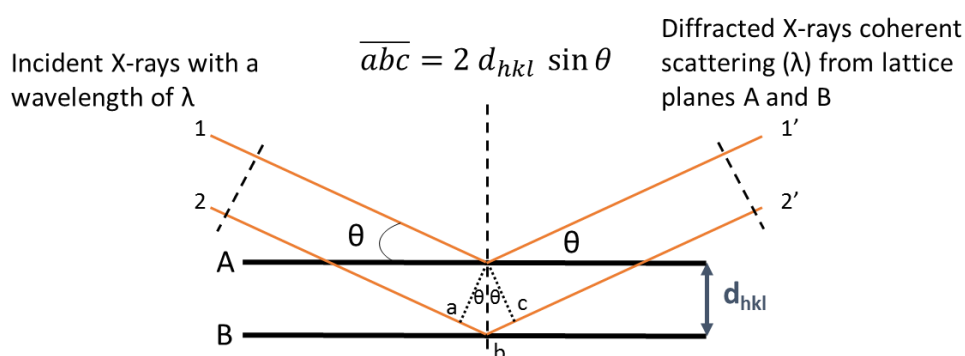


Figure 30: Geometric representation of Bragg's law

In the case of powders, all the scattered rays are simultaneously generated thanks to the random orientation of the crystal lattices of the single particles.

The primary information obtained from a diffraction pattern is the identification of the crystalline phase of a material, from which we can have indirect information on the unit cell. In the diffractogram, every single peak can be attributed to the respective lattice plan thanks to the nomenclature of the Miller's indices. The indices (h, k, l) define a plan that is orthogonal to the vector of the reciprocal lattice (Figure 31).

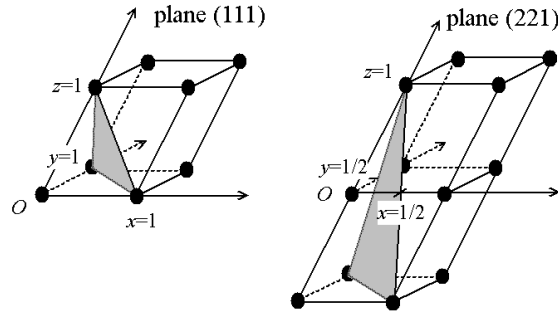


Figure 31: Determination of Miller's indices (hkl)

Through the XRD analysis it is also possible to determine the coherent length of the crystals, which constitute the powder. In the case of nanoparticles, the broadening of the peaks can be correlated to the average dimensions of the crystals through Scherer's formula [49]:

$$L = \frac{K \lambda}{\beta \cos \theta}$$

Where  $L$  is the average size of the crystalline domain,  $K$  is the geometrical factor linked to the cell's type [65] (its value is usually set as 0.89),  $\lambda$  is the wavelength of the X-rays radiation (1.54056 Å),  $\beta$  is the full-width-at-half-maximum of a peak, and  $\theta$  is the incident angle between the direction of the incoming radiation and the plans of the crystal lattice. This formula is applied to the peak with maximum intensity or to the two main peaks.

Using Scherer's formula we determined the crystallite size from the (-111) and (111) diffraction peaks. Let us focus on the (-111) diffraction peak of hafnium oxide nanoparticles synthesized at pH 9.5, at 120 °C for 48 hours. Furthermore, the measured full-width-at-half-maximum,  $\beta$ , can be related with the following formula:

$$\beta = \beta_O + \beta_G + \beta_L$$

Where  $\beta_O$  is the width due to instrumental optic defaults,  $\beta_G$  is the width related to the constraints (which are negligible) and  $\beta_L$  is the real full-width-at-half-maximum. Thus,

$$\beta_L = \beta - \beta_O$$

$\beta_0$  is given by the manufacturer following the formula:

$$\beta_0 = 0.15926 - 0.00444X + 9.03 \cdot 10^{-5}X^2 - 7.67571 \cdot 10^{-7}X^3 + 2.51295 \cdot 10^{-9}X^4$$

With  $X = 2\theta$  (°)

For the (-111) diffraction peak, the  $2\theta$  value is:

$$2\theta = 28.38^\circ, \text{ so } 2\theta = 0.495 \text{ rad}$$

$$\text{Hence, } \beta_0 = 0.090^\circ, \text{ so } \beta_0 = 0.00157 \text{ rad}$$

The full-width-at-half-maximum is:

$$\beta = 0.50^\circ, \text{ so } \beta = 0.0087 \text{ rad}$$

Thus, we can determine the crystallite size:

$$L = \frac{K \lambda}{\beta_L \cos(\theta)} = \frac{K \lambda}{(\beta - \beta_0) \cos(\theta)} = \frac{0.89 \times 0.154056}{(0.0087 - 0.00157) \times \cos\left(\frac{0.495}{2}\right)} = 20 \text{ nm}$$

#### ❖ Transmission Electron Microscopy (TEM)

To obtain information on NPs real size, on the size distribution and on the possible formation of aggregates, the samples were studied by Transmission Electron Microscopy (Figure 32). In Bordeaux, I have used: JEOL 1400Plus (accelerating voltage 120 kV) at PLAtforme de CAcractérisation des MATériaux (PLACAMAT) and HITACHI H7650 and in Aveiro, a HITACHI H9000 (accelerating voltage 300 kV). High Resolution Transmission Electron Microscopy (HRTEM) was performed on a JEOL 2200FS.

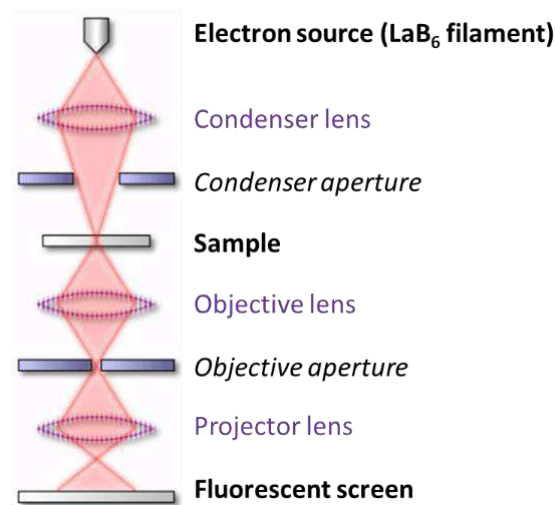


Figure 32: Schematic representation of a Transmission Electron Microscope

The transmission electron microscope is based on the detection of transmitted electrons when a focalized electron beam interacts with the sample. An electron gun (source of the electrons) with a narrow energy distribution in high vacuum is focused through a magnetic field on the sample via the condenser lens. The electrons interact with the sample placed on a sample holder. The electrons transmitted by the sample arrive on a fluorescent screen where the electron energy is turned into visible light allowing the visualization of the sample projection. HRTEM analysis allows the study of the material at the atomic scale. Thanks to the high resolution (0.05 nm), we have information on the distance between the lattice planes and on the crystalline phase of the products.

Drops of diluted dispersions of NPs are air-dried on carbon films deposited on 300-mesh copper grids. To determine, the size of the nanoparticles, more than 300 NPs are measured on several TEM pictures recorded for different regions on the TEM grid.

#### ❖ Dynamic Light Scattering (DLS)

The dynamic light scattering analysis allows the determination of the hydrodynamic diameter distribution of a suspension of particles. The instrument used is a Zetasizer Nano ZS commercialized by Malvern. The equipment makes use of non-invasive back scatter (NIBS) technology to perform particle size analysis in the range of 0.6 nm to 6 mm, according to the manufacturer.

DLS can be performed on a time scale measured in minutes rather than hours. In DLS, scattering intensity fluctuations are monitored across  $\mu\text{s}$  time scales and then correlated. The intensity fluctuations are a consequence of particle motion, and the measured property in the correlation analysis is the distribution of diffusion coefficients. The size is then calculated using the Stokes-Einstein equation:

$$R_h = \frac{k_B T}{6 \pi \eta D}$$

Where  $R_h$  is the hydrodynamic radius,  $k_B$  is the Boltzmann constant,  $T$  is the temperature,  $\eta$  is the solvent viscosity and  $D$  is the diffusion coefficient [66].

The hydrodynamic diameter obtained by DLS measurement is indicative of the apparent size of the hydrated/solvated particle (Figure 33). Thus, the hydrodynamic diameter is the value obtained adding the real diameter of the particle to the thickness of the solvation shell.

Moreover, if the particles are not spherical, rotational motion must be considered as well because the scattering of the light will be different depending on the orientation, and the measure of the hydrodynamic diameter is given by the diameter of the theoretical rounded particle whose diameter is close to the particle length. And, if the particles are aggregated the DLS analysis will measure the diameter of the aggregates.

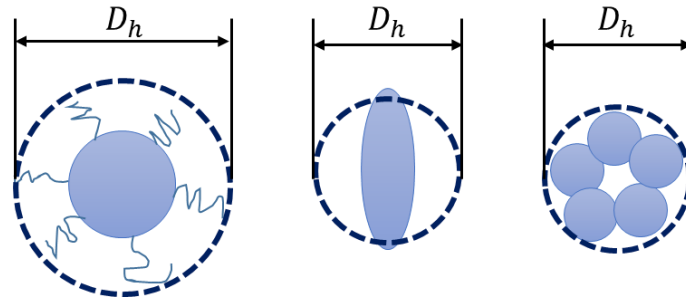


Figure 33: Representation of hydrodynamic diameter  $D_h$  calculated for different systems

#### ❖ Zetametry

The zeta potential analysis is performed on Zetasizer Nano ZS commercialized by Malvern.

The application of an electric field to charged particles placed in a liquid generates the mobility of these particles. This mobility can be quantified through an electrophoresis technique. The Zetametry allows to follow the movement of suspended particles when an electric field is applied. The electrophoretic mobility is related to the zeta potential. The zeta potential is the potential generated by the formation of the electric bilayer, responsible of the particle stability in suspension.

Briefly, zeta potential is the electrostatic potential which is localized very close to the surface of particles suspended in liquids [67]. Zeta potential ( $\zeta$ ) is responsible for particle-particle repulsion forces in suspensions. Figure 34 illustrates a particle suspended in a liquid. The slipping plane or shear plane is where the zeta potential is located versus the potential in the bulk solution. Within this slipping plane, the liquid is bound to the particle while it moves freely outside this boundary. The net potential far from the particle (in the bulk of the liquid) is zero.

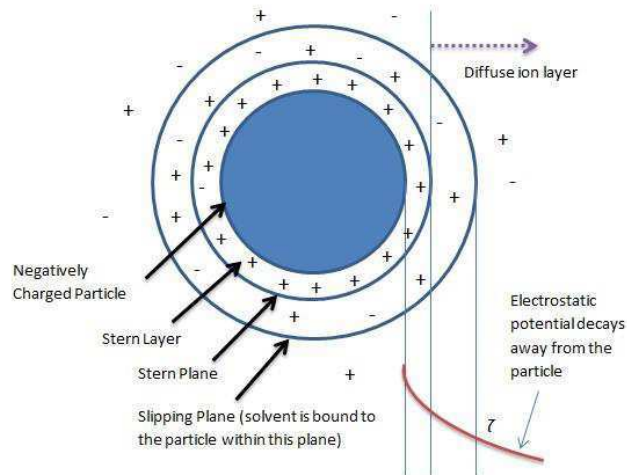


Figure 34: Representation of zeta potential of a negatively charged particle suspended in a liquid [67]

In aqueous media, zeta potential is typically generated when the ions on the particle surface dissociate, creating an electric charge close to the surface surrounded by a cloud of counterions. Various ion types can diffuse in and out through the slipping plane which allows the variation of zeta potential according to the ionic composition in the liquid depending on the pH value. Ions may also participate in chemical reactions within the slipping plane which can affect the zeta potential. Sample dilution can significantly shift the Zeta potential as ions may adsorb or desorb from the particle. Zeta potential can be positive or negative, or zero (Isoelectric point, IEP) depending on the liquid (solvent) pH or ion type and concentration [68].

Moreover, Henry's equation correlates the electrophoretic mobility and the zeta potential:

$$\mu_{\varepsilon} = \frac{2 \varepsilon \zeta f(ka)}{3 \eta}$$

Where  $\mu_{\varepsilon}$  is the electrophoretic mobility,  $\varepsilon$  is the permittivity of the media,  $\zeta$  is the zeta potential,  $f(ka)$  is the Henry's function and  $\eta$  is the viscosity. Two values are generally used as approximations for  $f(ka)$  determination. The value of 1.5 is used for an aqueous solution (Smoluchowski approximation), and 1.0 is used for a media with a low dielectric constant (Huckel approximation). Thus, the previous equation becomes:

$$\mu_{\varepsilon} = \frac{\varepsilon \zeta}{\eta}$$

Experimentally, hafnium oxide nanoparticles are prepared in a suspension of 300 mL of distilled water. This suspension is then separated in two. In the first one, sodium hydroxide is slowly added to increase, little by little, the pH value from neutral to higher value. And in the

second volume, nitric acid is also slowly added to progressively decrease the pH value from neutral to lower ones. Thus, sample solutions with different pHs are collected and ready for analysis. Thus, the curve of the zeta potential as a function of pH can be plotted.

#### ❖ Analyses of specific surface area (BET)

The measure of the specific surface area is based on the determination of the gaseous nitrogen volume necessary to form an adsorbed monolayer on the surface of the sample at 78 K. The adsorption is a surface phenomenon in which a liquid or gaseous molecule is fixed by Van der Waals interactions. The results are then analyzed by the model of Brunauer, Emmett and Teller (BET method). This model allows the determination of the specific surface area of the nanoparticles given in m<sup>2</sup>/g.

Knowing the amount  $n_m^a$  of nitrogen necessary to fill a molecular monolayer on the surface and the area  $\sigma_m$  occupied by a single adsorbed molecule ( $\sigma_m = 0.162 \text{ nm}^2$  at 77.4 K), it is possible to determine the specific surface area ( $a$ ) with the following equation [69]:

$$a = \frac{A}{m^s} = \left( \frac{n_m^a}{m^s} \right) N_A \sigma_m$$

where A is the area with a monolayer of nitrogen,  $m^s$  the adsorbate mass, and  $N_A$  the Avogadro constant.

#### ❖ Infrared spectroscopy (IR)

The Fourier transform infrared spectroscopy used was MIRacle 10 (single reflection ATR accessory) SHIMADZU. Through infrared spectroscopy, we can have information on the vibrational modes of the functional groups present in a molecule and sometimes also on the rotational modes, and thus on the nature of the analyzed product [70].

Infrared spectroscopy is an optic spectroscopy that is based on the interaction between the dipoles generated by the vibrations of the molecules and the electric field of light. An infrared photon hits the sample which absorbs the energy in a vibrational level, promoting the system from a fundamental vibrational state to an excited one. A molecule has a finite number of vibrational modes ( $3N-6$ , where N is the number of atoms) which depends on the geometry of the molecule. The selection rules define the nature of the active vibrational modes of the molecule.

## Bibliography

1. Hevesy, G., The Discovery and Properties of Hafnium. *Chemical Reviews* **1925**, 2 (1), 1-41.
2. Peacock, P.; Robertson, J., Band offsets and Schottky barrier heights of high dielectric constant oxides. *Journal of Applied Physics* **2002**, 92 (8), 4712-4721.
3. Miikkulainen, V.; Leskelä, M.; Ritala, M.; Puurunen, R. L., Crystallinity of inorganic films grown by atomic layer deposition: Overview and general trends. *Journal of Applied Physics* **2013**, 113 (2), 2.
4. Wang, J.; Li, H.; Stevens, R., Hafnia and hafnia-toughened ceramics. *J Mater Sci* **1992**, 27 (20), 5397-5430.
5. Huber, E. J.; Holley, C. E., Enthalpy of formation of hafnium dioxide. *Journal of Chemical & Engineering Data* **1968**, 13 (2), 252-253.
6. Perevalov, T.; Gritsenko, V.; Erenburg, S.; Badalyan, A.; Wong, H.; Kim, C., Atomic and electronic structure of amorphous and crystalline hafnium oxide: X-ray photoelectron spectroscopy and density functional calculations. *Journal of Applied Physics* **2007**, 101 (5), 053704.
7. Zhao, X.; Vanderbilt, D., First-principles study of structural, vibrational, and lattice dielectric properties of hafnium oxide. *Physical Review B* **2002**, 65 (23), 233106.
8. Ruh, R.; Garrett, H.; Domagala, R.; Tallan, N., The System Zirconia-Hafnia. *Journal of the American Ceramic Society* **1968**, 51 (1), 23-28.
9. Boganov, A.; Rudenko, V.; Makarov, L., X-ray Study of Zirconium and Hafnium Dioxides at Temperatures up to 2750 C. *Doklady Akademii Nauk SSSR (USSR) English translation currently published in a number of subject-oriented journals* **1965**, 160.
10. Zhu, H.; Tang, C.; Fonseca, L.; Ramprasad, R., Recent progress in ab initio simulations of hafnia-based gate stacks. *J Mater Sci* **2012**, 47 (21), 7399-7416.
11. Gritsenko, V.; Nasyrov, K.; Novikov, Y. N.; Aseev, A.; Yoon, S.; Lee, J.-W.; Lee, E.-H.; Kim, C., A new low voltage fast SONOS memory with high-k dielectric. *Solid-State Electronics* **2003**, 47 (10), 1651-1656.
12. Gritsenko, V.; Nasyrov, K.; Gritsenko, D.; Novikov, Y. N.; Aseev, A.; Lee, J.; Lee, J.-W.; Kim, C., A new memory element based on silicon nanoclusters in a ZrO<sub>2</sub> insulator with a high permittivity for electrically erasable read-only memory. *Semiconductors* **2005**, 39 (6), 716-721.
13. Wong, H.; Iwai, H., On the scaling issues and high-κ replacement of ultrathin gate dielectrics for nanoscale MOS transistors. *Microelectronic Engineering* **2006**, 83 (10), 1867-1904.
14. Wong, H.; Ng, K.; Zhan, N.; Poon, M.; Kok, C., Interface bonding structure of hafnium oxide prepared by direct sputtering of hafnium in oxygen. *Journal of Vacuum Science & Technology B: Microelectronics and Nanometer Structures Processing, Measurement, and Phenomena* **2004**, 22 (3), 1094-1100.
15. Sixteen Eco-Friendly, Faster and 'Cooler' Chips Incorporate 45nm Hafnium-Based High-k Metal Gate Transistors
16. Maggiorella, L.; Barouch, G.; Devaux, C.; Pottier, A.; Deutsch, E.; Bourhis, J.; Borghi, E.; Levy, L., Nanoscale radiotherapy with hafnium oxide nanoparticles. *Future Oncology* **2012**, 8, 1167-1181.
17. Marill, J.; Anesary, N. M.; Zhang, P.; Vivet, S.; Borghi, E.; Levy, L.; Pottier, A., Hafnium oxide nanoparticles: toward an in vitro predictive biological effect? *Radiation Oncology* **2014**, 9, 150/1-150/23.
18. Sherck, N. J.; Won, Y.-Y., A Simulation Study on the Feasibility of Radio Enhancement Therapy with Calcium Tungstate and Hafnium Oxide Nanoparticles. *arXiv preprint arXiv:1608.05302* **2016**.
19. Pottier, A.; Borghi, E.; Levy, L., New use of metals as nanosized radioenhancers. *Anticancer research* **2014**, 34 (1), 443-453.
20. Levy, L.; Pottier, A.; Rouet, A.; Marill, J.; Devaux, C.; Germain, M., Inorganic nanoparticles of high density to destroy cells in-vivo. Google Patents: 2014.
21. Pottier, A.; Borghi, E.; Levy, L., Metals as radio-enhancers in oncology: The industry perspective. *Biochemical and Biophysical Research Communications* **2015**, 468 (3), 471-475.
22. Jayaraman, V.; Bhavesh, G.; Chinnathambi, S.; Ganesan, S.; Aruna, P., Synthesis and characterization of hafnium oxide nanoparticles for bio-safety. *Materials Express* **2014**, 4, 375-383.
23. Dorvel, B. R.; Reddy, B.; Go, J.; Duarte Guevara, C.; Salm, E.; Alam, M. A.; Bashir, R., Silicon Nanowires with High-k Hafnium Oxide Dielectrics for Sensitive Detection of Small Nucleic Acid Oligomers. *ACS Nano* **2012**, 6 (7), 6150-6164.
24. Larkin, J.; Henley, R.; Bell, D. C.; Cohen-Karni, T.; Rosenstein, J. K.; Wanunu, M., Slow DNA Transport through Nanopores in Hafnium Oxide Membranes. *ACS Nano* **2013**, 7 (11), 10121-10128.

25. Lee, M.; Zine, N.; Baraket, A.; Zabala, M.; Campabadal, F.; Caruso, R.; Trivella, M. G.; Jaffrezic-Renault, N.; Errachid, A., A novel biosensor based on hafnium oxide: Application for early stage detection of human interleukin-10. *Sensors and Actuators B: Chemical* **2012**, *175* (Supplement C), 201-207.
26. Senthil Srinivasan, V. S.; Pandya, A., Dosimetry aspects of hafnium oxide metal-oxide-semiconductor (MOS) capacitor. *Thin Solid Films* **2011**, *520* (1), 574-577.
27. Nanobiotix: the independent data monitoring committee recommends the continuation of the ongoing phase II/III trial of NBTXR3 in soft tissue sarcoma. *Nanobiotix* March 23, 2017.
28. Ramadoss, A.; Krishnamoorthy, K.; Kim, S. J., Facile synthesis of hafnium oxide nanoparticles via precipitation method. *Materials Letters* **2012**, *75*, 215-217.
29. Tromp, R. M.; Hannon, J. B., Thermodynamics of Nucleation and Growth. *Surface Review & Letters* **2002**, *9* (3/4), 1565.
30. Ramadoss, A.; Krishnamoorthy, K.; Kim, S. J., Novel synthesis of hafnium oxide nanoparticles by precipitation method and its characterization. *Materials Research Bulletin* **2012**, *47* (9), 2680-2684.
31. Jayaraman, V.; Sagadevan, S.; Sudhakar, R., Studies on Optical and Electrical Properties of Hafnium Oxide Nanoparticles. *Journal of Electronic Materials* **2017**, 1-6.
32. Ramos-Gonzalez, R.; Garcia-Cerda, L. A.; Quevedo-Lopez, M. A., Study of the surface modification with oleic acid of nanosized HfO<sub>2</sub> synthesized by the polymerized complex derived sol-gel method. *Applied Surface Science* **2012**, *258*, 6034-6039.
33. Ramos-Gonzalez, R.; Garcia-Cerda, L. A.; Alshareef, H. N.; Gnade, B. E.; Quevedo-Lopez, M. A., Study of hafnium(IV) oxide nanoparticles synthesized by polymerized complex and polymer precursor derived sol-gel methods. *Materials Science Forum* **2010**, *644*, 75-78.
34. Tang, J.; Fabbri, J.; Robinson, R. D.; Zhu, Y.; Herman, I. P.; Steigerwald, M. L.; Brus, L. E., Solid-Solution Nanoparticles: Use of a Nonhydrolytic Sol-Gel Synthesis To Prepare HfO<sub>2</sub> and Hf<sub>x</sub>Zr<sub>1-x</sub>O<sub>2</sub> Nanocrystals. *Chemistry of Materials* **2004**, *16*, 1336-1342.
35. Cushing, B. L.; Kolesnichenko, V. L.; O'Connor, C. J., Recent Advances in the Liquid-Phase Syntheses of Inorganic Nanoparticles. *Chemical Reviews* **2004**, *104* (9), 3893-3946.
36. Niederberger, M.; Garnweitner, G.; Pinna, N.; Neri, G., Non-aqueous routes to crystalline metal oxide nanoparticles: Formation mechanisms and applications. *Progress in Solid State Chemistry* **2006**, *33*, 59-70.
37. Buha, J.; Arcon, D.; Niederberger, M.; Djerdj, I., Solvothermal and surfactant-free synthesis of crystalline Nb<sub>2</sub>O<sub>5</sub>, Ta<sub>2</sub>O<sub>5</sub>, HfO<sub>2</sub>, and Co-doped HfO<sub>2</sub> nanoparticles. *Physical Chemistry Chemical Physics* **2010**, *12*, 15537-15543.
38. Stefanic, G.; Molcanov, K.; Music, S., A comparative study of the hydrothermal crystallization of HfO<sub>2</sub> using DSC/TG and XRD analysis. *Materials Chemistry and Physics* **2005**, *90*, 344-352.
39. Štefanić, G.; Musić, S.; Molčanov, K., The crystallization process of HfO<sub>2</sub> and ZrO<sub>2</sub> under hydrothermal conditions. *Journal of Alloys and Compounds* **2005**, *387* (1-2), 300-307.
40. De Roo, J.; De Keukeleere, K.; Feys, J.; Lommens, P.; Hens, Z.; Van Driessche, I., Fast, microwave-assisted synthesis of monodisperse HfO<sub>2</sub> nanoparticles. *J Nanopart Res* **2013**, *15* (7), 1-11.
41. Elizariario, S. A.; Cavalcante, L. S.; Sczancoski, J. C.; Pizani, P. S.; Varela, J. A.; Espinosa, J. W. M.; Longo, E., Morphology and photoluminescence of HfO<sub>2</sub> obtained by microwave-hydrothermal. *Nanoscale Research Letters* **2009**, *4* (.), 1371-1379.
42. Meskin, P. E.; Sharikov, F. Y.; Ivanov, V. K.; Churagulov, B. R.; Tretyakov, Y. D., Rapid formation of nanocrystalline HfO<sub>2</sub> powders from amorphous hafnium hydroxide under ultrasonically assisted hydrothermal treatment. *Materials Chemistry and Physics* **2007**, *104*, 439-443.
43. Yoshimura, M.; Sōmiya, S., Hydrothermal synthesis of crystallized nano-particles of rare earth-doped zirconia and hafnia. *Materials Chemistry and Physics* **1999**, *61* (1), 1-8.
44. Ceron, E. N.; Rodriguez Gattorno, G.; Guzman-Mendoza, J.; Garcia-Hipolito, M.; Falcony, C., Photoluminescence response of HfO<sub>2</sub>:Eu<sup>3+</sup> obtained by hydrothermal route. *Open Journal of Synthesis Theory and Applications* **2013**, *2*, 73-77.
45. Montes, E.; Ceron, P.; Rivera Montalvo, T.; Guzman, J.; Garcia-Hipolito, M.; Soto-Guzman, A. B.; Garcia-Salcedo, R.; Falcony, C., Thermoluminescent characterization of HfO<sub>2</sub>:Tb<sup>3+</sup> synthesized by hydrothermal route. *Applied Radiation and Isotopes* **2014**, *83*, 196-199.
46. Sahraneshin, A.; Takami, S.; Hojo, D.; Minami, K.; Arita, T.; Adschiri, T., Synthesis of shape-controlled and organic-hybridized hafnium oxide nanoparticles under sub- and supercritical hydrothermal conditions. *The Journal of Supercritical Fluids* **2012**, *62* (0), 190-196.
47. Sahraneshin, A.; Asahina, S.; Togashi, T.; Singh, V.; Takami, S.; Hojo, D.; Arita, T.; Minami, K.; Adschiri, T., Surfactant-Assisted Hydrothermal Synthesis of Water-Dispersible Hafnium Oxide Nanoparticles in Highly Alkaline Media. *Crystal Growth and Design* **2012**, *12*, 5219-5226.

48. Ivanov, V. K.; Baranchikov, A. E.; Tret'yakov, Y. D., Crystallization of hydrous zirconia and hafnia during hydrothermal treatment. *Russian journal of inorganic chemistry* **2010**, *55* (5), 665-669.
49. Alexander, L. E.; Klug, H. P., *X-ray Diffraction Procedures for Polycrystalline and Amorphous Materials*. 1954.
50. Ramadoss, A.; Kim, S. J., Synthesis and characterization of HfO<sub>2</sub> nanoparticles by sonochemical approach. *Journal of Alloys and Compounds* **2012**, *544*, 115-119.
51. Denkewicz, R. P.; TenHuisen, K. S.; Adair, J. H., Hydrothermal crystallization kinetics of m-ZrO<sub>2</sub> and t-ZrO<sub>2</sub>. *Journal of Materials Research* **1990**, *5* (11), 2698-2705.
52. Dinh, C.-T.; Nguyen, T.-D.; Kleitz, F.; Do, T.-O., Shape-controlled synthesis of highly crystalline titania nanocrystals. *ACS Nano* **2009**, *3* (11), 3737-3743.
53. Yin, H.; Wada, Y.; Kitamura, T.; Kambe, S.; Murasawa, S.; Mori, H.; Sakata, T.; Yanagida, S., Hydrothermal synthesis of nanosized anatase and rutile TiO<sub>2</sub> using amorphous phase TiO<sub>2</sub>. *Journal of Materials Chemistry* **2001**, *11* (6), 1694-1703.
54. Davar, F.; Hassankhani, A.; Loghman-Estarki, M. R., Controllable synthesis of metastable tetragonal zirconia nanocrystals using citric acid assisted sol-gel method. *Ceramics International* **2013**, *39* (3), 2933-2941.
55. Liu, X.; Chen, Y.; Wang, L.; Peng, D.-L., Transition from paramagnetism to ferromagnetism in HfO<sub>2</sub> nanorods. *Journal of Applied Physics* **2013**, *113*, 076102/1-076102/3.
56. Song, P.; Chen, G.; Wei, Z.; Chang, Y.; Zhang, W.; Liang, J., Rapid crystallization of poly (l-lactic acid) induced by a nanoscaled zinc citrate complex as nucleating agent. *Polymer* **2012**, *53* (19), 4300-4309.
57. Jiang, B.; Yin, H.; Jiang, T.; Yan, J.; Fan, Z.; Li, C.; Wu, J.; Wada, Y., Size-controlled synthesis of anatase TiO<sub>2</sub> nanoparticles by carboxylic acid group-containing organics. *Materials Chemistry and Physics* **2005**, *92* (2), 595-599.
58. Hidalgo, M.; Aguilar, M.; Maicu, M.; Navío, J. A.; Colón, G., Hydrothermal preparation of highly photoactive TiO<sub>2</sub> nanoparticles. *Catalysis Today* **2007**, *129* (1), 50-58.
59. Shannon, R., Revised effective ionic radii and systematic studies of interatomic distances in halides and chalcogenides. *Acta Crystallographica Section A* **1976**, *32* (5), 751-767.
60. Wiatrowska, A.; Zych, E., Modeling Luminescent Properties of HfO<sub>2</sub>:Eu Powders with Li, Ta, Nb, and V Codopants. *The Journal of Physical Chemistry C* **2012**, *116*, 6409-6419.
61. Villanueva-Ibanez, M.; Le Luyer, C.; Dujardin, C.; Mugnier, J., Elaboration, structural and spectroscopic properties of rare earth-doped yttrium-hafnium sol-gel oxide powders for scintillation applications. *Materials Science and Engineering, B* **2003**, *B105*, 12-15.
62. Lauria, A.; Villa, I.; Fasoli, M.; Niederberger, M.; Vedda, A., Multifunctional Role of Rare Earth Doping in Optical Materials: Nonaqueous Sol-Gel Synthesis of Stabilized Cubic HfO<sub>2</sub> Luminescent Nanoparticles. *ACS Nano* **2013**, *7*, 7041-7052.
63. Taniguchi, T.; Sakamoto, N.; Watanabe, T.; Matsushita, N.; Yoshimura, M., Rational Hydrothermal Route to Monodisperse Hf<sub>1-x</sub>Eu<sub>x</sub>O<sub>2-x/2</sub> Solid Solution Nanocrystals. *The Journal of Physical Chemistry C* **2008**, *112* (13), 4884-4891.
64. Stout, G. H.; Jensen, L. H., *X-ray structure determination: a practical guide*. Macmillan New York: 1968; Vol. 2.
65. Langford, J. I.; Wilson, A., Scherrer after sixty years: a survey and some new results in the determination of crystallite size. *Journal of Applied Crystallography* **1978**, *11* (2), 102-113.
66. Berne, B. J.; Pecora, R., *Dynamic light scattering: with applications to chemistry, biology, and physics*. Courier Corporation: 1976.
67. Hunter, R. J., *Introduction to modern colloid science*. Oxford University Press: 1993.
68. An overview of the zeta potential. Particle sciences Drug development services: 2012.
69. Rouquerol, F.; Luciani, L.; Llewellyn, P.; Denoyel, R.; Rouquerol, J., Texture des matériaux pulvérulents ou poreux. *Techniques de l'ingénieur. Analyse et caractérisation* **2003**, *2* (P1050), p1050. 1-p1050. 24.
70. Siesler, H. W.; Ozaki, Y.; Kawata, S.; Heise, H. M., *Near-infrared spectroscopy: principles, instruments, applications*. John Wiley & Sons: 2008.



# Chapter 4: Optical imaging and nanothermometry



## Table of contents

Introduction.....	153
I - Luminescence imaging background .....	153
I. 1. Optical imaging.....	153
I. 2. Luminescence principles .....	155
I. 2. a. Excitation and emission spectra .....	155
I. 2. b. Perrin-Jablonski diagram .....	156
I. 2. c. Up-conversion phenomenon .....	158
I. 3. Lanthanide luminescence.....	159
I. 3. a. Discrete <i>f-f</i> transition.....	159
I. 3. b. Broad energy bands.....	160
I. 3. c. <i>f-d</i> transition .....	160
I. 4. Thermometer applications .....	161
I. 4. a. Principles.....	161
I. 4. b. Single center nanothermometers .....	162
I. 4. c. Multicenter nanothermometry .....	163
II - Mono doping of HfO <sub>2</sub> with lanthanide .....	168
II. 1. Europium (Eu <sup>3+</sup> ) insertion.....	168
II. 2. Terbium (Tb <sup>3+</sup> ) insertion .....	172
III - Nanothermometry applications.....	174
III. 1. Excitation spectra .....	174
III. 2. Temperature dependence of the luminescence.....	176
III. 3. Integrated intensity .....	177
III. 4. Experimental thermometric parameter .....	179
III. 5. Relative sensitivity.....	180
Conclusion .....	181

Characterization method ..... 182  
Bibliography..... 183

## Introduction

HfO<sub>2</sub> nanoparticles (NPs) doped with trivalent lanthanide ions, such as europium, terbium and gadolinium, were prepared in chapter 3, and in this chapter their luminescence properties are studied. I start by presenting briefly some basic ideas of lanthanide based luminescence. Then, the luminescence properties of NPs doped with Eu<sup>3+</sup> and Tb<sup>3+</sup> are discussed and, lastly, I show that NPs co-doped with Eu<sup>3+</sup>, Tb<sup>3+</sup> and Gd<sup>3+</sup> perform as ratiometric luminescence nanothermometers.

### I - Luminescence imaging background

#### I. 1. Optical imaging

Over the last decade, optical imaging techniques have attracted much interest because they can image tissue anatomy, physiology, metabolic and molecular function. Their main advantage is the detection of luminescent dyes at low concentration and the use of non-ionizing and harmless radiation. Thus, the design of objects for *in vivo* optical imaging of tumor tissues has been attracting many researchers [1]. The data may be collected in several ways, reflectance, transillumination, tomography and diffuse pattern (Figure 1). In reflectance, the excitation light (input) impinges on the object surface and the luminescence light (output) is collected on the same side of the object (Figure 1a). In transillumination, the object is illuminated on the opposite side of the data collection, so that the light propagates through the object (Figure 1b). Figure 1c shows an illustration of data collection where multiple point source transillumination data are time-shared around a cylindrical geometry. Different geometries and the use of reflected data can also be used for tomographic purposes. The direction indicated by the arrows shows the general photon trajectory established. The pattern of collected data is diffusive, as is evidenced from the experimental measurements shown in Figure 1d obtained from a transilluminated homogeneous diffusive cylinder.

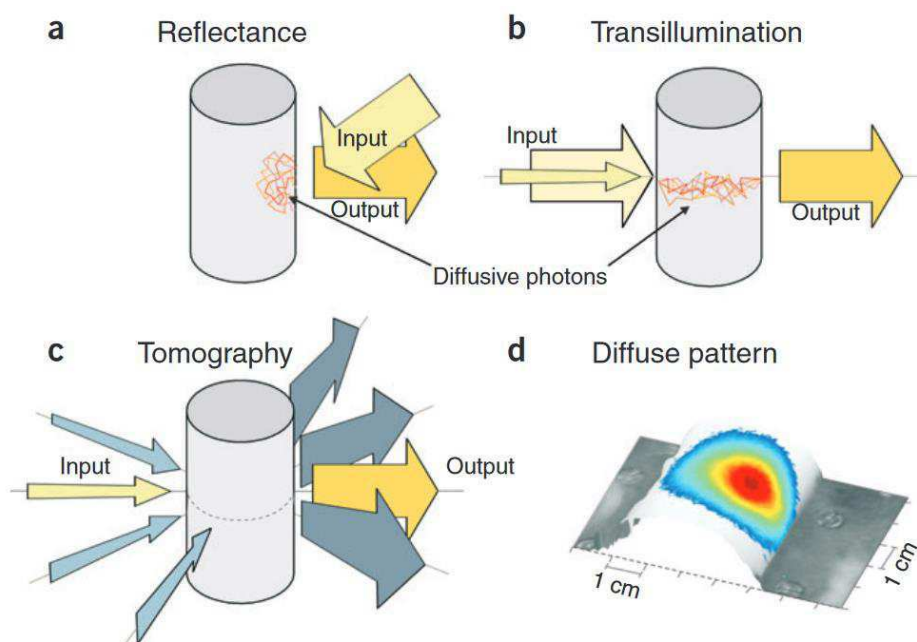


Figure 1: Modes of data collection for optical imaging [1]

Light is one of the most convenient vectors for transmitting signals, and when well-chosen wavelengths are used the penetration depth can be substantial and light can easily reach regions with a complex molecular structure, not accessible to other messengers.

Among the studied NPs, semiconductor quantum dots (QDs) are potential candidates for imaging as they are highly luminescent, tunable in the entire visible range, and are much more photostable than the organic luminophores. Quantum dots have been exploited for both *in vitro* and *in vivo* imaging [2-6]. Another type of luminescent acting as imaging systems are those based on trivalent lanthanide ions ( $\text{Ln}^{3+}$ ), which feature easy spectral and time discrimination of their emission bands, and cover the visible and NIR (Near Infrared) spectral ranges. Lanthanide ions are widely studied and can be found in homogeneous time-resolved luminescent assays [7-10], optimization of bioconjugation methods for lanthanide luminescent chelates [11-12], and time-resolved luminescence microscopy [13-14] that resulted in applications of lanthanides luminescent bioprobes (LLBs) [11, 15] in many fields of biology, biotechnology and medicine including tissue [16-18] and cell imaging [19-20], analyte sensing [21] and monitoring drug delivery [22].

In order to design optical nanoparticles, it is important to be aware of the basic luminescence concepts and ideas and, thus, these are here briefly reviewed.

## I. 2. Luminescence principles

The phenomena involving energy absorption and subsequent light emission are classified generically under the term of luminescence. Excitation by absorbance of a photon leads to a class of important luminescent species, which fluoresce or phosphoresce. In general, fluorescence is “fast” (ns time scale) while phosphorescence is “slow” (time scale up to hours or days). Fluorescence is used for processes, occurring without change in spin, typically  $S_1 \rightarrow S_0$  (singlet to singlet ground state) or  ${}^2F_{5/2} \rightarrow {}^2F_{7/2}$  ( $\text{Yb}^{3+}$ ) transitions. Phosphorescence pertains transitions involving a change in spin, most commonly  $T_1 \rightarrow S_0$  (triplet to singlet ground state) [23]. The energy used in the excitation of luminescent materials gives rise to a classification of luminescence processes, such as: photoluminescence, when the excitation is performed by electromagnetic radiation; cathodoluminescence, when a beam of electrons is used; electroluminescence, when excitation comes from an electric voltage; triboluminescence, when a mechanical energy is the source of excitation; and chemiluminescence, when the energy of a chemical reaction is generating the luminescence [24]. Thus, the luminescence is the emission of light occurring from electronically excited states that have been populated by an external excitation source to a fundamental state [25].

### I. 2. a. Excitation and emission spectra

Figure 2 shows typical excitation and emission spectra of a luminescent dye. These spectra are generated by a spectrofluorimeter, which includes two spectrometers: an illuminating one and an analyzing one. First, the sample is irradiated at a given wavelength causing some fluorescence. A luminescent emission spectrum is obtained by scanning with the analyzing spectrometer using this fixed illumination wavelength. The analyzer is then fixed at the brightest emission wavelength, and an excitation spectrum is obtained by scanning with the illuminating spectrometer and measuring the variation in emission intensity at this fixed wavelength.

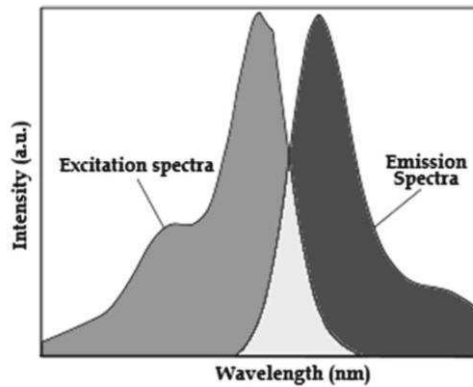


Figure 2: Typical excitation and emission spectra for a luminescent dye [26]

### 1. 2. b. Perrin-Jablonski diagram

To describe the processes subsequent to light absorption by an emitting center, it was found convenient to use an energy diagram in which the electronic states of the emitting center are represented together with arrows indicating the possible transitions between them, the Perrin-Jablonski diagram [27]. Figure 3(a) shows a simplified Perrin-Jablonski diagram while the figure 3(b) shows a more complete diagram.

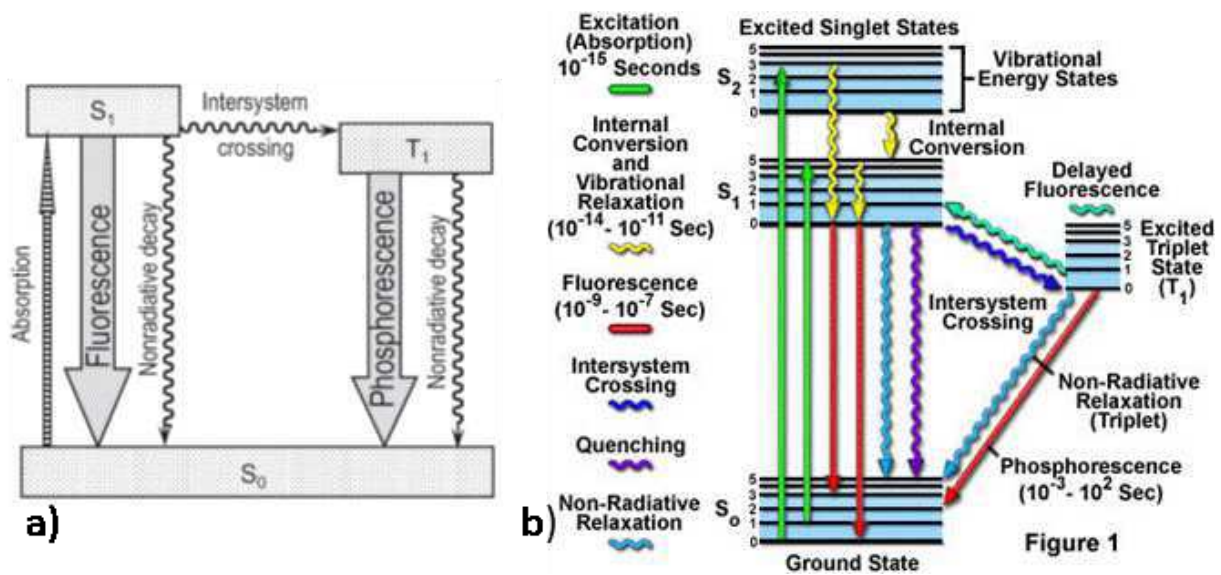


Figure 3: (a) simplified [28] and (b) complete [29] Perrin-Jablonski diagram

The Perrin-Jablonski diagram describes several possibilities for an electron to go back to the ground state, such as quenching, non-radiative relaxation, fluorescence, internal conversion and vibrational relaxation, intersystem crossing and phosphorescence. The different possibilities are detailed in the following parts.

### I. 2. b. i. Radiative transition

The radiative transition consists of absorption of the emitted light from a donor molecule or ion by the acceptor species. For such a transfer to take place, the emission of the donor has to coincide with the absorption of the acceptor. Energy levels should be close enough to allow absorption and then emission. The discrepancy between the positions of the band maxima of absorption and emission spectra of the same electronic transition leads to a Stokes shift [30]. Moreover, the difference between absorption and emission wavelength is described as Stokes shift (Figure 4a). The shift for the transition within  $4f$  shell results from the fact that the absorption and emission takes place between different levels. Usually, absorption corresponds to the transition from ground state to higher excited states. Electrons in the higher excited state then lose energy to the lattice until the state lying just below the previous excited states is available. When the difference between the adjacent states is large, the energy corresponding to this transition cannot be transferred to the lattice and it is given out in the form of emission. The emission, thus, corresponds to the transition from the intermediate state to the ground state.

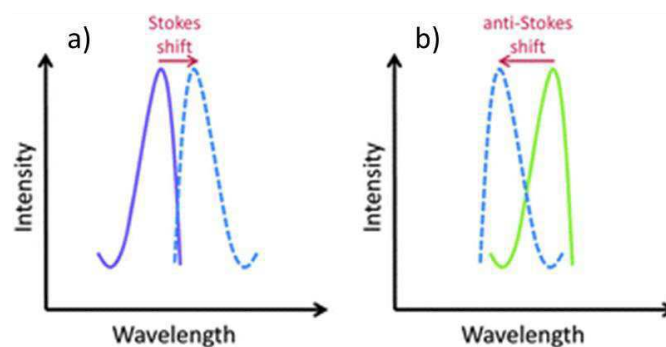


Figure 4: Schematic illustration of (a) the Stokes (down-conversion) and (b) anti-Stokes (up-conversion) shifts. Solid and dotted lines represent absorption and emission spectra respectively [30]

### I. 2. b. ii. Non-radiative transition

Not all materials exhibit luminescence even if their molecules or atoms can be excited to a higher state. This is due to the existence of a non-radiative pathway in the return to the ground state, such as internal conversion or non-radiative relaxation (Figure 3). The energy absorbed by the materials, which is not emitted as radiation is dissipated to the crystal lattice in a solid. The population of an excited state and the energy difference between the ground state and excited states are important factors affecting the luminescence of a material. And, it is crucial to decrease these radiationless processes competing with the radiation process.

### I. 2. b. iii. Multiphonon relaxation

In condensed-matter physics, a phonon is a unit of vibrational energy arising from oscillating atoms within a crystal. Multiphonon relaxation is a well-understood process for lanthanide ions. Excited electronic levels of lanthanides in solids decay non-radiatively by exciting lattice vibrations (phonons). When the energy gap between the excited level and the next lower electronic level is larger than the phonon energy, several lattice phonons are emitted, in order to bridge this energy gap. The most energetic vibrations are responsible for the nonradiative decay since such a process can conserve energy in the lowest order [31].

### I. 2. c. Up-conversion phenomenon

Up-conversion is the phenomenon whereby one or more photons of lower energy are absorbed by a material and re-emitted as a higher energy photon (Figure 4b). Materials with these properties (called up-converters) can be tuned to respond to near infrared energy and emit a range of photon energies at visible wavelengths. Thus, they can be used to detect particles in the human body, which is transparent to infrared. A major type of up-converters is based on lanthanides doping of various metals oxides or fluorides [32-33]. Up-conversion in such materials can occur by several mechanisms [32, 34] that rely on a multitude of accessible excited states of the different lanthanide cations. The general diagram in Figure 5 summarizes some of the absorption-emission processes leading to up-conversion. The vertical arrows represent absorption or emission of a photon, while the curved arrows represent energy transfer between species (usually ions).

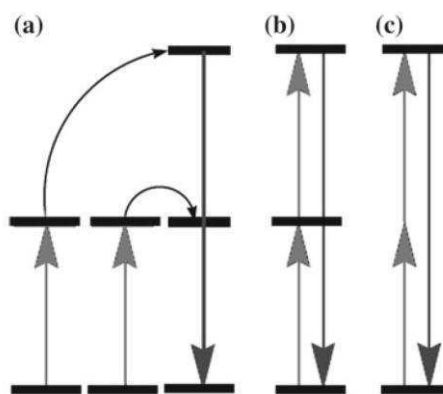


Figure 5: Simplified representation of some upconversion processes(adapted from [34])

- Mechanism (a) is the most common in lanthanide systems: each of two photo-excited lanthanide ions (same, or different, element), transfers energy to a third ion, which emits from the higher energy state. Ytterbium ( $\text{Yb}^{3+}$ ) is commonly used as a primary

absorber of input photoradiation, which transfers energy to emitter ions, commonly erbium ( $\text{Er}^{3+}$ ) and thulium ( $\text{Tm}^{3+}$ ) [33]. The energy transfer upconversion efficiency is surprisingly high, and of the three mechanisms shown in Figure 5 this is the most efficient one.

- In (b), the initial absorption leads to an intermediate excited state, which lies long enough to allow ready absorption of a second photon to give a higher excited state (called 2-step absorption). Emission from this state produces a higher energy upconverted photon. This process is about two orders of magnitude less efficient than (a).
- Mechanism (c) is a two-photon absorption, this time without a real intermediate excited state. This implies a simultaneous absorption of two photons, which inevitably has a lower probability, and the mechanism is thus much less efficient.

### I. 3. Lanthanide luminescence

Lanthanide atoms lie within the sixth row of the periodic table. Lanthanide ions are usually trivalent. Electronic configuration of trivalent lanthanide ions is considered as a singularity since it features an unfilled  $4f$  shell, partially screened from the environment by the electrons in the  $5s^2$  and  $5p^6$  shells (except for  $\text{La}^{3+}$  and  $\text{Lu}^{3+}$ ). Ions corresponding to configurations  $4f^0$  ( $\text{La}^{3+}$ ),  $4f^7$  ( $\text{Gd}^{3+}$ ), and  $4f^{14}$  ( $\text{Lu}^{3+}$ ) are stable. Lanthanides next to these three ions tend to exchange electron and acquire this stable configuration. To understand the luminescent properties of lanthanide ions, it is necessary to consider their energy levels. The energy level may be divided into several categories; the two main ones correspond to  $4f^n$  configuration and to  $4f^{n-1}5d$  configuration.

Due to the partial electronic shielding of the  $4f$  orbitals by the filled  $5s^2$  and  $5p^6$  subshells, the emission lines of lanthanide ions are typically very narrow and the corresponding lifetimes are relatively long, from a few microseconds to a few milliseconds [25].

#### I. 3. a. Discrete $f$ - $f$ transition

The number of discrete  $4f$  energy levels is large, except for  $\text{Ce}^{3+}$  and  $\text{Yb}^{3+}$ . For instance,  $\text{Gd}^{3+}$  has as many as 327 levels of  $4f$  configuration. Usually only the level relevant to photoluminescence that can be excited by UV light are mentioned and other levels are ignored. The transitions within  $4f$  shells are strictly forbidden, because the parity does not change. However, some forbidden transitions can be observed due to the fact that the

interactions of the lanthanide ions with crystal field or with the lattice vibrations can mix states of different parities into  $4f$  states (selection rules of Laporte [35]). Vibronic transitions of lanthanide ions [36] are due to the coupling of the  $4f^n$  states with the vibrational mode of the lattice.

### I. 3. b. Broad energy bands

In addition to the discrete  $4f$  levels, broad bands are usually present and play an important role in excitation. Two groups of bands can be defined. In the first group, one of the  $4f$  electrons raises to the higher  $5d$  levels (I. 3. c). The second group comprises charge transfer bands, between electrons from the host matrix to the energy levels of the lanthanide ions.

### I. 3. c. $f-d$ transition

$4f^{n-1}5d$  levels may be understood as formed by the electron in the  $5d$  orbital interacting with  $4f^{n-1}$  core. As a consequence of this strong crystal field effect on the  $5d$  electron,  $4f^{n-1}5d$  configurations of lanthanide ions in solids are very different from those of free ions.  $4f^n \rightarrow 4f^{n-1}5d$  absorption of most of the lanthanide (+3) and lanthanide (+2) ions exhibit two features. First, they consist of strong bands corresponding to the components of  $5d$  orbital split in the crystal field. Consequently, their spectra are similar when ions are embedded in same types of host. Second, the structures of  $5d$  bands can be fitted to energy differences in the ground multiplets of the  $4f^{n-1}$  configurations.

For most of the trivalent lanthanide ions, transitions from configuration  $4f^n$  to  $4f^{n-1}5d$  correspond to wavenumbers exceeding  $50\,000\text{ cm}^{-1}$  (below  $< 200\text{ nm}$ ) and thus not accessible to UV excitation. Exceptions are  $\text{Ce}^{3+}$  and  $\text{Tb}^{3+}$  for which these transitions are accessible to UV excitation. The Table 1 compares the characteristics of  $f-f$  and  $f-d$  transitions.

	<i>f-f</i>	<i>f-d</i>
<b>Electric dipole oscillator strength</b>	$10^{-6}$	$10^{-1} - 10^{-2}$
<b>Ion lattice coupling</b>	weak	strong
<b>Emission wavelength</b>	200 – 500 nm	150 – 1000 nm
<b>Line width</b>	$10\text{ cm}^{-1}$	$>1000\text{ cm}^{-1}$
<b>Lifetime</b>	$10^{-2} - 10^{-5}\text{ s}$	$10^{-8} - 10^{-6}\text{ s}$

Table 1: Comparison of  $f-f$  and  $f-d$  transition of lanthanides [26]

## I. 4. Thermometer applications

### I. 4. a. Principles

Luminescence nanothermometry exploits the relationship between temperature and luminescence properties to achieve thermal sensing from the spatial and spectral analysis of the generated light [37]. Six parameters are known to define the emission of a given material: intensity, band-shape, spectral position, polarization, lifetime and bandwidth. These six parameters can be modified with temperature, increasing or decreasing, as shown in figure 6 and thus different nanothermometry classes can be defined [37].

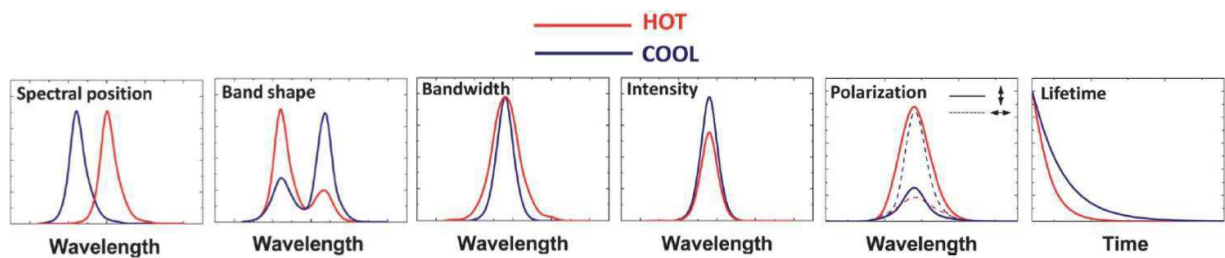


Figure 6: Schematic representation of the possible effects caused by a temperature increment on the luminescence. Red lines correspond to higher temperatures [37].

Band shape luminescence can be achieved following two main schemes. In the first approach, luminescence bands are generated by different emitting centers so that the temperature-induced band-shape change arises either from the different thermal quenching of each center or from the thermally induced changes in the energy transfer rates among these centers. In contrast, in the second approach, the different bands are generated by a unique luminescence center and the band shape modifications is generally caused by a thermally-induced redistribution of the population among the different levels of the unique emitting center. One advantage of this band-shape nanothermometer type compared to the intensity one is the independence between relative luminescence intensity and local concentration of emitting centers [25]. Here are some examples of nanothermometers found in the literature: based on QDs [38-41], carbon nanotubes [42-49], metal-organic frameworks [50-55]. Moreover, the mechanism of lanthanide band shape nanothermometer depends on whether the luminescence bands under analysis are generated by a single type of lanthanide (called single center) or by a combination of different lanthanides (called multi center).

#### I. 4. b. Single center nanothermometers

The lanthanide luminescence intensity depends on several parameters among which temperature is a most critical one. A large number of mechanisms may link the luminescence intensity with the temperature including: the activation of the multiphonon decay probability, the activation of the energy transfer between lanthanide ions or quenching centers, the population redistribution due to Boltzmann statistics, presence of phonon-assisted conversion processes and thermal enhancement of energy transfer processes between lanthanide ions and the host levels or charge transfer states [25]. A profusion of mechanisms can influence the thermal dependency of intensity of each emission, such as fluctuations in the concentration of NPs, and the power of the excitation. Thus, not all the lanthanide ions can be used for this kind of nanothermometry but only those possessing radiative states with an energy gap around a few hundred of nm (4 – 12 eV). The lanthanides used are: neodymium ( $\text{Nd}^{3+}$ ) [56], thulium ( $\text{Tm}^{3+}$ ) [57], europium ( $\text{Eu}^{3+}$ ) [58], erbium ( $\text{Er}^{3+}$ ) [56, 59-60], dysprosium ( $\text{Dy}^{3+}$ ) [61] and ytterbium ( $\text{Yb}^{3+}$ ) [57].

Suzuki *et al.* reported an example of thermometer depending on the intensity luminescence based on europium to detect a temperature increase in HeLa cells after changing the extracellular  $\text{Ca}^{2+}$  concentration. This system was able to detect in real time intracellular temperature variations as small as 1 °C in the biophysical range [62]. Another example of nanothermometer based on one emission intensity can be found in the work by Peng using  $\text{Y}_2\text{O}_3$  NPs doped with europium ions [63]. He described the decrease of the emission intensity associated with the  ${}^5D_0 \rightarrow {}^7F_2$  transition to an increase of the temperature in the 10 – 300 K range when the NPs were excited at 580 nm. Instead, when the system was pumped at 488 nm, the emission intensity increased with increasing the temperature, reaching a maximum at *ca.* 550 K, and then decreased for higher temperatures. The explanation for these differences, proposed by the authors, was the modification that the excitation wavelength can trigger in the dynamics, population density and thermally activated electron distribution of the energy states. Indeed, this is a proof of the complicated behavior of the thermal dependence of emission intensities of lanthanide ions. Nevertheless, for applications in which the excitation can be standardized and the concentration of NPs is highly controlled, thermometry based on the measurements of the luminescence intensity ratio between more than one lanthanide ion has also been investigated.

### I. 4. c. Multicenter nanothermometry

One of the most common techniques to sense temperature using lanthanides ions is in fact based on the modifications of the intensity of the luminescence. However, instead of using a single emission line as explained above, a second emission band is used as a reference to take advantage of a ratio of intensities. The use of two bands can solve the fluctuations due to a modification of NPs concentration or excitation power density reaching the sample. However, the complicated dynamics of lanthanide ions usually involve more than one temperature-dependent phenomenon, such as non-resonant energy transfer or multiphonon relaxation (*cf.* I. 2. b). Thus, it is difficult to predict and control the behavior of the luminescence spectra due to their complexity, which affect the various emitting levels.

In order to define a reliable intensity ratio, Luminescence Intensity Ratio (LIR) technique has been set up, and is since then the most widespread strategy for thermometry involving lanthanide ions [37]. The LIR technique is based on the intensity ratio between two different energy levels that are thermally coupled, meaning that both levels are separated by an energy gap small enough to allow the promotion of electrons to the upper state using thermal energy. Thus, as both levels are close to each other, the non-radiative relaxation from the upper level to the lower one has higher probability to occur. Hence, both states are related and share the electronic population in such a way that the intensity ratio between their emissions is independent of the excitation source and of the fluctuations in concentrations, enabling a reliable system to sense temperature.

The emission probability for each energy level depends on many different parameters but one of the most crucial parameters is the energy gap between the lanthanide energy levels (*e.g.* level 1 and level 2 with a higher energy). If this gap is small and comparable to the thermal energy  $k_B T$ , where  $k_B$  is the Boltzmann constant and  $T$  is the temperature (K), then it is not possible to populate a single level since, due to the Boltzmann statistics, the population is redistributed among energy levels with similar energy. Thus, the population of the high-energy state  $N_2$  is given by:

$$N_2 = N_1 \exp\left(\frac{-\Delta E}{k_B T}\right) \quad (1)$$

where  $N_1$  is the population of level 1 and  $\Delta E$  is the energy gap between levels 1 and 2. As both states are populated, there are two contributions to the overall luminescence spectrum with

two bands at different energies. The intensity of the band corresponding to the de-excitation from level  $i$  down to the ground state,  $I_i$  is given by:

$$I_i = c_i(\nu)A_i g_i h\nu_i \times N_i = \varphi_i N_i \quad (2)$$

where  $h$  is the Plank's constant,  $A_i$  is the spontaneous emission rate of the level,  $g_i$  its degeneracy and  $c_i(\nu)$  is the response of the detection system at the emission frequency  $\nu_i$ .

$\varphi_i$  is a constant with a value which depends on a great amount of geometrical factors as well as on intrinsic properties of the emitting level such as branching ratios and luminescence quantum efficiency. The ratio between intensities of level 1 and level 2 is:

$$\frac{I_2}{I_1} = \frac{\varphi_2 N_2}{\varphi_1 N_1} = \frac{\varphi_2}{\varphi_1} \exp\left(\frac{-\Delta E}{k_B T}\right) = B \exp\left(\frac{-\Delta E}{k_B T}\right) \quad (3)$$

and, the experimental determination of the intensity ratio can lead to temperature determination. An appreciable thermal sensitivity is achieved only if the energy gap between emitting levels is small in order to induce large population redistribution with small temperatures changes. The last equation (equation (3)) is used in the LIR techniques to thermally calibrate a system [64]. The constant  $B$  depends on the experimental system and on spectroscopic parameters of the material:

$$B = \frac{c_2(\nu)A_2 g_2 h\nu_2}{c_1(\nu)A_1 g_1 h\nu_1} \quad (4)$$

The dependence of this constant on the detection system can make the method less exploitable. However, the two energy states involved are close in energy, so the approximation  $c_2(\nu) \nu_2 / c_1(\nu) \nu_1 \sim 1$  holds [65]. Hence, the main parameters influencing  $B$  are the spontaneous emission rate, which generally depends on the host, and the degeneracy of the level, which varies with the symmetry of the optical centers [66].

The two levels involved in LIR should have the following characteristics [67-69]:

- An energy gap between the two states smaller than  $2000 \text{ cm}^{-1}$  ( $< 0.25 \text{ eV}$ ) is required to allow the thermal coupling and a high population in the upper level.
- Due to the need of good resolution between the selected lines, the energy gap should be higher than  $200 \text{ cm}^{-1}$  ( $> 0.02 \text{ eV}$ )
- For both states involved, the luminescence intensity should be high to ensure easy detection of the optical signal.

Lanthanide ions with appropriate states for thermometry based on LIR are Er<sup>3+</sup>/Yb<sup>3+</sup> [70-73] Eu<sup>3+</sup>/Tb<sup>3+</sup> [50-51, 74].

The absolute sensitivity,  $S$ , of a thermal probe is given by:

$$S = \frac{d(LIR)}{dT} = B \exp\left(\frac{-\Delta E}{k_B T}\right) \times \frac{\Delta E}{k_B T^2} = LIR \times \frac{\Delta E}{k_B T^2} \quad (5)$$

Sensitivity is indicative of the performance of the sensor. As shown, in equation (5), the sensitivity depends on the LIR value at each temperature and, thus, both  $B$  and  $\Delta E$  influence it. Due to the lanthanide ion properties, with the valence electrons shielded from the environment, the effect of the crystal field is weak, meaning that large variations in these two parameters,  $B$  and  $\Delta E$ , are not expected. Thus, the absolute sensitivity cannot be compared between two systems. This is the reason why, to compare several systems, a relative sensitivity has been defined as follows:

$$S_r(T) = \frac{1}{\Delta} \left| \frac{\partial \Delta}{\partial T} \right| \quad (6)$$

Li and coworkers studied the effect of the size and shape of NPs on the sensitivity of the sensor based on NaYF<sub>4</sub> co-doped with Er and Yb. The authors investigated bulk powders (0.8-1.2 μm), nanowires (4.8 μm – 140 nm), nanorods (1.1 μm – 140 nm), and nanoplates (48 – 62 nm) and their relative sensitivities, following 980 nm excitation. The highest sensitivity was observed at 393 K for all morphologies with a value of 0.45 × 10<sup>-3</sup> K<sup>-1</sup> for the nanoplates [75]. Alencar studied the size effect of NPs based on Er<sup>3+</sup>-doped BaTiO<sub>3</sub> on 980 nm excitation and showed that the particle size played an important role, due to the number of carbonate and hydroxyl ions adsorbed on the surface of the nanocrystals. Smaller NPs were found to possess a lower thermal sensitivity. The effect of size and shape of NPs doped with Er on the sensitivity was investigated [76]. However, it is possible to use different host materials or different lanthanide ions to change the value of  $B$  and  $\Delta E$  and impact the sensitivity. For example, in the case of ions such as Nd<sup>3+</sup>-based NPs, the intensity ratio was defined between two Stark components, the <sup>4</sup>F<sub>3/2</sub> → <sup>4</sup>I<sub>9/2</sub> transition was the one exploited in ratiometric nanothermometry [77]. Wawrzynczyk *et al.* synthesized Nd<sup>3+</sup>-doped NaYF<sub>4</sub> and by ratiometrically calculating the changes in the two Stark level emission intensities at 863 and 870 nm, they were able to develop a ratiometric temperature correlation over the range of 0 – 150 °C with a thermal sensitivity of 0.1% K<sup>-1</sup> [77]. Rocha *et al.*, investigated the development of a Nd<sup>3+</sup>

nanothermometer, using  $\text{LaF}_3$  as a host. Opting for a core-shell architecture ( $\text{LaF}_3:\text{Nd}^{3+}@\text{LaF}_3$ ), the thermometer was established by monitoring the 863 and 885 nm emissions (from two different Stark levels) to give an intensity ratio, achieving a thermal resolution of 2 °C in the temperature range from 10 to 60 °C [71, 78].

Another relevant example is the use of the intensity ratio between europium and terbium. For instance, the luminescent thermometer consisting of terbium ( $\text{Tb}^{3+}$ ) and europium ( $\text{Eu}^{3+}$ ) co-doped  $\gamma\text{-Fe}_2\text{O}_3$  nanoparticles [50-51] is designed to show an excited triplet state with energy slightly above that of the  $\text{Tb}^{3+}$   $^5\text{D}_4$  emitting state. Moreover, the small energy difference between the  $\text{Tb}^{3+}$  and host states caused the occurrence of a  $\text{Tb}^{3+}$  to host energy transfer process, which is strongly temperature dependent, as it is a phonon assisted process [50-51]. Figure 7 depicts the variation of the emission intensities of  $\text{Tb}^{3+}$  and  $\text{Eu}^{3+}$  as a function of the temperature for such NPs. When the temperature increases, the terbium emission peak decreases, while the one of europium slightly increases, remains stable before decreasing again.

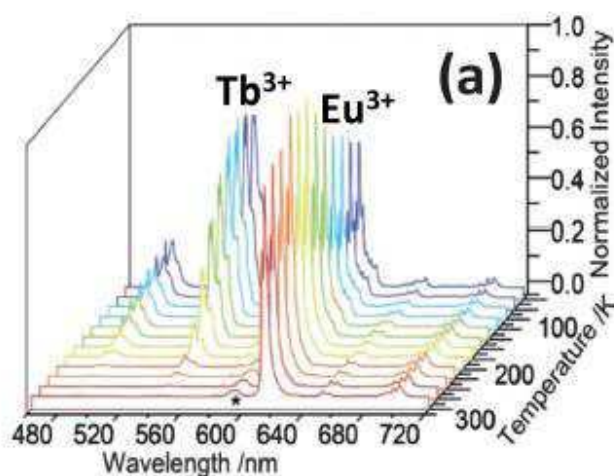


Figure 7: Temperature dependence of the luminescence generated by  $\text{Eu}^{3+}$ ,  $\text{Tb}^{3+}$  co-doped  $\gamma\text{-Fe}_2\text{O}_3$  nanoparticles after UV optical excitation [51]

Another example where the phosphor thermometer consisted in a  $\text{Tb}^{3+}/\text{Tm}^{3+}$  co-doped  $\text{Y}_2\text{O}_3$  system was also reported [79].

Eventually, let's mention some examples of metal organic luminescent compounds doped with  $\text{Eu}^{3+}$  and  $\text{Tb}^{3+}$ , which are also reported in the literature as nanothermosensors [53]. Instead of single molecules, the combination of metals and ligands forming metal organic frameworks (MOF) may be used as thermometric sensors. The thermometric process is in this

case based on the energy transfer between ions within the solid framework. The emission of the ions is sensitized by organic ligands with a suitable triplet-state energy, which determines the sensitivity and working range of the thermometer. In the last 20 years, luminescent MOFs have attracted attention due to their potential applications in chemical sensing, light-emitting devices, and biomedicine [80]. The first ratiometric luminescent MOF thermometer, based on the integrated intensity of the  $\text{Tb}^{3+}$  ( $^5D_4 \rightarrow ^7F_5$ ) and  $\text{Eu}^{3+}$  ( $^5D_0 \rightarrow ^7F_2$ ) emissions has been reported by Cui *et al* [53]. In the past five years, several examples of mixed lanthanides-MOF as luminescent-based nanothermometers have been reported [81-83]. However, only a few of them present nanosized particles. Cadiou *et al.* reported Ln-MOF NPs showing excellent performance as ratiometric luminescent nanothermometers in the physiological temperature range (300 – 320 K) [52] with a sensitivity around  $0.15 \text{ \%K}^{-1}$ .

This part showed that it is possible to create ratiometric nanothermometers based on the integrated intensity of  $\text{Tb}^{3+}$  ( $^5D_4 \rightarrow ^7F_5$ ) and  $\text{Eu}^{3+}$  ( $^5D_0 \rightarrow ^7F_2$ ) emissions. Thus, the nanoparticles I have synthesized allow investigating the luminescence properties of  $\text{HfO}_2$  NPs doped with europium and then with terbium and, subsequently, studying the evolution of luminescence with temperature (NPs doped with europium, terbium and gadolinium).

## II - Mono doping of HfO<sub>2</sub> with lanthanide

### II. 1. Europium (Eu<sup>3+</sup>) insertion

The measurements were performed on HfO<sub>2</sub> NPs doped with 5% of Eu, synthesized at 180 °C, pH 9.5 for 48 hours (chapter 3, IV-1-a) (TEM size: 39 ± 9 nm; XRD size: 21 nm; shape: rhombus and smooth, monoclinic).

Figure 8 shows the room temperature excitation and emission spectra of Eu<sup>3+</sup> - doped HfO<sub>2</sub> NPs. The excitation spectrum was monitored with an emission wavelength of 614 nm, while the emission spectrum was measured with 270 nm excitation. The emission spectrum is dominated by the <sup>5</sup>D<sub>0</sub> → <sup>7</sup>F<sub>2</sub> transition, whereas the excitation spectrum of the <sup>5</sup>D<sub>0</sub> → <sup>7</sup>F<sub>2</sub> line (*i.e.* 614 nm) features the transitions from <sup>7</sup>F<sub>0,1</sub> levels. Furthermore, according to the literature, the large band peaking at 253 nm is ascribed to a charge transfer (CT) band between the matrix and Eu<sup>3+</sup> [84].

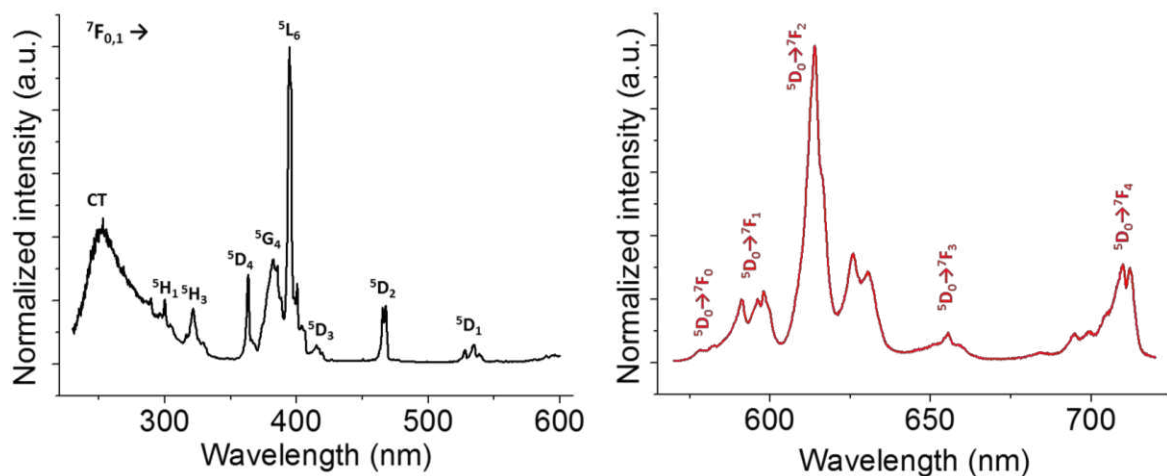


Figure 8: Room temperature excitation spectrum on the left ( $\lambda_{em} = 614$  nm) and emission spectrum on the right at  $\lambda_{exc} = 270$  nm

Further studies were performed at low temperature (14 K) to determine whether Eu<sup>3+</sup> was localized in one or in several sites. Emission spectra were recorded with an excitation wavelength of 394 nm, at room temperature and at 14 K (Figure 9). Moreover, two emission spectra were recorded with an excitation wavelength of 270 nm and 396 nm at 14 K (Figure 10).

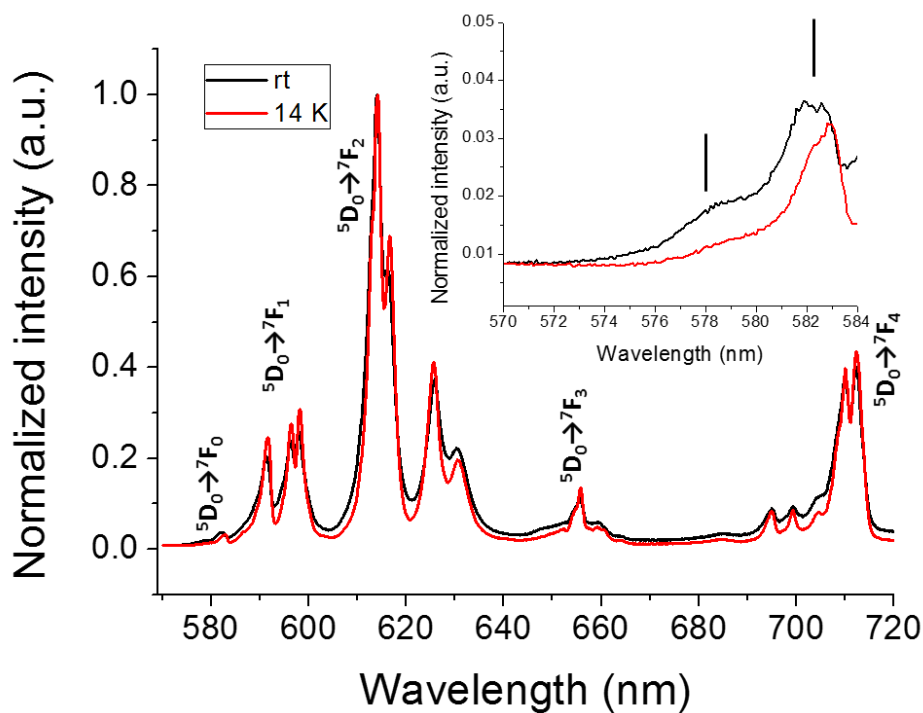


Figure 9: Emission spectra at  $\lambda_{exc} = 394$  nm at room temperature (in black) and at 14 K (in red). The inset is a zoom of the  $^5D_0 \rightarrow ^7F_0$ . The vertical lines show the peaks corresponding to two Stark levels.

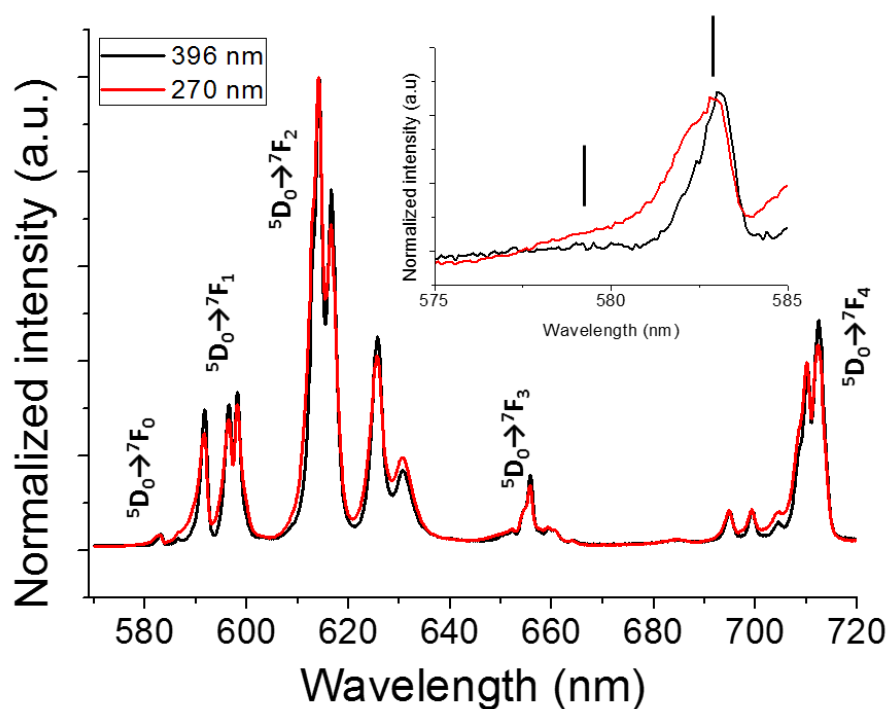


Figure 10: Emission spectra at  $\lambda_{exc} = 396$  nm (in black) and 270 nm (in red) at 14 K. The inset is a zoom of the  $^5D_0 \rightarrow ^7F_0$ . The vertical lines show the peaks corresponding to two Stark levels.

Each transition is a superposition of Stark levels. According to Binnemans [85], for a  ${}^7F_J$  the maximum number of the Stark level is equal to  $2J + 1$ , meaning that if europium sits in one site the  ${}^5D_0 \rightarrow {}^7F_0$  transition should give a single band. Yet, the  ${}^5D_0 \rightarrow {}^7F_0$  transition around 572 – 585 nm consists of two large bands, showing the presence of more than one local environment for  $\text{Eu}^{3+}$ . Moreover, the two bands are broad (FWHM of  $50 \text{ cm}^{-1}$  and of  $66 \text{ cm}^{-1}$ , values were obtained by fitting with two Gaussian lines the luminescence intensity as a function of the energy in  $\text{cm}^{-1}$ ) indicating that  $\text{Eu}^{3+}$  are distributed in two families of very similar local sites.

${}^5D_0$  emission decay curves were monitored within the  ${}^5D_0 \rightarrow {}^7F_2$  transition (614 nm) under different excitation wavelengths: 270 nm (charge transfer band) and 394 nm (direct excitation into  $\text{Eu}^{3+} {}^5L_6$  level). Both decay curves were well reproduced by a two-exponential function, revealing the presence of two decay components ascribed to Eu1 and Eu2 centres. A good quality fit ( $R > 0.9999$ ) was obtained using a bi-exponential function (Figure 11), yielding two lifetime values. Table 2 presents the lifetime values and the errors are determined by the fitting error.

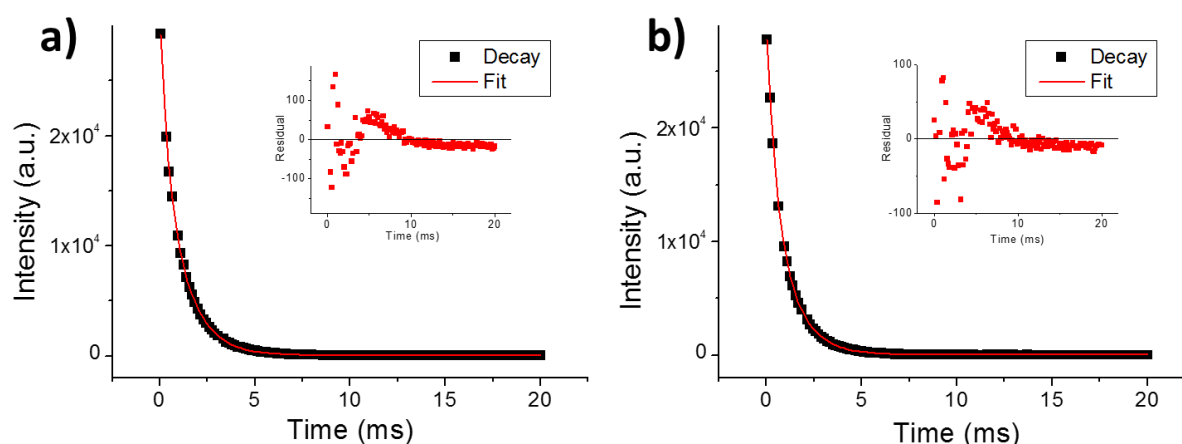


Figure 11: Luminescence decay curve of  $\text{Eu}^{3+}:\text{HfO}_2$  NPs (a)  $\lambda_{exc} = 394 \text{ nm}$ , (b)  $\lambda_{exc} = 270 \text{ nm}$  and  $\lambda_{em} = 614 \text{ nm}$ . The red solid lines denotes the best double exponential fit to the data and the insert shows the fitting residual

	Lifetimes	
	$\tau_1(\text{ms})$	$\tau_2(\text{ms})$
$\lambda_{exc} = 394 \text{ nm}$	$0.364 \pm 0.009$	$1.237 \pm 0.008$
$\lambda_{exc} = 270 \text{ nm}$	$0.440 \pm 0.007$	$1.201 \pm 0.008$

Table 2: Lifetimes of  $\text{Eu}^{3+}:\text{HfO}_2$  NPs at two excitation wavelengths (394 nm and 270 nm)

According to the lifetime values in Table 2 and following the arguments of Planelles-Arago *et al.* [86], we assume the fast component (lower lifetime value) to be due to the  $\text{Eu}^{3+}$  ions on the NPs surface (Eu1 emitting centres), whereas the slow component (higher lifetime value) is attributed to  $\text{Eu}^{3+}$  ions in the NPs core (Eu2 centres). Hydroxyl ( $-\text{OH}$ ) groups (from water molecules) present in the  $\text{Eu}^{3+}$  first coordination shell, are indeed well-known luminescence quenchers (since they absorb in resonance with the  $\text{Eu}^{3+}$  ion), favoring non-radiative relaxation [87]. The short lifetime values of Eu1 centres are related to the existence of OH groups in the first coordination shell, favoring non-radiative pathways. Regarding Eu2 emitting centres, located inside the NPs, the interaction between  $\text{Eu}^{3+}$  ions and OH groups from water molecules is efficiently hindered, providing longer lifetime values.

According to Ferreira *et al.* [88], the lifetime is often higher for the charge transfer than for direct excitation in  $\text{Eu}^{3+}$ . However, explaining why this effect is higher for the Eu1 centres (in the NPs core) than for Eu2 centres, will require further studies, beyond the scope of this thesis.

## II. 2. Terbium (Tb<sup>3+</sup>) insertion

The measurements were performed on HfO<sub>2</sub> NPs doped with 5% of Tb, synthesized at 180 °C, pH 9.5 for 48 hours (chapter 3, IV-1-b). (TEM size: 39 ± 12 nm; XRD size: 15 nm; shape: rhombus and smooth, monoclinic).

Figure 12 shows the room temperature excitation and emission spectra of Tb<sup>3+</sup>-doped HfO<sub>2</sub> NPs. The excitation spectrum was monitored with an emission wavelength of 543 nm, while the emission spectrum was measured with 280 nm excitation. The latter is dominated by the <sup>5</sup>D<sub>4</sub> → <sup>7</sup>F<sub>5</sub> transition, whereas the excitation spectrum of the <sup>5</sup>D<sub>4</sub> → <sup>7</sup>F<sub>5</sub> line (e.g. 543 nm) features the transitions from <sup>7</sup>F<sub>0,1</sub> levels. Furthermore, according to the literature, we can ascribed the large band peaking at 246 nm as a charge transfer (CT) between the matrix and Tb<sup>3+</sup> [89].

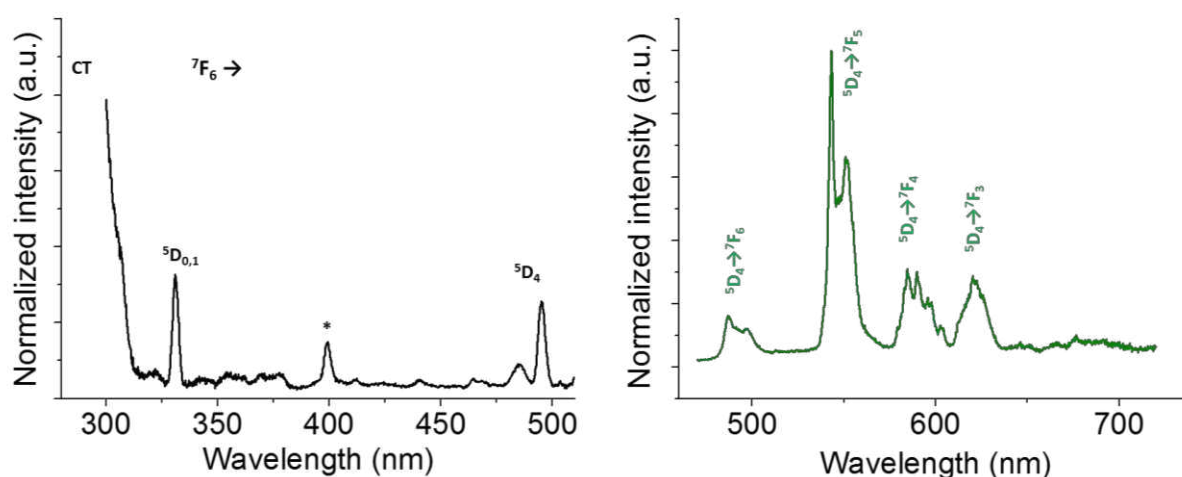


Figure 12: Room temperature excitation spectrum in black ( $\lambda_{em} = 543$  nm) and emission spectrum in green at  $\lambda_{exc} = 280$  nm. (Peak labeled as \* is an experimental artefact which appears in systems with low luminescence intensity)

According to the study made on the insertion of europium in the matrix of HfO<sub>2</sub>, we can suppose that Tb<sup>3+</sup> has also two local environment. Tb1 is assigned to Tb<sup>3+</sup> in the NPs core whereas Tb2 is ascribed to Tb<sup>3+</sup> on the NPs surface. <sup>5</sup>D<sub>4</sub> emission decay curves were monitored within the <sup>5</sup>D<sub>4</sub> → <sup>7</sup>F<sub>5</sub> transition (543 nm) under an excitation wavelength of 270 nm (charge transfer band). The decay curve was well reproduced by a two-exponential function, revealing the presence of two decay components ascribed to Tb1 and Tb2 centres. A good quality fit ( $R > 0.999$ ) was obtained using a bi-exponential function (Figure 13), yielding two lifetime values (Table 3).

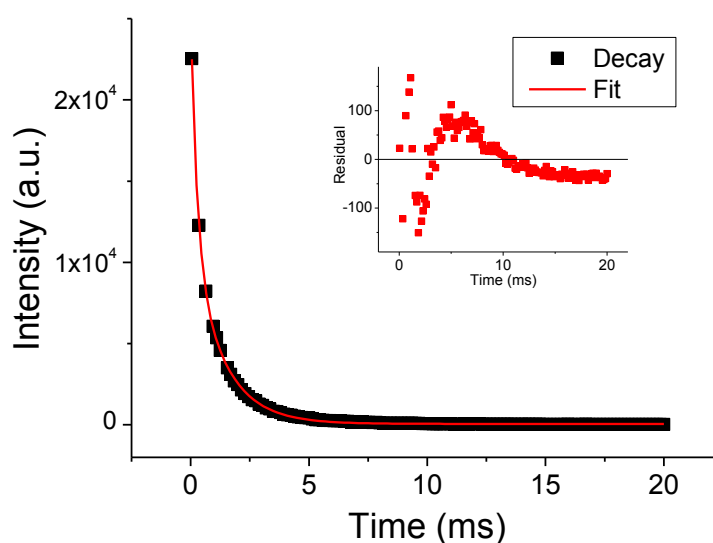


Figure 13: Luminescence decay curve of  $Tb^{3+}:HfO_2$  NPs,  $\lambda_{exc} = 270$  nm and  $\lambda_{em} = 543$  nm. The red solid lines denotes the best double exponential fit to the data.

	Lifetimes	
	$\tau_1$ (ms)	$\tau_2$ (ms)
$\lambda_{exc} = 270$ nm	$0.261 \pm 0.006$	$1.312 \pm 0.016$

Table 3: Lifetimes of  $Tb^{3+}:HfO_2$  NPs at an excitation wavelengths (270 nm)

Thus, according to the discussion made for the europium insertion in the hafnium oxide matrix, we attribute the fast component (lower lifetime) to  $Tb^{3+}$  on the NPs surface (Tb1 centres), whereas the slow component (longer lifetime) is assigned to  $Tb^{3+}$  in NPs core (Tb2 centres).

### III - Nanothermometry applications

Nanothermometry properties of samples  $\text{Eu}_{0.01}\text{Tb}_{0.03}\text{Gd}_{0.16}:\text{HfO}_2$ ,  $\text{Eu}_{0.03}\text{Tb}_{0.05}\text{Gd}_{0.12}:\text{HfO}_2$ , and  $\text{Eu}_{0.05}\text{Tb}_{0.10}\text{Gd}_{0.05}:\text{HfO}_2$  were studied. Firstly, the excitation spectra were recorded, in order to confirm  $\text{Tb}^{3+}$ -to- $\text{Eu}^{3+}$  energy transfer. Then, the emission spectra were measured at different temperature from 12 K to 325 K. Finally, the sensitivity of the nanothermometer was determined.

#### III. 1. Excitation spectra

For the three samples, excitation spectra were recorded monitoring at the  $\text{Eu}^{3+}$  and  $\text{Tb}^{3+}$  emission (Figure 14, Figure 15 and Figure 16).

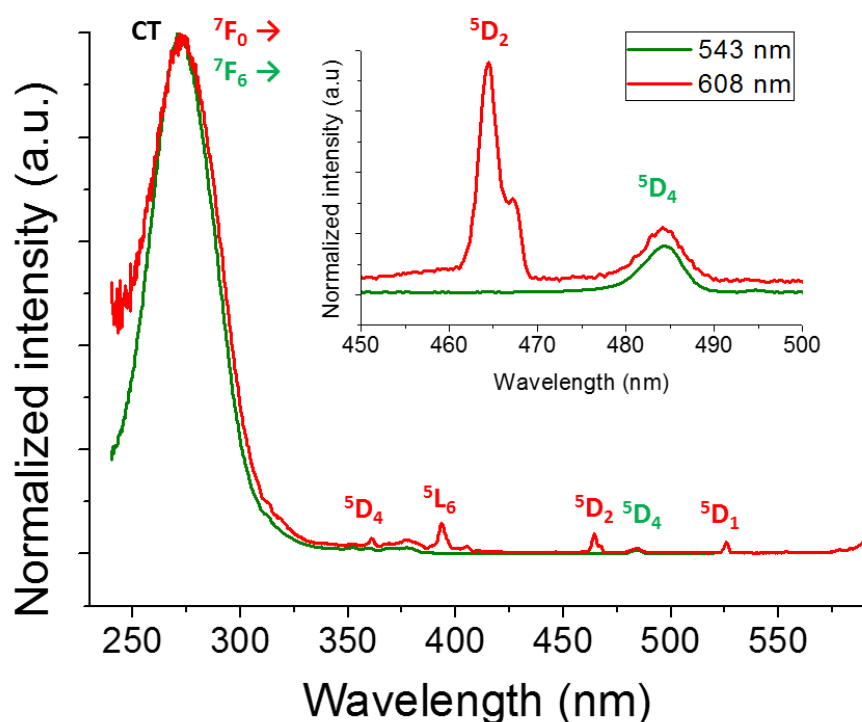


Figure 14: Excitation spectra of  $\text{Eu}_{0.01}\text{Tb}_{0.03}\text{Gd}_{0.16}:\text{HfO}_2$  monitoring emission at 608 nm ( $\text{Eu}^{3+}$ , red lines) and 543 nm ( $\text{Tb}^{3+}$ , green lines) recorded at 13 K

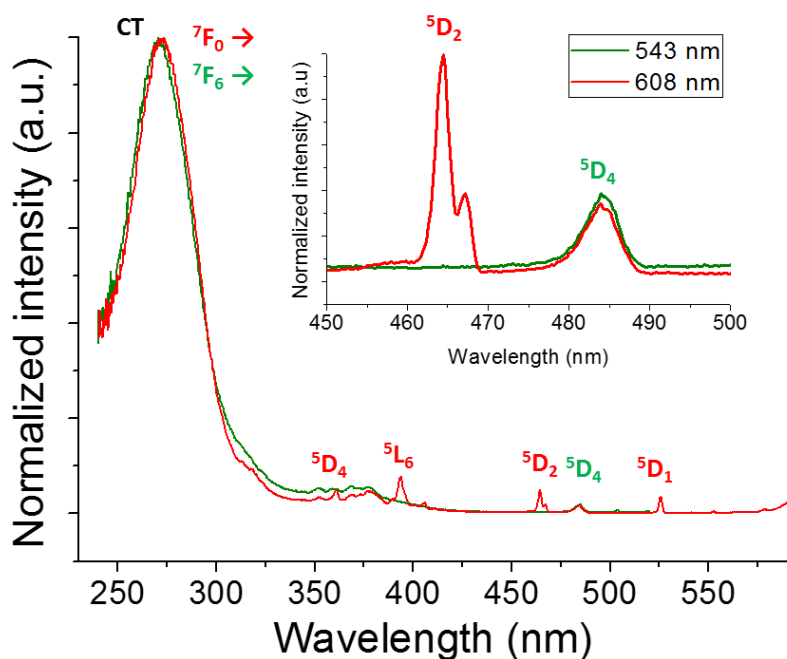


Figure 15: Excitation spectra of  $\text{Eu}_{0.03}\text{Tb}_{0.05}\text{Gd}_{0.12}:\text{HfO}_2$  monitoring emission at 608 nm ( $\text{Eu}^{3+}$ , red lines) and 543 nm ( $\text{Tb}^{3+}$ , green lines) recorded at 13 K

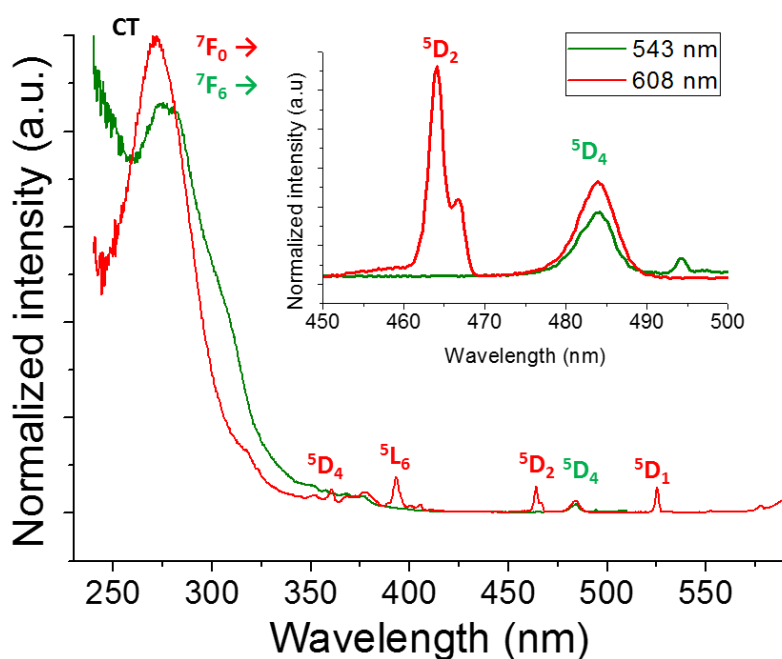


Figure 16: Excitation spectra of  $\text{Eu}_{0.05}\text{Tb}_{0.10}\text{Gd}_{0.05}:\text{HfO}_2$  monitoring emission at 608 nm ( $\text{Eu}^{3+}$ , red lines) and 543 nm ( $\text{Tb}^{3+}$ , green lines) recorded at 13 K

For the three samples, in each emission spectra monitoring emission at 608 nm ( $\text{Eu}^{3+}$ ), at 484 nm ( $\text{Tb}^{3+}$ ), the characteristic transition of terbium  ${}^7F_6 \rightarrow {}^5D_4$  is observable [90]. Thus, the excitation spectra confirmed  $\text{Tb}^{3+}$ -to- $\text{Eu}^{3+}$  energy transfer.

### III. 2. Temperature dependence of the luminescence

Here, the emission spectra are plotted as a function of temperature. For the three samples, an emission spectrum was recorded with an excitation wavelength of 280 nm with a step of 25 K.

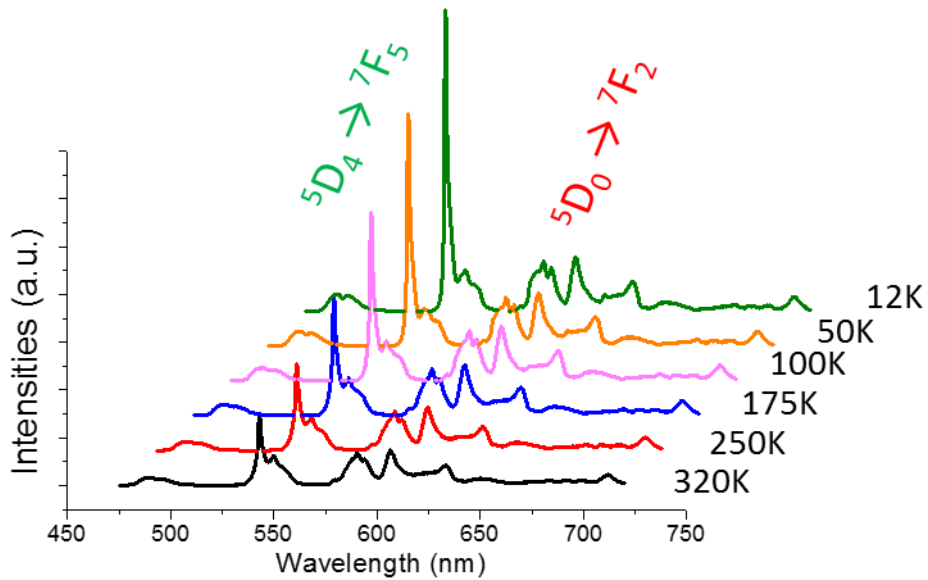


Figure 17: Emission spectra of  $\text{Eu}_{0.01}\text{Tb}_{0.03}\text{Gd}_{0.16}:\text{HfO}_2$  at several temperatures with an excitation wavelength of 280 nm.

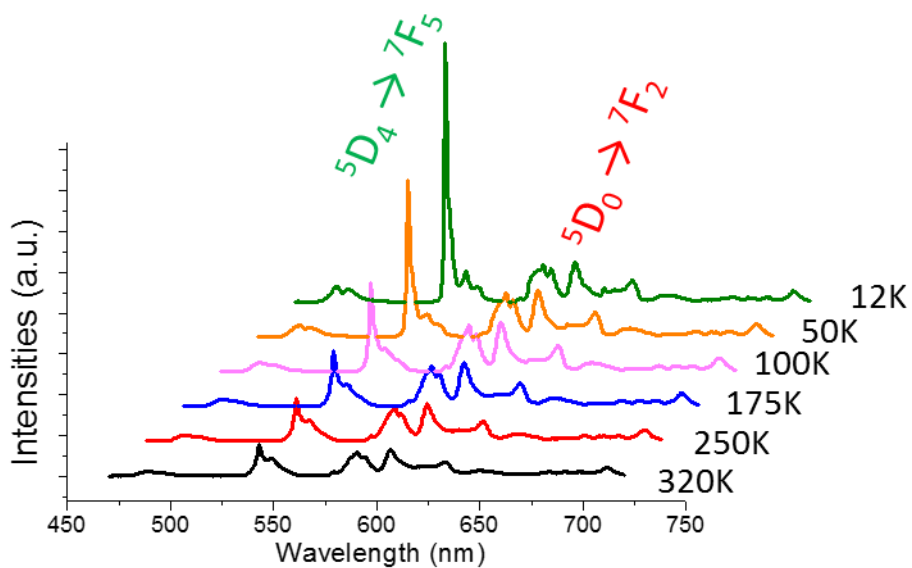


Figure 18: Emission spectra of  $\text{Eu}_{0.03}\text{Tb}_{0.05}\text{Gd}_{0.12}:\text{HfO}_2$  at several temperatures with an excitation wavelength of 280 nm.

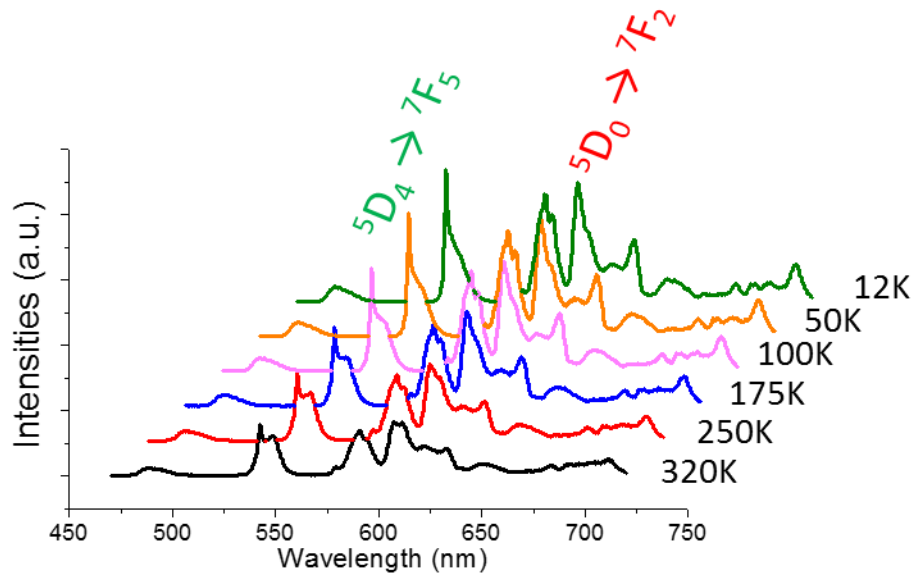


Figure 19: Emission spectra of  $\text{Eu}_{0.05}\text{Tb}_{0.10}\text{Gd}_{0.05}:\text{HfO}_2$  at several temperatures with an excitation wavelength of 280 nm.

Figure 17 and Figure 18 show an important decrease of the intensity of the terbium band at 543 nm with increasing temperature, while Figure 19 shows a relatively smaller decrease of this band. Increasing the temperature might promote the  $\text{Tb}^{3+}$ -to- $\text{Eu}^{3+}$  energy transfer.

### III. 3. Integrated intensity

To quantify the evidence in these figures, we need to measure the areas under the curves of the main emissions of terbium, 543 nm ( ${}^5D_4 \rightarrow {}^7F_5$ ), and europium, 608 nm ( ${}^5D_0 \rightarrow {}^7F_2$ ) and 720 nm ( ${}^5D_0 \rightarrow {}^7F_4$ ). For europium, two peaks are considered because the first peak around 608 nm slightly overlaps with a terbium peak ( ${}^5D_4 \rightarrow {}^7F_3$ ). Thus, the integrations were carried out from 537 to 570 nm for terbium ( ${}^5D_4 \rightarrow {}^7F_5$ ), from 600 to 640 nm for the first europium peak ( ${}^5D_0 \rightarrow {}^7F_2$ ) and from 704 to 720 nm for the second europium peak ( ${}^5D_0 \rightarrow {}^7F_4$ ) (Figure 20).

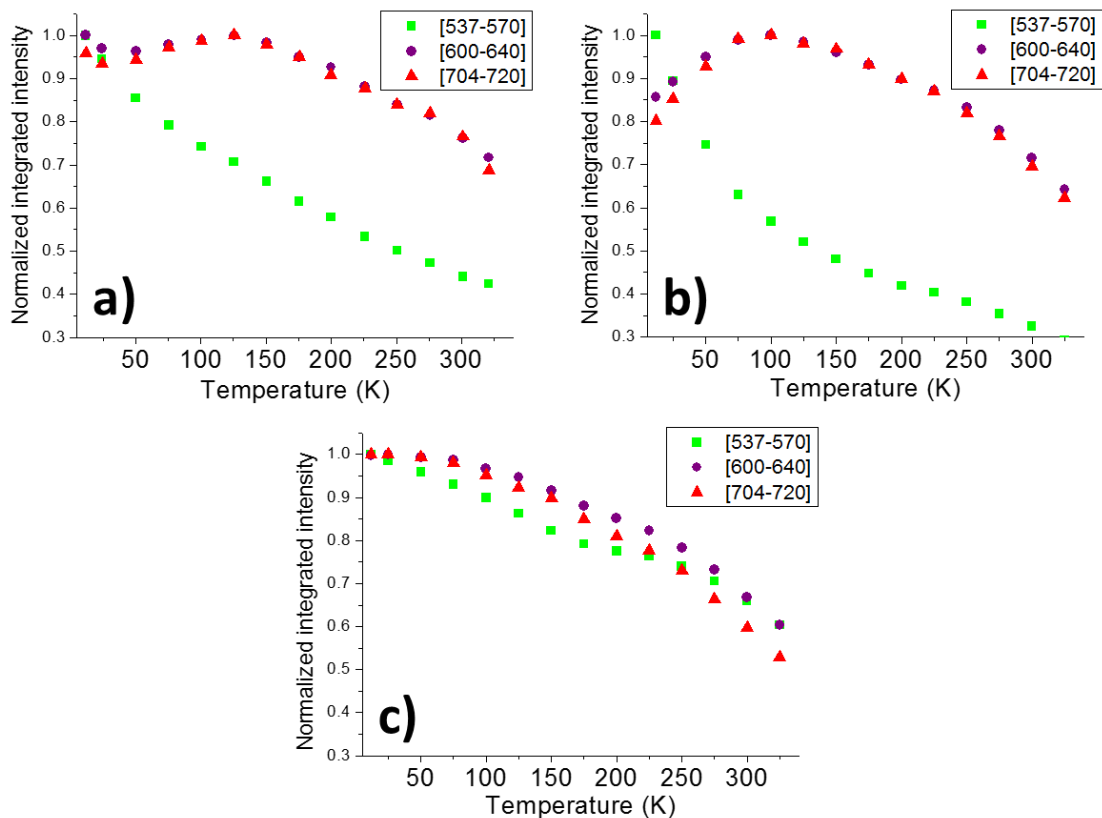


Figure 20: Integrated intensities of three peaks of the emission spectra (green,  ${}^5D_4 \rightarrow {}^7F_5$  of terbium, purple,  ${}^5D_0 \rightarrow {}^7F_2$  of europium and red,  ${}^5D_0 \rightarrow {}^7F_4$  of europium) of a)  $\text{Eu}_{0.01}\text{Tb}_{0.03}\text{Gd}_{0.16}:\text{HfO}_2$  b)  $\text{Eu}_{0.03}\text{Tb}_{0.05}\text{Gd}_{0.12}:\text{HfO}_2$  and c)  $\text{Eu}_{0.05}\text{Tb}_{0.10}\text{Gd}_{0.05}:\text{HfO}_2$ .

These graphs allow us to see better the evolution of the intensity of the terbium and europium peaks. Thus, for  $\text{Eu}_{0.01}\text{Tb}_{0.03}\text{Gd}_{0.16}:\text{HfO}_2$  the intensity of the europium bands remains stable up to 180 K, and it decreases from 1 to 0.7 at room temperature. Intensity of the terbium bands decreases with the increase of the temperature. Concerning  $\text{Eu}_{0.03}\text{Tb}_{0.05}\text{Gd}_{0.12}:\text{HfO}_2$ , the emission of europium increases with the temperature up to 80 K, it remains stable from 80 K to 180 K, after which it decreases. The emission intensity of terbium decreases with the increase of the temperature. For  $\text{Eu}_{0.05}\text{Tb}_{0.10}\text{Gd}_{0.05}:\text{HfO}_2$ , the emission intensities of europium and terbium both decrease with the increase of the temperature.

The decrease in the emission intensity is usually due to one or more non-radiative mechanisms [86]. Considering the emission spectra of hafnium oxide doped only with europium and the two broad bands  ${}^5D_0 \rightarrow {}^7F_0$ , at 578 (17 301  $\text{cm}^{-1}$ ) and 582 nm (17 182  $\text{cm}^{-1}$ ), we can determine an energy migration between the  ${}^5D_0$  levels of two  $\text{Eu}^{3+}$  sites of 119  $\text{cm}^{-1}$ . Yet, the emission intensities of the previous curves start to decrease around 180 K, which is

equivalent to a thermal energy ( $k_B T$ ) of  $125 \text{ cm}^{-1}$ . Thus, we can speculate that we have beyond 180 K, some energy transfer between Eu1 and Eu2 ions.

### III. 4. Experimental thermometric parameter

Before determining the sensitivity of the nanothermometers we need to calculate the experimental thermometric parameter,  $\Delta$ , as a function of the temperature:

$$\Delta = \frac{I_{Tb}}{I_{Eu}}$$

The experimental thermometric parameters are plotted in Figure 21.

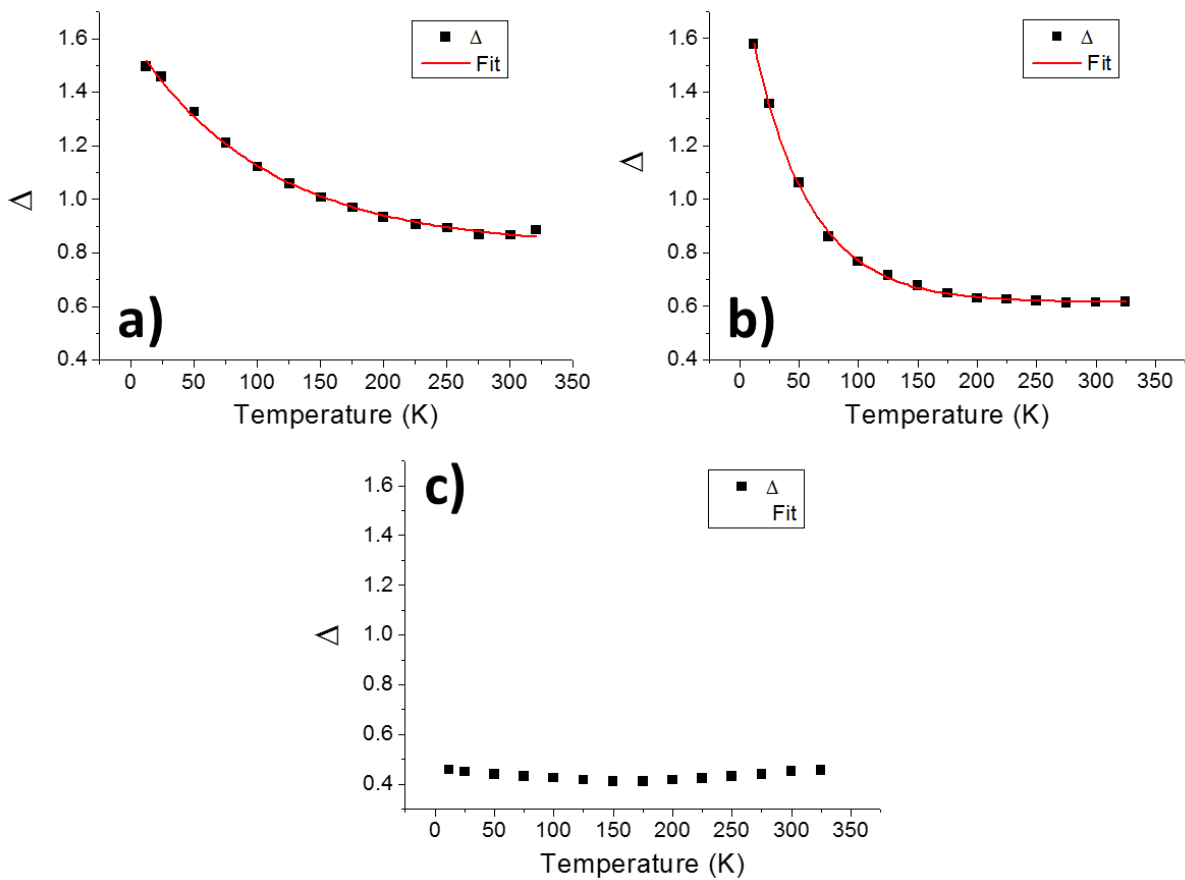


Figure 21: Experimental thermometric parameter determined by the ratio of the intensity of the terbium peak ( ${}^5D_4 \rightarrow {}^7F_5$ ) by the intensity of the europium peak ( ${}^5D_0 \rightarrow {}^7F_2$ ) of a)  $\text{Eu}_{0.01}\text{Tb}_{0.03}\text{Gd}_{0.16}:\text{HfO}_2$  b)  $\text{Eu}_{0.03}\text{Tb}_{0.05}\text{Gd}_{0.12}:\text{HfO}_2$  and c)  $\text{Eu}_{0.05}\text{Tb}_{0.10}\text{Gd}_{0.05}:\text{HfO}_2$ .

We did not study the possible mechanisms behind the luminescence, and we will not discuss the temperature dependence of  $\Delta$ . Thus, we fitted the experimental thermometric parameter with an empirical exponential decay function, in order to determine the following parameters and to obtain information about the performance:  $C$ ,  $\alpha$  and  $\Delta_0$  according to the following equation:  $\Delta = \Delta_0 + C e^{-\alpha T}$  [74].

	$\Delta_0$	$C$	$\alpha$
Eu <sub>0.01</sub> Tb <sub>0.03</sub> Gd <sub>0.16</sub> :HfO <sub>2</sub>	0.82	0.78	0.0094
Eu <sub>0.03</sub> Tb <sub>0.05</sub> Gd <sub>0.12</sub> :HfO <sub>2</sub>	0.61	1.24	0.021
Eu <sub>0.05</sub> Tb <sub>0.10</sub> Gd <sub>0.05</sub> :HfO <sub>2</sub>	-	-	-

Table 4: Determination of the parameter  $\Delta_0$ ,  $C$  and  $\alpha$  by the decay exponential fitting of the experimental thermometric parameter.

For the third sample, the ratio between the intensities of Tb<sup>3+</sup> and Eu<sup>3+</sup> is almost constant with the temperature, meaning that this sample cannot act as a nanothermometer.

### III. 5. Relative sensitivity

To determine the relative sensitivity of a nanothermometer, we use the formula (6):

$$S_r(T) = \frac{1}{\Delta} \left| \frac{\partial \Delta}{\partial T} \right|$$

$$S_r(T) = \frac{1}{\Delta_0 + C e^{-\alpha T}} \left| \frac{\partial (\Delta_0 + C e^{-\alpha T})}{\partial T} \right|$$

$$S_r(T) = \frac{1}{\Delta_0 + C e^{-\alpha T}} |-\alpha C e^{-\alpha T}|$$

$$S_r(T) = \frac{\alpha C e^{-\alpha T}}{\Delta_0 + C e^{-\alpha T}}$$

A plot of  $S_r(T)$  as a function of the temperature yields the relative sensitivity of the nanothermometer (Figure 22).

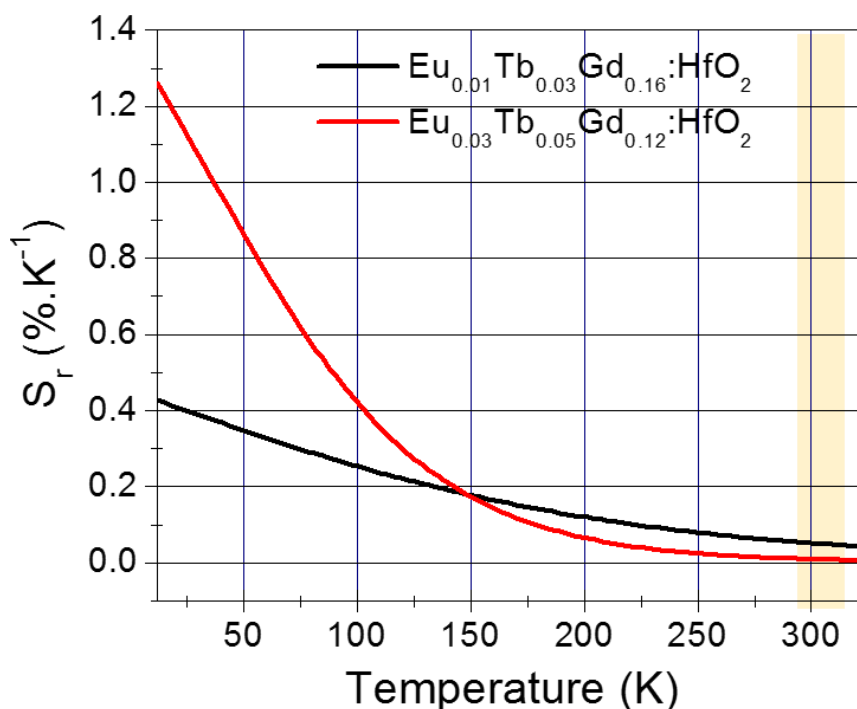


Figure 22: Relative sensitivity of  $\text{Eu}_{0.01}\text{Tb}_{0.03}\text{Gd}_{0.16}:\text{HfO}_2$  (in black) and  $\text{Eu}_{0.03}\text{Tb}_{0.05}\text{Gd}_{0.12}:\text{HfO}_2$  (in red). The yellow rectangle shows the biological range of temperatures (from 25 °C to 40 °C)

The sensitivity of  $\text{Eu}_{0.03}\text{Tb}_{0.05}\text{Gd}_{0.12}:\text{HfO}_2$  increases considerably below 150 K, almost 0 % $\text{K}^{-1}$  at room temperature. In contrast,  $\text{Eu}_{0.01}\text{Tb}_{0.03}\text{Gd}_{0.16}:\text{HfO}_2$  has a lower overall sensitivity, but its sensitivity at room temperature is better, *ca.* 0.1 % $\text{K}^{-1}$ . As we seek to measure the temperature of living cells, the latter sample is preferable for thermometry.

## Conclusion

Doping of  $\text{HfO}_2$  nanoparticles with  $\text{Ln}^{3+}$  ions endows them with luminescence properties. Under UV irradiation, these nanoparticles emit in the visible range, green ( $\text{Tb}^{3+}$ ) and red ( $\text{Eu}^{3+}$ ) light. Moreover, the insertion of three lanthanide ( $\text{Eu}^{3+}$ ,  $\text{Tb}^{3+}$ ,  $\text{Gd}^{3+}$ ) ions in the hafnium oxide matrix results in temperature dependence of the luminescence, which was exploited for ratiometric thermometry. Among the three samples studied,  $\text{Eu}_{0.01}\text{Tb}_{0.03}\text{Gd}_{0.16}:\text{HfO}_2$  exhibited the best sensitivity (0.1 % $\text{K}^{-1}$ ) at room temperature.

## Characterization method

The photoluminescence spectra were recorded between 14 K and room temperature with a modular double grating excitation spectrofluorimeter with a TRIAX 320 emission monochromator (Fluorolog-3, Jobin Yvon-SPex) coupled to a R928 Hamamatsu photomultiplier, using the front face acquisition mode, on pellet of the samples. The excitation source was 450 W Xenon lamp. The emission spectra were corrected for detection and optical spectral response of the spectrofluorimeter and the excitation spectra were weighed for the spectral distribution of the lamp intensity using a photodiode reference detector. The lifetime measurements were acquired with the setup described for the luminescence spectra using a pulsed Xe-Hg lamp (6  $\mu$ s pulse at half width and 20 – 30  $\mu$ s tail).

## Bibliography

1. Ntziachristos, V.; Ripoll, J.; Wang, L. V.; Weissleder, R., Looking and listening to light: the evolution of whole-body photonic imaging. *Nature Biotechnology* **2005**, *23* (3), 313-320.
2. Wang, F.; Banerjee, D.; Liu, Y.; Chen, X.; Liu, X., Upconversion nanoparticles in biological labeling, imaging, and therapy. *Analyst* **2010**, *135* (8), 1839-1854.
3. Michalet, X.; Pinaud, F.; Bentolila, L.; Tsay, J.; Doose, S.; Li, J.; Sundaresan, G.; Wu, A.; Gambhir, S.; Weiss, S., Quantum dots for live cells, in vivo imaging, and diagnostics. *Science* **2005**, *307* (5709), 538-544.
4. Medintz, I. L.; Uyeda, H. T.; Goldman, E. R.; Mattoussi, H., Quantum dot bioconjugates for imaging, labelling and sensing. *Nature materials* **2005**, *4* (6), 435-446.
5. Petryayeva, E.; Algar, W. R.; Medintz, I. L., Quantum dots in bioanalysis: a review of applications across various platforms for fluorescence spectroscopy and imaging. *Applied spectroscopy* **2013**, *67* (3), 215-252.
6. Pansare, V.; Hejazi, S.; Faenza, W.; Prud'homme, R. K., Review of long-wavelength optical and NIR imaging materials: contrast agents, fluorophores and multifunctional nano carriers. *Chemistry of materials: a publication of the American Chemical Society* **2012**, *24* (5), 812.
7. Hagan, A.; Zuchner, T., Lanthanide-based time-resolved luminescence immunoassays. *Analytical and bioanalytical chemistry* **2011**, *400* (9), 2847-2864.
8. Yuan, J.; Wang, G., Lanthanide-based luminescence probes and time-resolved luminescence bioassays. *TrAC Trends in Analytical Chemistry* **2006**, *25* (5), 490-500.
9. Bazin, H.; Trinquet, E.; Mathis, G., Time resolved amplification of cryptate emission: a versatile technology to trace biomolecular interactions. *Reviews in Molecular Biotechnology* **2002**, *82* (3), 233-250.
10. Albizu, L.; Cottet, M.; Kralikova, M.; Stoev, S.; Seyer, R.; Brabet, I.; Roux, T.; Bazin, H.; Bourrier, E.; Lamarque, L., Time-resolved FRET between GPCR ligands reveals oligomers in native tissues. *Nature chemical biology* **2010**, *6* (8), 587-594.
11. Bünzli, J.-C. G., Lanthanide luminescence for biomedical analyses and imaging. *Chemical Reviews* **2010**, *110* (5), 2729-2755.
12. Hovinen, J.; Guy, P. M., Bioconjugation with stable luminescent lanthanide (III) chelates comprising pyridine subunits. *Bioconjugate Chemistry* **2008**, *20* (3), 404-421.
13. Suhling, K.; French, P. M.; Phillips, D., Time-resolved fluorescence microscopy. *Photochemical & Photobiological Sciences* **2005**, *4* (1), 13-22.
14. Connally, R. E.; Piper, J. A., Time-Gated Luminescence Microscopy. *Annals of the New York Academy of Sciences* **2008**, *1130* (1), 106-116.
15. Moore, E. G.; Samuel, A. P.; Raymond, K. N., From antenna to assay: lessons learned in lanthanide luminescence. *Accounts of Chemical Research* **2009**, *42* (4), 542-552.
16. Chauvin, A.-S.; Thomas, F.; Song, B.; Vandevyver, C. D.; Bünzli, J.-C. G., Synthesis and cell localization of self-assembled dinuclear lanthanide bioprobes. *Philosophical Transactions of the Royal Society of London A: Mathematical, Physical and Engineering Sciences* **2013**, *371* (1995), 20120295.
17. Hess, B. A.; Kedzierski, A.; Smentek, L.; Bornhop, D., Role of the Antenna in Tissue Selective Probes Built of Lanthanide–Organic Chelates. *The Journal of Physical Chemistry A* **2008**, *112* (11), 2397-2407.
18. Song, B.; Vandevyver, C. D.; Deiters, E.; Chauvin, A.-S.; Hemmilä, I.; Bünzli, J.-C. G., A versatile method for quantification of DNA and PCR products based on time-resolved Eu III luminescence. *Analyst* **2008**, *133* (12), 1749-1756.
19. Li, Y.; Tang, J.; Pan, D.-X.; Sun, L.-D.; Chen, C.; Liu, Y.; Wang, Y.-F.; Shi, S.; Yan, C.-H., A Versatile Imaging and Therapeutic Platform Based on Dual-Band Luminescent Lanthanide Nanoparticles toward Tumor Metastasis Inhibition. *ACS Nano* **2016**, *10* (2), 2766-2773.
20. Montgomery, C. P.; Murray, B. S.; New, E. J.; Pal, R.; Parker, D., Cell-penetrating metal complex optical probes: targeted and responsive systems based on lanthanide luminescence. *Accounts of Chemical Research* **2009**, *42* (7), 925-937.
21. dos Santos, C. M.; Harte, A. J.; Quinn, S. J.; Gunnlaugsson, T., Recent developments in the field of supramolecular lanthanide luminescent sensors and self-assemblies. *Coordination Chemistry Reviews* **2008**, *252* (23), 2512-2527.
22. Fan, Y.; Yang, P.; Huang, S.; Jiang, J.; Lian, H.; Lin, J., Luminescent and mesoporous europium-doped bioactive glasses (MBG) as a drug carrier. *The Journal of Physical Chemistry C* **2009**, *113* (18), 7826-7830.
23. Melhuish, W., Nomenclature, symbols, units and their usage in spectrochemical analysis-Part VI: molecular luminescence spectroscopy. *Pure and Applied Chemistry* **1984**, *56* (2), 231-245.
24. Blasse, G.; Grabmaier, B., *Luminescent materials*. Springer-Verlag Berlin: 1994; Vol. 44.

25. Henderson, B.; Imbusch, G. F., *Optical spectroscopy of inorganic solids*. Oxford University Press: 2006; Vol. 44.
26. Shinde, K. N.; Dhoble, S.; Swart, H.; Park, K., Basic Mechanisms of Photoluminescence. In *Phosphate Phosphors for Solid-State Lighting*, Springer: 2012; pp 41-59.
27. Jablonski, A., Efficiency of anti-Stokes fluorescence in dyes. *Nature* **1933**, *131* (839-840), 21.
28. Valeur, B.; Berberan-Santos, M. N., *Molecular fluorescence: principles and applications*. John Wiley & Sons: 2012.
29. Fluorescence Microscopy: Basic Concepts in Fluorescence. **2015**.
30. Simon, Y. C.; Weder, C., Low-power photon upconversion through triplet-triplet annihilation in polymers. *Journal of Materials Chemistry* **2012**, *22* (39), 20817-20830.
31. Gschneidner, K. A.; Eyring, L.; Lander, G. H., *Handbook on the physics and chemistry of rare earths*. Elsevier: 2002; Vol. 32.
32. Mader, H. S.; Kele, P.; Saleh, S. M.; Wolfbeis, O. S., Upconverting luminescent nanoparticles for use in bioconjugation and bioimaging. *Current Opinion in Chemical Biology* **2010**, *14* (5), 582-596.
33. Wu, X.; Chen, G.; Shen, J.; Li, Z.; Zhang, Y.; Han, G., Upconversion Nanoparticles: A Versatile Solution to Multiscale Biological Imaging. *Bioconjugate Chemistry* **2015**, *26*, 166-175.
34. Joubert, M.-F., Photon avalanche upconversion in rare earth laser materials. *Optical Materials* **1999**, *11* (2-3), 181-203.
35. Goudsmit, S.; Gropper, L., Many-electron selection rules. *Physical Review* **1931**, *38* (2), 225.
36. Meijerink, A.; de Mello Donega, C.; Ellens, A.; Sytsma, J.; Blasse, G., Vibronic transitions of rare earth ions. *Journal of Luminescence* **1994**, *58*, 26-32.
37. Jaque, D.; Vetrone, F., Luminescence nanothermometry. *Nanoscale* **2012**, *4*, 4301-4326.
38. Albers, A. E.; Chan, E. M.; McBride, P. M.; Ajo-Franklin, C. M.; Cohen, B. E.; Helms, B. A., Dual-emitting quantum dot/quantum rod-based nanothermometers with enhanced response and sensitivity in live cells. *Journal of the American Chemical Society* **2012**, *134*, 9565-9568.
39. Chen, I. H.; Lai, W. T.; Li, P. W., Realization of solid-state nanothermometer using Ge quantum-dot single-hole transistor in few-hole regime. *Applied Physics Letters* **2014**, *104*, 243506/1-243506/5.
40. Haro-Gonzalez, P.; Martinez-Maestro, L.; Martin, I. R.; Garcia-Sole, J.; Jaque, D., High-Sensitivity Fluorescence Lifetime Thermal Sensing Based on CdTe Quantum Dots. *Small* **2012**, *8*, 2652-2658.
41. Zhou, D.; Zhang, H., Critical Growth Temperature of Aqueous CdTe Quantum Dots is Non-negligible for Their Application as Nanothermometers. *Small* **2013**, *9*, 3195-3197.
42. Ansari, R.; Daliri, M.; Hosseinzadeh, M., On the van der Waals interaction of carbon nanotubes as electromechanical nanothermometers. *Acta Mechanica Sinica* **2013**, *29*, 622-632.
43. Gao, Y.; Bando, Y., Carbon nanothermometer containing gallium. *Nature* **2002**, *415*, 599.
44. Kwon, H.; Kim, M.; Meany, B.; Piao, Y.; Powell, L. R.; Wang, Y., Optical Probing of Local pH and Temperature in Complex Fluids with Covalently Functionalized, Semiconducting Carbon Nanotubes. *The Journal of Physical Chemistry C* **2015**, *119*, 3733-3739.
45. Liu, Z.; Bando, Y.; Hu, J.; Ratinac, K.; Ringer, S. P., A novel method for practical temperature measurement with carbon nanotube nanothermometers. *Nanotechnology* **2006**, *17*, 3681-3684.
46. Popov, A. M.; Bichoutskaia, E.; Lozovik, Y. E.; Kulish, A. S., Nanoelectromechanical systems based on multi-walled nanotubes: nanothermometer, nanorelay, and nanoactuator. *Physica Status Solidi A* **2007**, *204*, 1911-1917.
47. Popov, A. M.; Lozovik, Y. E.; Bichoutskaia, E.; Ivanchenko, G. S.; Lebedev, N. G.; Krivorotov, E. K., An electromechanical nanothermometer based on thermal vibrations of carbon nanotube walls. *Physics of the Solid State* **2009**, *51*, 1306-1314.
48. Rahmat, F.; Thamwattana, N.; Hill, J. M., Carbon nanotube oscillators for applications as nanothermometers. *Journal of Physics A: Mathematical and Theoretical* **2010**, *43*, 405209/1-405209/26.
49. Tan, C. M.; Jia, J.; Yu, W., Temperature dependence of the field emission of multiwalled carbon nanotubes. *Applied Physics Letters* **2005**, *86*, 263104/1-263104/3.
50. Brites, C. D.; Lima, P. P.; Silva, N. J.; Millan, A.; Amaral, V. S.; Palacio, F.; Carlos, L. D., Lanthanide-based luminescent molecular thermometers. *New Journal of Chemistry* **2011**, *35* (6), 1177-1183.
51. Brites, C. D.; Lima, P. P.; Silva, N. J.; Millán, A.; Amaral, V. S.; Palacio, F.; Carlos, L. D., A Luminescent Molecular Thermometer for Long Term Absolute Temperature Measurements at the Nanoscale. *Advanced Materials* **2010**, *22* (40), 4499-4504.
52. Cadiau, A.; Brites, C. D. S.; Costa, P. M. F. J.; Ferreira, R. A. S.; Rocha, J.; Carlos, L. D., Ratiometric nanothermometer based on an emissive Ln<sup>3+</sup>-organic framework. *ACS Nano* **2013**, *7*, 7213-8.

53. Cui, Y.; Xu, H.; Yue, Y.; Guo, Z.; Yu, J.; Chen, Z.; Gao, J.; Yang, Y.; Qian, G.; Chen, B., A luminescent mixed-lanthanide metal–organic framework thermometer. *Journal of the American Chemical Society* **2012**, *134* (9), 3979-3982.
54. Wang, Z.; Ananias, D.; Carne-Sanchez, A.; Brites, C. D. S.; Imaz, I.; Maspoch, D.; Rocha, J.; Carlos, L. D., Lanthanide–Organic Framework Nanothermometers Prepared by Spray-Drying. *Advanced Functional Materials* **2015**, *25*, 2824-2830.
55. Zhou, Y.; Yan, B.; Lei, F., Postsynthetic lanthanide functionalization of nanosized metal-organic frameworks for highly sensitive ratiometric luminescent thermometry. *Chemical Communications* **2014**, *50*, 15235-15238.
56. Haro-González, P.; Martín, I.; Martín, L.; León-Luis, S. F.; Pérez-Rodríguez, C.; Lavín, V., Characterization of Er<sup>3+</sup> and Nd<sup>3+</sup> doped Strontium Barium Niobate glass ceramic as temperature sensors. *Optical Materials* **2011**, *33* (5), 742-745.
57. Li, D.; Wang, Y.; Zhang, X.; Yang, K.; Liu, L.; Song, Y., Optical temperature sensor through infrared excited blue upconversion emission in Tm<sup>3+</sup>/Yb<sup>3+</sup> codoped Y<sub>2</sub>O<sub>3</sub>. *Optics Communications* **2012**, *285* (7), 1925-1928.
58. Bizzak, D.; Chyu, M., Use of a laser-induced fluorescence thermal imaging system for local jet impingement heat transfer measurement. *International journal of heat and mass transfer* **1995**, *38* (2), 267-274.
59. Carlson, M. T.; Khan, A.; Richardson, H. H., Local temperature determination of optically excited nanoparticles and nanodots. *Nano Letters* **2011**, *11* (3), 1061-1069.
60. Leon-Luis, S. F.; Monteseuro, V.; Rodriguez-Mendoza, U. R.; Rathaiah, M.; Venkatramu, V.; Lozano-Gorriñ, A. D.; Valiente, R.; Munoz, A.; Lavin, V., Optical nanothermometer based on the calibration of the Stokes and upconverted green emissions of Er<sup>3+</sup> ions in Y<sub>3</sub>Ga<sub>5</sub>O<sub>12</sub> nano-garnets. *RSC Advances* **2014**, *4*, 57691-57701.
61. Heyes, A.; Seefeldt, S.; Feist, J., Two-colour phosphor thermometry for surface temperature measurement. *Optics & Laser Technology* **2006**, *38* (4), 257-265.
62. Suzuki, M.; Tseeb, V.; Oyama, K.; Ishiwata, S. i., Microscopic detection of thermogenesis in a single HeLa cell. *Biophysical Journal* **2007**, *92* (6), L46-L48.
63. Peng, H.; Song, H.; Chen, B.; Wang, J.; Lu, S.; Kong, X.; Zhang, J., Temperature dependence of luminescent spectra and dynamics in nanocrystalline Y<sub>2</sub>O<sub>3</sub>:Eu<sup>3+</sup>. *The Journal of Chemical Physics* **2003**, *118* (7), 3277-3282.
64. Svelto, O., Principles of Lasers. **2010**.
65. Marta, Q.; Eugenio, C.; Fernando, C.; Marina, V.; Amador, C. C., Temperature Sensing with Up-Converting Submicron-Sized LiNbO<sub>3</sub>:Er<sup>3+</sup>/Yb<sup>3+</sup> Particles. *Applied Physics Express* **2011**, *4* (2), 022601.
66. Huefner, S., Optical spectra of transparent rare earth compounds. **1978**.
67. Kumar Rai, V., Temperature sensors and optical sensors. *Applied Physics B: Lasers & Optics* **2007**, *88* (2), 297-303.
68. Wade, S. A.; Collins, S. F.; Baxter, G. W., Fluorescence intensity ratio technique for optical fiber point temperature sensing. *Journal of Applied Physics* **2003**, *94* (8), 4743-4756.
69. Quintanilla, M.; Benayas, A.; Naccache, R.; Vetrone, F., Luminescent Nanothermometry with Lanthanide-doped Nanoparticles. In *Thermometry at the Nanoscale*, 2015; pp 124-166.
70. Wang, S.; Westcott, S.; Chen, W., Nanoparticle Luminescence Thermometry. *The Journal of Physical Chemistry B* **2002**, *106* (43), 11203-11209.
71. Rocha, U.; Upendra Kumar, K.; Jacinto, C.; Ramiro, J.; Caamaño, A. J.; García Solé, J.; Jaque, D., Nd<sup>3+</sup> doped LaF<sub>3</sub> nanoparticles as self-monitored photo-thermal agents. *Applied Physics Letters* **2014**, *104* (5), 053703.
72. Dong, N.-N.; Pedroni, M.; Piccinelli, F.; Conti, G.; Sbarbati, A.; Ramírez-Hernández, J. E.; Maestro, L. M.; Iglesias-de la Cruz, M. C.; Sanz-Rodríguez, F.; Juarranz, A.; Chen, F.; Vetrone, F.; Capobianco, J. A.; Solé, J. G.; Bettinelli, M.; Jaque, D.; Speghini, A., NIR-to-NIR Two-Photon Excited CaF<sub>2</sub>:Tm<sup>3+</sup>, Yb<sup>3+</sup> Nanoparticles: Multifunctional Nanoprobes for Highly Penetrating Fluorescence Bio-Imaging. *ACS Nano* **2011**, *5* (11), 8665-8671.
73. Zheng, K.; Liu, Z.; Lv, C.; Qin, W., Temperature sensor based on the UV upconversion luminescence of Gd<sup>3+</sup> in Yb<sup>3+</sup>–Tm<sup>3+</sup>–Gd<sup>3+</sup> codoped NaLuF<sub>4</sub> microcrystals. *Journal of Materials Chemistry C* **2013**, *1* (35), 5502-5507.
74. Ananias, D.; Brites, C. D. S.; Carlos, L. D.; Rocha, J., Cryogenic Nanothermometer Based on the MIL-103(Tb,Eu) Metal–Organic Framework. *European Journal of Inorganic Chemistry* **2016**.
75. Li, D.; Shao, Q.; Dong, Y.; Jiang, J., Thermal sensitivity and stability of NaYF<sub>4</sub>:Yb<sup>3+</sup>, Er<sup>3+</sup> upconversion nanowires, nanorods and nanoplates. *Materials Letters* **2013**, *110*, 233-236.
76. Alencar, M. A. R. C.; Maciel, G. S.; de Araújo, C. B.; Patra, A., Er<sup>3+</sup>-doped BaTiO<sub>3</sub> nanocrystals for thermometry: Influence of nanoenvironment on the sensitivity of a fluorescence based temperature sensor. *Applied Physics Letters* **2004**, *84* (23), 4753-4755.
77. Wawrzynczyk, D.; Bednarkiewicz, A.; Nyk, M.; Strek, W.; Samoc, M., Neodymium (III) doped fluoride nanoparticles as non-contact optical temperature sensors. *Nanoscale* **2012**, *4* (22), 6959-6961.

78. Rocha, U.; Jacinto da Silva, C.; Ferreira Silva, W.; Guedes, I.; Benayas, A.; Martínez Maestro, L.; Acosta Elias, M.; Bovero, E.; van Veggel, F. C. J. M.; García Solé, J. A.; Jaque, D., Subtissue Thermal Sensing Based on Neodymium-Doped LaF<sub>3</sub> Nanoparticles. *ACS Nano* **2013**, *7* (2), 1188-1199.
79. Ishiwada, N.; Fujioka, S.; Ueda, T.; Yokomori, T., Co-doped Y<sub>2</sub>O<sub>3</sub>: Tb<sup>3+</sup>/Tm<sup>3+</sup> multicolor emitting phosphors for thermometry. *Optics Letters* **2011**, *36* (5), 760-762.
80. Millan, A.; Carlos, L. D.; Brites, C. D. S.; Silva, N. J. O.; Pinol, R.; Palacio, F., Organic-inorganic hybrids thermometry. *RSC Nanoscience Nanotechnology* **2016**, *38*, 237-272.
81. Rao, X.; Song, T.; Gao, J.; Cui, Y.; Yang, Y.; Wu, C.; Chen, B.; Qian, G., A Highly Sensitive Mixed Lanthanide Metal–Organic Framework Self-Calibrated Luminescent Thermometer. *Journal of the American Chemical Society* **2013**, *135* (41), 15559-15564.
82. D'Vries, R. F.; Álvarez-García, S.; Snejko, N.; Bausá, L. E.; Gutiérrez-Puebla, E.; de Andrés, A.; Monge, M. Á., Multimetal rare earth MOFs for lighting and thermometry: tailoring color and optimal temperature range through enhanced disulfobenzoic triplet phosphorescence. *Journal of Materials Chemistry C* **2013**, *1* (39), 6316-6324.
83. Han, Y.-H.; Tian, C.-B.; Li, Q.-H.; Du, S.-W., Highly chemical and thermally stable luminescent Eu x Tb 1–x MOF materials for broad-range pH and temperature sensors. *Journal of Materials Chemistry C* **2014**, *2* (38), 8065-8070.
84. Ceron, E. N.; Rodriguez Gattorno, G.; Guzman-Mendoza, J.; Garcia-Hipolito, M.; Falcony, C., Photoluminescence response of HfO<sub>2</sub>:Eu<sup>3+</sup> obtained by hydrothermal route. *Open Journal of Synthesis Theory and Applications* **2013**, *2*, 73-77.
85. Binnemans, K.; Görrler-Walrand, C., Application of the Eu<sup>3+</sup> ion for site symmetry determination. *Journal of rare earths* **1996**, *14* (3), 173-180.
86. Planelles-Aragó, J.; Cordoncillo, E.; Ferreira, R. A.; Carlos, L. D.; Escribano, P., Synthesis, characterization and optical studies on lanthanide-doped CdS quantum dots: new insights on CdS→lanthanide energy transfer mechanisms. *Journal of Materials Chemistry* **2011**, *21* (4), 1162-1170.
87. Horrocks, W. D.; Sudnick, D. R., Lanthanide ion luminescence probes of the structure of biological macromolecules. *Accounts of Chemical Research* **1981**, *14* (12), 384-392.
88. Ferreira, R. A. S.; Nolasco, M.; Roma, A. C.; Longo, R. L.; Malta, O. L.; Carlos, L. D., Dependence of the Lifetime upon the Excitation Energy and Intramolecular Energy Transfer Rates: The 5D<sub>0</sub> Eu<sup>III</sup> Emission Case. *Chemistry – A European Journal* **2012**, *18* (38), 12130-12139.
89. Montes, E.; Ceron, P.; Rivera Montalvo, T.; Guzman, J.; Garcia-Hipolito, M.; Soto-Guzman, A. B.; Garcia-Salcedo, R.; Falcony, C., Thermoluminescent characterization of HfO<sub>2</sub>:Tb<sup>3+</sup> synthesized by hydrothermal route. *Applied Radiation and Isotopes* **2014**, *83*, 196-199.
90. Ananias, D.; Paz, F. A. A.; Yufit, D. S.; Carlos, L. D.; Rocha, J., Photoluminescent Thermometer Based on a Phase-Transition Lanthanide Silicate with Unusual Structural Disorder. *Journal of the American Chemical Society* **2015**, *137* (8), 3051-3058.





# Chapter 5: Relaxometry



## Table of contents

Introduction.....	192
I - Magnetic Resonance Imaging (MRI) background .....	195
I. 1. Magnetism.....	195
I. 1. a. Spin .....	195
I. 1. b. Atoms or ions spin orbital momentum .....	196
I. 1. c. Magnetic properties of a material.....	197
I. 1. d. Some magnetic parameters .....	199
I. 2. Magnetic Resonance Imaging (MRI) .....	199
I. 2. a. Spin and resonance .....	199
I. 2. b. Relaxation phenomenon .....	201
I. 2. c. Image contrast <b>T1</b> and <b>T2</b> weighting.....	203
I. 2. d. Types of MRI contrast agents.....	204
I. 3. Examples in biomedicine.....	205
I. 3. a. Gd <sup>3+</sup> - based contrast agents .....	205
I. 3. b. Iron based MRI agents.....	208
I. 3. c. Lanthanide-based MRI agents .....	209
II - Results and discussion.....	211
II. 1. Low magnetic field (20 MHz).....	211
II. 2. High magnetic field (400 and 500 MHz).....	216
Conclusion .....	217
Experimental part.....	218
Bibliography.....	219

## Introduction

Magnetic resonance imaging (MRI) is a widely used non-invasive tool to visualize soft tissues in the body [1]. Among the benefits of this technique are: (i) the high resolution leading to anatomical information, useful for instance in cancer diagnostics, and (ii) the absence of ionizing radiation. MRI is based on the detection of NMR signals originated by protons of water and fat molecules in the body when placed in a magnetic field. A magnetic field is applied to the region of interest, which is then modulated by radio waves. The nuclear proton magnetic moments interact with the incident radio waves, and the absorption of photons leads to magnetic effect in the tissue that can be exploited to produce MRI images [2].

The key advantage of MRI is that it is safer for the patients than other imaging techniques that use highly ionizing radiations, such as X-rays in computed tomography (CT) [3], or gamma radiation emitted in Positron Emission Tomography (PET) [4-5]. Compared to CT, MRI provides a much higher contrast between the different soft tissues of the body. Compared with PET, despite its lower sensitivity, MRI provides a higher spatial resolution (around  $1 \times 1 \times 1 \text{ mm}^3$ ). Therefore, in modern medicine, MRI has emerged as one of the most powerful techniques for the diagnosis and treatment of human diseases [6].

The main limitation of MRI is its low sensitivity, which may be improved using clinical scanners with high magnetic fields ( $B_0$ ), commonly 1.5 to 3.0 Tesla, in 25,000 MRI systems used worldwide. The largest human MRI scanner is present at NeuroSpin research centre in Saclay, France, equipped with the most powerful magnet in the world, generating a magnetic field of 11.7 Tesla (Figure 1).  $B_0$  values of 7 T to 17.2 T are used in pre-clinical MRI research. However, these high field instruments are prohibitively expensive for normal clinical use, and very high fields also limit the attainable resolution.



Figure 1: The MRI magnet of the NeuroSpin CEA research centre, Saclay, France, weights 130 tons and produces a magnetic field of 11.7 Tesla.

Another technological advancement is the capability to enhance the MRI image contrast between normal and diseased tissues by injecting compounds that influence some property of the water protons in order to visualize an effect. Such MRI contrast agents may be paramagnetic, superparamagnetic, or ferromagnetic compounds that shorten the  $T_1$  (spin-lattice) or  $T_2$  (spin-spin) relaxation times of protons located in their surroundings. This effect is due to an increase in the rate of change of high nuclear energy spin states (proton spin aligned against the applied magnetic field) to low nuclear energy spin states (proton spin aligned along the applied magnetic field). Contrast agents are used *in vivo* at a much lower concentration than the surrounding water protons. By acting on the relaxation properties of water protons close to them, they induce contrast between normal and diseased tissue when they concentrate in the later tissue.

Image contrast depends on variations in intrinsic parameters of the tissue protons, such as proton density and relaxation times, between different tissues.  $T_1$  contrast agents are usually based on  $Gd^{3+}$  ions coordinated to a multidentate chelating molecule, such as Gd-DTPA, see Figure 2 (where diethylenetriaminepentaacetic acid (DTPA), 1,4,7,10-tetracarboxymethyl-1,4,7,10-tetraazacyclododecane (DOTA)). Paramagnetic  $Gd^{3+}$  ion is responsible for changing the contrast by shortening the relaxation times of the surrounding hydrogen protons [7-8].

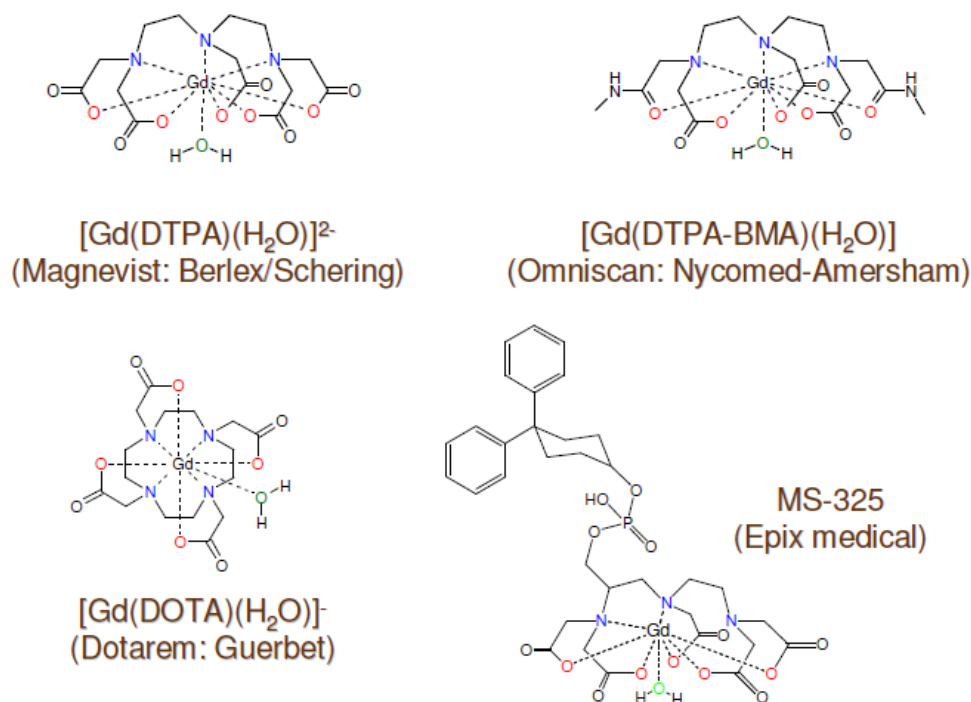


Figure 2: Schematic representation of the molecular structures of some commercial contrast agents. The brand names are given in brackets.

This thesis aims at producing alternative gadolinium-containing contrast agents for magnetic resonance imaging based on hafnium oxide nanoparticles, and to characterizing their relaxivity.

## I - Magnetic Resonance Imaging (MRI) background

Our goal is to synthesize nanoparticles (NPs) with several functionalities. In this part, we will focus on the use of NPs as contrast agents for magnetic resonance imaging. This implies that the material itself has to be magnetic. The first part will introduce the concepts and fundamental theory of magnetic properties in the solid state. The second part will introduce the magnetic resonance imaging concepts.

### I. 1. Magnetism

#### I. 1. a. Spin

The spin is an intrinsic quantum property depending on the characteristics of each particle such as type, mass and electric charge. As every quantum parameter, the spin values are discrete and are subjected to the uncertainty principle. For a particle with a spin quantum number  $S = 1/2$  (e.g., an electron), there are only two distinct spin states characterized by  $m_s = \pm 1/2$  where  $m_s$  is the spin magnetic number.

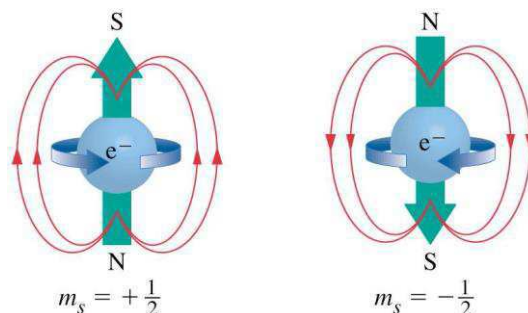


Figure 3: The two distinct spin states of an electron [9]

The orbital magnetic moment  $\vec{\mu}_L$  of a particle (of charge,  $q$ , and mass,  $m$ ) can be defined as:

$$\vec{\mu}_L = \frac{q}{2m} \vec{L} \quad (1)$$

where  $\vec{L}$  is the orbital angular momentum. To the orbital magnetic moment of a particle (of charge,  $q$ , and mass,  $m$ ), a spin magnetic moment ( $\vec{\mu}_S$ ) is associated according to:

$$\vec{\mu}_S = g \frac{q}{2m} \vec{S} \quad (2)$$

where  $\vec{S}$  the spin angular momentum and  $g$  is a dimensionless quantity called Landé  $g$  - factor. The  $g$  value depends on the particles type (e.g., for the electron,  $g$  is 2.0023).

Furthermore, the total magnetic moment is the sum of the orbital magnetic moment and the spin magnetic moment:

$$\vec{\mu} = \vec{\mu}_L + \vec{\mu}_S = \mu_B \vec{L} + \mu_B g \vec{S} = \mu_B (\vec{L} + g \vec{S}) \quad (3)$$

where  $L$  is the orbital angular momentum quantum number,  $S$  the spin angular momentum quantum number,  $\mu_B$  the Bohr magneton.

An electron is characterized by  $S = 1/2$  and  $g = 2.0023$ , we introduce the Bohr magneton (symbol  $\mu_B$ ), a physical constant and the natural unit for expressing the magnetic moment of an electron caused by either its orbital or spin angular momentum:

$$\mu_B = \frac{e\hbar}{2m_e} = 9.274 \times 10^{-24} \text{ JT}^{-1} \quad (4)$$

### 1. 1. b. Atoms or ions spin orbital momentum

The spin of atoms or ions, made of several stable elementary particles (protons, neutrons and electrons), results from the spin and orbital momentum of the individual particles. A diamagnetic atom has no unpaired electrons ( $\mu = 0$ ) whereas a paramagnetic atom has unpaired electrons and, thus, it has a permanent magnetic moment  $\mu$ , resulting from these electrons.

The effective magnetic moment,  $\mu_{eff}$ , (Langevin) of atoms or ions, when no orbital contribution is present, is given by:

$$\mu_{eff} = g_e \sqrt{S(S+1)} \times \mu_B \quad (5)$$

$g_e$  can be replaced by 2 and  $S$  by  $n/2$ , where  $n$  is the number of unpaired electrons:

$$\mu_{eff} = \sqrt{n(n+2)} \times \mu_B \quad (6)$$

This formula represents the contribution of the paramagnetic susceptibility due only to the electron spin. However, if the metal ion has a ground state  $^{(2S+1)}\Gamma$  with an orbital angular moment, the formula becomes:

$$\mu_{eff} = g_J \sqrt{J(J+1)} \times \mu_B \quad (7)$$

where  $J$  is the total angular moment ( $J = L + S$ ) and  $g_J$  (the Landé g factor) is defined by the following expression:

$$g_J = \frac{3}{2} + \frac{[S(S+1) - L(L+1)]}{2J(J+1)} \quad (8)$$

Table 1 lists the magnetic properties of the rare-earth trivalent cations, where Gd<sup>3+</sup> shows the highest  $g_J$  value compared to the other rare-earth elements (7 unpaired electrons).

Ln <sup>III</sup>	Conf.	n	Ground state	1 <sup>st</sup> exc. state	$\Delta E/\text{cm}^{-1}$	$g_J$	$\mu_{\text{calc}}$ (3-28)	$\mu_{\text{exp}}$
Ce	f <sup>1</sup>	1	<sup>2</sup> F <sub>5/2</sub>	<sup>2</sup> F <sub>7/2</sub>	2200	0.86	2.54	2.5-2.8
Pr	f <sup>2</sup>	2	<sup>3</sup> H <sub>4</sub>	<sup>3</sup> H <sub>5</sub>	2100	0.80	3.58	3.2-3.6
Nd	f <sup>3</sup>	3	<sup>4</sup> I <sub>9/2</sub>	<sup>4</sup> I <sub>11/2</sub>	1900	0.73	3.62	3.2-3.6
Pm	f <sup>4</sup>	4	<sup>5</sup> I <sub>4</sub>	<sup>5</sup> I <sub>5</sub>	1600	0.60	2.68	
Sm	f <sup>5</sup>	5	<sup>6</sup> H <sub>5/2</sub>	<sup>6</sup> H <sub>7/2</sub>	1000	0.29	0.85	1.3-1.5
Eu	f <sup>6</sup>	6	<sup>7</sup> F <sub>0</sub>	<sup>7</sup> F <sub>1</sub>	300		0	3.1-3.4
Gd	f <sup>7</sup>	7	<sup>8</sup> S <sub>7/2</sub>	<sup>6</sup> P <sub>7/2</sub>	32000	2.00	7.94	7.9-8.1
Tb	f <sup>8</sup>	6	<sup>7</sup> F <sub>6</sub>	<sup>7</sup> F <sub>5</sub>	2000	1.50	9.72	9.2-9.7
Dy	f <sup>9</sup>	5	<sup>6</sup> H <sub>15/2</sub>	<sup>6</sup> H <sub>13/2</sub>	3300	1.33	10.65	10.1-10.6
Ho	f <sup>10</sup>	4	<sup>5</sup> I <sub>8</sub>	<sup>5</sup> I <sub>7</sub>	5300	1.25	10.61	10.0-10.5
Er	f <sup>11</sup>	3	<sup>4</sup> I <sub>15/2</sub>	<sup>4</sup> I <sub>13/2</sub>	6500	1.20	9.58	9.2-9.6
Tm	f <sup>12</sup>	2	<sup>3</sup> H <sub>6</sub>	<sup>3</sup> F <sub>4</sub>	5800	1.17	7.56	7.0-7.3
Yb	f <sup>13</sup>	1	<sup>2</sup> F <sub>7/2</sub>	<sup>2</sup> F <sub>5/2</sub>	10000	1.14	4.54	4.3-4.6

Table 1: Effective magnetic moments of 4f trivalent ions at 250 °C [9]

### 1. 1. c. Magnetic properties of a material

The magnetic properties of a material depend strongly on the electronic structure of the elements constitutive of this material. Diamagnetism comes from the electron circulation in atoms or molecules and is present as a negative contribution to the external magnetic field. This is generally a weak type of magnetism, which is valid for elements having full electron shells. The presence of unpaired electrons gives rise to a paramagnetic behavior, as described by the Curie law [10]:

$$\chi = \frac{C}{T} \quad (9)$$

where  $\chi$  is the magnetic susceptibility (representing the ability of the material to be magnetized in an external magnetic field),  $C$  is the Curie constant and  $T$  is the temperature in Kelvin. If a paramagnetic material is placed in an external magnetic field, the independent magnetic moments tend to align with the field and increase the total magnetic flux density. This alignment is temporary and when the external field is removed the moments immediately

become randomly oriented. In ferromagnetic materials, with a high density of states near the Fermi level, a cooperative influence produces magnetic domains. These domains consist of aligned magnetic moments which are strongly coupled to each other. Ferromagnetic materials usually have a very small net magnetic moment as the individual domains tend to magnetically compensate each other. When exposed to an external field, the internal magnetic moments align parallel to the field and the total magnetic field is enhanced. Ferromagnetic behavior is quite rare but it is shown for example by metals such as iron [11], nickel [12], cobalt [13] and gadolinium [14] in their metallic states. Above the so-called Curie temperature ( $T_C$ ), the thermal energy randomizes the magnetic spins and, thus, at high temperatures, ferromagnetic materials show a paramagnetic behavior. The magnetic susceptibility of ferromagnetic materials above the Curie temperature is described by the Curie-Weiss law [9]:

$$\chi = \frac{C}{T - \theta} \quad (10)$$

where  $\theta$  is the paramagnetic Curie temperature or the Weiss constant, which usually is slightly higher than  $T_C$ . Gadolinium is unusual, with a  $T_C$  of 293 K (which is approximately room temperature), whereas iron, nickel and cobalt have  $T_C$  values of about 1043, 630 and 1395 K respectively [15-16]. The temperature dependency of the magnetic susceptibility is illustrated in Figure 4 for a paramagnetic and a ferromagnetic material.

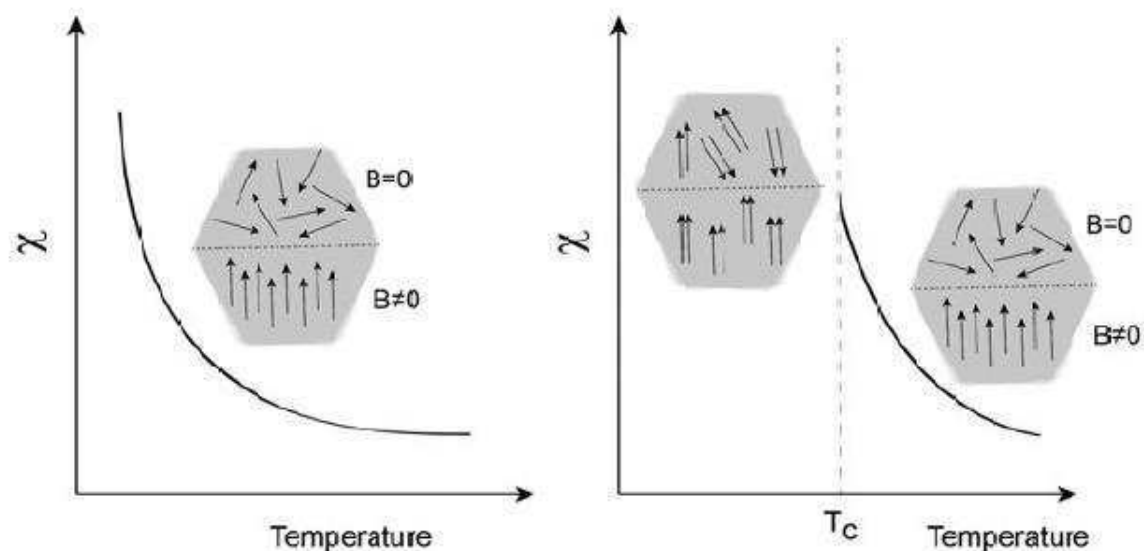


Figure 4: Schematic illustration showing the magnetic susceptibility of paramagnetic (left) and ferromagnetic (right) materials at different temperatures.

Another kind of magnetic behavior is observed in antiferromagnetic materials whose spins are coupled in an anti-parallel manner up to the Neel temperature ( $T_N$ ). Antiferromagnetic materials obey the Curie-Weiss law but, in contrast to the ferromagnetic materials, they have a negative Weiss constant.

The magnetic properties of NPs are influenced by both chemical composition and size of the nanoparticles. Superparamagnetism is an example of a size effect present in small iron oxide NPs with a size smaller than the ferromagnetic domains constitutive of the corresponding bulk material. The strong cooperative force aligning the spins in a specific direction is diminished in the small nanoparticle, and the spins can hence flip to the opposite direction in the absence of an applied field. As the flip time reversing the nanoparticle magnetic field is very short, the net magnetization appears to be zero. This behavior is very similar to paramagnetic ones with the main difference that it occurs below the Curie temperature.

#### I. 1. d. Some magnetic parameters

The first parameter to be defined here is the magnetic field,  $B$  or  $H$  in Tesla (T) or in Oersted (Oe), the second one the magnetization,  $M$ , in  $\text{emu}\cdot\text{mol}^{-1}$  or in  $\text{cm}^3\cdot\text{mol}^{-1}$ , the third is the magnetic susceptibility,  $\chi$ , in  $\text{emu}\cdot\text{K}\cdot\text{mol}^{-1}$ , or in  $\text{cm}^3\cdot\text{K}\cdot\text{mol}^{-1}$ , and the fourth one is the magnetic moment,  $\mu$ , in  $\mu_B$ .

### I. 2. Magnetic Resonance Imaging (MRI)

Magnetic Resonance Imaging (MRI) is a non-invasive technique that generates images of body soft tissues using nuclear magnetic resonance (NMR) principles. Nuclear magnetic resonance is a phenomenon involving atomic nuclei with a magnetic moment, such as  $^1\text{H}$ ,  $^{13}\text{C}$  and  $^{31}\text{P}$ , which absorb a specific energy amount when placed in a magnetic field. The most commonly used nucleus for imaging in biological systems is the hydrogen nucleus ( $^1\text{H}$ ) because of its abundance in the human body composed mainly of water and fat containing hydrogen atoms. Without the presence of the external field, the spin vectors are randomly oriented in space and result in no bulk magnetization.

#### I. 2. a. Spin and resonance

Under an external magnetic field  $B_0$  parallel to the  $Oz$  axis, the nuclear spin vectors align either parallel or antiparallel to the external field. Moreover, when the spins align within the magnetic field, they precess (a rotational movement of the spins describing a double cone

around  $B_0$  axis, called the Larmor precession) around  $B_0$  at an angle of  $54.7^\circ$  (called magical angle) [17]. Furthermore, there is an energy splitting between the two nuclear spin states ( $+1/2$  and  $-1/2$ ). Due to the higher stability of the fundamental ground state, the number of parallel spins is higher than those of antiparallel spins and a net magnetization ( $M_{z0}$ ) is created along the Oz axis (cf. figure 5).

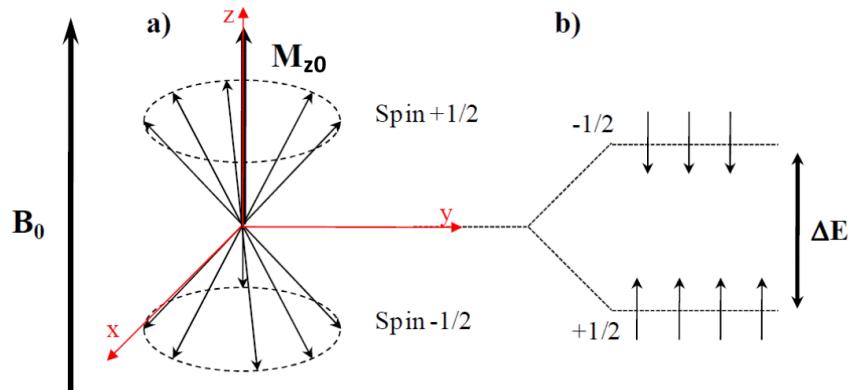


Figure 5: a) Magnetic moments of protons under a magnetic field  $B_0$ . At the equilibrium, the total magnetization is parallel to  $B_0$ . b) Protons partition by energy levels at equilibrium under a magnetic field  $B_0$ . [18]

When a specific energy amount that fulfills the resonance condition, is applied to the system, spin states are excited. The frequency corresponding to this specific energy amount is proportional to the applied field strength according to [17, 19]:

$$\omega = \gamma \times B_0 \quad (11)$$

where  $\omega$  is called the Larmor frequency (MHz),  $\gamma$  is the gyromagnetic ratio of the specific nucleus and  $B_0$  is the magnetic field strength (T). For example, the proton gyromagnetic ratio is  $\gamma = 42.58 \text{ MHz} \cdot \text{T}^{-1}$ , and for which  $B_0 = 1.5 \text{ T}$  results in a Larmor frequency of  $63.9 \text{ MHz}$ , in the radio frequency range [17].

Applying a radiofrequency pulse  $B_1$  induces a change in the spin states distribution that can be detected as a changed overall magnetization. For example, when a  $90^\circ$  radiofrequency pulse is applied with a  $B_1$  magnetic field along the Ox axis, the  $M_z$  magnetization disappears after excitation, and a  $M_{xy}$  transverse magnetization is created as the spins precess (rotate) in the Ozy plane perpendicular to  $B_1$ . A short delay after excitation, when  $B_1$  is turned off, the  $M_{z0}$  magnetization will be regained and the equilibrium state recovered. The return to the ground state from the excited state process is called spin-relaxation (cf. figure 6).

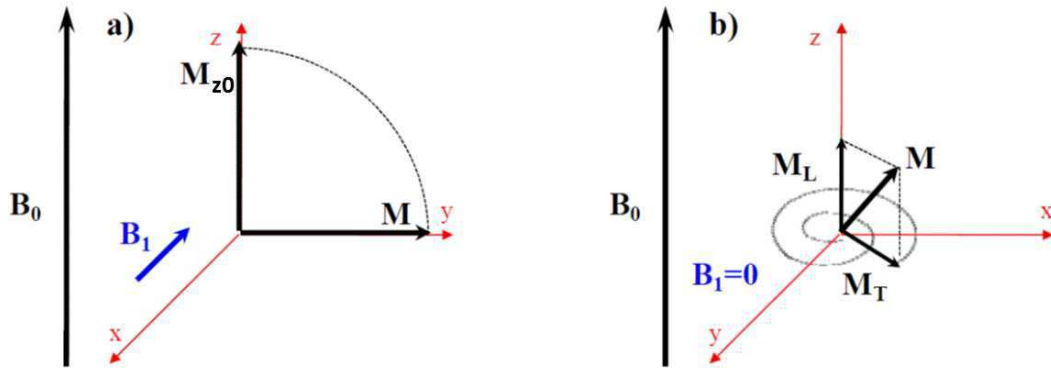


Figure 6: Magnetization modification ( $M_{z0} \rightarrow M$ ) under a radiofrequency pulse  $B_1$  b) Magnetization  $M$  relaxes to equilibrium  $M_{z0}$ . [18]

### 1. 2. b. Relaxation phenomenon

The main relaxation processes which influence the magnetic resonance signal are those described by two  $T_1$  and  $T_2$  relaxation times.

#### 1. 2. b. i. $T_1$ relaxation or longitudinal relaxation time

As these relaxation processes have a first order kinetics (Bloch equations), the magnetization changes are exponential and can be described by their rate constants,  $R_1 = 1/T_1$  and  $R_2 = 1/T_2$ .  $T_1$  is a time constant describing the exponential process of  $M_z$  returning to its equilibrium value,  $M_{z0}$ .  $T_1$  is usually called the longitudinal time constant or the spin lattice relaxation time constant [20]. This relaxation time depends on interactions between the hydrogen nucleus and fluctuating magnetic dipoles in its close environment. Here is the longitudinal relaxation expression [19] as a function of  $T_1$ :

$$M_z = M_{z0}(1 - e^{-\frac{t}{T_1}}) \quad (12)$$

where  $t$  is the time. A schematic illustration of  $M_z$  magnetization recovery after an applied  $90^\circ$  pulse is shown in figure 6 by  $M_L$ .

#### 1. 2. b. ii. $T_2$ relaxation or transverse relaxation time

On the other hand,  $T_2$  is a time constant describing the process of  $M_{xy}$  decay to zero after excitation.  $T_2$  is often called the transverse relaxation time constant or the spin-spin relaxation time constant [20]. This relaxation time depends on precessing protons dephasing after excitation. As the different spins experience small differences in the magnetic field,

dephasing occurs as they precess at slightly different frequencies. Here is the transverse relaxation expression [19]:

$$M_{xy} = M_{xy0} e^{-\frac{t}{T_2}} \quad (13)$$

where  $t$  is the time. A schematic illustration of phase coherence loss in the (Oxy) plane after an applied  $90^\circ$  pulse is shown in figure 6 by  $M_T$ .

In equations (12) and (13), we can see that  $M_z$  is a function that increases with time which approaches  $M_{z0}$  for long  $t$  values whereas  $M_{xy}$  is a decreasing function with time. If  $t = T_1$  then  $M_z \approx 0.63 M_{z0}$ , whereas if  $t = T_2$  the transverse magnetization  $M_{xy}$  decreases by a factor of  $e^{-1}$  (cf. equation (13)). Furthermore, the shapes of these two functions are dependent on the specific  $T_1$  and  $T_2$  values (Figure 7). Moreover, the  $T_1$  and  $T_2$  relaxation processes are entirely independent of one another but occur simultaneously. The decay of the transverse magnetization  $M_{xy}$  is always faster than (or equal to) the increase of the longitudinal magnetization  $M_z$ . This means that  $T_2$  is always shorter than or equal to the  $T_1$  [19].

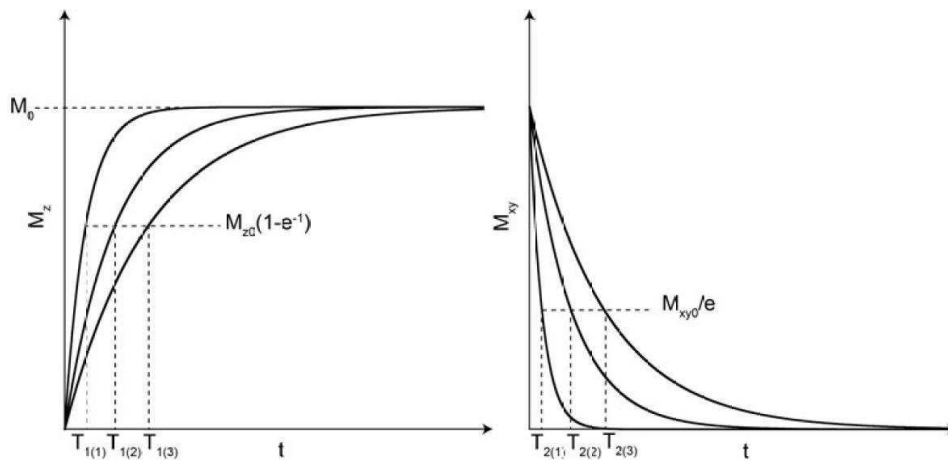


Figure 7: Graphs featuring  $M_z$  magnetization recover and  $M_{xy}$  magnetization decay. Graphs were plotted by using  $T_{1(1,2,3)} = 500, 1200$  and  $2000$  ms and  $T_{2(1,2,3)} = 300, 1000$  and  $1800$  ms [21].

### 1. 2. b. iii. $T_1$ and $T_2$ measurement

A vast number of different pulse sequences are used in spin states excitation in MRI.  $T_1$  and  $T_2$  relaxation times can be monitored using an inversion recovery pulse sequence and a spin echo pulse sequence, respectively (Figure 8). In the inversion recovery sequence, a  $180^\circ$  pulse rotates the magnetization to the negative z-direction, which, after partial recovery during the time delay (TI), is monitored by a  $90^\circ$  reading pulse, which rotates it into the XY plane. By

studying the longitudinal magnetization at various time delays after excitation, an exponential curve is mathematically fitted to the measured points and from this curve  $T_1$  is determined.

In the spin echo sequence, the magnetization is flipped into the x-y plane by a  $90^\circ$  pulse. The spins start to dephase and the x-y magnetization decreases gradually. The spins are refocused by applying a  $180^\circ$  pulse at a certain time points and a signal (echo) can be recorded at a time equal to the echo time.  $T_2$  is calculated from a curve fitted to the transverse magnetization magnitude for different echo times.

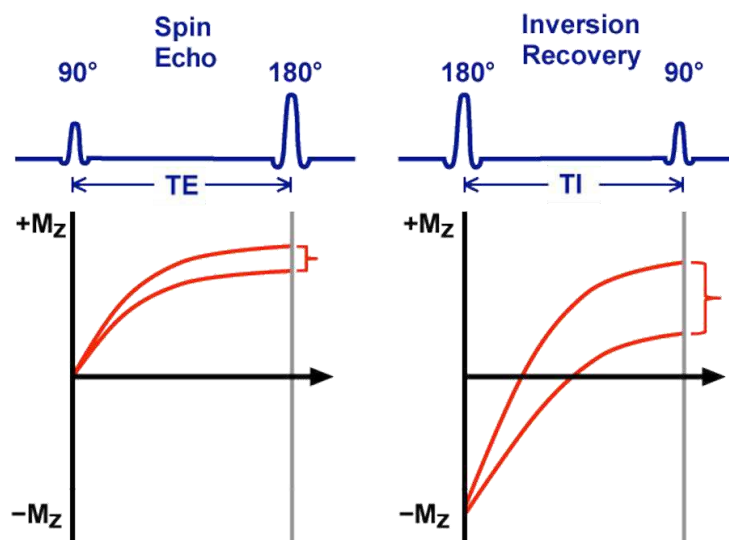


Figure 8: Spin echo and inversion recovery pulse sequences [22]

### 1. 2. c. Image contrast $T_1$ and $T_2$ weighting

Contrast in magnetic resonance imaging can be affected by intrinsic factors, such as  $T_1$ ,  $T_2$  and density of tissue protons, or by extrinsic factors. The later can be changed in the measurement by modifying, for example, the echo time (TE) and repetition time (TR), which is the time between the repeated units of pulses. The choice of TE and TR strongly affects the signal intensity,  $S$ , when using spin echo sequences as follows (valid when  $TR \gg TE$ ) [19]:

$$S = k\rho(1 - e^{-\frac{TR}{T_1}}) e^{-\frac{TE}{T_2}} \quad (14)$$

where  $k$  is a constant and  $\rho$  the spin density in the sample. For example, the choice of a very long TR induces a full recovery on  $M_z$  the magnetization before the application of the next excitation pulse takes place. This implies that tissues with different  $T_1$  values cannot be distinguished. On the contrary, when choosing a short TR, a strong  $T_1$  effect can be achieved

separating structures with different  $T_1$  values in the image. Thus, the repetition time can be used to control  $T_1$ -weighting degree. The  $T_2$ -weighting degree can be also controlled by TE choice. In general, the use of pulse sequences with long TE increases the ability to distinguish between tissues having different  $T_2$  relaxation times. However, the optimal choice of TR and TE depends on specific tissues [17].

#### I. 2. d. Types of MRI contrast agents

From the physical point of view, MRI contrast agents can be classified into two broad categories.

- $T_1$  contrast agents, which usually enhance the longitudinal (spin – lattice) relaxation rates ( $R_1$ ) of water protons present in tissue more than the transverse (spin – spin) relaxation rates ( $R_2$ ). The addition of such contrast agents causes the nuclei to appear as bright spots of increased intensity on  $T_1$  weighted images due to the increased relaxation rate. Thus, these are positive contrast agents. Interaction between the excited nuclei and their surrounding environment gives rise to the  $T_1$  (spin – lattice) relaxation process. Examples of such contrast agents are gadolinium or manganese chelates [1, 7].
- $T_2$  contrast agents, on the other hand, largely increase transverse (spin – spin) relaxation rates ( $R_2$ ) and cause a decrease in signal intensity. Therefore, these are negative contrast agents. Relaxation caused by  $T_2$  agents arises from the interaction between the excited nuclei and those with lower energy. Superparamagnetic iron oxide particles are  $T_2$  agents [23-24].

The majority of the MRI contrast agents are complexes of  $Gd^{3+}$ , an ion that lies at the midpoint of the lanthanide series. It has the maximum number of unpaired electrons (seven) among all lanthanide ions and, thus, a large magnetic moment (7.9  $\mu_B$ ). This, coupled with a long electronic relaxation time (1 – 10 ps) [25], makes  $Gd^{3+}$  the best relaxation agent candidate. However, free  $Gd^{3+}$  is extremely toxic both *in vivo* as well as *in vitro* because its ionic radius (93.8 pm) is nearly equal to that of  $Ca^{2+}$ , resulting in strong binding to biological systems where  $Ca^{2+}$  is needed, such as calcium channels and calcium-binding proteins. In order to ensure the safe clinical use,  $Gd^{3+}$  must be complexed with organic chelating ligands with which it exhibits very strong association constants. It then forms kinetically inert and thermodynamically stable complexes with these multidentate organic ligands. Since the coordination number of  $Gd^{3+}$  is

nine, octodentate ligands are particularly suited, as in stable complexes the ninth coordinate bond is formed by a water molecule. The N and O donor atoms of the organic ligand together with a single water molecule attached directly to the central ion ( $Gd^{3+}$ ) lie on the primary coordination sphere. Solvent molecules weakly interact with chelated  $Gd^{3+}$  and, thus, occupy the secondary coordination sphere. Diethylenetriaminepentaacetic acid (DTPA), 1,4,7,10-tetracarboxymethyl-1,4,7,10-tetraazacyclododecane (DOTA), and some of their derivatives (Figure 2) have already been approved for clinical use because they form stable complexes with  $Gd^{3+}$  [7, 26-28].

### I. 3. Examples in biomedicine

#### I. 3. a. $Gd^{3+}$ - based contrast agents

The inverse of the relaxation time defines the relaxation rate ( $R_i = 1/T_i$ ). The contrast agent (CA) relaxivity can be defined by the paramagnetic relaxation rate enhancement per mM concentration of CA. It can be calculated by plotting relaxation rates as a function of contrast agent concentration. A linear function appears and the slope gives the relaxivity ( $r_i$ ) in  $mM^{-1}.s^{-1}$  according to [29]:

$$\frac{1}{T_i} = \left(\frac{1}{T_i}\right)_d + r_i[CA] \quad i = 1, 2 \quad (15)$$

where  $[CA]$  represents contrast agent concentration and  $d$  stands for diamagnetic contribution (*i.e.*, the solvent relaxation rate in the absence of the contrast agent). The  $r_2/r_1$  values are often also reported. Positive contrast agents usually have  $r_2/r_1$  ratios in the range of 1 to 2 whereas negative contrast agents can have  $r_2/r_1$  ratios around 10 or even more [30].

The measured longitudinal proton relaxation rate,  $R_1^{obs} = 1/T_1^{obs}$ , is the sum of a paramagnetic ( $R_1^p$ ) and a diamagnetic ( $R_1^d$ ) contribution as expressed in equation (16), where  $r_1$  is the proton relaxivity:

$$R_1^{obs} = R_1^d + R_1^p = R_1^d + r_1[Gd^{3+}] \quad (16)$$

A similar expression applies for  $r_2$ .

The relaxivity can be divided into an inner and outer sphere term as follows:

$$r_1 = r_{1is} + r_{1os} \quad (17)$$

The inner sphere term is given in equation (18), where  $q$  is the number of inner sphere water molecules [31].

$$r_{1is} = \frac{1}{1000} \times \frac{q}{55.55} \times \frac{1}{T_{1m}^H + \tau_m} \quad (18)$$

The longitudinal and transverse relaxation rates of inner sphere protons,  $R_{1M} = 1/T_{1m}^H$  and  $R_{2M} = 1/T_{2m}^H$  are expressed by equations (19) and (20), where  $r_{GdH}$  is the effective distance between the electron charge and the  $^1\text{H}$  nucleus,  $\omega_I$  is the proton resonance frequency and  $\omega_S$  is the Larmor frequency of the  $\text{Gd}^{3+}$  electron spin.

$$R_{1M} = \frac{1}{T_{1m}^H} = \frac{2}{15} \left( \frac{\mu_0}{4\pi} \right)^2 \frac{\hbar^2 \gamma_I^2 \gamma_S^2}{r_{GdH}^6} S(S+1) \times [3J(\omega_I; \tau_{d1}) + 7J(\omega_S; \tau_{d2})] \quad (19)$$

$$R_{2M} = \frac{1}{T_{2m}^H} = \frac{1}{15} \left( \frac{\mu_0}{4\pi} \right)^2 \frac{\hbar^2 \gamma_I^2 \gamma_S^2}{r_{GdH}^6} S(S+1) \times [4J(0) + 3J(\omega_I; \tau_{d1}) + 13J(\omega_S; \tau_{d2})] \quad (20)$$

$$\frac{1}{\tau_{di}} = \frac{1}{\tau_m} + \frac{1}{\tau_{RH}} + \frac{1}{T_{ie}} \quad i = 1, 2 \quad (21)$$

where  $\tau_{di}$ ,  $\tau_m$ , and  $\tau_{RH}$  are the total correlation time for the dipolar interaction and the correlation times for water exchange and for the rotation of the  $\text{Gd} - \text{H}_{\text{water}}$  vector, while  $T_{ie}$  are the electrons spin relaxation (or correlation) times (equation (21) and Figure 9).  $R_{2M}$  differs from  $R_{1M}$  mainly in the first term. It is well-known in NMR that frequencies near zero contribute to  $R_2$  but not to  $R_1$  (first term). This term originates from the  $J(0)$  term [1].

For small molecular weight chelates (fast rotation), the spectral density function is expressed as in equation (22):

$$J(\omega; \tau) = \left( \frac{\tau}{1 + \omega^2 \tau^2} \right) \quad (22)$$

The longitudinal and transverse electronic relaxation rates,  $1/T_{1e}$  and  $1/T_{2e}$ , are expressed by equations (23) and (24), where  $\tau_V$  is the electronic correlation time for the modulation of the zero-field-splitting interaction and  $\Delta^2$  is the mean square zero-field-splitting energy.

$$\left( \frac{1}{T_{1e}} \right)^{ZFS} = \frac{1}{25} \Delta^2 \tau_V [4S(S+1) - 3] \left( \frac{1}{1 + \omega_S^2 \tau_V^2} + \frac{4}{1 + 4\omega_S^2 \tau_V^2} \right) \quad (23)$$

$$\left(\frac{1}{T_{2e}}\right)^{ZFS} = \Delta^2 \tau_V \left( \frac{5.26}{1 + 0.372 \omega_S^2 \tau_V^2} + \frac{7.18}{1 + 1.24 \omega_S \tau_V} \right) \quad (24)$$

The outer-sphere contribution can be described by equations (25) and (26), where  $N_A$  is the Avogadro constant,  $D_{GdH}$  is the diffusion coefficient for the diffusion of a water proton away from a  $Gd^{3+}$  complex,  $a_{GdH}$  is the distance of closest approach of the protons to  $Gd^{3+}$  and  $J_{os}$  is its associated spectral density function as given by equation (27), where  $\tau_{GdH}$  is the diffusion correlation time of GdL [32-34].

$$R_{1os} = \frac{32N_A\pi}{405} \left(\frac{\mu_0}{4\pi}\right)^2 \frac{\hbar^2 \gamma_I^2 \gamma_S^2}{a_{GdH} D_{GdH}} S(S+1) [3J_{os}(\omega_I; T_{1e}) + 7J_{os}(\omega_S; T_{2e})] \quad (25)$$

$$R_{2os} = \frac{16N_A\pi}{405} \left(\frac{\mu_0}{4\pi}\right)^2 \frac{\hbar^2 \gamma_I^2 \gamma_S^2}{a_{GdH} D_{GdH}} S(S+1) [4J_{os}(0) + 3J_{os}(\omega_I; T_{1e}) + 13(\omega_S; T_{2e})] \quad (26)$$

$$J_{os}(\omega; T_{je}) = Re \left[ \frac{1 + 14 \left( i\omega\tau_{GdH} + \frac{\tau_{GdH}}{T_{je}} \right)^{\frac{1}{2}}}{1 + \left( i\omega\tau_{GdH} + \frac{\tau_{GdH}}{T_{je}} \right)^{\frac{1}{2}} + 49 \left( i\omega\tau_{GdH} + \frac{\tau_{GdH}}{T_{je}} \right) + 19 \left( i\omega\tau_{GdH} + \frac{\tau_{GdH}}{T_{je}} \right)^{\frac{3}{2}}} \right] \quad (27)$$

$j = 1, 2$

$r_i$  relaxivities are influenced by various parameters, among which are the external magnetic field strength ( $B_0$ ) and the contrast agent metal ion electronic properties. These electronic properties include the magnitude of the magnetic dipole characterized by the spin ( $S$ ) and the correlation time concerning the electron spin relaxation ( $T_{1e,2e}$ ). Other chemically important parameters are the number of water molecules coordinated to the metal ion ( $q$ ), their residence lifetime at the site ( $\tau_M$ ) and the rotational correlation time ( $\tau_R$ ) characterizing the dynamics of the rotation motion of the contrast agent complex in solution (cf. figure 9). At 1.5 T field strengths, the rotational dynamics correlation time ( $\tau_R$ ), which depends on the contrast agent size, shape and internal rigidity, typically is more important than the electron spin relaxation, and thus greatly affects its efficiency [1, 29].

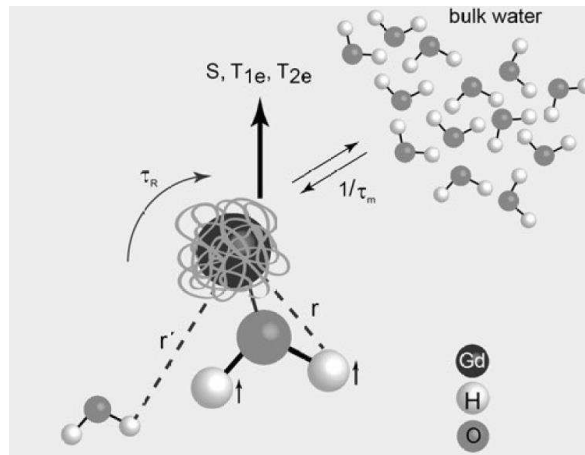


Figure 9: Molecular parameters influencing the  $r_1$  relaxivity induced by a  $Gd^{3+}$  contrast agent [35]

The most efficient contrast agents preferentially have a high number of water molecules coordinated to the metal ( $q$ ), a slow rotational dynamics and a short water residence lifetime to ensure an efficient water exchange and a high relaxivity [1]. However, complexes with  $q > 1$  have usually lower stability.

### 1.3.b. Iron based MRI agents

Two iron oxide contrast agent types exist: superparamagnetic iron oxides (SPIO) and ultrasmall superparamagnetic iron oxides (USPIO). USPIOs, with diameters lower than 40 nm, are constituted by a single iron oxide crystal surrounded by an organic or inorganic coating, while SPIOs have several iron oxide crystals inside the coating and are larger. Suspended colloids of iron oxide NPs constitute these contrast agents which reduce water proton  $T_2$  values of absorbing tissues when they are injected before imaging. SPIO and USPIO have been successfully used for liver tumor enhancement [36]. Furthermore, iron oxide NPs such as magnetite ( $Fe_3O_4$ ) and maghemite ( $\gamma-Fe_2O_3$ ) are promising materials in several biomedical applications [37-39]. As iron is naturally present in metalloproteins, it can be metabolized through its natural metabolic cycle, and for this reason it is considered as nontoxic [40]. NPs of this kind with no targeting organic functions (vectors) attached to their coating can passively target tumor tissues by the enhanced permeability and retention (EPR) effect, which result from the leaky and complex topology of tumor vessels resulting from angiogenesis. Alternatively to the EPR effect, these NPs may reach the target by conjugating their coating with organic vectors that specifically recognize overexpressed tumor cell receptors (active targeting). Also, by taking advantage of their magnetic properties, it is possible to guide them to the tumor tissues with an external magnetic field of suitable strength. Therefore,

superparamagnetic NPs (SPIOs) have been developed as  $T_2$  contrast agents for MRI [38, 41]. The theory for the relaxation induced by SPIO and USPIO is quite different [8].

### I. 3. c. Lanthanide-based MRI agents

Many MRI CAs are based on gadolinium chelated with organic ligand (Figure 2) [1-2] or in its oxide form [42]. Nowadays compounds of  $Gd^{3+}$  are used in MRI scans to improve the clarity of the scanned images of body's internal structures [43]. As opposed to free  $Gd^{3+}$  known to be highly toxic [44-45], gadolinium oxide or chelated gadolinium don't show the same toxicity [44]. This is the reason why gadolinium is still used in contrast agents [46-47]. Furthermore,  $Gd^{3+}$  can be trapped in silica [47-48], metal oxides [49] or in its oxide form [42]. In this work,  $Gd^{3+}$  is inserted in the hafnium oxide lattice of NPs in order to provide them with magnetic properties and synthesize multimodal NPs. Thus, hafnium oxide NPs containing lanthanide ions other than  $Gd^{3+}$  with a suitable size may be used as potential MRI agents and in radiotherapy, a further doping with various other lanthanide ions providing as well optical imaging.

Let us examine now the magnetic properties of these other lanthanides. Their nuclear relaxation properties differ from what was described in the previous part (I. 3. a). Indeed, some of them have quite high magnetic moments and much shorter electron spin relaxation times, especially those in the second half of the series ( $\tau_e$ ) (Table 2) [25].

	Gadolinium	Europium	Terbium	Erbium	Ytterbium
$\tau_e(s)$	$10^{-8} - 10^{-9}$	$5 \cdot 10^{-14} - 10^{-14}$	$8 \cdot 10^{-13} - 2 \cdot 10^{-13}$	$8 \cdot 10^{-13} - 3 \cdot 10^{-13}$	$5 \cdot 10^{-13} - 2 \cdot 10^{-13}$

Table 2: Electron spin relaxation times of some lanthanides [25]

The equations for the inner-sphere paramagnetic relaxation include not only the dipolar terms ( $R_{idd}$ ) but also the Curie spin terms ( $R_{ics}$ ):

$$R_{iM} = R_{idd} + R_{ics} \quad , \quad i = 1, 2 \quad (28)$$

The dipolar terms ( $R_{idd}$ ) are given by equations (19) and (20), where  $S$  and  $g_e$  are replaced by  $J$  and  $g_J$ , respectively, and  $r_{GdH}$  is replaced by  $r_{LnH}$ . As  $\tau_e(T_{1e}, T_{2e})$  is very short, it dominates the correlation times  $\tau_{d1}$  and  $\tau_{d2}$  (see equation (21)). For this reason, for  $Ln^{3+} \neq Gd^{3+}$  ions, the dipolar relaxation effect, which is proportional to  $\tau_e$  in extremely narrowing conditions ( $\omega \cdot \tau_d \ll 1$ ), is much smaller than for  $Gd^{3+}$  complexes. However, the Curie spin contribution must be taken into account [50]:

$$R_{1M} = \frac{2}{5} \left( \frac{\mu_0}{4\pi} \right)^2 \frac{\omega_l^2 g_J^4 \mu_B^4 (J(J+1))^2}{(3kT)^2 r_{LnH}^6} \frac{3\tau_{Curie}}{1 + \omega_l^2 \tau_{Curie}^2} \quad (29)$$

$$R_{2M} = \frac{1}{5} \left( \frac{\mu_0}{4\pi} \right)^2 \frac{\omega_l^2 g_J^4 \mu_B^4 (J(J+1))^2}{(3kT)^2 r_{LnH}^6} \left( 4\tau_{Curie} + \frac{3\tau_{Curie}}{1 + \omega_l^2 \tau_{Curie}^2} \right) \quad (30)$$

where  $\tau_{Curie} = (\tau_R^{-1} + \tau_M^{-1})^{-1}$  (the inner-sphere Curie term is not influenced by electron spin relaxation). The term  $g_J^4 \mu_B^4 (J(J+1))^2$  in equations (29) and (30) can be replaced by the experimental  $\mu_{eff}$  values (Table 1). The Curie contribution is often dominating over the dipolar contribution for all  $Ln^{3+} \neq Gd^{3+}$  ions. Also, due to the presence of the squared Larmor frequency ( $\omega_l^2$ ), the Curie contribution increases with the square of the magnetic field.

The outer-sphere contribution for  $Ln^{3+} \neq Gd^{3+}$  ions has the usual dipole-dipole contribution represented by equations (25) to (27), with  $S$ ,  $g_e$  and  $GdL$  replaced by  $J$ ,  $g_J$  and  $LnL$  respectively. These terms depend on  $\tau_D$  ( $10^{-9} - 10^{-11}$  s) and  $\tau_e$  ( $10^{-12} - 10^{-14}$  s). Finally, for very short electron relaxation times ( $\tau_e \ll \tau_D$ ), as in  $Ln^{3+} \neq Gd^{3+}$ , an additional contribution to the outer-sphere relaxation can be provided by the Curie spin interaction modulated by  $\tau_D$ . [51].

$$R_{1os} = \frac{32N_A\pi}{405} \left( \frac{\mu_0}{4\pi} \right)^2 \frac{1000N_A[Ln]\omega_l^2 g_J^4 \mu_B^4 (J(J+1))^2}{3(kT)^2 a_{GdH} D_{LnH}} [3J_{os}(\omega_l; T_{1e}) + 7J_{os}(\omega_s; T_{2e})] \quad (31)$$

$$R_{2os} = \frac{16N_A\pi}{405} \left( \frac{\mu_0}{4\pi} \right)^2 \frac{1000N_A[Ln]\omega_l^2 g_J^4 \mu_B^4 (J(J+1))^2}{3(kT)^2 a_{GdH} D_{LnH}} [4J_{os}(0) + 3J_{os}(\omega_l; T_{1e}) + 13(\omega_s; T_{2e})] \quad (32)$$

These terms also depend on  $\omega_l^2$  and the electron spin relaxation times.

## II - Results and discussion

### II. 1. Low magnetic field (20 MHz)

The suspensions of the nanoparticles of  $\text{HfO}_2$  doped with lanthanides ions remained stable throughout the NMR measurements, allowing the collection of consistent relaxation data. The suspensions of nanoparticles for the measurements was made at neutral pH in distilled water, and sonicated during 5 minutes. Table 3 shows the proton relaxivity values ( $r_1$  and  $r_2$ ), determined at 25 °C and 37 °C for  $\text{Gd}_{0.26}\text{HfO}_2$ ,  $\text{Eu}_{0.01}\text{Tb}_{0.03}\text{Gd}_{0.16}\text{HfO}_2$ ,  $\text{Eu}_{0.03}\text{Tb}_{0.05}\text{Gd}_{0.12}\text{HfO}_2$ ,  $\text{Yb}_{0.01}\text{Er}_{0.05}\text{Gd}_{0.19}\text{HfO}_2$  and  $\text{Yb}_{0.02}\text{Er}_{0.10}\text{Gd}_{0.13}\text{HfO}_2$  water suspensions. These relaxivities were calculated from the observed linear dependence of the  $R_i = 1/T_i$ , ( $i = 1,2$ ) relaxation rates on the concentration of the  $\text{Gd}^{3+}$  ions present in all samples, shown in Figure 10, Figure 11, Figure 12 and Figure 13.

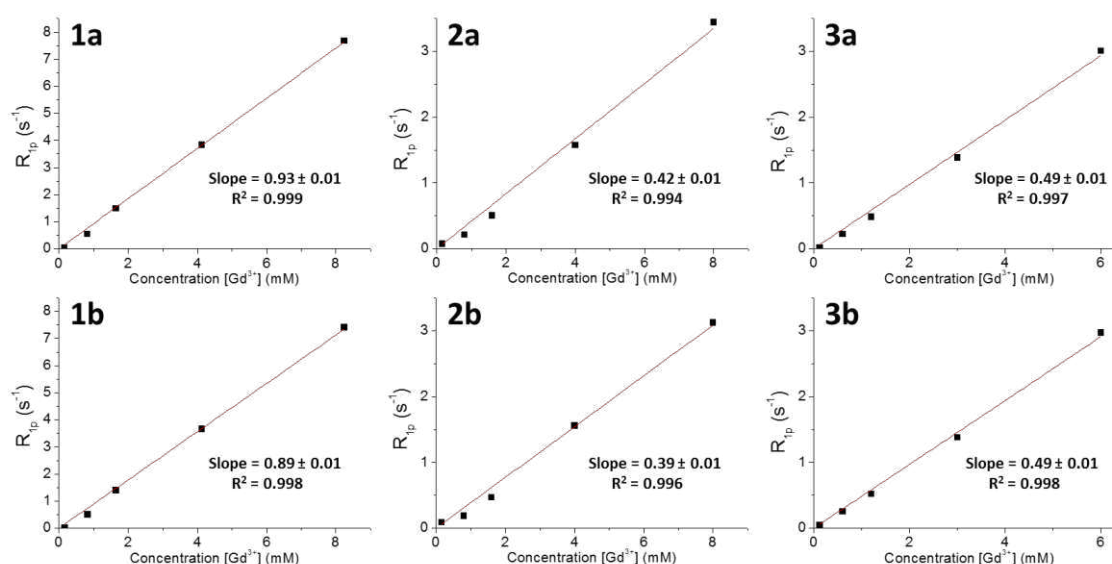


Figure 10:  $R_1$  values measured at 20 MHz; (a) 25 °C and (b) 37 °C and samples 1-  $\text{Gd}_{0.26}\text{HfO}_2$ ; 2-  $\text{Eu}_{0.01}\text{Tb}_{0.03}\text{Gd}_{0.16}\text{HfO}_2$ ; 3-  $\text{Eu}_{0.03}\text{Tb}_{0.05}\text{Gd}_{0.12}\text{HfO}_2$ .

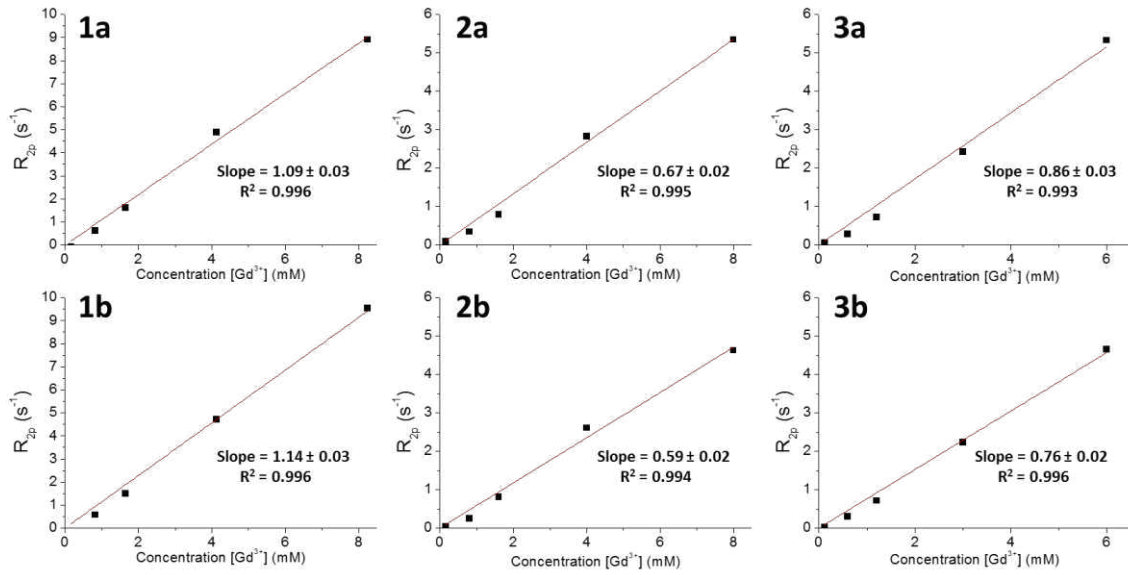


Figure 11:  $R_2$  values measured at 20 MHz; (a) 25 °C and (b) 37 °C and samples 1-  $Gd_{0.26}:HfO_2$ ; 2-  $Eu_{0.01}Tb_{0.03}Gd_{0.16}:HfO_2$ ; 3-  $Eu_{0.03}Tb_{0.05}Gd_{0.12}:HfO_2$ .

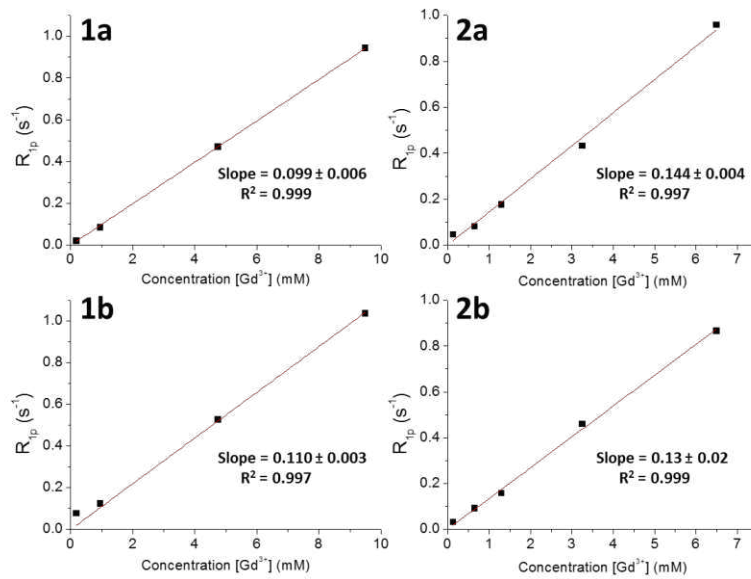


Figure 12:  $R_1$  values measured at 20 MHz; (a) 25 °C and (b) 37 °C and samples 1-  $Yb_{0.01}Er_{0.05}Gd_{0.19}:HfO_2$ ; 2-  $Yb_{0.02}Er_{0.10}Gd_{0.13}:HfO_2$ .

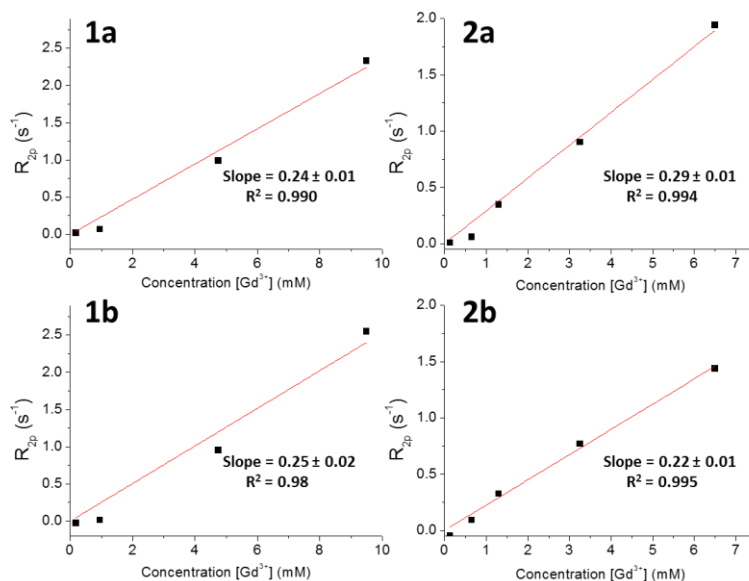


Figure 13:  $R_2$  values measured at 20 MHz; (a) 25 °C and (b) 37 °C and samples 1-  $\text{Yb}_{0.01}\text{Er}_{0.05}\text{Gd}_{0.19}:\text{HfO}_2$ ; 2-  $\text{Yb}_{0.02}\text{Er}_{0.10}\text{Gd}_{0.13}:\text{HfO}_2$ .

$r_1$  and  $r_2$  values are expected to have inner- and outer-sphere contributions (equation (17)). The experimental  $r_1$  and  $r_2$  values obtained are quite small, much lower than the commercial  $\text{Gd}^{3+}$ -based contrast agent  $\text{Gd}(\text{DTPA})$  values ( $r_1 = 4.10 \text{ mM}^{-1}\text{s}^{-1}$  and  $r_2 = 4.57 \text{ mM}^{-1}\text{s}^{-1}$  at 20 MHz and 25 °C). As the percentage of  $\text{Gd}^{3+}$  ions on the surface of the  $\text{Gd}_{0.26}:\text{HfO}_2$  nanoparticles directly exposed to solvent water molecules is very small due to the low ratio of gadolinium at the surface of the NPs, the contribution of the inner-sphere relaxation mechanism to  $r_1$  and  $r_2$  is negligible, as observed previously for other systems [52-55]. Like the inner-sphere term (equation (28)), the outer-sphere terms also have contributions from the dipole-dipole,  $R_{idd}$ , and Curie spin,  $R_{ics}$ , relaxation mechanisms. However, for  $\text{Gd}^{3+}$ -containing systems, the dipole-dipole contribution is dominant, because it depends on long ( $10^{-8} - 10^{-9} \text{ s}$ )  $\tau_e$  ( $T_{1e}$  and  $T_{2e}$ ) values (equations (25) - (27)). As this contribution is inversely proportional to  $a_{\text{GdH}}$ , the distance of closest approach of the protons to  $\text{Gd}^{3+}$ , the outer-sphere term of the  $r_1$  and  $r_2$  values is also very small, explaining the very small observed relaxivities.

For the system where  $\text{Gd}^{3+}$  was partially replaced by other paramagnetic  $\text{Ln}^{3+}$  ( $\text{Eu}^{3+}$ ,  $\text{Tb}^{3+}$ ,  $\text{Er}^{3+}$  or  $\text{Yb}^{3+}$ ), the relaxivities per mM of total mass decrease in a way that depends on the type of cation. This is expected because  $\text{Gd}^{3+}$  has a much slower electronic relaxation time than  $\text{Eu}^{3+}$ ,  $\text{Tb}^{3+}$ ,  $\text{Er}^{3+}$  or  $\text{Yb}^{3+}$  and the relaxation mechanisms for systems containing  $\text{Ln} \neq \text{Gd}$  are different. Besides the dipole-dipole contribution, the Curie spin mechanism also contributes to the outer-sphere relaxation, as described by equations (31) and (32). Therefore, for the mixed

nanoparticles systems,  $\text{Ln}_x\text{Ln}'_y\text{Gd}_z:\text{HfO}_2$ , when compared to  $\text{Gd}_{0.26}:\text{HfO}_2$  there are outer-sphere relaxation contributions from pairs of  $\text{Ln}^{3+}$  and  $\text{Ln}'^{3+}$  ions replacing some of the  $\text{Gd}^{3+}$  ions, with both dipolar and Curie spin contributions. The dipolar terms for these contributions (modified equations (25) - (27), with  $S$ ,  $g_e$  and  $\text{GdL}$  replaced by  $J$ ,  $g_J$  and  $\text{LnL}$  respectively), depend on  $\tau_D$  ( $10^{-9} - 10^{-11}$  s), through  $D_{\text{LnH}}$ , and  $\tau_e$  ( $10^{-12} - 10^{-14}$  s), depend on the  $\mu_{eff}^2$  on the lanthanide ions and are independent of the Larmor frequency  $\omega_l = \frac{\gamma}{2\pi} B_0$ , and, thus, magnetic field  $B_0$ . The Curie spin mechanism with  $\tau_e \ll \tau_D$  (equations (31) - (32)) depends on the square of the magnetic field  $B_0$  (through  $\omega_l^2$ ) and on  $\mu_{eff}^4$ . The classification of the lanthanide ions,  $\text{Ln}^{3+}$ , according to their effective magnetic moment ( $\mu_{eff}$ ) is  $\text{Tb} \sim \text{Er} > \text{Gd} > \text{Yb} > \text{Eu}$  (Table 1), while their electronic relaxation times ( $\tau_e$ ) are  $\text{Gd} \gg \text{Tb} > \text{Er} \gg \text{Yb} > \text{Eu}$  (Table 2), which give the same order of expected dipolar relaxation. Therefore, the differences between  $\text{Gd}_{0.26}:\text{HfO}_2$  and the other systems,  $\text{Ln}_x\text{Ln}'_y\text{Gd}_z:\text{HfO}_2$ , will depend on the relative percentage of each lanthanide ions and their nature.

For  $\text{Eu}_{0.03}\text{Tb}_{0.05}\text{Gd}_{0.12}:\text{HfO}_2$  and  $\text{Eu}_{0.01}\text{Tb}_{0.03}\text{Gd}_{0.16}:\text{HfO}_2$  NPs, the  $r_1$  and  $r_2$  relaxivities decrease substantially relatively to  $\text{Gd}_{0.26}:\text{HfO}_2$ , as the total stoichiometry of Ln decreases from 0.26 Gd to 0.20 (Gd + Tb + Eu).

For  $\text{Eu}_{0.03}\text{Tb}_{0.05}\text{Gd}_{0.12}:\text{HfO}_2$ , where  $\text{Gd}^{3+}$  ions are replaced by  $\text{Eu}^{3+}$  and  $\text{Tb}^{3+}$ , the  $r_1$  values (referred to one mM  $\text{Gd}^{3+}$ ) increase slightly when compared to the  $\text{Eu}_{0.01}\text{Tb}_{0.03}\text{Gd}_{0.16}:\text{HfO}_2$  NPs (Table 3). The dipolar relaxation contribution is expected to decrease when more  $\text{Gd}^{3+}$  ions are replaced by  $\text{Eu}^{3+}$  and  $\text{Tb}^{3+}$ , while, the opposite is expected for the Curie spin contribution, due to larger  $\mu_{eff}$  of  $\text{Tb}^{3+}$ . Therefore, the later mechanism has a non-negligible contribution, even at 20 MHz.

The  $r_2$  values of these samples are larger than the  $r_1$  values due to the contribution of slow motions in the NPs dynamics, increasing the  $J(0)$  terms. Their relative values in the two samples have the same behavior as  $r_1$ : for  $\text{Eu}_{0.03}\text{Tb}_{0.05}\text{Gd}_{0.12}:\text{HfO}_2$  the  $r_2$  values (referred to one mM  $\text{Gd}^{3+}$ ) increase much more clearly when compared to the  $\text{Eu}_{0.01}\text{Tb}_{0.03}\text{Gd}_{0.16}:\text{HfO}_2$  NPs (Table 3), reflecting a stronger influence of the Curie spin term.

20 MHz	$r_1$ (s <sup>-1</sup> )		$r_2$ (s <sup>-1</sup> )	
	25 °C	37 °C	25 °C	37 °C
<b>Gd<sub>0.26</sub>:HfO<sub>2</sub></b>	0.93 ± 0.01	0.89 ± 0.01	1.09 ± 0.03	1.14 ± 0.03
<b>Eu<sub>0.01</sub>Tb<sub>0.03</sub>Gd<sub>0.16</sub>:HfO<sub>2</sub></b>	0.42 ± 0.01	0.39 ± 0.01	0.67 ± 0.02	0.59 ± 0.03
<b>Eu<sub>0.03</sub>Tb<sub>0.05</sub>Gd<sub>0.12</sub>:HfO<sub>2</sub></b>	0.49 ± 0.01	0.49 ± 0.01	0.86 ± 0.03	0.76 ± 0.01
<b>Yb<sub>0.01</sub>Er<sub>0.05</sub>Gd<sub>0.19</sub>:HfO<sub>2</sub></b>	0.099 ± 0.006	0.110 ± 0.003	0.24 ± 0.01	0.25 ± 0.02
<b>Yb<sub>0.02</sub>Er<sub>0.10</sub>Gd<sub>0.13</sub>:HfO<sub>2</sub></b>	0.144 ± 0.004	0.13 ± 0.02	0.29 ± 0.01	0.22 ± 0.01

Table 3: Calculated <sup>1</sup>H relaxivity values,  $r_i$  ( $i = 1, 2$ ), determined at 20 MHz at 25 °C and 37 °C for samples Gd<sub>0.26</sub>:HfO<sub>2</sub>, Eu<sub>0.01</sub>Tb<sub>0.03</sub>Gd<sub>0.16</sub>:HfO<sub>2</sub> and Eu<sub>0.03</sub>Tb<sub>0.05</sub>Gd<sub>0.12</sub>:HfO<sub>2</sub>.

For Yb<sub>0.02</sub>Er<sub>0.10</sub>Gd<sub>0.13</sub>:HfO<sub>2</sub> and Yb<sub>0.01</sub>Er<sub>0.05</sub>Gd<sub>0.19</sub>:HfO<sub>2</sub> NPs, where 0.12 and 0.06 Gd<sup>3+</sup> ions are replaced by Yb<sup>3+</sup> and Er<sup>3+</sup>, the  $r_1$  and  $r_2$  values (referred to one mM Gd<sup>3+</sup>) decrease substantially relative to the Tb/Eu samples, reflecting their lower dipolar relaxation effect and the much lower Curie spin effect of Yb<sup>3+</sup> relative to the other ions. There is a very small decrease of  $r_1$  of Yb<sub>0.01</sub>Er<sub>0.05</sub>Gd<sub>0.19</sub>:HfO<sub>2</sub> when compared to Yb<sub>0.02</sub>Er<sub>0.10</sub>Gd<sub>0.13</sub>:HfO<sub>2</sub> NPs (Table 3) reflecting the larger dipolar relaxation effect of Er<sup>3+</sup> vs Yb<sup>3+</sup>.

The  $r_2$  values of these samples are also larger than the  $r_1$  values due to the same effect as described above. For Yb<sub>0.02</sub>Er<sub>0.10</sub>Gd<sub>0.13</sub>:HfO<sub>2</sub>, where Gd<sup>3+</sup> ions are replaced by Yb<sup>3+</sup> and Er<sup>3+</sup>, the  $r_2$  values (referred to one mM Gd<sup>3+</sup>) again increase compared to the Yb<sub>0.01</sub>Er<sub>0.05</sub>Gd<sub>0.19</sub>:HfO<sub>2</sub> NPs (Table 3), also reflecting the dipolar mechanism.

The temperature dependence of  $r_1$  and  $r_2$  for the samples doped with Eu<sup>3+</sup> and Tb<sup>3+</sup>, as well as with Yb<sup>3+</sup> and Er<sup>3+</sup>, is generally the same as for the sample with only Gd<sup>3+</sup>: a slight decrease of the relaxation rates with the increase of the temperature is observed, as expected by the SBM and Curie spin relaxation theory.

## II. 2. High magnetic field (400 and 500 MHz)

Table 4 shows the proton relaxivity values ( $r_1$  and  $r_2$ ), determined at 25 °C and magnetic field strength corresponding at 20 MHz, 400 MHz and 500 MHz, for  $Gd_{0.26}:HfO_2$  and  $Eu_{0.01}Tb_{0.03}Gd_{0.16}:HfO_2$  water suspensions.

		$r_1$ ( $s^{-1}$ )	$r_2$ ( $s^{-1}$ )
<b>20 MHz</b>	$Gd_{0.26}:HfO_2$	$0.93 \pm 0.01$	$1.09 \pm 0.03$
	$Eu_{0.01}Tb_{0.03}Gd_{0.16}:HfO_2$	$0.42 \pm 0.01$	$0.67 \pm 0.02$
<b>400 MHz</b>	$Gd_{0.26}:HfO_2$	$0.54 \pm 0.01$	$2.46 \pm 0.02$
	$Eu_{0.01}Tb_{0.03}Gd_{0.16}:HfO_2$	$0.45 \pm 0.01$	$1.58 \pm 0.03$
<b>500 MHz</b>	$Gd_{0.26}:HfO_2$	$0.42 \pm 0.02$	$4.82 \pm 0.04$
	$Eu_{0.01}Tb_{0.03}Gd_{0.16}:HfO_2$	$0.36 \pm 0.01$	$2.40 \pm 0.07$

Table 4: Calculated  $^1H$  relaxivity values,  $r_i$  ( $i = 1,2$ ), determined at 20, 400 and 500 MHz at 25 °C for samples  $Gd_{0.26}:HfO_2$  and  $Eu_{0.01}Tb_{0.03}Gd_{0.16}:HfO_2$ .

$r_1$  values decrease with increasing frequency (Table 4), as expected for the standard outer-sphere dipolar mechanisms of proton relaxation.  $r_2$  values undergo a large increase when the measuring frequency increases (Table 4 and Figure 14). This indicates that the  $T_2$  relaxation process, besides the dipolar mechanism operating for  $T_1$  relaxation, also has a strong outer-sphere contribution from field inhomogeneities created by the magnetized particles that the water protons experience as they diffuse nearby and which increase with the square of the external magnetic field strength (equation (32)). The strong outer sphere contribution can be explained by the fact that the percentage of lanthanide ions at the surface of the nanoparticles is very small and, thus, they cannot directly bind water molecules in their inner-sphere and exchange water protons with the medium.

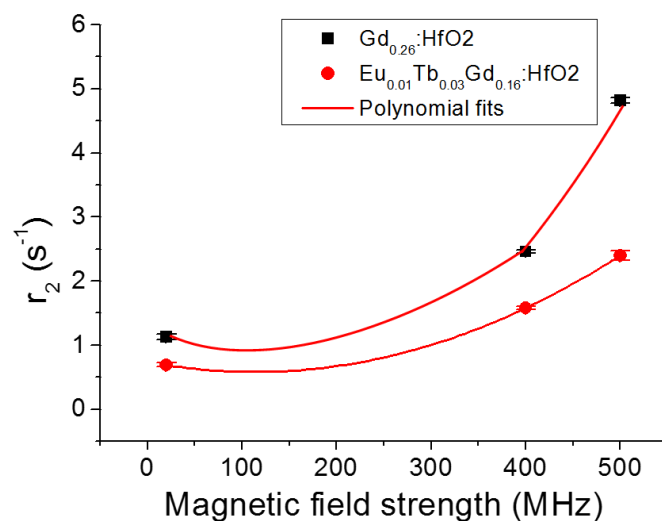


Figure 14: Relaxivity  $r_2$  values as a function of the magnetic field strength. The red lines are the polynomial fits of the experimental data acquired at 20, 400 and 500 MHz

## Conclusion

Hafnium oxide nanoparticles doped with lanthanides cations ( $\text{Gd}^{3+}$ ,  $\text{Tb}^{3+}$  and  $\text{Eu}^{3+}$ ) have low  $r_1$  and  $r_2$  values at low frequency (20 MHz), with  $r_2/r_1$  ratios in the 1.0 – 1.8 range, indicating that they could act as  $T_1$ -weighted (positive) MRI contrast agents, although not very efficiently. Nanoparticles doped with  $\text{Gd}^{3+}$ ,  $\text{Er}^{3+}$  and  $\text{Yb}^{3+}$ , with lower relaxivities and  $r_2/r_1$  ratios in the 2.1 – 2.4 range, also perform as  $T_1$ -weighted (positive) MRI contrast agents. At higher frequencies, due to the increased Curie spin contribution, their  $r_2$  values increase substantially, with  $r_2/r_1$  ratios larger than 2 (3.5 to 11.9), and they may be classified as  $T_2$ -weighted (negative) contrast agents.

## Experimental part

The NPs of hafnium oxide were suspended in distilled water, then sonicated in an ultrasound bath for 5 minutes. The molar amount of the gadolinium was calculated from the molar percentage inserted in the matrix of hafnium oxide. And then, the molar concentration was ascertained by a dilution factor. First, a 50 mM solution of HfO<sub>2</sub> (S<sub>0</sub>) was prepared, by a dissolution of 150 mg of powder suspended in 15 mL of distilled water for each studied sample. Then, 5 NMR tubes were prepared by dilution as follows:

Concentration of HfO <sub>2</sub>	V (μL) of S <sub>1</sub>	V (μL) of distilled water
50 mM	600	(-)
25 mM	300	300
10 mM	120	480
5 mM	60	540
1 mM	12	588

Thus, 5 NMR tubes were ready to make the measurements at 20 MHz. In order to determine the relaxivities, we needed to determine the concentration of Gd<sup>3+</sup> in the sample. The calculation was made as follows:

For example for the sample Gd<sub>0.26</sub>:HfO<sub>2</sub>, in S<sub>1</sub>, we have suspended 150 mg of HfO<sub>2</sub> in 15 mL of water, so the number of moles of Hf is:  $n = C \times V = 50 \times 10^{-3} \times 15 \times 10^{-3} = 0.750 \text{ mmol}$ . Yet, the molar percentage of Gd<sup>3+</sup> in this sample is 26%, so the number of moles of Gd<sup>3+</sup> in S<sub>1</sub> is:  $n_{Gd} = 26\% \times 0.750 = 0.195 \text{ mmol}$ . Thus, the concentration of Gd<sup>3+</sup> in the samples can be ascribed to:  $[Gd^{3+}] = \frac{n_{Gd}}{V} = \frac{0.195}{15 \times 10^{-3}} = 13 \text{ mmol.L}^{-1}$ .

At each concentration (50, 25, 10, 5 and 1 mM) and at each temperature (25 and 37 °C), the  $T_i$  (i=1, 2) were measured 3 times. Then,  $R_i$  was determined by the following equation:

$$R_1 = \frac{1}{T_{i \text{ obs}}} - \frac{1}{T_{i \text{ water}}}$$

Then,  $R_i$  was plotted as a function of the concentration of Gd<sup>3+</sup>, and the slope of this graph gave  $r_i$  in s<sup>-1</sup> (referred to one mM Gd<sup>3+</sup>).

<sup>1</sup>H longitudinal and transverse relaxation times (T<sub>1</sub> and T<sub>2</sub> respectively) of aqueous suspensions of nanoparticles were measured at 20 MHz on a Bruker Minispec mq20 relaxometer and at 500 MHz (B<sub>0</sub> = 11.7 T) on a Varian Unity 500 NMR spectrometer, at 25 and 37 °C.

## Bibliography

1. Caravan, P., Strategies for increasing the sensitivity of gadolinium based MRI contrast agents. *Chemical Society Reviews* **2006**, *35* (6), 512-523.
2. Rajan, S. S., *MRI: a conceptual overview*. Springer Science & Business Media: 1997.
3. Xi, D.; Dong, S.; Meng, X.; Lu, Q.; Meng, L.; Ye, J., Gold nanoparticles as computerized tomography (CT) contrast agents. *RSC Advances* **2012**, *2* (33), 12515-12524.
4. Phelps, M. E., Positron emission tomography provides molecular imaging of biological processes. *Proceedings of the National Academy of Sciences* **2000**, *97* (16), 9226-9233.
5. Pichler, B. J.; Wehrl, H. F.; Kolb, A.; Judenhofer, M. S. In *Positron emission tomography/magnetic resonance imaging: the next generation of multimodality imaging?*, Seminars in nuclear medicine, Elsevier: 2008; pp 199-208.
6. Gallez, B.; Swartz, H. M., In vivo EPR: when, how and why? *NMR in Biomedicine* **2004**, *17* (5), 223-225.
7. Geraldes, C. F. G. C.; Laurent, S., Classification and basic properties of contrast agents for magnetic resonance imaging. *Contrast Media & Molecular Imaging* **2009**, *4* (1), 1-23.
8. Laurent, S.; Forge, D.; Port, M.; Roch, A.; Robic, C.; Vander Elst, L.; Muller, R. N., Magnetic Iron Oxide Nanoparticles: Synthesis, Stabilization, Vectorization, Physicochemical Characterizations, and Biological Applications. *Chemical Reviews* **2008**, *108* (6), 2064-2110.
9. Larionava, J., Ingénierie Moléculaire et Magnétisme. *Cours Ecole Nationale Supérieure de Chimie de Montpellier* **2013**.
10. Smart, L. E.; Moore, E. A., *Solid state chemistry: an introduction*. CRC press: 2012.
11. Hettich, G.; Mehrer, H.; Maier, K., Self-diffusion in ferromagnetic  $\alpha$ -iron. *Scripta Metallurgica* **1977**, *11* (9), 795-802.
12. Beaurepaire, E.; Merle, J.-C.; Daunois, A.; Bigot, J.-Y., Ultrafast spin dynamics in ferromagnetic nickel. *Physical Review Letters* **1996**, *76* (22), 4250.
13. Portis, A.; Gossard, A., Nuclear resonance in ferromagnetic cobalt. *Journal of Applied Physics* **1960**, *31* (5), S205-S213.
14. Vaterlaus, A.; Beutler, T.; Meier, F., Spin-lattice relaxation time of ferromagnetic gadolinium determined with time-resolved spin-polarized photoemission. *Physical Review Letters* **1991**, *67* (23), 3314.
15. Graham Jr, C., Magnetic behavior of gadolinium near the Curie point. *Journal of Applied Physics* **1965**, *36* (3), 1135-1136.
16. Wolfson, R.; Pasachoff, J. M., *Physics for scientists and engineers*. Addison Wesley Longman: 1999.
17. Weishaupt, D.; Köchli, V. D.; Marincek, B., *How does MRI work?: an introduction to the physics and function of magnetic resonance imaging*. Springer Science & Business Media: 2008.
18. Doyon, D., *IRM: Imagerie par résonance magnétique*. Elsevier Masson: 2004.
19. Atkins, P.; De Paula, J., *Elements of physical chemistry*. Oxford University Press: 2013.
20. Na, H. B.; Song, I. C.; Hyeon, T., Inorganic Nanoparticles for MRI Contrast Agents. *Advanced Materials* **2009**, *21*, 2133-2148.
21. Hornak, J., *The Basics of MRI*. Henrietta, NY: Interactive Learning Software. 2010.
22. AD Elster, E. L. <http://mriquestions.com/why-use-ir.html> (accessed 2017-09-12).
23. Yan, G.-P.; Robinson, L.; Hogg, P., Magnetic resonance imaging contrast agents: Overview and perspectives. *Radiography* **2007**, *13*, e5-e19.
24. Qin, J.; Laurent, S.; Jo, Y. S.; Roch, A.; Mikhaylova, M.; Bhujwalla, Z. M.; Muller, R. N.; Muhammed, M., A High-Performance Magnetic Resonance Imaging T2 Contrast Agent. *Advanced Materials* **2007**, *19* (14), 1874-1878.
25. Bertini, I.; Luchinat, C.; Parigi, G.; Ravera, E., *NMR of Paramagnetic Molecules: Applications to Metallobiomolecules and Models*. Elsevier: 2016; Vol. 2.
26. Jacques, V.; Desreux, J., New classes of MRI contrast agents. *Contrast Agents I* **2002**, 123-164.
27. Sherry, A. D.; Caravan, P.; Lenkinski, R. E., Primer on gadolinium chemistry. *Journal of Magnetic Resonance Imaging* **2009**, *30* (6), 1240-1248.
28. Brücher, E., Kinetic stabilities of gadolinium (III) chelates used as MRI contrast agents. *Contrast Agents I* **2002**, 103-122.
29. Lauffer, R. B., Paramagnetic metal complexes as water proton relaxation agents for NMR imaging: theory and design. *Chemical Reviews* **1987**, *87* (5), 901-927.
30. Caravan, P.; Ellison, J. J.; McMurry, T. J.; Lauffer, R. B., Gadolinium (III) chelates as MRI contrast agents: structure, dynamics, and applications. *Chemical Reviews* **1999**, *99* (9), 2293-2352.

31. Luz, Z.; Meiboom, S., Proton relaxation in dilute solutions of cobalt (II) and nickel (II) ions in methanol and the rate of methanol exchange of the solvation sphere. *The Journal of Chemical Physics* **1964**, *40* (9), 2686-2692.
32. Freed, J. H., Dynamic effects of pair correlation functions on spin relaxation by translational diffusion in liquids. II. Finite jumps and independent T<sub>1</sub> processes. *The Journal of Chemical Physics* **1978**, *68* (9), 4034-4037.
33. Polnaszek, C. F.; Bryant, R. G., Self-diffusion of water at the protein surface: a measurement. *Journal of the American Chemical Society* **1984**, *106* (2), 428-429.
34. Koenig, S. H.; Brown, R. D.; Spiller, M.; Chakrabarti, B.; Pande, A., Intermolecular protein interactions in solutions of calf lens alpha-crystallin. Results from 1/T<sub>1</sub> nuclear magnetic relaxation dispersion profiles. *Biophysical Journal* **1992**, *61* (3), 776-785.
35. Caravan, P.; Farrar, C. T.; Frullano, L.; Uppal, R., Influence of molecular parameters and increasing magnetic field strength on relaxivity of gadolinium- and manganese-based T<sub>1</sub> contrast agents. *Contrast Media & Molecular Imaging* **2009**, *4*, 89-100.
36. Nakamura, H.; Ito, N.; Kotake, F.; Mizokami, Y.; Matsuoka, T., Tumor-detecting capacity and clinical usefulness of SPIO-MRI in patients with hepatocellular carcinoma. *J Gastroenterol* **2000**, *35* (11), 849-855.
37. Pinho, S. L. C.; Laurent, S.; Rocha, J.; Roch, A.; Delville, M.-H.; Mornet, S.; Carlos, L. D.; Vander Elst, L.; Muller, R. N.; Geraldes, C. F. G. C., Relaxometric Studies of  $\gamma$ -Fe<sub>2</sub>O<sub>3</sub>@SiO<sub>2</sub> Core Shell Nanoparticles: When the Coating Matters. *The Journal of Physical Chemistry C* **2012**, *116*, 2285-2291.
38. Pinho, S. L. C.; Pereira, G. A.; Voisin, P.; Kassem, J.; Bouchaud, V.; Etienne, L.; Peters, J. A.; Carlos, L.; Mornet, S.; Geraldes, C. F. G. C.; Rocha, J.; Delville, M.-H., Fine Tuning of the Relaxometry of  $\gamma$ -Fe<sub>2</sub>O<sub>3</sub>@SiO<sub>2</sub> Nanoparticles by Tweaking the Silica Coating Thickness. *ACS Nano* **2010**, *4*, 5339-5349.
39. Le Trequesser, Q.; Seznec, H.; Delville, M.-H., Functionalized nanomaterials: their use as contrast agents in bioimaging: mono- and multimodal approaches. *Nanotechnology Reviews* **2013**, *2*, 125-169.
40. Gupta, A. K.; Wells, S., Surface-modified superparamagnetic nanoparticles for drug delivery: preparation, characterization, and cytotoxicity studies. *NanoBioscience, IEEE Transactions on* **2004**, *3* (1), 66-73.
41. Pankhurst, Q. A.; Connolly, J.; Jones, S. K.; Dobson, J., Applications of magnetic nanoparticles in biomedicine. *Journal of Physics D: Applied Physics* **2003**, *36*, R167-R181.
42. Zhou, L.; Gu, Z.; Liu, X.; Yin, W.; Tian, G.; Yan, L.; Jin, S.; Ren, W.; Xing, G.; Li, W.; Chang, X.; Hu, Z.; Zhao, Y., Size-tunable synthesis of lanthanide-doped Gd<sub>2</sub>O<sub>3</sub> nanoparticles and their applications for optical and magnetic resonance imaging. *Journal of Materials Chemistry* **2012**, *22*, 966-974.
43. Bellin, M.-F., MR contrast agents, the old and the new. *European Journal of Radiology* **2006**, *60* (3), 314-323.
44. Bartolini, M.; Pekar, J.; Chettle, D.; McNeill, F.; Scott, A.; Sykes, J.; Prato, F.; Moran, G., An investigation of the toxicity of gadolinium based MRI contrast agents using neutron activation analysis. *Magnetic resonance imaging* **2003**, *21* (5), 541-544.
45. Hirano, S.; Suzuki, K. T., Exposure, metabolism, and toxicity of rare earths and related compounds. *Environmental health perspectives* **1996**, *104* (Suppl 1), 85.
46. Chen, R.; Ling, D.; Zhao, L.; Wang, S.; Liu, Y.; Bai, R.; Baik, S.; Zhao, Y.; Chen, C.; Hyeon, T., Parallel Comparative Studies on Mouse Toxicity of Oxide Nanoparticle- and Gadolinium-Based T<sub>1</sub> MRI Contrast Agents. *ACS Nano* **2015**.
47. Pinho, S. L. C.; Faneca, H.; Geraldes, C. F. G. C.; Delville, M.-H.; Carlos, L. D.; Rocha, J., Lanthanide-DTPA grafted silica nanoparticles as bimodal-imaging contrast agents. *Biomaterials* **2012**, *33*, 925-935.
48. Pinho, S. L. C.; Faneca, H.; Geraldes, C. F. G. C.; Rocha, J.; Carlos, L. D.; Delville, M.-H., Silica nanoparticles for bimodal MRI-optical imaging by grafting Gd<sup>3+</sup> and Eu<sup>3+</sup>/Tb<sup>3+</sup> complexes. *European Journal of Inorganic Chemistry* **2012**, *2012*, 2828-2837.
49. Ribot, E. J.; Miraux, S.; Konsman, J. P.; Bouchaud, V.; Pourtau, L.; Delville, M. H.; Franconi, J. M.; Thiaudière, E.; Voisin, P. J., In vivo MR tracking of therapeutic microglia to a human glioma model. *NMR in Biomedicine* **2011**, *24* (10), 1361-1368.
50. Guéron, M., Nuclear relaxation in macromolecules by paramagnetic ions: a novel mechanism. *Journal of Magnetic Resonance (1969)* **1975**, *19* (1), 58-66.
51. Vigouroux, C.; Belorizky, E.; Fries, P., NMR approach of the electronic properties of the hydrated trivalent rare earth ions in solution. *The European Physical Journal D-Atomic, Molecular, Optical and Plasma Physics* **1999**, *5* (2), 243-255.
52. Park, J. Y.; Baek, M. J.; Choi, E. S.; Woo, S.; Kim, J. H.; Kim, T. J.; Jung, J. C.; Chae, K. S.; Chang, Y.; Lee, G. H., Paramagnetic Ultrasmall Gadolinium Oxide Nanoparticles as Advanced T<sub>1</sub> MRI Contrast Agent: Account for Large Longitudinal Relaxivity, Optimal Particle Diameter, and In Vivo T<sub>1</sub> MR Images. *ACS Nano* **2009**, *3* (11), 3663-3669.

53. Pereira, G.; Ananias, D.; Rocha, J.; Amaral, V.; Muller, R.; Vander Elst, L.; Tóth, É.; Peters, J.; Geraldes, C., NMR relaxivity of Ln<sup>3+</sup>-based zeolite-type materials. *Journal of Materials Chemistry* **2005**, *15* (35-36), 3832-3837.
54. Debasu, M. L.; Ananias, D.; Pinho, S. L. C.; Geraldes, C. F. G. C.; Carlos, L. D.; Rocha, J., (Gd,Yb,Tb)PO<sub>4</sub> up-conversion nanocrystals for bimodal luminescence-MR imaging. *Nanoscale* **2012**, *4* (16), 5154-5162.
55. Goglio, G.; Kaur, G.; Pinho, S. L.; Penin, N.; Blandino, A.; Geraldes, C. F.; Garcia, A.; Delville, M. H., Glycine–Nitrate Process for the Elaboration of Eu<sup>3+</sup>-Doped Gd<sub>2</sub>O<sub>3</sub> Bimodal Nanoparticles for Biomedical Applications. *European Journal of Inorganic Chemistry* **2015**, *2015* (7), 1243-1253.



# Conclusions and perspectives



The goal of my thesis, which unfolded as part of a wider project, was to develop TiO<sub>2</sub> and HfO<sub>2</sub> nanoparticles with potential applications in the biomedical field.

In this context, I have accomplished the hydrothermal synthesis of TiO<sub>2</sub> and HfO<sub>2</sub> nanoparticles (respectively, Chapters 2 and 3). The synthetic parameters were optimized to obtain nanoparticles with a size suitable for biological applications (30 to 60 nm). By adjusting the composition of a mixture of the structuring agents, triethanolamine and oleic acid, TiO<sub>2</sub> nanoparticles were prepared with a range of sizes and morphologies. Altering the pH change the habit of hafnium oxide NPs, while increasing the temperature decreased the nanoparticle size. Moreover, up to three different types of lanthanide ions were inserted in the hafnium oxide matrix, endowing the nanoparticles with luminescence properties for imaging and thermometry (chapter 4), and potential as T<sub>2</sub>-weighted MRI contrast agents (chapter 5). Among all the compositions studied, the most promising nanoparticles had composition Eu<sub>0.01</sub>Tb<sub>0.03</sub>Gd<sub>0.16</sub>:HfO<sub>2</sub> and, thus, they were fully characterized with several techniques (Figure 1). The outlook of the near future is to study these nanoparticles in real radiotherapy applications.

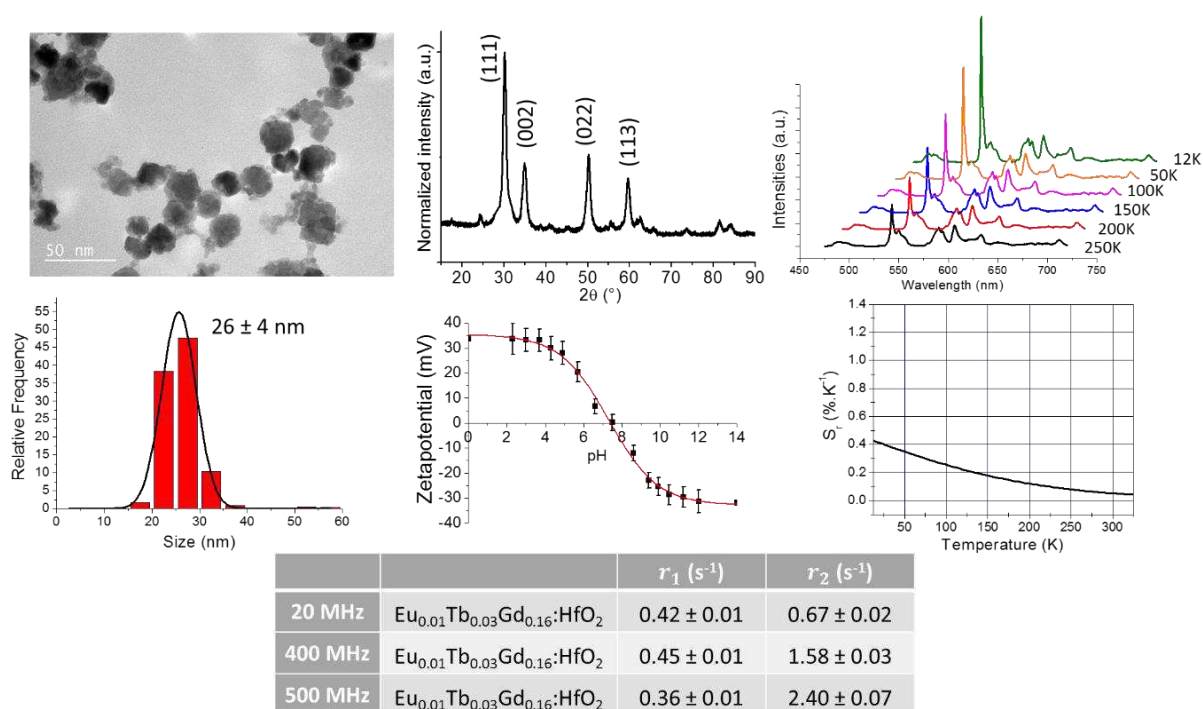


Figure 1: Characteristics of the sample Eu<sub>0.01</sub>Tb<sub>0.03</sub>Gd<sub>0.16</sub>:HfO<sub>2</sub> (TEM micrograph, size distribution, XRD pattern, Zetametry, emission spectra as a function of the temperature, relative sensitivity as a nanothermometer, relaxivities)

The interaction of TiO<sub>2</sub> NPs with human cells was studied, namely the quantification of their internalization, and intracellular localization in the different cell compartments [1]. The same procedure is in progress for HfO<sub>2</sub> NPs.

As I conclude my thesis, an outstanding challenge remains to be addressed: the study of the metabolic pathways induced by the concomitant use of ionizing radiation and NPs. We have obtained in collaboration with CENBG and Institut Bergonié suggest some preliminary results about a combined effect of ionizing radiation and TiO<sub>2</sub> NPs (Figure 2) whose mechanism is still under study.

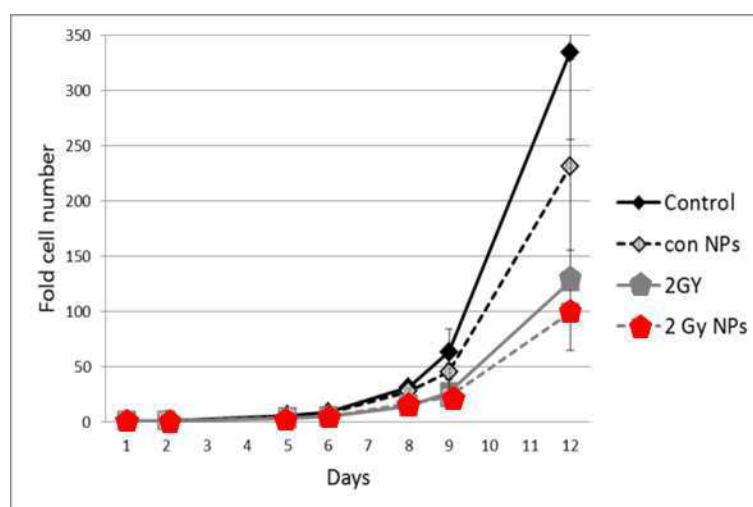


Figure 2: Evolution of the cell numbers after several irradiations dose by photons (6MeV) with HeLa Cells and scrolled nanosheets TiO<sub>2</sub> NPs. The concentration of the NPs in this study is 2 $\mu\text{g}\cdot\text{cm}^{-2}$ .

In the case of scrolled nanosheets of the TiO<sub>2</sub> NPs on HeLa cells, without irradiation, the internalization induced a decrease of the number of cells in comparison with the number of cells obtained without any NPs. Thus, we can suppose that there is a number of cells who dies due to the toxicity of the scrolled nanosheets. If we compare now, the number of cells without NPs and with and without irradiation, the results show a decrease of the number of cells with irradiation, meaning that the ionizing radiation induces some cell death. With irradiation and in the presence of NPs, the number of cells is more decreased than without NPs. Indeed, these preliminary results seem to confirm the sensitizing effect instead of the enhancing effect.

However, more studies are needed to confirm this conclusion, using hafnium dioxide and titanium dioxide NPs with the same cell lines. It will be also interesting to study the effect of the dose irradiation, the concentration of the NPs as a function of the various cancer cell lines.

## Bibliography

1. Simon, M.; Saez, G.; Muggiolu, G.; Lavenas, M.; Le Trequesser, Q.; Michelet, C.; Devès, G.; Barberet, P.; Chevet, E.; Dupuy, D.; Delville, M.-H.; Seznec, H., In situ quantification of diverse titanium dioxide nanoparticles unveils selective endoplasmic reticulum stress-dependent toxicity. *Nanotoxicology* **2017**, *11* (1), 134-145.

THÈSE EN COTUTELLE PRÉSENTÉE  
POUR OBTENIR LE GRADE DE  
**DOCTEUR DE**  
**L'UNIVERSITÉ DE BORDEAUX**  
**ET DE L'UNIVERSITÉ D'AVEIRO**

ÉCOLE DOCTORALE DES SCIENCES CHIMIQUES  
ÉCOLE DOCTORALE DE QUÍMICA D'AVEIRO  
SPÉCIALITÉ PHYSICO-CHIMIE DE LA MATIÈRE CONDENSÉE

Par Magali LAVENAS

**Multifunctional nanoparticles for imaging and tracking with  
potential applications in radiotherapy**

Sous la direction de Marie-Hélène DELVILLLE  
et de João ROCHA

Soutenue le mercredi 6 décembre 2017

Membres du jury :

M. PIO Casimiro Adrião	Universidade de Aveiro	Président
Mme BEGIN-COLLIN Sylvie	Université de Strasbourg	Rapporteur
M. GERALDES Carlos FGC	Universidade de Coimbra	Rapporteur
Mme DELVILLE Marie-Hélène	ICMCB, CNRS	Directeur de thèse
M. ROCHA João	Universidade de Aveiro	Directeur de thèse
M. TOUPANCE Thierry	Université de Bordeaux	Examinateur
Mme BERMUDEZ Veronica Zea	Universidade de Trás-os-Montes e Alto Douro	Examinateur
M. FARINHA José	Universidade de Lisboa	Examinateur
M. CARLOS Luis D	Universidade de Aveiro	Invité

## Table des matières

Introduction.....	3
I - Chapitre 1: Etat de l'art .....	3
II - Chapitre 2 : Synthèse de nanoparticules de TiO <sub>2</sub> .....	4
III - Chapitre 3 : Synthèse de nanoparticules de HfO <sub>2</sub> .....	6
IV - Chapitre 4 : Imagerie optique et nanothermométrie .....	9
V - Chapitre 5 : Relaxométrie.....	10
Conclusion .....	11
Bibliographie .....	11

## Introduction

Une des plus grandes causes de mortalité aujourd'hui est le cancer. Actuellement, les nanotechnologies ont permis le développement de nouvelles approches dans le traitement du cancer. Ainsi, il est devenu nécessaire de concevoir et modéliser des nanoparticules (NPs) multimodales et d'évaluer leur application thérapeutique potentielle. Les nanoparticules inorganiques étudiées dans le cadre de ce travail sont basées sur des oxydes métalliques (e.g.  $\text{TiO}_2$  and  $\text{HfO}_2$ ) et présentent plusieurs fonctionnalités permettant leur localisation et leur quantification en utilisant différentes techniques telles que l'IRM et l'imagerie optique.

Cette thèse est divisée en cinq chapitres. Tout d'abord, le chapitre 1 fait un état de l'art sur les caractéristiques nécessaires pour l'utilisation de nanoparticules dans le domaine biomédical, ainsi que le choix des nanoparticules qui vont être étudiées. Ensuite, la synthèse et la caractérisation de nanoparticules de  $\text{TiO}_2$  et  $\text{HfO}_2$  sont présentées respectivement dans le chapitre 2 et le chapitre 3. Finalement, les propriétés optiques de ces nanoparticules sont détaillées dans le chapitre 4, tandis que les mesures de relaxivité sont expliquées dans le chapitre 5.

### I - Chapitre 1: Etat de l'art

Tout d'abord, les différents modes d'injection de nanoparticules dans le corps humain sont détaillés. Il existe entre autres l'injection par intraveineuse, la diffusion par la peau, ou encore par injection directement dans une tumeur. Par intraveineuse, les deux mécanismes qui permettent aux nanoparticules d'atteindre les cellules cancéreuses sont le ciblage actif et le ciblage passif [1]. Le premier est dû à une reconnaissance clé-serrure grâce à une fonctionnalisation des nanoparticules à l'aide d'anticorps, de protéines... Le ciblage passif, quant à lui, profite des interstices créés entre les cellules endothéliales. Les nanoparticules passent donc dans ces interstices et s'accumulent donc dans la tumeur.

Quand des oxydes métalliques sont bombardés par des rayonnements ionisants, un grand nombre d'électrons sont produits localement, augmentant la dose d'énergie dans la tumeur. Ainsi, l'efficacité de la radiothérapie est améliorée en minimisant la dose d'irradiation sur les cellules saines environnantes. Deux mécanismes peuvent avoir lieu : la radiopotentialisation et la radiosensibilisation. Plus le numéro atomique de l'atome est élevé, plus le nombre

d'électrons générés localement le sera aussi, il s'agit de la radiopotentialisation [2]. Le second mécanisme (radiosensibilisation) est basé sur la toxicité des nanoparticules. Les nanoparticules, internalisées par les cellules, induisent un stress et une modification dans la concentration des ions. Ainsi, les cellules sont fragilisées et sont donc moins susceptibles de résister aux rayonnements ionisants [3]. Notre but est donc d'étudier deux types d'oxydes métalliques afin de montrer quel mécanisme est le plus plausible. Nous avons fait le choix d'étudier le dioxyde de titane (numéro atomique faible) et d'hafnium (numéro atomique élevé). L'objectif sera donc de synthétiser des nanoparticules de taille et de morphologie contrôlées de dioxyde de titane et de dioxyde d'hafnium.

## II - Chapitre 2 : Synthèse de nanoparticules de TiO<sub>2</sub>

Le dioxyde de titane, TiO<sub>2</sub> est couramment utilisé dans les crèmes solaires, comme additif dans les aliments (E 171). Le TiO<sub>2</sub> est un composé inerte chimiquement possédant un indice de réfraction élevé (2.61). Le dioxyde de titane se retrouve sous trois formes cristallines qui sont l'anatase, le rutile ou la brookite.

Plusieurs méthodes de synthèses de nanoparticules ont été développées dans la littérature. La méthode sol-gel, qui permet de synthétiser des nanoparticules à partir d'alkoxydes de métal, M(OR)<sub>4</sub> en présence d'une solution aqueuse de former un gel. Ces réactions sont très généralement effectuées à température ambiante, et permettent de synthétiser des sphères de TiO<sub>2</sub> de plusieurs centaines de nanomètres [4-5]. Cependant, le plus gros désavantage de cette technique est la nécessité de traitement thermique afin d'avoir une cristallisation de nanoparticules. Ainsi, un phénomène d'agrégation des nanoparticules apparaît et aboutit à la difficulté de redisperser ces NPs pour de futures applications biologiques.

Une autre méthode développée est la synthèse hydrothermale. Nian *et al.* montrent qu'il est possible d'obtenir des nanoparticules de TiO<sub>2</sub> et de contrôler leurs tailles et leurs formes en variant le pH, à partir de P25. Le P25 est constitué de nanoparticules de TiO<sub>2</sub> synthétisées commercialement par voie aérosol. Elles sont constituées à 80% d'anatase et à 20% de rutile. Nous avons décidé de développer nos NPs de TiO<sub>2</sub> à partir de P25. Le P25 subit un premier traitement hydrothermal à 130 °C pendant 23 h dans des conditions très basiques pour former des nanofeuillets enroulés. Puis ces nanofeuillets forment des nanoaiguilles après un second traitement hydrothermal à pH 9.5, à 140 °C pendant 3 jours (Figure 1).

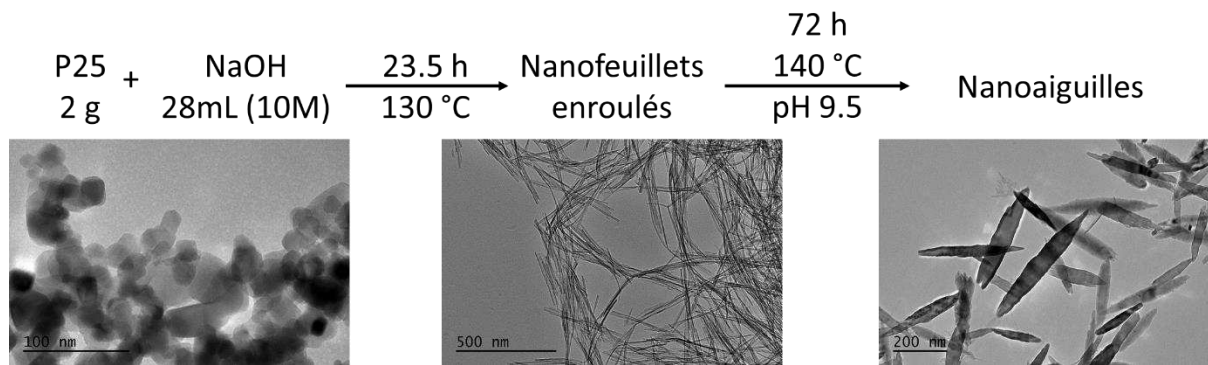


*Figure 1: Méthode de synthèse de nanoaiguilles de  $\text{TiO}_2$  à partir de P25 [6]*

Par cette méthode de synthèse, des nanoaiguilles de  $\text{TiO}_2$  sont obtenues avec une longueur d'environ 350 nm et une largeur de 46 nm (Figure 2s).

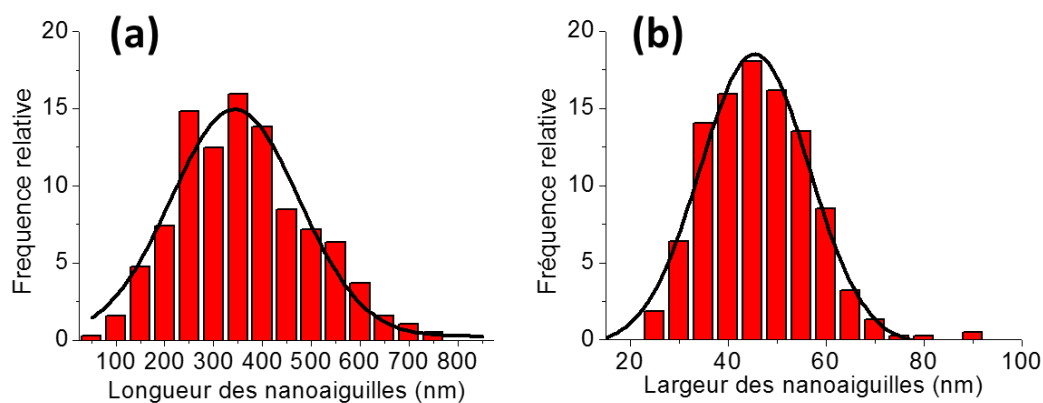


*Figure 2: Distribution (a) en longueur et (b) en largeur des nanoaiguilles de  $\text{TiO}_2$  (statistiques effectuées sur plus de 300 NPs)*

Ainsi les nanoaiguilles obtenues sont trop longues pour être utilisées pour des applications biologiques, c'est la raison pour laquelle des agents structurants ont été utilisés pour décroître leur taille. Les agents structurants étudiés sont l'acide oléique (OA) et la triéthanolamine (TEOA) [7]. L'utilisation seule de ces agents n'aboutit pas à une diminution de la taille des nanoaiguilles, il faut un effet couplé de ces deux agents afin de diminuer drastiquement leur taille (Figure 3).

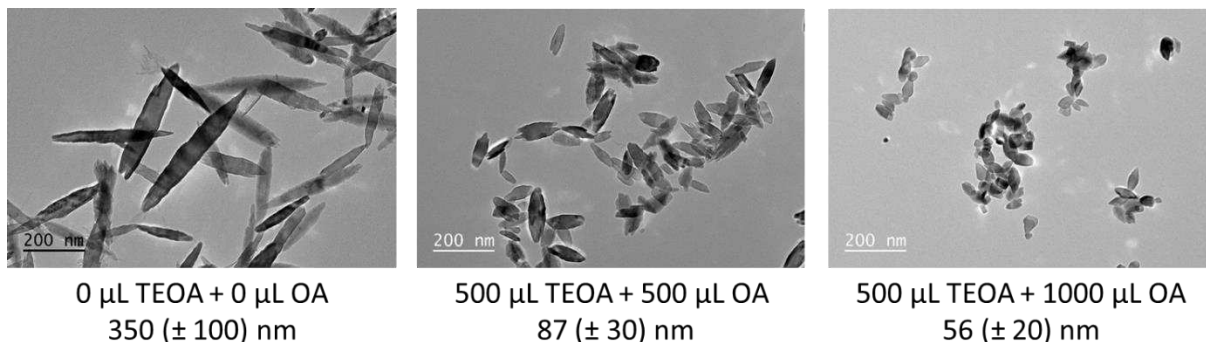


*Figure 3: Effet du volume de TEOA et d'OA sur la longueur des NPs de  $TiO_2$  synthétisées avec un pH initial de 9.5 à 140 °C pendant 3 jours.*

Ainsi, l'objectif d'obtenir des NPs de taille comprise entre 30 et 60 nm a été atteint.

### III - Chapitre 3 : Synthèse de nanoparticules de $HfO_2$

La synthèse de dioxyde d'hafnium a été beaucoup moins étudiée. Cependant, quelques travaux permettent de synthétiser des NPs de  $HfO_2$  par méthode de précipitation [8-9], par voie sol-gel [10] et par voie hydrothermale [11-12]. Nous avons décidé de choisir la voie hydrothermale pour les mêmes raisons. Nous avons basé notre travail sur le papier de Štefanić auquel les analyses par microscopie ont été ajoutées. Les synthèses ont été effectuées à partir de tétrachlorure d'hafnium ( $HfCl_4$ ), le pH est ajusté par ajout d'une solution de soude à 0.1 M. La synthèse conduit à l'obtention de NPs cristallines sous la phase monoclinique. Tout d'abord, l'influence de la valeur du pH initial a été étudiée (Figure 4), montrant une différence de forme et d'aspect des NPs. A pH 3, des NPs de formes géométriques sont obtenues, tandis qu'à pH 9.5, des NPs présentant des formes de losanges sont observées et à pH 13, ce sont des NPs en forme de grain de riz qui sont obtenues. Pour la suite, le pH conduisant à des NPs avec la distribution statistique la plus faible a été choisi.

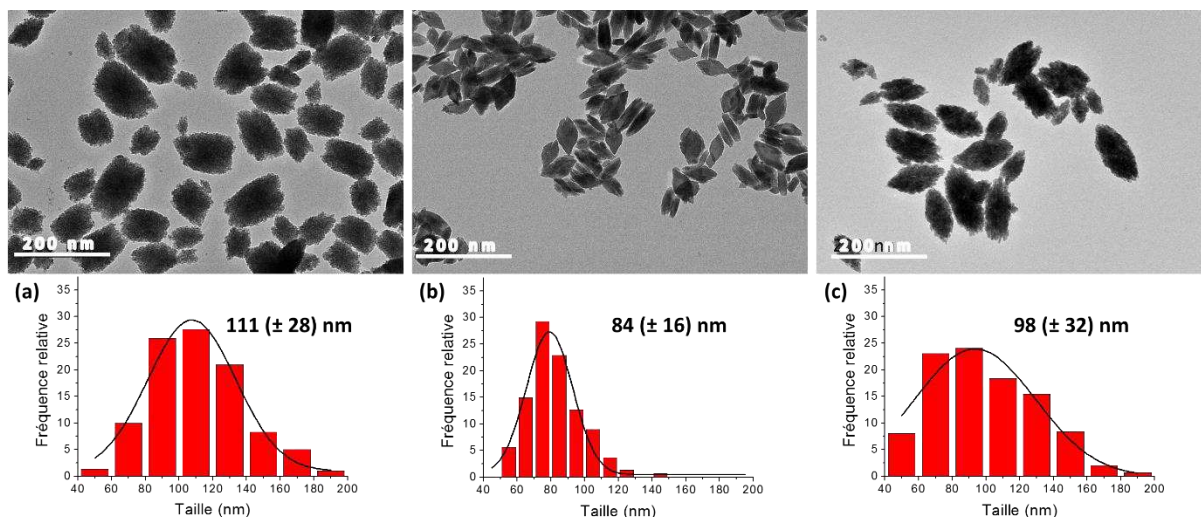


Figure 4: TEM images et distributions statistiques de la taille des nanoparticules de  $\text{HfO}_2$  synthétisées à 120 °C pendant 48 h à pH (a) 3, (b) 9.5 et (c) 13

Cependant, la taille des NPs obtenue est trop importante pour l'application visée. Le temps de réaction et la température de traitement hydrothermal ont été étudiés afin de diminuer la taille des NPs (Figure 5).

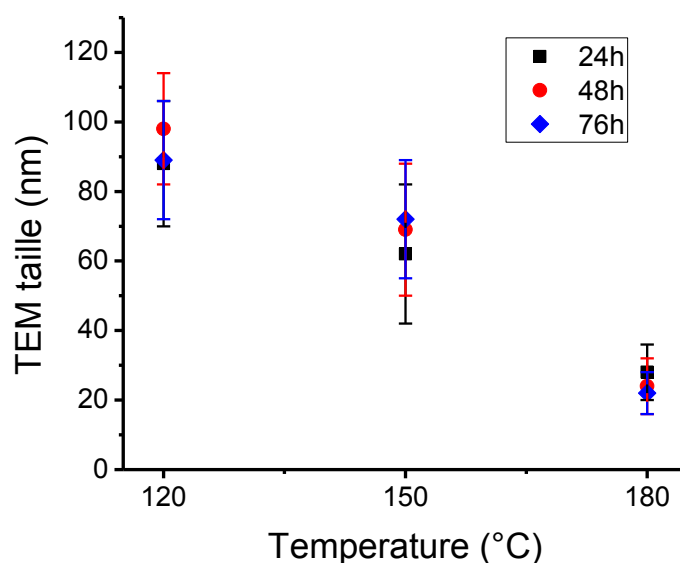


Figure 5: Diminution de la taille des NPs en fonction de la température, à pH 9.5

Ainsi, en travaillant à pH 9.5, 180 °C et pendant 48 heures, nous pouvons obtenir des NPs de l'ordre de 30 nm, satisfaisant pour les applications visées.

Maintenant, afin d'obtenir des NPs portant plusieurs fonctionnalités, des lanthanides peuvent être insérés dans la matrice du  $\text{HfO}_2$ . Lors de l'insertion de lanthanides, un changement de structure cristalline est observé (Figure 6).

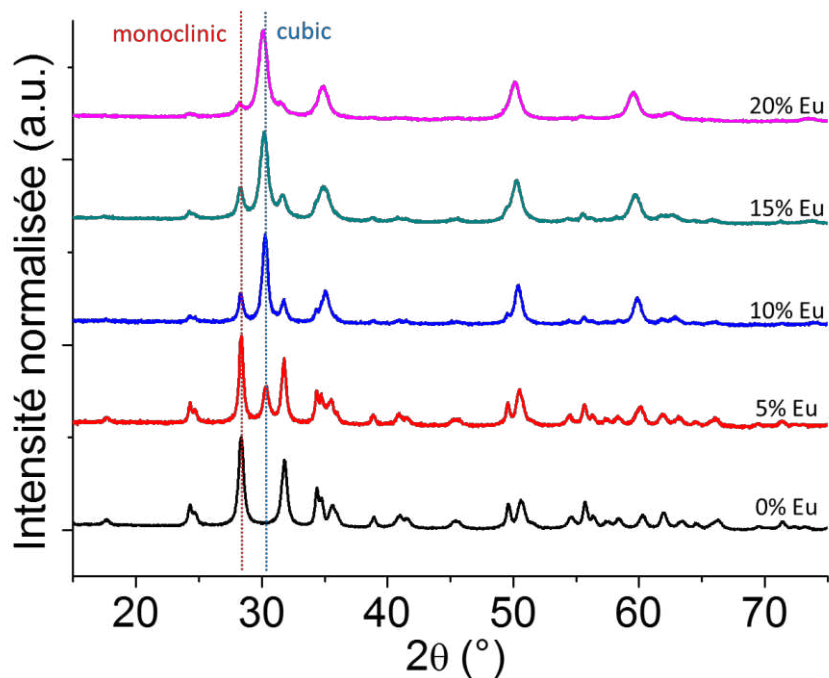


Figure 6: Diffractogramme RX présentant l'évolution de la structure cristalline des NPs de  $\text{HfO}_2$  avec l'insertion de différents pourcentages d'Europium

Le passage de la phase monoclinique à cubique est observé lors de l'insertion d'euporium de terbium et de gadolinium. Ainsi, pour de futures applications en imagerie optique et magnétique, les 3 lanthanides précédemment cités ont été insérés dans la même matrice de  $\text{HfO}_2$  avec un pourcentage total de lanthanide de 20% pour obtenir uniquement la phase cubique (Figure 7).

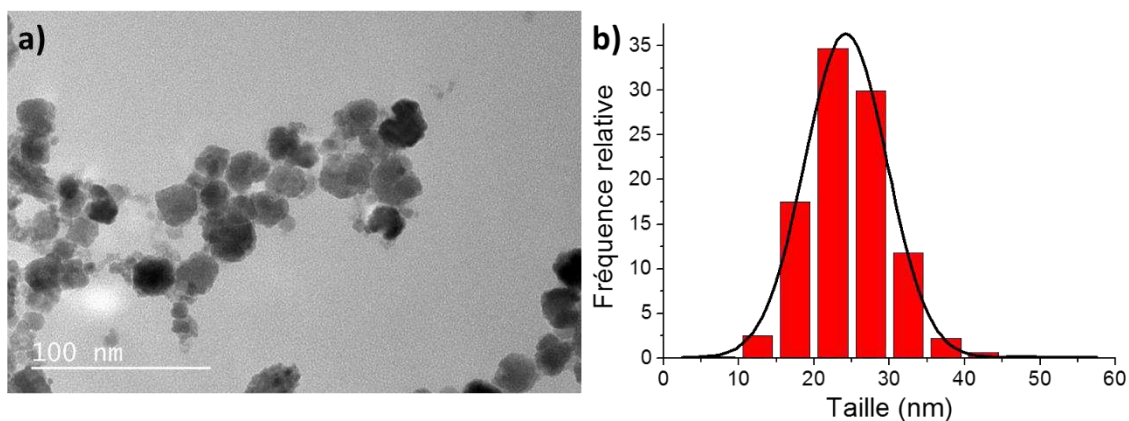


Figure 7: (a) Images TEM et (b) distribution statistique en taille des NPs de  $\text{HfO}_2$  avec 20% de lanthanides synthétisées à 180 °C, avec un pH initial de 9.5 et pendant 48 heures

Différentes ratio entre les 3 lanthanides ont été choisis et les notations suivantes seront utilisées par la suite:  $\text{Eu}_{0.01}\text{Tb}_{0.03}\text{Gd}_{0.16}:\text{HfO}_2$  pour  $\text{HfO}_2$ : 1%Eu, 3%Tb, 16%Gd,  $\text{Eu}_{0.03}\text{Tb}_{0.05}\text{Gd}_{0.12}:\text{HfO}_2$  pour  $\text{HfO}_2$ : 3%Eu, 5%Tb, 12%Gd et,  $\text{Eu}_{0.05}\text{Tb}_{0.10}\text{Gd}_{0.05}:\text{HfO}_2$  pour  $\text{HfO}_2$ : 5%Eu, 10%Tb, 5%Gd.

## IV - Chapitre 4 : Imagerie optique et nanothermométrie

Après avoir réussi à synthétiser des NPs susceptibles de présenter plusieurs fonctionnalités, il nous faut maintenant les caractériser. Tout d'abord, les nanoparticules de  $\text{HfO}_2$  dopées avec un seul type de lanthanide ont été caractérisées par leurs spectres d'excitation et d'émission. La transition caractéristique de l'euporium ( $^5\text{D}_0 \rightarrow ^7\text{F}_2$ ) et celle du terbium ( $^5\text{D}_4 \rightarrow ^7\text{F}_5$ ) sont observées respectivement à 614 nm et à 543 nm responsables des couleurs caractéristiques, rouge pour l'euporium et vert pour le terbium.

La nanothermométrie est basée sur un équilibre entre les niveaux  $^5\text{D}_4$  du Tb et  $^5\text{D}_0$  de l'Eu qui varie en fonction de la température. Ainsi, en analysant les spectres d'émission des NPs en fonction de la température, on peut créer une base de données qui pourra ensuite servir à la détermination précise de la température. De plus, pour déterminer l'efficacité d'un nanothermomètre, il est nécessaire de calculer sa sensibilité relative. Ainsi, les spectres d'émission des NPs dopées avec Eu, Gd et Tb ont été mesurés de 12 K à 325 K (Figure 8) et les sensibilités relatives déterminées (Figure 9).

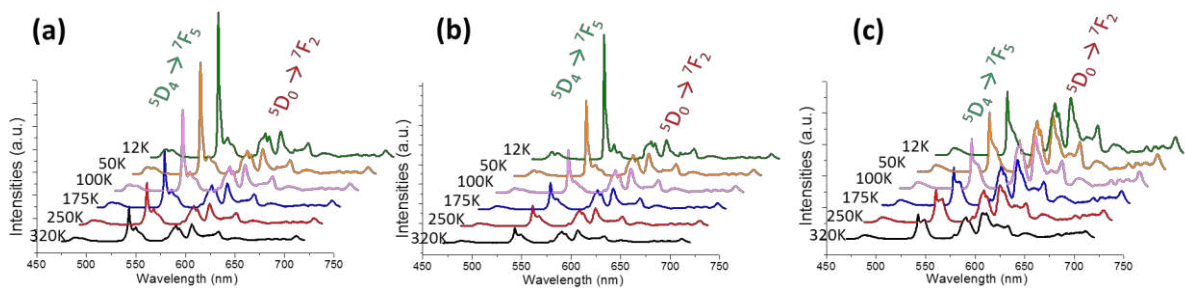


Figure 8: Spectres d'émission de (a)  $\text{Eu}_{0.01}\text{Tb}_{0.03}\text{Gd}_{0.16}:\text{HfO}_2$ , (b)  $\text{Eu}_{0.03}\text{Tb}_{0.05}\text{Gd}_{0.12}:\text{HfO}_2$  et de (c)  $\text{Eu}_{0.05}\text{Tb}_{0.10}\text{Gd}_{0.05}:\text{HfO}_2$  en fonction de la température sous une excitation de 280 nm

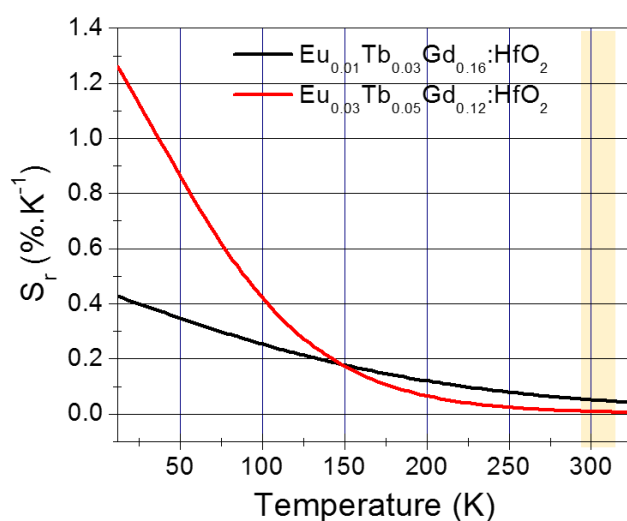


Figure 9: Sensibilités relatives déterminées à l'aide du ratio d'intensité de la bande caractéristique du Tb et celle de l'Eu.

## V - Chapitre 5 : Relaxométrie

Les mesures de  $r_1$  et  $r_2$  ont été effectuées sur plusieurs échantillons, à deux températures et à différentes valeurs de champs magnétiques (20, 400 et 500 MHz).

20 MHz	$r_1$ (s <sup>-1</sup> )		$r_2$ (s <sup>-1</sup> )	
	25 °C	37 °C	25 °C	37 °C
<b>Gd<sub>0.26</sub>:HfO<sub>2</sub></b>	0.93 ± 0.01	0.89 ± 0.01	1.09 ± 0.03	1.14 ± 0.03
<b>Eu<sub>0.01</sub>Tb<sub>0.03</sub>Gd<sub>0.16</sub>:HfO<sub>2</sub></b>	0.42 ± 0.01	0.39 ± 0.01	0.67 ± 0.02	0.59 ± 0.03
<b>Eu<sub>0.03</sub>Tb<sub>0.05</sub>Gd<sub>0.12</sub>:HfO<sub>2</sub></b>	0.49 ± 0.01	0.49 ± 0.01	0.86 ± 0.03	0.76 ± 0.01
<b>Yb<sub>0.01</sub>Er<sub>0.05</sub>Gd<sub>0.19</sub>:HfO<sub>2</sub></b>	0.099 ± 0.006	0.110 ± 0.003	0.24 ± 0.01	0.25 ± 0.02
<b>Yb<sub>0.02</sub>Er<sub>0.10</sub>Gd<sub>0.13</sub>:HfO<sub>2</sub></b>	0.144 ± 0.004	0.13 ± 0.02	0.29 ± 0.01	0.22 ± 0.01

Figure 10: Valeurs de relaxivité des protons,  $r_i$  ( $i=1,2$ ), déterminées à 20 MHz à 25 °C et 37 °C

## Conclusion

Ainsi, l'objectif de synthétiser des nanoparticules de taille et de morphologie contrôlées de dioxyde de titane et de dioxyde d'hafnium a été atteint. Nous avons réussi à insérer des lanthanides dans la matrice de HfO<sub>2</sub> lui conférant de nombreuses propriétés, tant optique que magnétique.

## Bibliographie

1. Nie, S.; Xing, Y.; Kim, G. J.; Simons, J. W., Nanotechnology applications in cancer. *Annual Review Biomedical Engineering* **2007**, *9*, 257-288.
2. Kobayashi, K.; Usami, N.; Porcel, E.; Lacombe, S.; Le Sech, C., Enhancement of radiation effect by heavy elements. *Mutation Research, Reviews in Mutation Research* **2010**, *704*, 123-131.
3. Kwatra, D.; Venugopal, A.; Anant, S., Nanoparticles in radiation therapy: a summary of various approaches to enhance radiosensitization in cancer. *Translational Cancer Research* **2013**, *2* (4), 330-342.
4. Matijević, E.; Budnik, M.; Meites, L., Preparation and mechanism of formation of titanium dioxide hydrosols of narrow size distribution. *Journal of Colloid and Interface Science* **1977**, *61* (2), 302-311.
5. Eiden-Assmann, S.; Widoniak, J.; Maret, G., Synthesis and Characterization of Porous and Nonporous Monodisperse Colloidal TiO<sub>2</sub> Particles. *Chemistry of Materials* **2004**, *16* (1), 6-11.
6. Nian, J.-N.; Teng, H., Hydrothermal Synthesis of Single-Crystalline Anatase TiO<sub>2</sub> Nanorods with Nanotubes as the Precursor. *The Journal of Physical Chemistry B* **2006**, *110*, 4193-4198.
7. Sugimoto, T.; Zhou, X.; Muramatsu, A., Synthesis of uniform anatase TiO<sub>2</sub> nanoparticles by gel-sol method: 4. Shape control. *Journal of Colloid and Interface Science* **2003**, *259* (1), 53-61.
8. Ramadoss, A.; Kim, S. J., Synthesis and characterization of HfO<sub>2</sub> nanoparticles by sonochemical approach. *Journal of Alloys and Compounds* **2012**, *544*, 115-119.
9. Jayaraman, V.; Bhavesh, G.; Chinnathambi, S.; Ganesan, S.; Aruna, P., Synthesis and characterization of hafnium oxide nanoparticles for bio-safety. *Materials Express* **2014**, *4*, 375-383.
10. Ramos-Gonzalez, R.; Garcia-Cerda, L. A.; Alshareef, H. N.; Gnade, B. E.; Quevedo-Lopez, M. A., Study of hafnium(IV) oxide nanoparticles synthesized by polymerized complex and polymer precursor derived sol-gel methods. *Materials Science Forum* **2010**, *644*, 75-78.
11. Buha, J.; Arcon, D.; Niederberger, M.; Djerdj, I., Solvothermal and surfactant-free synthesis of crystalline Nb<sub>2</sub>O<sub>5</sub>, Ta<sub>2</sub>O<sub>5</sub>, HfO<sub>2</sub>, and Co-doped HfO<sub>2</sub> nanoparticles. *Physical Chemistry Chemical Physics* **2010**, *12*, 15537-15543.
12. Štefanić, G.; Musić, S.; Molčanov, K., The crystallization process of HfO<sub>2</sub> and ZrO<sub>2</sub> under hydrothermal conditions. *Journal of Alloys and Compounds* **2005**, *387* (1-2), 300-307.

## **Titre : Synthèse de nanoparticules multifonctionnelles pour le diagnostic et l'imagerie médicale avec de futures applications en radiothérapie**

**Résumé :** Une des plus grande cause de mortalité aujourd'hui est le cancer. Actuellement, les nanotechnologies ont permis le développement de nouvelles approches dans le traitement du cancer. Ainsi, il est devenu nécessaire de concevoir et modeler des nanoparticules (NPs) multimodales et d'évaluer leur application thérapeutique potentielle. Les nanoparticules inorganiques étudiées dans le cadre de ce travail sont basées sur des oxydes métalliques (*e.g.* TiO<sub>2</sub> and HfO<sub>2</sub>) et présentent plusieurs fonctionnalités permettant leur localisation et leur quantification en utilisant différentes techniques telles que l'IRM et l'imagerie optique. Notamment grâce à l'insertion de terres rares dans la matrice des NPs. D'autre part, comme la température des cellules saines et cancéreuses diffère, la détermination locale de la température peut être intéressante et obtenue par l'étude de la luminescence d'une paire de terres rares judicieusement choisie.

Ainsi, des NPs de TiO<sub>2</sub> et de HfO<sub>2</sub> ont été synthétisées par voie hydrothermale, permettant un contrôle de leur taille et de leur morphologie. De plus, des terres rares, comme l'euprimum, le terbium et le gadolinium ont été insérées au sein des matrices d'oxyde d'hafnium permettant d'obtenir des nanoparticules multifonctionnelles, basées sur la détection par imagerie optique et magnétiques et la détection de la température (nanothermomètre). Les NPs ont été caractérisées et des mesures de relaxivité ont été effectuées. La luminescence de ces NPs a été étudiée et a permis la mise au point d'un nanothermomètre avec une sensibilité de 0.1 %.K<sup>-1</sup>.

**Mots clés :** nanoparticules, imagerie, radiothérapie, terre-rare, multifonctionnelles

---

## **Title: Multifunctional nanoparticles for imaging and tracking with potential applications in radiotherapy**

**Abstract:** Cancer is one of the main cause of mortality in the world. Recently, nanotechnologies have led to new approaches in cancer therapy. In this context, it is important to design multimodal nanoparticles (NPs) and assess their therapeutic potential. The inorganic NPs studied here are based on metal oxides (*e.g.*, TiO<sub>2</sub> and HfO<sub>2</sub>) exhibiting functionalities that allow their localization and tracking using various techniques (MRI, luminescence), as well as their quantification. For this purpose, rare-earth elements are inserted in the metal oxide matrices. As the lethal temperatures for healthy and tumor cells are different, it is also important to ascertain the temperature of the cells during ionizing radiation treatment. This may be achieved based on the light emission of suitable pairs of rare-earth elements.

Thus, titania and hafnia nanoparticles were synthesized by the hydrothermal method enabling the control of morphology and size. Furthermore, the hafnia matrices were doped with rare-earth elements, such as europium, terbium and gadolinium, endowing NPs with functionalities such as luminescence tracking, magnetic resonance imaging and nanothermometry. The chemical characterizations were performed and the relaxivity constants were assessed. The luminescence response was also studied, and one nanothermometer with a sensitivity at room temperature ca. 0.1 %.K<sup>-1</sup> was obtained.

**Keywords:** nanoparticles, imaging, radiotherapy, rare-earth, multifunctional

---

## **Unité de recherche**

Institut de Chimie de la Matière Condensée de Bordeaux (ICMCB) – UPR 9048

Institute of Materials (CICECO), Universidade de Aveiro